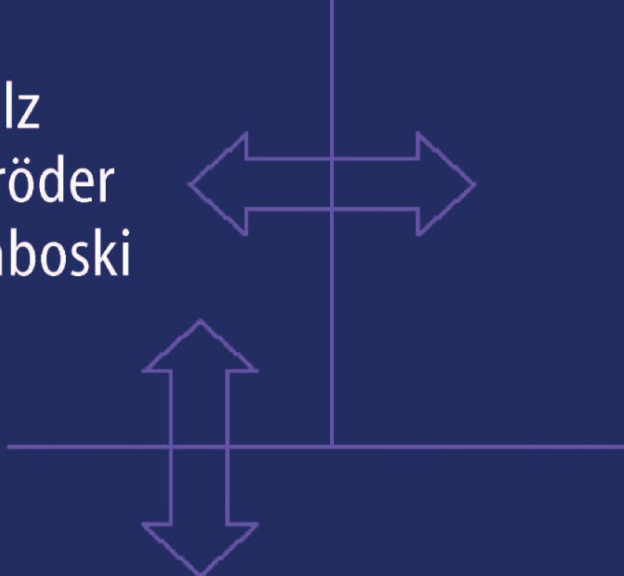


F. Scholz  
U. Schröder  
R. Gulaboski



# Electrochemistry of Immobilized Particles and Droplets

 Springer

F. Scholz • U. Schröder • R. Gulaboski

---

Electrochemistry of  
Immobilized Particles and Droplets



Fritz Scholz • Uwe Schröder  
Rubin Gulaboski

# Electrochemistry of Immobilized Particles and Droplets

With a Foreword by John O'M. Bockris  
(Gainesville, Florida)

With 200 Figures and 15 Tables

 Springer

**Prof. Dr. Fritz Scholz**  
Universität Greifswald  
Institut für Chemie und Biochemie  
Soldmannstraße 23  
17489 Greifswald  
Germany  
*e-mail: fscholz@uni-greifswald.de*

**Dr. Rubin Gulaboski**  
Present address:  
Departamento de Química  
Faculdade de Ciências  
Universidade do Porto  
Rua do Campo Alegre, 687  
469-007 Porto  
Portugal

**Dr. Uwe Schröder**  
Universität Greifswald  
Institut für Chemie und Biochemie  
Soldmannstraße 16  
17489 Greifswald  
Germany  
*e-mail: uweschr@uni-greifswald.de*

Library of Congress Control Number: 2004109921

**ISBN 3-540-22005-4 Springer Berlin Heidelberg New York**

This work is subject to copyright. All rights are reserved, whether the whole or part of the material is concerned, specifically the rights of translation, reprinting, reuse of illustrations, recitation, broadcasting, reproduction on microfilm or in any other way, and storage in data banks. Duplication of this publication or parts thereof is permitted only under the provisions of the German Copyright Law of September 9, 1965, in its current version, and permission for use must always be obtained from Springer. Violations are liable for prosecution under the German Copyright Law.

**Springer is a part of Springer Science+Business Media**  
springeronline.com

© Springer-Verlag Berlin Heidelberg 2005  
Printed in Germany

The use of designations, trademarks, etc. in this publication does not imply, even in the absence of a specific statement, that such names are exempt from the relevant protective laws and regulations and therefore free for general use.

Typesetting: Computer to film by authors' data  
Cover design: design & production, Heidelberg  
Production: Verlagsservice Heidelberg  
Printed on acid-free paper 2/3130XT 5 4 3 2 1 0

## Foreword

Fundamental Electrode Kinetics is represented by treatments of reactions such as  $\text{O}_2 + 4\text{H}^+ + 4\text{e}^- \rightleftharpoons 2\text{H}_2\text{O}$ , - still important in the theory of electrocatalysis. As for the cutting edge in Electrochemistry is concerned, that is now far away into areas of complexity. In this fascinating book Professor Scholz and his colleagues have written academically about a group of phenomena bordering on practical reality.

The material in the book develops out from a vast change which came to Electrochemistry in the 1960's when it was realized that metals were not the only materials which could act as electrodes: germanium and silicon were the first to be examined but the leading principle which allowed such developments was the many orders of magnitude change in conductivity which is brought about by impurities naturally present or added.

Professor Scholz' book takes a certain group of metallic and non-metallic materials, -immobilized particles and droplets, -and presents their electrochemistry. Much of this detailed work involves three phase boundary and many fuel-cell oriented electrochemists will be familiar with something similar arising in the theory of some types of porous electrodes.

The treatments in this book are certainly modern - to make sure of this the authors have a preliminary chapter in which they compress a description of work before about 1990, -dealing, e.g., with colloids and sandwich electrodes. Then comes chapter 2 in which three phase electrodes are met. After that comes a solid chapter on the experimental methods of the field: for example, -how does one immobilize small particles for measurement; or attach droplets? Chapter 4 is called Hyphenated Techniques and it brings out the applications to the field of spectro-electrochemistry. Chapter 5 concerns immobilized particles and here we realize the full complexity of the systems treated, e.g., voltammograms are shown of systems containing several phases; and relevant data on the electrochemistry of minerals is described. The theory of such systems is presented with impressive clarity and detail.

The last chapter (6) is about droplets and the electrochemistry of compounds dissolved therein and includes a properly modern discussion of the electrochemistry of liquid-liquid interfaces.

Treatments of the thermodynamics of these systems is fully described but the kinetic treatments are less than full because of the interplay of resistance effects, concentration overpotential and the basic electron transfer kinetics which is position dependent. There is good opportunity for impedance spectroscopy in these systems. Descriptions of many electrochemical events seldom met elsewhere is given, e.g., ion transfer from water to nitrobenzene, atom-force microscopy to study immobilized silver nano-crystals and their oxidation, which proceeds via an oversaturated silver halide solution.

The book gives strong attention to quartz crystal micro-balance, able to record changes of nanograms. Impressive sensitivity of  $10^{-3}$  K is exhibited by equipment used to determine entropy changes in hexacyanoferrates. The description given in Chapter 4 of the thermodynamics of minerals is impressive – and will find application, e.g., in rechargeable  $\text{MnO}_2$  cells. Descriptions of the penetration of particles by redox reactions through micro-crystals typifies some of the material.

I read this book with increasing pleasure. It is certainly specialized, but in my opinion its significance is greatly increased by the fact that it clearly represents an attempt by these German colleagues to gather descriptions of work closely approaching that of real systems – and for that they should be greatly thanked, and their book widely distributed.

Gainesville, Florida, November 2004

John O'M. Bockris

## Preface

Electrochemistry provides a range of powerful techniques, which can be used to study liquid electrolyte solutions, solid electrolytes, metal and semiconductor electrodes as well as mixed ion and electron conductors. The most important question in deciding on the applicability of electrochemical techniques has always been on the *how* of making an electrode or a solution of a compound to be studied. This has set the most serious limitations to general applications. An important step forward in the applicability of electrochemistry has been achieved by showing that a mechanical immobilization of *particles* onto the surface of inert electrodes allows electrochemical measurements on any compound or material, provided it does not dissolve in the electrolyte solution. Organic liquids and solutions immiscible with aqueous electrolyte solutions, can be immobilized on electrode surfaces in the form of *droplets*. The electrochemistry presented in this monograph is very diverse while there is one common feature: all electrodes with immobilized electroactive particles and droplets are characterized by *electron* transfer and an *ion* transfer occurring simultaneously at one and the same electrode. As a result, the model of a *three-phase electrode* will be the guiding principle throughout the entire book.

This monograph summarizes the content of more than 300 publications listed at the end of the book in a bibliography. They are referenced as, e.g., "B 235". Additional references that do not belong to the bibliography are cited as footnotes on the respective pages.

The book introduces the experimental basis and theoretical foundations of the electrochemistry of immobilized particles and droplets. The authors are aware that various results and theoretical considerations from other fields of electrochemistry would deserve to be mentioned as well; however the scope of this book limits such detail.

The mechanical immobilization of particles and droplets on electrode surfaces has proved to be useful for solving both fundamental and applied issues: quantitative analysis of alloys; qualitative detection of alloy phases; study of the electrochemical corrosion of metal particles; identification of mineral phases; quantitative analysis of minerals and inorganic compounds; determination of thermodynamic data of solid compounds and of the rate constants of electrochemically driven dissolution of solid com-

pounds; qualitative and quantitative determination of the composition of solid solutions; elucidation of electrochemically driven isomerizations and other reactions of solid compounds; study of insertion electrochemical systems; elucidation of solid-to-solid electrochemical reactions and of structure-reactivity relations of solid compounds; understanding of the thermodynamics of solid-state electrochemical transformations; determination of the Gibbs energies of ion transfer between an aqueous electrolyte and an immiscible organic solvent; study of the geometric reaction pathways in solid particles and droplets, etc. The growing number of applications of the new technique in several laboratories around the world may lead to much broader usage in the future, once the results are critically compiled and presented in a comprehensive treatise. One of us (F. Sch.) has initiated this project, the other two co-authors having applied and developed it further within the past few years. We hope to provide a first-hand survey, to help others to make successful use of the new technique. Electrochemical measurements on immobilized particles and droplets are an attractive addition to spectroscopic, diffraction, and microscopic techniques, as used by inorganic, organic, physical, analytical, and material chemists, who face the task of characterizing solid compounds and materials as well as immiscible liquids and solutions.

Here I would like to acknowledge the contributions of many students, co-workers, co-operation partners, guest scientists, and friends. I cannot list them all; their names can be found in the bibliography at the end of the book. However, I like to name just a few here: Lutz Nitschke was the student who performed the first experiments with immobilized particles; Birgit Meyer intensively studied minerals and contributed significantly to the general methodology; Ales Dostal from Prague started the work with metal hexacyanometalates that was continued by Uwe Schröder, Heike Kahlert, Michael Hermes, and Antje Widmann; Milivoj Lovrić and his wife Šebojka Komorsky-Lovrić (Croatia) contributed extensively to the theoretical and experimental studies with immobilized particles and droplets and became very good friends of my group in Berlin at the Humboldt University and later at the University of Greifswald. Maximiliano Bárcena-Soto (Mexico) developed the *in situ* calorimetry, and Ulrich Hasse successfully uses *in situ* AFM. Thanks also go to Valentin Mirčeski (Macedonia) and to Zbigniew Stojek (Poland). Uwe Schröder established the microscopic diffuse reflectance spectroscopy and was an active member in the hexacyanometalate project in my group and in the ionic liquid project in Richard Compton's group at Oxford University. Rubin Gulaboski (Macedonia), who performed most of the measurements in liquid-liquid ion transfer at Greifswald, and Uwe Schröder are thanked for agreeing to co-authoring this monograph. I am especially indebted to Alan Bond (Austra-

lia) who invited me to his lab and who became so much interested in this new field of electrochemistry that dozens of fascinating landmark papers have been published by his group. Keith Oldham (Canada) has been an inspiring cooperator and discussions with him are a pleasure to acknowledge. Frank Marken (UK) and Tomáš Grygar (Czech Rep.) are acknowledged for frequent exchanges of ideas and manuscripts. Mikhail Vorotyntsev (France) kindly discussed Chapter 2 with me. Finally I want to thank my family, Gudrun, Christiane, and Thilo for their patience.

Greifswald, Germany, November 2004

Fritz Scholz

# Contents

<b>1 Earlier Developed Techniques</b> .....	1
1.1 Solid Materials.....	2
1.1.1 Compact Electrodes.....	2
1.1.2 Electrochemistry of Suspensions and Colloids.....	4
1.1.3 Paste and Composite Electrodes.....	7
1.1.4 Sandwich Electrodes.....	8
1.2 Immiscible Liquids and Solutions .....	9
<b>2 Electrodes with Immobilized Particles and Droplets –   Three-Phase Electrodes</b> .....	11
<b>3 The Experiment</b> .....	19
3.1 Electrodes, Electrolytes and Electrochemical Cells .....	19
3.1.1 Electrodes .....	19
3.1.2 Electrolytes and Electrochemical Cells .....	22
3.2 Immobilisation of Particles.....	23
3.3 Attachment of Droplets.....	25
3.3.1 Attachment of Single Droplets .....	26
3.3.2 Attachment of Arrays of Microdroplets .....	27
3.4 The Electrochemical Measurement .....	29
<b>4 Hyphenated Techniques</b> .....	31
4.1 Optical Techniques and Spectroelectrochemistry.....	32
4.1.1 In Situ Spectroscopy.....	32
4.1.2 In Situ Light Microscopy and Microscopic Spectroelectro- chemistry.....	35
4.1.3 In Situ Electron Spin Resonance Spectroscopy.....	45
4.1.4 Ex Situ Spectroscopy.....	47



4.2 Atomic Force Microscopy and Scanning Tunnelling Microscopy .....	49
4.3 Electrochemical Quartz Crystal Microbalance .....	56
4.4 In Situ X-ray Diffraction .....	58
4.5 In Situ Calorimetry .....	62
<b>5 Immobilized Particles .....</b>	<b>75</b>
5.1 Metals and Alloys .....	77
5.2 Minerals and Pigments .....	81
5.2.1 Phase Identification .....	82
5.2.2 Quantitative Determination of a Phase in a Phase Mixture .....	91
5.2.3 Quantitative Analysis of the Composition of a Phase .....	93
5.2.4 Determination of Thermodynamic Data of Minerals .....	96
5.3 Solid Solutions – Identification and Quantitative Analysis.....	98
5.3.1 The Solid Solution System CuS-CuSe .....	100
5.3.2 The Solid Solution System AgCl-AgBr .....	102
5.3.3 Solid Solutions of Metal Hexacyanometalates .....	102
5.3.4 Solid Solutions of Oxides .....	106
5.4 Organometallics and Organic Compounds .....	107
5.4.1 Voltammetry of Organometallic Compounds .....	108
5.4.2 Voltammetry of Organic Compounds .....	117
5.4.3 Overview of Studied Compounds.....	122
5.5 Electrochemically Initiated Chemical Reactions of Solid Particles .....	124
5.5.1 Electrochemically Initiated Isomerizations .....	124
5.5.2 Electrochemically Initiated Substitutions .....	128
5.6 Assessing Structure-Property Relationships .....	134
5.6.1 Solid Metal Hexacyanometalates .....	134
5.6.2 The Stability Constants of Metal Dithiocarbamate Complexes and their Structure.....	138
5.7 Assessing Kinetic Properties of Electrochemical Dissolution Reactions .....	141
5.8 The Electrochemistry of Single Particles .....	147
5.9 Chemical and Enzymatic Conversion of Immobilized Particles ..	149
5.9.1 In Situ Studies.....	149
5.9.2 Ex Situ Studies .....	152
5.10 The Screening of Electrocatalysts .....	153
5.11 Theoretical Aspects of the Voltammetry of Immobilized Particles.....	155
5.11.1 Staircase Voltammetry with Finite Diffusion Space .....	155
5.11.2 The Propagation of a Redox Reaction through Microcrystals.....	158

---

5.11.3 The Effect of the Electrolyte Concentration on the Voltammetric Response of Insertion Electrodes .....	161
5.11.4 Solid State Voltammetry at a Three-Phase Junction .....	164
5.11.5 The Effect of Crystal Size and Shape on Electrochemical Signals .....	167
5.11.6 Redox Mixed Phases and Miscibility Gaps .....	171
5.11.7 Electrochemically Driven Formation of Bilayered Systems .....	178
<b>6 Immobilized Droplets .....</b>	<b>183</b>
6.1 The Electrochemistry of Redox Liquids .....	187
6.1.1 Electrochemically Driven Ion Transfer Reactions .....	189
6.1.2 Voltammetric Study of Chemically Facilitated Ion Transfer Processes across the Liquid   Liquid Interface .....	197
6.1.3 Photochemical and Chemical Reactions at Immobilized Microdroplets of Redox Liquids .....	200
6.2 The Electrochemistry of Compounds Dissolved in Droplets .....	209
6.2.1 The Determination of Standard Gibbs Energies of Transfer of Anions .....	215
6.2.2 The Determination of Standard Gibbs Energies of Transfer of Cations .....	222
6.3 Theoretical Models for the Voltammetry of Immobilized Droplets .....	227
6.3.1 Droplets of Organic Solvents with Dissolved Electroactive Compound .....	227
6.3.2 Droplets of Electroactive Liquids .....	243
<b>7 Bibliography .....</b>	<b>255</b>
<b>Subject Index .....</b>	<b>285</b>

# 1 Earlier Developed Techniques

The first electrochemical experiments were performed with solid materials, esp. metals. However, these experiments, conducted in the 18<sup>th</sup> and 19<sup>th</sup> centuries, were directed towards the elucidation of the basic features of the electrical action of chemical substances, and the chemical action of electricity. Initially, metals played the major role; only later it became obvious that many chemical compounds possess metallic or semi-conducting properties that can be utilized in electrochemical cells. Parallel to the studies of new electrode materials solid electrolytes were discovered and entire solid galvanic cells could be constructed. In this book we will entirely neglect pure solid electrolytes because this is a field in its own and the subject of many thorough treatises<sup>1-4</sup>.

Focusing on solid electrodes, two directions have been followed: One being the study of the properties of solid electrodes, esp. with respect to possible application, be it in electrochemical refining of metals, galvanic coating, primary and secondary batteries, technical electrolysis or others; the second direction being the application of electrochemical measurements to acquire information on the composition or structure of solids. The latter aspect is analytical, whereas the first one is synthetic. Parallel to these attempts fundamental research on the electrochemical properties of solid electrodes has been performed.

In the first section (1.1) we want to discuss the methods developed in the past which have enabled electrochemical studies of solid materials. The second section (1.2) is devoted to techniques for studying electrochemical phenomena of immiscible liquids. To obtain information on the electrochemistry of liquids or solutions that are immiscible with water

- 
- <sup>1</sup> Gellings PJ, Bouwmeester HJM (eds) (1996) The CRC Handbook of Solid State Electrochemistry. CRC Press, Boca Raton
  - <sup>2</sup> Bruce PG (ed) (1995) Solid State Electrochemistry. Cambridge University Press, Cambridge
  - <sup>3</sup> Rickert H (1985) Solid State Electrochemistry. An Introduction. Springer-Verlag, Berlin Heidelberg New York
  - <sup>4</sup> Maier J (2000) Festkörper – Fehler und Funktion, Prinzipien der Physikalischen Festkörperchemie. Teubner, Stuttgart

several approaches have been developed so far. A brief survey of the available techniques is given to prepare the reader for the chapter on immobilized droplets.

## 1.1 Solid Materials

### 1.1.1 Compact Electrodes

When the electrochemical properties of metals or alloys are to be studied, the simplest way is to fabricate electrodes, e.g., as disks, cylinders etc., from the target metal. These electrodes are generally polycrystalline and the energetic inhomogeneity of the electrode surface has to be born in mind. The use of well-characterized surfaces of single crystals has tremendously helped understanding the electrochemistry of metals <sup>5</sup>. Since the electrochemical literature abounds in detailed descriptions of electrode fabrications, we omit this subject area along with that on metal electrodeposition <sup>6-7</sup> in this volume.

In practice, the fabrication of compact electrodes is comparably inefficient and time consuming. The development of "*pressed cells*" sought to overcome this problem. These are cells with a counter electrode and a reference electrode, but with a missing bottom <sup>8-12</sup>. Instead of the bottom there is only a rubber ring so that the cell can be pressed onto a metal specimen with a flat surface. Electrolyte solution can be filled in, and the electrochemical measurements can be performed with the metal at the bottom serving as the working electrode.

The preceding does not imply that in the case of metals and alloys there is no reason for applying the technique of immobilized particles. There are cases where the metal to be studied cannot be destroyed, e.g., antique objects etc., or cases where the fabrication of electrodes would be too

---

<sup>5</sup> Kolb D (2001) *Angew Chem* 113:1198-1220

<sup>6</sup> Fischer H (1954) *Elektrokristallisation von Metallen*. Springer-Verlag, Berlin Heidelberg New York

<sup>7</sup> Budevski E, Staikov G, Lorenz WJ (1996) *Electrochemical Phase Formation and Growth*. VCH, Weinheim

<sup>8</sup> Slepushkin VV (1980) *Zh Anal Khim* 35:249-253

<sup>9</sup> Slepushkin VV, Mykovnina GS (1985) *Zashcita Metallov* 21:280-282

<sup>10</sup> Slepushkin VV (1987) *Zh Anal Khim* 42:606-616

<sup>11</sup> Slepushkin VV, Stifatov BM, Neiman EYa (1994) *Zh Anal Khim* 49:911-919

<sup>12</sup> Slepushkin VV, Stifatov BM (1996) *Zh Anal Khim* 51:553-511

expensive with respect to the obtainable information. In Chapter 5.1 we will give examples of such applications.

Compact electrodes made of minerals have been extensively studied in cases where the minerals exert sufficient conductivity and manage to be machined as electrodes <sup>13-14</sup>.

### **Electrography**

Electrography, introduced independently by A. Glazunov and H. Fritz, is an obsolete technique, however, it deserves reference, as it was a first direct electrochemical analysis of solid materials <sup>15</sup>. The principle is that a solid specimen is pressed on a paper which is soaked with an electrolyte solution. By anodic oxidation of the surface of the solid specimen the reaction products (e.g., nickel(II) ions) react with a reagent in the paper (e.g., dimethylglyoxime) to give colored reaction product (red in case of nickel(II) and dimethylglyoxime). This produces a print that clearly shows the distribution of the reactive element (nickel, in our example) on the surface of the specimen. Fig. 1.1 shows the experimental arrangement and Fig. 1.2 an electrographic print depicting the distribution of nickel in an ore.

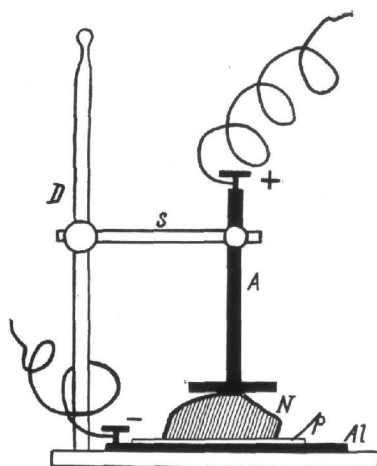


**Fig. 1.1.** Experimental arrangement in electrography: A anode, AL cathode, N mineral, p paper soaked with a reagent solution <sup>15</sup>

<sup>13</sup> Canturija VA, Vigdergauz VE (1993) *Elektrokhimija sulfidov, teorija i praktika flotacii*. Nauka, Moskva

<sup>14</sup> Holliday RI, Richmond WR (1990) *J Electroanal Chem* 288:83-98

<sup>15</sup> Jirkovský R (1934) *Mikrochemie (N.F. 9)* 15:331-342



**Fig. 1.2.** Electrographic print of a nickel ore. The black parts represent the originally red spots of nickel dimethylglyoxime complex that have been formed where nickel ions were released into the reagent paper by oxidation of the nickel mineral<sup>15</sup>

## 1.1.2 Electrochemistry of Suspensions and Colloids

### *Non-Colloidal Suspensions*

It is very appealing to obtain information on the electrochemistry of solid materials by studying suspensions of solid particles in electrolyte solutions. Laitinen and Kolthoff have shown that suspended silver halides exhibit electroactivity<sup>16-20</sup>. Micka has performed a series of systematic studies on the behavior of particles suspended in electrolyte solutions<sup>21-26</sup>. He has used the dropping mercury electrode in quite and in stirred

---

<sup>16</sup> Laitinen HA, Kolthoff IM (1941) *J Phys Chem* 45:1079-1093

<sup>17</sup> Laitinen HA, Jennings WP, Parks TD (1946) *Ind Eng Chem, Anal Ed* 18:355-358

<sup>18</sup> Laitinen HA, Jennings WP, Parks TD (1946) *Ind Eng Chem, Anal Ed* 18:358-359

<sup>19</sup> Kolthoff IM, Kuroda PK (1951) *Anal Chem* 23:1306-1309

<sup>20</sup> Kolthoff IM, Stock JT (1955) *Analyst* 80:860-870

<sup>21</sup> Micka K (1956) *Coll Czech Chem Comm* 21:647-651

<sup>22</sup> Micka K (1957) *Coll Czech Chem Comm* 22:1400-1410

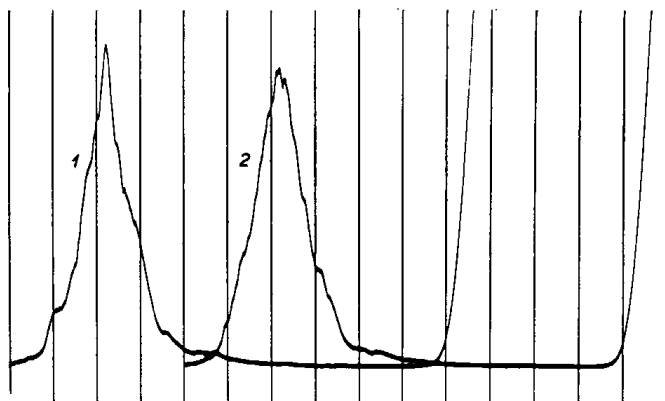


Fig. 1.3. Polarogram of a suspension of 40 mg charcoal in 10 ml 0.1 M KCl solution. Recording of the polarograms was started at 0 V in a Heyrovský cell, i.e., the potential refers to that of the bottom mercury<sup>23</sup>

solutions. Most of the suspended compounds (insoluble salts and oxides) gave peak-shaped polarograms with a maximum at or near the point of zero charge (*pzc*) of the mercury electrode. In many cases there was an additional reduction current at very negative potentials. Figure 1.3 shows the polarogram of a charcoal suspension exhibiting the typical peak-shaped signal. The signals were usually very noisy. Whereas Micka has explained the current peak at the point of zero charge by adsorption of the particles, Dausheva and Songina<sup>27</sup> have discussed the stability of the electrolyte film at the electrode in dependence on the electrode potential. They have assumed that only around the *pzc* this film is fragile enough to allow impinging particles penetrating it and contacting the metal surface allowing electron transfer. The same authors have experimentally shown that mercury(I) iodide particles strongly adhere at a mercury electrode only in the vicinity of the *pzc*<sup>28</sup>. Certainly, the surface charge of the particles has to be taken into account to understand the interaction of suspended particles with a charged electrode surface.

<sup>23</sup> Micka K (1960) Depolarisation of the dropping mercury electrode by suspensions of insoluble substances. In: *Advances in Polarography, Proceedings of the second international congress*. Longmuir IS (ed), Vol. 3, Pergamon Press, Oxford, pp 1182-1190

<sup>24</sup> Micka K (1965) *Coll Czech Chem Comm* 30:235-245

<sup>25</sup> Micka K, Kadlec O (1966) *Coll Czech Chem Comm* 31:3837-3844

<sup>26</sup> Micka K (1968) *Fresenius' Z Analyt Chem* 234:119-121

<sup>27</sup> Dausheva MR, Songina OA (1973) *Uspekhi Khim* 42:323-342

<sup>28</sup> Songina OA, Dausheva MR (1965) *Elektrokhim* 1:1464-1468

Franklin et al. have pioneered work using electrodes covered with a polymer film in-situ formed in suspensions of mineral particles<sup>29-32</sup>. The authors have used cationic surfactant-styrene-aqueous sodium hydroxide emulsions and have observed specific signals of the suspended mineral particles. However, no detailed analysis of the electrode surface, of the state of the suspended particles, and of the mechanism of electrode reactions have been published.

The electrochemistry of slurries and suspensions has also attracted attention from a technical point of view.

### **Colloidal Solutions**

Majer has been the first to observing a signal in colloidal iron(III) hydroxide solutions<sup>33</sup> when magnesium ions were present. Since that first observation, for a long time no further studies have been published. All the classic books on polarography of the 20<sup>th</sup> century do not refer to any work in this field. Perhaps the paradigmatic statement of J. Heyrovský that only “really dissolved compounds” give polarograms<sup>34</sup> is responsible for this. Probably attempts have been made in vain to obtain voltammograms of colloidal solutions, and this experience did not help either in developing the subject. Pauli and Valkó have remarked in their monograph on the electrochemistry of colloids that “the simple case of a primary deposition by electron acceptance or delivery seems not to occur in case of colloids”<sup>35</sup>. However, they have given some examples of hydrogen and oxygen evolution in the course of electrolysis of colloid solutions. Sometimes, precipitations are caused by pH changes in the electrolysis. Within the last 30 years the electrochemistry of colloidal solutions and that

---

<sup>29</sup> Franklin TC, Nnodimele R, Adeniyi WK, Hunt D (1987) *J Electrochem Soc* 134: 2150-2153

<sup>30</sup> Franklin TC, Nnodimele R, Adeniyi WK, Hunt D (1988) *J Electrochem Soc* 135: 1944-1946

<sup>31</sup> Franklin TC, Adeniyi WK (1988) *Anal Chim Acta* 207:311-317

<sup>32</sup> Franklin TC, Darlington J, Nnodimele R, Duty RC (1992) *Heterogeneous Catalysts for Use in Anodic Electrosyntheses and Electrodestruction of Organic Compounds in Aqueous Surfactant Systems*. In: *Electrochemistry in Colloids and Dispersions*. Mackay RA, Texter J (eds) VCH, New York, pp 319-329

<sup>33</sup> Majer V (1943) *Chem listy* 37:202-204

<sup>34</sup> Heyrovský J (1941) *Polarographie. Theoretische Grundlagen, praktische Ausführung und Anwendungen der Elektrolyse mit der tropfenden Quecksilberelektrode*. Springer, Wien, p 273

<sup>35</sup> Pauli W, Valkó E (1929) *Elektrochemie der Kolloide*. Springer, Wien, p 296



of colloidal particles on electrode surfaces has made advancements <sup>36</sup>, however, publications on the voltammetry of colloidal solutions reporting characteristic signals of colloidal substances are still rare. Interesting examples like tin, titanium and mixed titanium-iron oxides, have been published by M. Heyrovský et al. <sup>37-39</sup>. However, even in these cases it is a primary reduction of protons that causes chemical reductions of the metal centers in the colloidal particles. The majority of publications concern either the heterogeneous electron transfer between colloidal semi-conducting particles and dissolved species <sup>40</sup>, or even secondary effects of colloids on other electrochemical systems. It is important for the subject of this book *that the use of colloidal solutions cannot be regarded as a way to access the electrochemistry of solid substances.*

### 1.1.3 Paste and Composite Electrodes

The use of paste electrodes has been by far the most popular technique for studying the electrochemistry of solid materials <sup>41-43</sup>. The powdered sample material is mixed with a binder and with an “inert” conducting material, as, e.g., graphite powder. The liquid binder can be an organic liquid immiscible with the aqueous electrolyte solution used for the electrochemical measurements, or, it can be exactly the same aqueous electrolyte. Both techniques have their advantages and disadvantages. An organic liquid binder prevents ingress of the aqueous electrolyte into the paste and allows the paste to be stable towards the electrolyte solution. The paste can be thick enough to be kept in a holder even when the outlet is turned downwards. However, organic binders, e.g., paraffin oil, may

---

<sup>36</sup> Mackay RA, Texter J (eds) (1992) *Electrochemistry in Colloids and Dispersions*. VCH, New York

<sup>37</sup> Heyrovský M, Jirkovský J, Müller B (1995) *Langmuir* 11:4293-4299

<sup>38</sup> Heyrovský M, Jirkovský J, Štruplová-Bartáčková M (1995) *Langmuir* 11:4300-4308

<sup>39</sup> Heyrovský M, Jirkovský J, Štruplová-Bartáčková M (1995) *Langmuir* 11:4309-4312

<sup>40</sup> Mulvaney P (1998) Zeta Potential and Colloid Reaction Kinetics, in: *Nanoparticles and Nanostructured Films*. Fendler JH (ed) Wiley-VCH Weinheim, pp 275-306

<sup>41</sup> Brainina KhZ, Neyman EJa (1982) *Tverdogaznye reakcii v elektroanaliticheskoj khimii*. Khimija, Moskva

<sup>42</sup> Brainina KhZ, Neyman EJa, Slepshkin VV (1988) *Inversionnyye elektroanaliticheskie metody*. Khimija, Moskva

<sup>43</sup> Brainina Kh, Neyman E (1993) *Electroanalytical stripping methods*. Wiley & Sons, New York

always spread on the surface of the particles of the graphite and the solid substance. Such films can influence the electrochemistry of solid compounds, and one can never be sure of how severe this effect will be. In this respect, the use of aqueous electrolytes as binders is preferable <sup>44</sup>. However, they can prompt chemical reactions with the solid, e.g., dissolutions. In some studies, such pre-dissolutions have been deliberately used for producing electrochemical signals of the “in-situ” dissolved species. It has been shown that these signals depend to some extent on the starting material, however, the processes at such electrodes are rather complex and such electrodes should be used with caution.

When the binder is solid the produced electrodes are usually called “composite electrodes”. The solid binder can be paraffin, polyethylene, Teflon, acryl polymers, etc. Also silica gel formed by hydrolysis of appropriate esters can be used.

#### 1.1.4 Sandwich Electrodes

Studying the electrochemistry of a solid material by sandwiching it between two solid electrodes requires the material to be negligibly electronically conductive, since, otherwise, it would short-circuit the cell. If the sandwiched compound is an ion conductor such experiments can yield information on its conductivity and on reactions of the solid ion conductor with the solid electrodes or with a gaseous phase. Such experiments have been performed in classic solid state electrochemistry, esp. at elevated temperatures <sup>1 - 3</sup>. However, there is a class of solid materials that lends itself to room temperature experiments because the compounds possess electroactive redox centers and additionally exert ion conductivity. No electronic current can flow through these materials unless an ionic current accompanies the electrons. Prussian blue and its analogues and many solid heteropoly salts and acids belong to this class. Various studies of the electrochemical behavior in such sandwich cells have been published so far <sup>45</sup>. Usually they have been performed in two-electrode arrangements, however, sometimes also under potentiostatic control using a reference electrode. Because of the more complex experimental design and the restrictions with respect to materials, this approach has found only limited application.

---

<sup>44</sup> Alonso Sedano A, Tascón García LM, Vázquez Barbado DM, Sánchez Batanero P (2003) *J Solid State Electrochem* 7:301-308

<sup>45</sup> Kulesza P, Malik A (1999) *Solid-State Voltammetry*. In: *Interfacial Electrochemistry, Theory, Experiment, and Applications*. Wieckowski A (ed) Marcel Dekker, New York pp 673-688

## 1.2 Immiscible Liquids and Solutions

Compounds, esp. organics that are too sparingly soluble in water, may be dissolved in organic solvents for electrochemical measurements. This is a classic approach; however, in several cases it is of interest to study the electrochemical reactions in the presence of an aqueous electrolyte solution. For this purpose, the idea of studying emulsions of the nonaqueous phase in an aqueous phase suggests itself. However, a price has to be paid, as many complicating additional phenomena are observed<sup>36</sup>.

At the interface of two immiscible liquid phases ions partition and thus a galvanic potential difference is established. Hence, by applying a potential difference across the interface it is possible to transfer ions. The ion transfer between two immiscible liquid phases has been established as a research field in its own<sup>46 - 48</sup>. These studies require the use of four-electrode potentiostats. In addition, supporting electrolytes must be present in the aqueous and the nonaqueous phases. Static liquid-liquid interfaces are most frequently used, although also dropping electrolyte electrodes have been developed and applied. In Chapter 6 of this monograph, the electrochemistry of immobilized droplets will be discussed. In this case, ion transfer reactions occur across the liquid-liquid interface accompanied by electron transfer reactions across the liquid (nonaqueous)-solid interface.

---

<sup>46</sup> Girault HH, Schiffrin DJ (1989) Electrochemistry of liquid-liquid interfaces. In: *Electroanalytical Chemistry*. Bard AJ (ed) vol 15, Marcel Dekker, New York

<sup>47</sup> Vanysek P (1996) *Modern Techniques in Electroanalysis*. Wiley, New York

<sup>48</sup> Volkov AG (ed) (2001) *Liquid Interfaces in Chemical, Biological, and Pharmaceutical Applications*. Marcel Dekker, New York

## 2 Electrodes with Immobilized Particles and Droplets – Three-Phase Electrodes

It is a common feature of electrodes with immobilized particles and droplets that three phases are in close contact with each other, i.e., each phase having an interface with the two other phases. This situation exists also in most of the so-called surface-modified or film electrodes, many battery and fuel cell electrodes, electrodes of the second kind, etc. In fact, the majority of surface-modified electrodes consist of arrays of particles that partially cover the electrode surface. It would be far beyond the scope of this book to include all chemical and electrochemical techniques to deposit films on electrodes. Here we shall deal only with electrodes where the particles or droplets have been mechanically attached with the aim of studying their electrochemistry. Before going into the details in the Chapters 5 and 6, we now want to outline the specificity of *three-phase electrodes*.

Figure 2.1 depicts the situation at a three-phase electrode, phase II being a particle or a droplet. Since the particle or droplet contains neutral molecules and ions with equal amounts of positive and negative charges, any electron transfer between phase I and phase II must be accompanied by an ion transfer between the phases II and III. The ion transfer is an indispen-

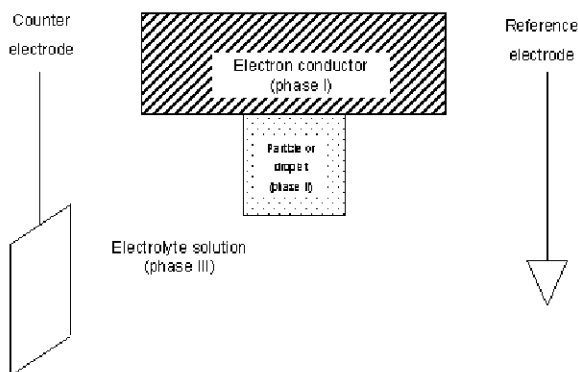


**Fig. 2.1.** Schematic drawing of a three-electrode cell with a working electrode on the surface of which a particle or a droplet is attached

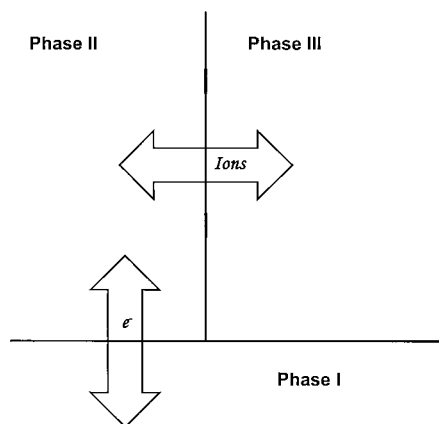


**Fig. 2.2.** Scheme of the simultaneous electron and ion transfer at a three-phase electrode

sable reaction to maintain the electroneutrality of phase II, provided that phase II does not only pass the electrons on from phase I to a redox species in solution. The latter may happen in systems where the particles exhibit electrocatalytic activity. It is a most important feature of the three-phase electrode with immobilized electroactive compounds that the *electron* and *ion* transfer must take place simultaneously at one electrode (cf. Fig. 2.2). The electron transfer between phase I and II can be disregarded only in the case of simple metal oxidations <sup>1</sup>.

Thermodynamically speaking, the three-phase electrode comprising a phase II that has redox centers and ion conductivity, is a *double electrode* (the German expression is *zweifache Elektrode* <sup>2</sup>). The formal thermodynamic analysis of a three-phase electrode is rather simple; however, there

<sup>1</sup> When a metal particle, e.g. Ag, attached to a gold electrode is anodically oxidized, the ion transfer is the transfer of  $\text{Ag}^+$  ions from the metal to the solution and the electron transfer occurs between gold and silver. Such kind of electron transfer between electronically conducting phases will, of course, always occur in electrochemistry, because any electrode needs another conductor at its terminal. It should be remembered that the interfacial potentials that build up between the electrodes and its terminal conducting connectors are responsible for the inaccessibility of single electrode potentials.

<sup>2</sup> Lange E, Göhr H (1962) *Thermodynamische Elektrochemie*. Hüthig Verlag, Heidelberg

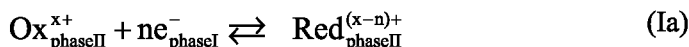
are general problems involved that have not been solved until today: Formally, one can split an overall equilibrium equation



with the Nernst equation

$$E = E_{\text{Ox/Red/C}}^{\ominus} + \frac{RT}{nF} \ln \frac{a_{\text{Ox}_{\text{phaseII}}^{x+}} a_{\text{C}_{\text{phaseIII}}^{+}}^n}{a_{\text{Red}_{\text{phaseII}}^{(x-n)+}} a_{\text{C}_{\text{phaseII}}^{+}}^n} \quad (2.1)$$

into two equilibria, one involving the transfer of electrons



and one involving the transfer of ions



with the following Nernst equations

$$E_{\text{I/II}} = E_{\text{Ox/Red}}^{\ominus} + \frac{RT}{nF} \ln \frac{a_{\text{Ox}_{\text{phaseII}}^{x+}}}{a_{\text{Red}_{\text{phaseII}}^{(x-n)+}}} \quad (2.2)$$

$$E_{\text{II/III}} = E_{\text{C}}^{\ominus} + \frac{RT}{F} \ln \frac{a_{\text{C}_{\text{phaseIII}}^{+}}}{a_{\text{C}_{\text{phaseII}}^{+}}} \quad (2.3)$$

The standard potentials are interrelated by the following equation:

$$E_{\text{Ox/Red/C}}^{\ominus} = E_{\text{Ox/Red}}^{\ominus} + E_{\text{C}}^{\ominus} \quad (2.4)$$

Both equilibria Ia and Ib are of *electrochemical* nature since a transfer of charged species between two phases takes place. When phase II is a solid, it is not yet clear how the activities of the species Ox, Red, and  $\text{Cat}^{+}$  in the solid have to be defined and how they could be determined. Further, no experiments are known that would lead to a separation of the free energies of the equilibria Ia and Ib in the case of solids. When phase II is a solution phase, the activities of Ox, Red, and  $\text{Cat}^{+}$  are in principle accessible, however, it remains the problem that an extrathermodynamic assumption is necessary for quantifying the free energy of ion transfer between the liquid phases II and III. Despite these inherent and still unresolved problems, progress has been made by rather simple models, e.g., assuming for solids that

that the activities of Ox and Red can be approximated by their molar ratios (Chapter 5), and by assuming that ions like tetraphenylarsomium cations and tetraphenylborate anions have the same free energy of ion transfer in systems like water-nitrobenzol (see Chapter 6).

The kinetic description of a three-phase electrode is much more complex since several aspects must be taken into account: (i) the kinetics of the electron transfer, (ii) the kinetics of the ion transfer, (iii) the electron and ion conductivity of the immobilized phase, and (iv) the size and shape of the immobilized phase. Thus it is not surprising that compared to the thermodynamics, the kinetics of three-phase electrodes with immobilized particles and droplets have been much less studied. Of course, most systems are even more complex than illustrated in Fig. 2.2. For example, the reactions at the three-phase electrode may lead to the dissolution of phase II or to the formation of a new solid (or liquid) phase IV. Such phase transformation may proceed via the solution phase (see Sect. 4.2: the oxidation of Ag to AgI, where the oxidation of Ag nanocrystals results first in the formation of an oversaturated AgI solution from which by a nucleation-growth mechanism the AgI crystals are formed in a follow-up process), or it can be a solid-to-solid phase transformation. An example of such a mechanism is the reduction of PbO to Pb discussed in Sect. 4.2 [B 184]. The model depicted in Fig. 2.3 was derived from the AFM results that show a reactions front proceeding through the PbO crystal. It was postulated that a reaction zone forms as an *interphase* between the PbO and Pb phases.

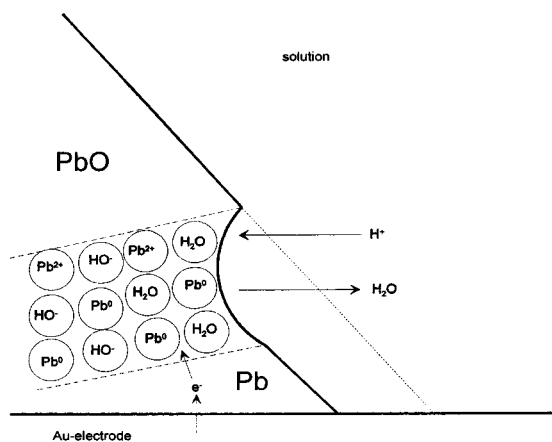


**Fig. 2.3.** Schematic model for the processes at a three-phase electrode gold/PbO/solution when PbO is reduced to Pb as a fourth phase [B 184]

Further mechanistic variations may result from the ion conductivity of phase II: if this phase is a good ion conductor, the electron transfer can start and proceed at the entire interface between the phases I and II. Parallel to this electron transfer, the ion transfer may take place across the interface between the phases II and III. Examples are the insertion electrochemical reactions of metal hexacyanoferrates (see examples in Sects. 5.3, 5.5, 5.6), and many other insertion electrochemical reactions, e.g., the reduction of “ $\text{MnO}_2$ ”. Even these reactions can be complicated, for example, when the reaction product is a poor ion conductor.

Of course, phase II may also be an insulator for both ions and electrons, like white phosphorus [B 157]. In this case the observed currents are much too high to be explained by a reaction that is confined to the three-phase junction line. It has been concluded from the electrochemical behavior of white phosphorus that the reaction proceeds via the formation of an ion-conducting phase IV, as depicted in Fig. 2.4.

Another possibility is that phase II attains ionic conductivity in the course of the electrochemical reaction, partly because ions are created

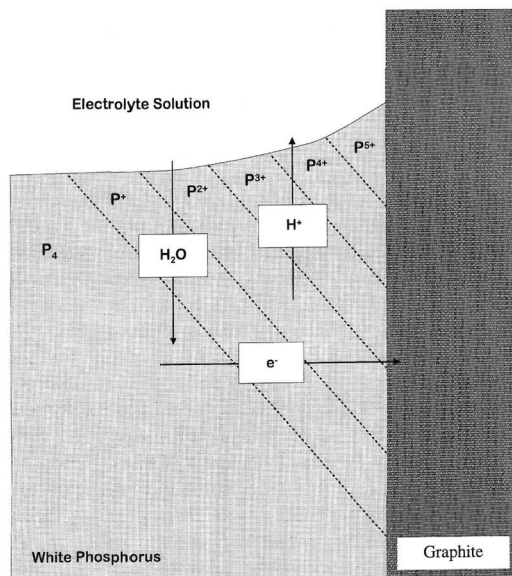


**Fig. 2.4.** Model for the electrochemical oxidation of white phosphorus at the three-phase junction electrolyte solution | phosphorus | graphite. The surface of the phosphorus will bend up due to the ingress of water and the expanding volume of the reaction products. The borders between the different phosphorus oxides, symbolized by the oxidation state of phosphorus, are certainly diffuse [B 154]



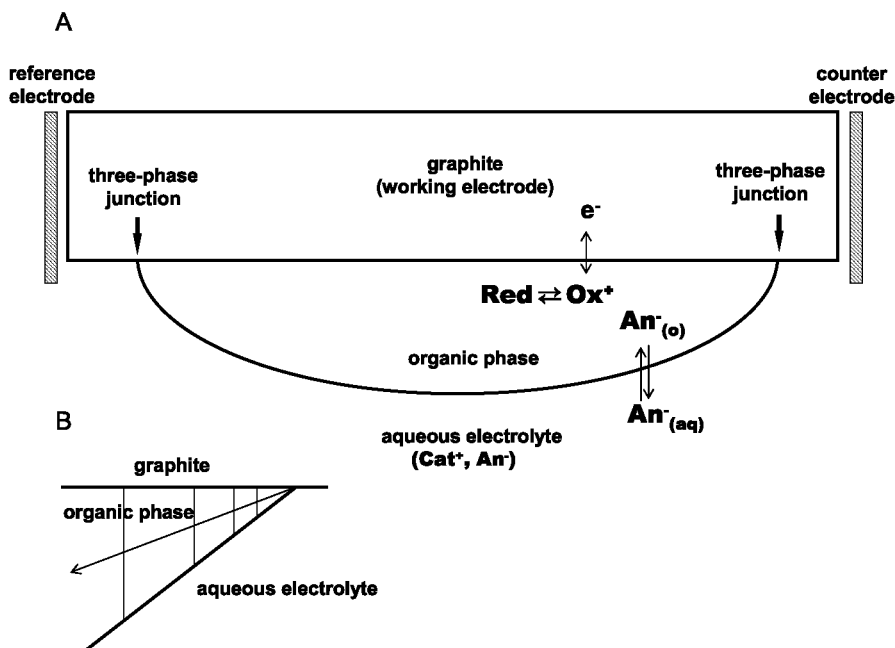


**Fig. 2.5.** **A** Schematic presentation of the situation when an organic phase droplet contains an electroactive form Red that is oxidized to  $\text{Ox}^+$  accompanied by a transfer of the anions  $\text{An}^-$  from an aqueous electrolyte solution to the organic phase. **B** Shows how the reaction products  $\text{Ox}^+$  and  $\text{An}^-$  spread from the three-phase junction into the droplet creating an ionic conductivity in the organic phase

from atoms or molecules in II, partly because ions are transferred from phase III to phase II. Such a reaction mechanism leads to an activation of the interface between phases I and II with respect to the electron transfer. Plenty of examples are given in Chapter 6, where the electrochemistry of immobilized droplets is discussed. Figure 2.5 illustrates such a situation, when an electroactive compound dissolved in a droplet of an organic solvent is oxidized, accompanied by a simultaneous ion transfer between the aqueous environments of the droplet and the organic phase. In Sect. 6.2 a detailed description of this situation will be given.

These examples of three-phase electrodes are given here to prepare the reader that this monograph deals with the special situation that arises when particles or droplets are immobilized on electrode surfaces. However, electrodes with immobilized particles or droplets must still be considered as simplified models for much more complex electrode situations, as they are frequently encountered in battery systems, technical electrolysis, etc. When carbon powder, manganese dioxide and an alkaline electrolyte are

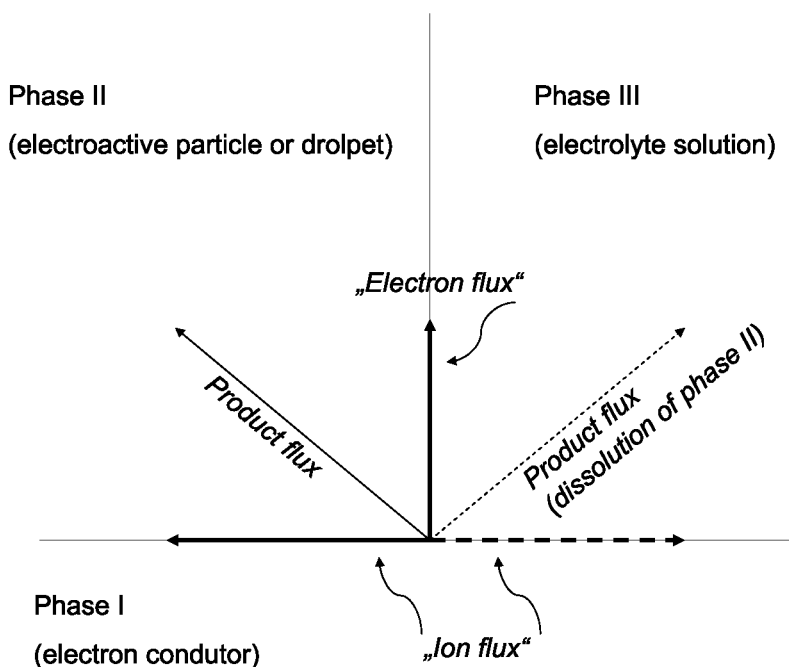


**Fig. 2.6.** Schematic view of a three-phase electrode. Phase I is an electron conductor (a metal or graphite), phase II is the immobilized solid or liquid electroactive phase, and phase III is the electrolyte solution. The electron flux shows the direction in which electrons can be transferred across the interface I/II and transported within phase II. The ion flux shows the direction in which ions can be transferred across interface II/III and within phase II (*full arrow*) or within phase III (*dashed arrow*). The product fluxes show in what direction the products may go

mixed to make the cathode of a Leclanché battery, the latter is nothing else but an extended three-phase electrode. Experiments of the kind described in this book may widen our understanding of such complex electrodes. In Fig. 2.6 an attempt has been made to give a general scheme for reactions starting at a three-phase junction line of a three-phase electrode. The properties of phase II determine the conductivity for electrons and ions in this phase. The properties of the two interfaces I/II and II/III determine the rate of electron transfer (I/II) and ion transfer (II/III). The transfer rates across the interfaces and the transport rates in phase II and phase III of the electrons and ions determine the size and direction of the fluxes of ions and electrons. The two fluxes determine the resulting flux of the products and the direction in which the reaction front spreads. The ion flux can be also directed into phase III, the solution, in which case phase II will dissolve; an example being the electrochemical dissolution of metal oxides as discussed in Sect. 5.7. Usually, one will observe that the advancement of

cussed in Sect. 5.7. Usually, one will observe that the advancement of the reaction into phase II or III will lead to an electron transfer spreading along the interface I/II and a spreading of ion transfer along the interface II/III. This way, the reaction that started at the three-phase junction line, i.e., a reaction that proceeds in that starting moment “around” a line, becomes a reaction across the two interfaces. There is only one example known so far, where the reaction remains confined to the three-phase junction line, because the transferred electrons and protons are used for a reduction of a chemical compound (see Sect. 6.1).

## **3 The Experiment**

### **3.1 Electrodes, Electrolytes and Electrochemical Cells**

#### **3.1.1 Electrodes**

Generally, all kinds of solid electrode materials can be used and have successfully been used to perform voltammetric measurements of immobilized particles and droplets. However, the suitability of an electrode material to a great deal depends on the electrode preparation, i.e., the immobilization procedure. Especially the mechanical immobilization of solid microparticles, see Sect. 3.2., requires a careful choice of the electrode material.

Graphite has become most widely used as the electrode base material. It combines a high chemical inertness with a wide potential window, low price, the ease of processing and a softness enabling the mechanical “sticking” of sample powder on an electrode surface. One of the greatest advantages of graphite-based electrodes lies in the ease of cleansing of the electrode from attached powder samples which is achieved by removing the upper electrode surface layer by abrasion or cutting (see Sect. 3.2).

#### ***Paraffin Impregnated Graphite Electrodes***

Amongst the graphite based electrodes the paraffin impregnated graphite electrodes (PIGE) are most successful. These electrodes consist of high-purity graphite rods whose pores are filled with paraffin in order to prevent high background currents and the spoiling of the electrode by ingressing solution [B 85]. To prepare PIGEs paraffin (melting point between 56 and 70 °C or higher) is melted in a closed vessel in a water bath. The graphite rods are added to the melt and the vessel is carefully evacuated. The melt remains under vacuum until no more bubbles evolve from the rods. It is then returned to ambient pressure which leads to a complete penetration of

the rod by the paraffin. The rods are removed from the melt before the paraffin solidifies and are placed onto filter paper in order to remove excess paraffin.

### ***Composite Electrodes***

Composite electrodes based on graphite powder as the electrode base material usually require polymer-resin based binders, e.g., polyester [B 195, B 217], or wax (“sticky carbon” [B 223]) in order to seal the pores and give the electrodes mechanical stability. The choice of a suitable binder is crucial as the chemical and physical inertness against the electrolyte solution, the thermal stability and the mechanical properties are dominantly ruled by the binder. The preparation procedure of composite electrodes is generally straightforward. It consists of a thorough mixing of the graphite powder and the binder, the mass ratio depending on the used binder, the desired mechanical stability of the electrode, and of the process of solidification. The latter may be accomplished by curing of the polymer resins [B 195] or by re-solidification of molten wax or paraffin.

### ***Basal Plane Pyrolytic Carbon***

Basal plane pyrolytic carbon [B 28, B 29] is very well suited for the voltammetry of particles and droplets. As the basal plane pyrolytic carbon is not penetrated by the electrolyte solution these electrodes do not require sealing with organic binder. This makes them equally well suited for measurements in aqueous and organic environments.

### ***Highly Orientated Pyrolytic Carbon (HOPG)***

This material possesses a highly fragile layer structure that bans the mechanical immobilization of particles as that could severely damage the material surface. However, HOPG is a favorite electrode material for scanning electrochemical microscopy (SECM) and atomic force microscopy (AFM) and has successfully been used for the microscopic investigation of solid microparticles (see, e.g., [B 147]).

### ***Pencil Lead Electrodes***

Pencil lead has been proposed for use as electrode material [B 48], and a comparison with PIGE electrodes showed comparable results. Its major advantage is its low price and universal availability.

### ***Boron Doped Diamond Electrodes***

Recently, boron doped diamond electrodes have received much attention [B 123, B 168, B 224] as their extreme hardness allows the direct sampling from compact and hard materials like metals and ceramics. Desirable properties like a high chemical inertness connected with a wide potential window as well as a low interfacial capacity in aqueous electrolytes and hence low background currents add to the value of these electrodes. However, the cleaning of the electrodes after a mechanical (abrasive) sample immobilization is rather tedious.

Marken et al. [B 168] have demonstrated that at boron doped diamond electrodes a facile oxidation and reduction of immobilized microdroplets of tetraalkylphenylenediamines can be achieved, which the authors attributed to a good adhesion of the organic material to the electrode surface.

### ***Glassy Carbon Electrodes***

Glassy carbon is less suited for a mechanical immobilization as particles do not easily adhere to it. Exceptions are soft organic or organometallic compounds which are able to stick to the glassy carbon surface [B 138]. At polished glassy carbon electrodes also the deposition of microdroplets by evaporation from organic solvents is rather difficult as the poor wetting properties and the therefore rather bad adherence of the droplets at the carbon surface often leads to the formation of larger droplets rather than the desired formation of an array of microdroplets. A possible way out is to roughen the surface of a glassy carbon electrode which fixes the position of the microdroplets at the surface. This procedure has also been used for the mechanical immobilization of solid inorganic compounds at glassy carbon [B 60]. In the latter communication it is demonstrated that the adherence of microparticles at GC electrodes is much weaker than at graphite electrodes, where particles are literally embedded into the electrode surface. However, glassy carbon electrodes have been deliberately chosen for particle immobilization to have an electrolyte layer sandwiched between the carbon and the particles to study the electron transfer catalysis of ions and compounds adsorbing at the particle surface [B 60].

### ***Metal Electrodes***

Due to their hardness and similar to glassy carbon, metal electrodes are generally less suited for the voltammetry of mechanically immobilized particles. However, metal electrodes have been successfully used for the investigation of soft samples like organic and organometallic solids. As demonstrated (see, for instance [B 138]), with gold, glassy carbon and

platinum electrodes very similar results are obtained. Applications like the electrochemical quartz crystal microbalance, EQCM (Chapter 4.3) require the use of gold electrodes [B 54, B 65]. (See also AFM/STM: Chapter 4.2, [B 184, B 278, B279]) and in situ calorimetry (Chapter 4.5, [B 219, B 220])

### 3.1.2 Electrolytes and Electrochemical Cells

The equipment to perform electrochemical studies of immobilized microparticles and microdroplets is the same as that used for conventional electrochemical measurements. Generally, a three-electrode arrangement consisting of a working electrode, an auxiliary and a reference electrode is utilized, the electrode control being achieved via a potentiostat. The cell design depends on the utilized working electrode and the purpose of the experiment and thus reaches from conventional glass cells to specially adapted constructions like for flow-through experiments, or for spectroelectrochemistry (Chapter 4.1).

The choice of the electrolyte depends on the nature of the studied compound and processes. In the vast majority of cases aqueous electrolyte solutions are used. However, organic solvents like acetonitrile can be used as well, provided their dielectric constant allows electrolyte salts to be dissolved in order to achieve sufficient conductivity. The major prerequisite for the choice of the electrolyte solvent is the insolubility or at least a very low solubility of the studied compound in the solvent.

After immobilization of the sample particles or droplets (see Chapters 3.2 and 3.3) the electrode is ready for measurement.

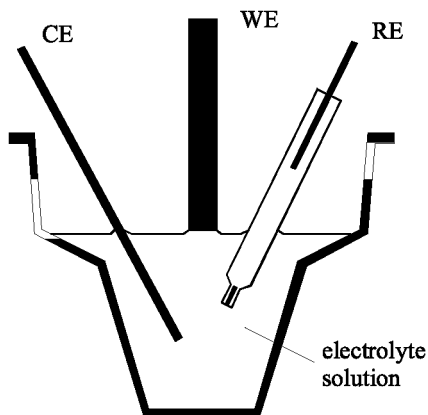


**Fig. 3.1.** Configuration of electrodes in an electrochemical cell for the voltammetry of immobilized microparticles and microdroplets

Figure 3.1 depicts a most appropriate configuration of the working electrode in the electrochemical cell. The working electrode (e.g., a PIGE) is dipped into the electrolyte solution and then slightly raised in order to make the solution adhering to the lower circular electrode surface. This ensures a reproducible active surface area without the necessity of insulating the shaft of the electrode. However, since the electrode shaft is not contaminated with sample particles or droplets, even an immersion of the electrode into the solution for some millimeters would only affect the background current.

### 3.2 Immobilization of Particles

When the sample is a powder with grain size in the  $\mu\text{m}$  range the easiest way to immobilize the particles on a paraffin impregnated electrode is to place a few milligrams on a glass plate or a glazed tile and gently rubbing the electrode rod with its lower circular surface on the sample spot (see Fig. 3.2). Usually, this results in the attachment of plenty of particles on the electrode. Most of them will be partly embedded in the soft graphite surface. Some of them will keep attached by adhesion and they may adhere so weakly that they can be washed off with water. Normally, no water remains at the hydrophobic electrode, so that this washing cannot dilute the



**Fig. 3.2.** Transfer of microparticles from a glass plate onto the surface of a paraffin impregnated graphite electrode (PIGE)



electrolyte solution. In fact, washing off the loose particles is even unnecessary because they would fall off from the electrode upon introduction to the electrolyte solution. A second way of immobilizing particles is to place a few milligrams of the powder on filter paper and rub the electrode on the sample spot. This has the advantage that a more even distribution is achieved and the loose particles are kept on the paper at the same time. Some preliminary experiments will give the necessary experience how much sample should be used, what is the right pressure when rubbing the electrode on the sample spot, and what are the best movements to rub. Occasionally, it may be adequate just to press the electrode on the sample spot without circular movements of the electrode. When metals and alloys are studied, it will suffice to gently rub the electrode on the surface of the metals and alloys, which is perhaps, but not necessarily, cleaned before. When the metals and alloys are very hard, some abrasive powder (e.g., high purity  $\text{Al}_2\text{O}_3$  or diamond) may be placed between the electrode and the compact sample. Because of its inertness the abrasive powder cannot interfere in the electrochemistry. Alternatively, very hard electrodes, as, e.g., boron doped diamond electrodes can be used. In the case of a very rare or very small sample the sampling can also be performed with a thin glassy carbon pin. In special cases, for example in AFM studies, the immobilization can be achieved by slow evaporation of a very dilute suspension of the powder (or even colloid) on the electrode surface. Care must be taken to avoid that the suspension forms large droplets that would leave patches of adhering particles, unsuitable for AFM/STM work. When the sample is a rather coarse powder, it is the best to crush a small amount in a mortar to obtain fine particles.

After having performed the electrochemical measurements, it is not less important to clean the electrode surface for the next measurements. The best way to clean a PIGE is to rub its surface on filter paper. This rubbing must be interrupted on the paper so that sample residues cannot be smeared from one end to the other. This is easily achieved by producing traces as depicted in Fig. 3.3. The electrode must be polished by keeping it perpendicular to the paper surface as to avoid a rounding of the edges. The electrode surface should be kept flat, as this helps very much in follow-up cleaning operations. Sometimes it may be advisable to fold a piece of clean filter paper around the shaft of the electrode and to wipe off possible remains of the sample that may have been transferred to that side during the polishing. After that, it is suggested to polish the lower circular surface again. The success of cleaning must be checked by recording a blank voltammogram. Without this, one can never trust that the measured response of a sample is caused by the fresh sample only, and not also resulting from



**Fig. 3.3.** Cleaning the surface of a PIGE by interrupted polishing on paper

previous measurements. In rare cases, when the particles are very hard and when they are not dissolved in the electrochemical measurements (this happens with some rather coarse steel particles) the left-over particles may be even pressed further into the electrode during polishing and it is not possible to get rid of them by this cleaning procedure. In such cases one has to remove a thin layer of the electrode on a very fine abrasive paper, followed by polishing the electrode surface on paper. The surface of the electrode can also be cleaned with the help of a razor blade. The best movement to polish an electrode surface is to write the number “8” on the paper, however, keeping the electrode as up-right as possible. Other points to remember in immobilizing samples are discussed in connection with the electrodes in Sect. 3.1.

### 3.3 Attachment of Droplets

Generally speaking, the major advantage of the voltammetry of droplets over other conventional techniques of probing liquid | liquid interfaces lies in the formation of *three-phase electrodes* comprising the *triple-phase junction* electrolyte|electrode|droplet, i.e., the circumference of the droplets. By allowing charge compensation along this boundary it is possible to study electrochemical reactions of ionically non-conducting liquids and non-polarizable liquids without the addition of supporting electrolyte to the organic liquid.

Consequently, the electrode preparation procedure must always ensure the presence of three-phase boundaries, and a complete coverage of the

electrode surface must be prevented. A full coverage with ionically non-conducting liquids would ultimately block the electrode.

One can distinguish between two approaches - the attachment of single droplets, and the attachment of an array of microdroplets. In the following sections the different strategies for the droplet immobilization will be listed and discussed.

Independent of the applied approach, and like in the case of other techniques that probe liquid|liquid interfaces, the voltammetry of droplets requires the studied liquids to be sufficiently immiscible with the chosen electrolyte solution. This requirement is crucial since due to the ratio of the volumes of the immobilized droplets and of the electrolyte solution the small droplets would very quickly dissolve in the surrounding electrolyte solution.

However, the solubility of many organic solvents in water cannot be neglected (e.g., the solubility of nitrobenzene in water is 0.2 mass% at 20°C). Thus, when working with solvent droplets, the electrolyte solution should always be saturated with the respective droplet solvent in order to prevent their dissolution and to ensure a long lifetime of the deposited droplet.

### 3.3.1 Attachment of Single Droplets

The attaching of a single droplet on the surface of an electrode can be achieved in many ways. The probably most sophisticated method is the laser trapping technique (see, e.g., Nakatani et al. <sup>1</sup>). In the following sections, however, only those approaches will be considered that are available without disproportional technical expenses.

Generally, the droplet attachment is straightforward. In order to transfer a defined, small volume of the liquid sample onto a large electrode surface, either  $\mu\text{L}$ -syringes or pipettes can be used. As an example, droplets of polar and nonpolar aprotic solvents containing dissolved electroactive species have been deposited in order to study transfer processes across the solvent|water interface facilitated by electrochemical reactions of electroactive species dissolved in the droplet [B 132]. For that, the authors have deposited 1-2  $\mu\text{L}$  of nitrobenzene, containing 1-100  $\text{mmol L}^{-1}$  of the electroactive species, on the surface of a paraffin impregnated graphite electrode [e.g. B 132, B 188] or a glassy carbon electrode [B 242] (5 mm diameter). This procedure forms a droplet with a diameter of approximately 0.5 - 2 mm [B 188, B 242].

---

<sup>1</sup> Nakatani K, Chikama K, Kitamura N (1999) In: *Advances in Photochemistry*, vol 24. Wiley-Interscience, New York, pp 173-223

More complicated is the attachment of single droplets at microelectrodes. This usually requires the use of an optical microscope and a micromanipulation system. Terui et al., for instance, have used a glass fiber with a tip radius of  $5\ \mu\text{m}$  in order to deposit single droplets of nitrobenzene of a diameter between  $25\ \mu\text{m}$  and  $100\ \mu\text{m}$  gold microelectrodes [B 153]. The attachment of single droplets at microelectrodes usually leads to conditions in which the droplet size is larger than the diameter of the electrode. Due to the absence of a three-phase junction water|electrode|droplet, this setup requires to add supporting electrolytes to the droplets.

As the surface tension of water is much higher than that of most organic liquids, it is comparably easier to study the voltammetry of immobilized droplets and films of organic liquids immersed in aqueous solution than vice versa. Immersing an electrode with attached droplets of an aqueous solution into an organic electrolyte solution can easily lead to the detachment of the droplets from the electrode. This is the reason that this experimental setup is only rarely used. An example is the communication of Ulmeanu et al. [B 180] who deposited single drops of a volume of  $10\ \mu\text{L}$  of the appropriate aqueous solution containing supporting electrolyte and the electroactive species on a freshly polished platinum electrode (surface area  $0.06\ \text{cm}^2$ ) mounted in a Teflon holder and immersed the electrode in 1,2-dichloroethane.

### 3.3.2 Attachment of Arrays of Microdroplets

In contrast to the above technique, the deposition of an array of microdroplets leads to the formation of extremely small droplets, down to femtoliter volumes [B 285]. The resulting drawback of a small electrochemical signal of the droplets compared to the large capacitive background current of the electrode surface is sidestepped by depositing a great number of droplets, distributed over the electrode surface.

Apart from chemical means (which are not going to be considered here) the most widely used technique for the deposition of arrays of microdroplets is the evaporation from a volatile solvent. In the first step, a defined amount of the sample liquid is dissolved in a volatile solvent (e.g., acetonitrile, dichloromethane). It has to be taken into account that growing concentrations of the compound in the solvent will eventually lead to an increased surface coverage and, eventually, to the formation of a continuous film rather than an array of microdroplets.

In the next step, a defined volume of this solution is transferred to the surface of an appropriate electrode. Graphite electrodes like paraffin impregnated electrodes and basal plane pyrolytic carbon electrodes seem

most suitable, as hydrophobic surface allows a good wetting and thus adherence of the organic solution (see also Chapter 3.1). Then, the solvent is evaporated in air or, if necessary, under inert gas atmosphere.

Naturally, this technique can be applied only for non-volatile compounds. Examples are redoxliquids like tetraalkyl substituted phenylenediamines (TRPDs) which have been deposited at basal plane pyrolytic carbon electrodes (see Chapter 6.1). As an example, Marken and coworkers transferred 1-50  $\mu\text{L}$  of freshly prepared solution of the compound dissolved in acetonitrile ( $0.1\text{--}1\text{ mmol L}^{-1}$ ) onto the electrode surface and evaporated the acetonitrile in air [e.g., B 74].

An important question to be addressed is, in what form and size the microdroplets are distributed at electrode surfaces. In a recent work, Wadhawan et al. [B 230] answered this question in an elegant manner. The authors examined the deposition pattern of *para*-*N,N,N',N'*-tetrahexylphenylenediamine (THPD) at basal plane pyrolytic carbon electrodes by taking advantage of the well-known abilities of the related *para*-phenylenediamine as a photographic developer. After the deposition of microdroplets of THPD, the modified electrode was dipped for a few seconds into a 0.1 M aqueous solution of silver perchlorate allowing the

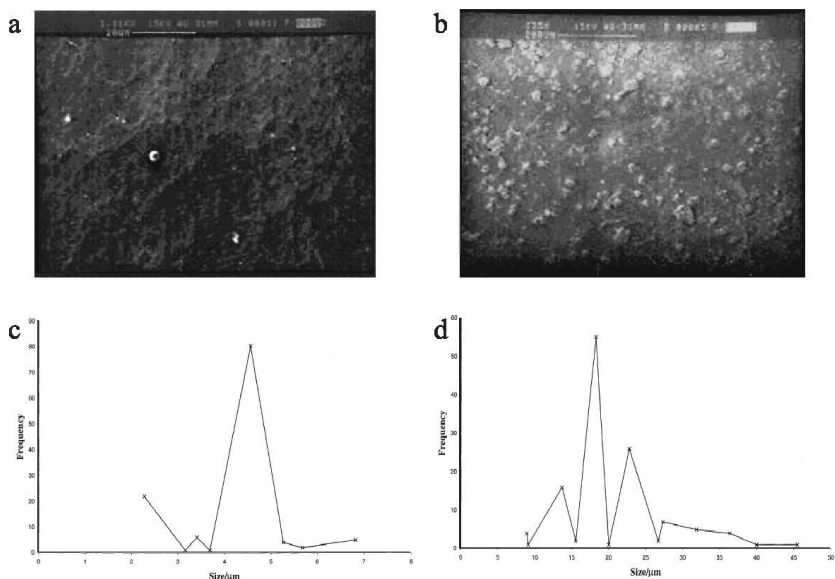


**Fig. 3.4.** a, b SEM image of a 4 nmol, and b 40 nmol of THPD deposited on a basal plane pyrolytic carbon electrode and immersed in  $\text{AgClO}_4$  for 10 s (at open circuit potential). c and d measured droplet distribution for the two coverages indicated in a and b [B 230]

following reaction to take place:



The chemical reaction takes place at the oil|water interface, covering the THPD droplets with a silver shell. These silver-plated droplets could now be imaged with the help of scanning electron microscopy, SEM, as shown in Fig. 3.4. For both depicted cases the droplets exhibit a very narrow size distribution, with an average size of 4.2  $\mu\text{m}$  (for 4 nmol THPD deposited) and 20.6  $\mu\text{m}$  (for 40 nmol THPD deposited). The experiments also supported earlier assumptions that the formation of the microdroplets takes place mainly within the troughs of the graphite surface.

At very smooth electrode surfaces the decreasing size of the solvent drop during evaporation can lead to the unwanted concentration of the redox liquid in the remaining solvent and thus to the formation of few bigger droplets in the center of the electrode. In order to yield a more even distribution of the droplets across the electrode surface it is possible to roughen the electrode surface mechanically prior to the droplet deposition. By doing this, spots with high surface energy are formed at which the droplet formation takes place inhibiting a coalescence of the droplets during the process of the solvent evaporation.

In order to achieve a sufficiently even distribution of the droplets at transparent indium tin oxide electrodes (ITOs) Marken [B 74] siliconized the ITO electrodes prior to the deposition of microdroplets of THPD redox liquid, which makes the electrode surface hydrophobic and thus allows a better adherence of the organic droplets at the electrode surface.

### 3.4 The Electrochemical Measurement

In principle, there is no limitation with respect to the electrochemical measuring technique when immobilized particles and droplets are studied. The entire arsenal of electrochemical techniques and also hyphenated (*in situ*) techniques is applicable<sup>2</sup>. It can be recommended to perform preliminary studies with cyclic voltammetry or linear scan voltammetry. Care must be taken in choosing the starting potential so that the compound to be studied is not undergoing any reaction at that potential. Generally, the scan rates most appropriate for studies of immobilized particles and droplets are similar to those used in solution studies, i.e., between 10 and 500  $\text{mV s}^{-1}$ . If

<sup>2</sup> Scholz F (ed) (2002) *Electroanalytical Chemistry. Guide to Experiments and Applications*. Springer-Verlag, Berlin Heidelberg New York

the voltammograms exhibit very broad signals, e.g., when they possess a half-peak width of 100 mV or more, it may be that too large amounts of the compound were immobilized on the electrode surface. In such a case some trials are necessary with deliberately chosen smaller amounts. Usually the signals will become narrower with decreasing amounts. If that is not the case, the broad signals may be an inherent property of the compound. When the electrode reaction is confined to the surface or the three-phase junction region, i.e., when no diffusion is involved, scan rates as high as  $5 \text{ V s}^{-1}$  can be used without any remarkable peak broadening [BIBLIO 83]. With electrode diameters in the range of 0.5 to 5 mm and a particle size of about 10  $\mu\text{m}$ , one observes peak currents between 1 and 500  $\mu\text{A}$  in cyclic voltammetric experiments, at voltammetric scan rates between 1 and 100  $\text{mV s}^{-1}$ .

In the case of completely chemically reversible systems, as, e.g., in case of Prussian blue and its analogues, it can be useful quantifying the amount of deposited material with the help of chronocoulometry. Of course, chronocoulometry will yield only the amount of electrochemically active particles. Particles that are adhering to the surface so loosely that an electron transfer is not possible, cannot contribute to the measured charge. Another problem could arise when the electrochemical reaction prompts the formation of an insulating layer on the surface of the particles or at the contact with the electrode. Although no such examples have been reported so far one must be aware of this possibility.

AC and pulse techniques can be suggested due to their high resolution power and simple peak evaluation. In case that metals or alloys are electrochemically dissolved by oxidation, or some oxides are dissolved by reduction, one must bear in mind that the scanning time with these techniques may be too small for a complete stripping. In that case some of the material will remain on the electrode surface and must be carefully removed before the next measurement.

## 4 Hyphenated Techniques

The depth of information obtainable from a single electroanalytical technique like the voltammetry of immobilized particles and droplets is naturally limited. Consequently, the combinations of electroanalytical techniques with non-electrochemical techniques become important and attractive. In particular, *in situ* combinations are powerful tools for investigating electrode processes. They are based on a simultaneous recording of electrochemical and non-electrochemical signals.

A number of restrictions apply to *in situ* combinations, mainly connected with the presence of the aqueous electrolyte solution. Thus, the use of vacuum spectrometric techniques employing electrons, ions or atoms for excitation or detection are restricted to be applied *ex situ* only. Most important are the spectroelectrochemical techniques, i.e., the combination of electroanalytical and spectroscopic techniques. The combination with electron spin resonance spectroscopy<sup>1-2</sup>, with Raman<sup>3-5</sup>, infrared<sup>6</sup> and UV-VIS spectroscopy<sup>7</sup> proved to be very powerful instruments for investigating electrode processes.

The adaptation of hyphenated techniques to the voltammetry of immobilized particles and droplets is not always straightforward. Some methods, like the electrochemical quartz crystal microbalance, EQCM, can be utilized literally instantaneously. Other, especially spectroelectrochemical techniques, generally require the building of adapted electrochemical cells

- 
- <sup>1</sup> Goldberg IB, McKinney TM (1984) Principles and Techniques of Electrochemical Electron Spin Resonance Experiments. In: Kissinger PT, Heinemann WR (eds) Laboratory Techniques in Electroanalytical Chemistry, Dekker, New York Basel, pp 675-699
  - <sup>2</sup> Bagchi RN, Bond AM, Scholz F (1989) Electroanalysis 1: 1-11
  - <sup>3</sup> Birke RL, Lu T, Lombardi JR, (1990) Surface Enhanced Raman Spectroscopy. In: Varma R, Selman JR (ed) Techniques for Characterization of Electrodes and Electrochemical Processes. Wiley, New York, pp 211-277
  - <sup>4</sup> Bard AJ, Faulkner LR (2001) Electrochemical Methods. 2<sup>nd</sup> ed. Wiley, New York, pp 704-709
  - <sup>5</sup> Arsov LD, Plieth W, Koßmehl G (1998) J Solid State Electrochem. 2: 355-368
  - <sup>6</sup> Kulesza PJ, Malik MA, Denca A, Strojek J (1996) Anal Chem 68: 2442-2446
  - <sup>7</sup> Mortimer RJ, Rosseinski DR (1984) JCS Dalton Trans 2059-2062



in order to meet the special conditions that arise from the specific geometry of the electrodes.

## 4.1 Optical Techniques and Spectroelectrochemistry

### 4.1.1 In Situ Spectroscopy

Optical spectroscopy in the UV-VIS range lends itself very well for the in situ observation of electrochemical reactions. For studying electrochemical reactions of species that are confined to an electrode surface, like of immobilized films, particles and droplets, a number of spectroelectrochemical techniques have been developed. They are based on two major set-ups:

- Measuring the transmission of a redox species, and the spectral changes during an electrochemical reaction.
- Measuring the reflectance of a deposited compound, and the changes in the reflectance spectra during the electrochemical experiment.

Basically, the simplest spectroelectrochemical experiment is to measure the change of the transmission of a light beam that is directed through an immobilized sample. Obviously, this requires the electrode to be optically transparent. The probably most used transparent electrode material for spectroelectrochemical applications is the semiconducting indium tin oxide (ITO), which is usually vacuum deposited on a quartz or glass substrate. ITO electrodes have been used, for example, for the spectroelectrochemical investigation of the electrochromic properties of inorganic and organic polymer films deposited electrochemically on the ITO electrodes<sup>8-10</sup>. However, since the vast majority of electrode materials are optically opaque, and many of the materials are highly reflecting, the utilization of reflectance measurements, e.g., at polished metal sheet electrodes is widespread in electrochemistry<sup>11</sup>.

---

<sup>8</sup> Kulesza PJ, Zamponi S, Malik MA, Miecznikowski K, Berrettoni M, Marassi R (1997) *J Solid State Electrochem* 1: 88-93

<sup>9</sup> Malinauskas A, Holze R, *Electrochim Acta* (1998) 43: 2563-2575

<sup>10</sup> Monk PMS, Mortimer RJ and Rosseinsky DR (1995) *Electrochromism: Fundamentals and Applications*. VCH, Weinheim

<sup>11</sup> Plieth W, Wilson GS, delaFe CG (1998) *Pure and Appl Chem* 70: 1395-1414

Generally, both, transmission and reflectance techniques, have been used based on a preliminary, mostly electrochemical, deposition of the target compound onto the electrode. However, they can also be exploited for studying mechanically immobilized particles and droplets. Due to the nature of the voltammetry of immobilized microparticles and microdroplets, however, they require some modification in order to make use of their full potential. One of the features of the voltammetry of immobilized microparticles and droplets is the generally low and partially uneven surface coverage of the compound at the electrode. Generally, it is not advisable to use thicker particle layers, since, apart from the generally poor adherence, the growing resistance between the particles often does not allow the entire layer to react through. In the case of microdroplets, a growing surface coverage generally leads to an increasing droplet size connected with the relative decrease of the length of the triple-phase junction and eventually to the formation of an insulating liquid layer. As it will be demonstrated in Chapter 4.1.2, the problem of applying optical observation and spectroscopic analysis to the voltammetry of immobilized microparticles and microdroplets has been successfully solved using optical microscopy.

An important example for the exploitation of transmission spectroelectrochemical measurements of immobilized microparticles is the study of indigo by Bond et al. [B 72]. Bond and coworkers have utilized UV-VIS spectroelectrochemistry in order to unravel the complex redox chemistry of indigo. They compared the spectroelectrochemical behavior of microparticles of indigo mechanically attached onto the surface of an ITO electrode and that of the compound dissolved in DMSO. For their investigation, the authors have used a spectroelectrochemical cell that allowed the study of both, the dissolved, and the microcrystalline compound (Fig. 4.1). For measurements of indigo microparticles, the compound has been transferred onto the ITO electrode surface by rubbing a thin layer with a cotton bud onto the electrode surface. This immobilization procedure must be performed very carefully as a scratching of the thin indium tin oxide layer would compromise the function of the electrode. For the study of the dissolved compound the authors have used a thin layer cell with a gold microgrid electrode as the working electrode.

Figure 4.2 shows the comparison of the changes of the absorption spectra of indigo during an electrochemical reduction of (b) the immobilized

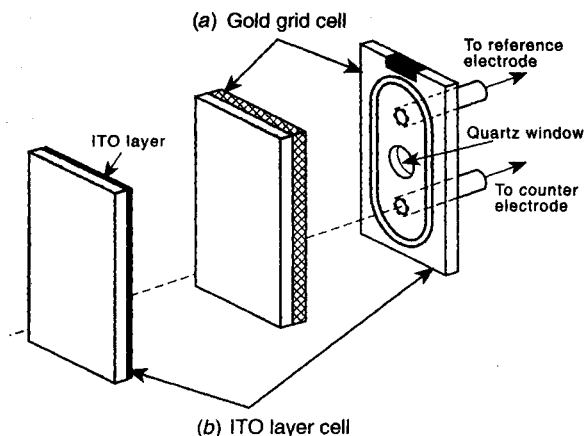


**Fig. 4.1.** Thin layer transparent electrochemical cells with a gold grid electrode for solution experiments and an ITO electrode coated on glass for electrochemical experiments using solids [B 72]

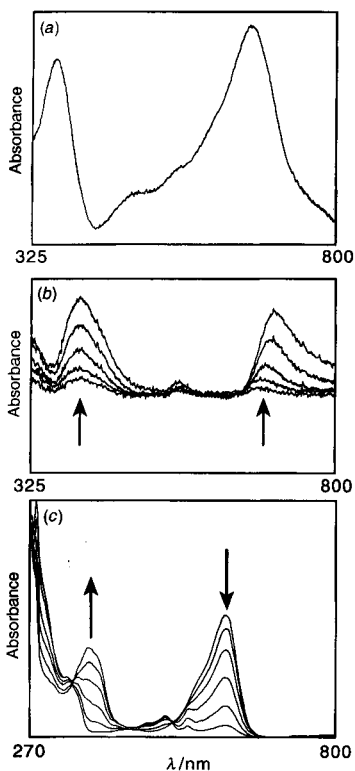


**Fig. 4.2.** UV-VIS absorption of indigo mechanically attached to an ITO electrode and immersed in  $1.28 \text{ mol L}^{-1}$  NaCl electrolyte solution. **b** Changes in the UV-VIS absorption of indigo on ITO (spectrum **a** was used as the background and only the background corrected absorbance was recorded) when a potential of  $-1.0 \text{ V vs. SCE}$  is applied (curves correspond to 5 s, 30 s, 2 min, 10 min and 30 min electrolysis). **c** In situ UV-VIS spectroelectrochemical monitoring of the reduction of  $2.4 \times 10^{-4} \text{ mol L}^{-1}$  indigo in DMF ( $0.1 \text{ mol L}^{-1}$  NBut<sub>4</sub>PF<sub>6</sub>,  $10 \text{ nmol L}^{-1}$  benzoic acid) (applied potential  $-1.0 \text{ V vs. SCE}$ ) [B 72]

solid, and (c) the dissolved compound. From the comparison of these spectra, which indicate remarkable differences in the reductive conversion of indigo, the authors have proposed a reaction scheme for the conversion of the immobilized compound that, without the spectroelectrochemical study, would not have been possible to derive (for further details see Chapter 5.4).

### **4.1.2 In Situ Light Microscopy and Microscopic Spectroelectrochemistry**

The low surface coverage in combination with the uneven distribution of the microparticles and droplets at a given electrode surface favor light microscopy for the observation of electrochemical reactions of these redox systems. As we will show in the following sections, the accessible information can range from the purely qualitative, visual observation of electrochemical processes to the quantitative evaluation with the help of coupled spectrometric equipment.

In situ light microscopy is a cheap and straightforward technique that enables the reaction to be followed with a spatial resolution down to micrometer scale. Compared to atomic force microscopy (AFM) this resolution appears to be rather low, but considering the low investment and operational costs of the equipment, the possible real-time observation of the electrode surface and additional information like color changes and the interrogation of the spatial progressing of a reaction, the in situ light microscopy has great potential. In general, again two techniques can be utilized – incident light microscopy and transmission light microscopy. Due to the different optical setup and therewith different requirements towards electrode material and sample nature, both techniques have their application domains.

#### ***In Situ Incident Light Microscopy***

For the in situ observation of electrochemical reactions at non-transparent electrodes conventional light microscopes equipped with an incident light unit can be used. Microscopes of this kind are typically used for ore microscopy, material and life science. The setup requires an adapted electrochemical cell that accommodates the working electrode, a reference and a counter electrode, equipped with a glass or quartz window. At very low cost, such cells can conveniently be produced from acryl. The geometry of the setup, i.e., the  $\circ R_0$  geometry of the optical path usually requires the specular reflectance of the electrode surface to be minimized. This can be

realized with the help of two polarizing filters, which are generally available at incident light microscopes, and which have to be arranged in a crossed ( $90^\circ$ ) position.

Two basic setups are possible, which are described in the following sections. As an example, an electrochemical cell has been presented for the *in situ* microscopic observation of electrochemical reactions of microcrystalline samples mechanically attached to the surface of paraffin impregnated graphite electrodes [B 58]. The authors have assembled an electrochemical cell with an ore microscope (Leitz Laborlux 12 POL S, Leica Mikroskopie und Systeme GmbH, Germany) in an upright position. This setup, however, requires the electrode to be fitted through the cell bottom, making the exchange of electrodes rather tedious and time-consuming. Turning the microscope upside down (or using an inverse microscope in the first place) offers the chance to construct a cell in which the electrode can be fitted from the top of the cell. An example for such a setup is presented in [B 67]. The authors have brought the microscope into the inverse position with the help of a scaffold. Now, a cell arrangement (see Fig. 4.3) could be used that allowed a rod electrode (paraffin impregnated graphite electrode, PIGE) to be fitted through the lid of the cell. This setup massively simplifies the electrode handling.

The use of a 20-fold magnifying objective lens in combination with 10-fold oculars resulted in a 200-fold magnification which allowed visualizing objects of a size of approximately  $10\ \mu\text{m}$  (see Fig. 4.4). Higher spatial resolutions are principally possible, however, the shrinking electrolyte layer thickness between the working electrode and the glass window goes along with a restriction of the diffusion from or to the electrode surface and thus with a strong deterioration of the voltammetric signals. The use of long-range object lenses might help overcoming this problem. For the study of immobilized microparticles, the electrode preparation is straightforward and follows the usual procedure of mechanical immobilization (Chapter 3.2.).

A similar technique has been used by Bond et. al [B 56, B 101] who employed a video capturing system in combination with a Nikon Epiphot inverted metallurgical microscope fitted with a long-working-distance objective lens and a CCD TV camera for a subsequent analysis of the optical data. From the captured images the authors could deduce that the electrochemical reactivity of microparticles of 7,7,8,8-tetracyanoquinodimethane (TCNQ) immobilized on polished gold electrodes strongly depends on the size of the particles. The authors found that the voltammetric responses of TCNQ at a scan rate of  $100\ \text{mV s}^{-1}$  were principally associated with the conversion of nano-size particles ( $< 1\ \mu\text{m}$ ), whereas the conversion rate of larger crystals did not suffice to contribute to the voltammetric signal.

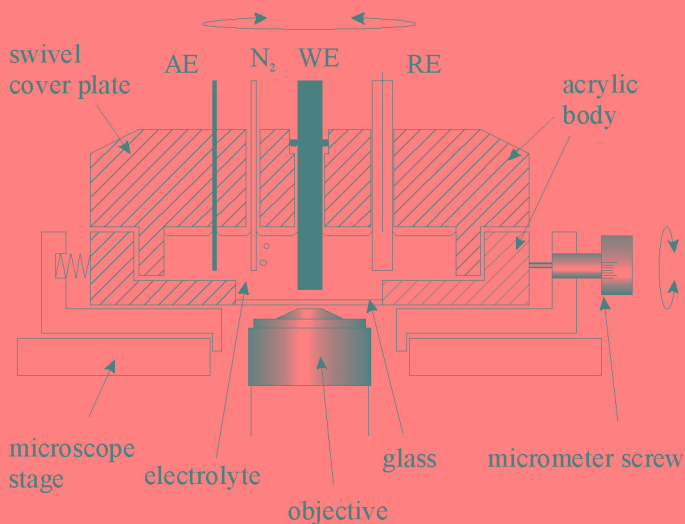


**Fig. 4.3.** Cross section of the electrochemical cell for in situ microscopic spectroelectrochemistry [B 67]

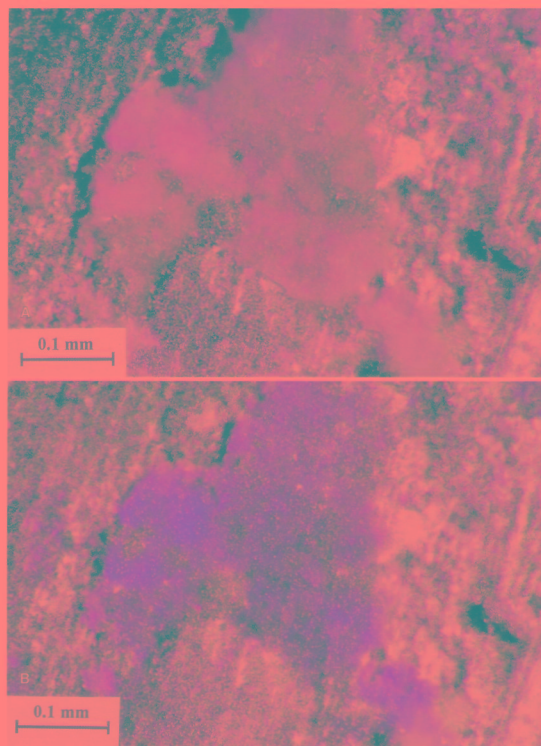


**Fig. 4.4. Top** Photographic image of silver octacyanomolybdate(IV) immobilized on a PIGE and immersed into 0.1 M AgNO<sub>3</sub>. **Bottom** The same particles after electrochemical oxidation at 0.75 V vs. Ag/AgCl to silver octacyanomolybdate(V) [B 58]

The purely qualitative analysis of the visual observation, however, leaves a lot of information concealed, and it is only a logic step to combine the microscopic observation with the in situ recording of the spectral information of the studied compound. This step can be done by taking advantage of the property of immobilized microparticles to scatter incident light. The resulting technique, the *microscopic in situ diffuse reflectance spectroelectrochemistry* [B 67], not only allows quantifying the electrochromic properties of the immobilized particles, it also gives access to mechanistic information on the studied electrochemical reaction. In reference [B 67], the authors demonstrate that for microparticles of silver octacyanomolybdate (IV/V), immobilized at a PIGE, in situ recorded microscopic diffuse reflectance spectra can be analyzed with the help the Kubelka-Munk function (Eq. 4.1 and Fig. 4.5). This function, which can be referred to as the analogue of the law of Bouguer-Lambert-Beer for powder samples, describes the ratio of absorbance and scattering of a given sample layer <sup>12</sup>.

$$F(R_{\infty}) = \frac{K}{S} = \frac{(1 - R_{\infty})^2}{2R_{\infty}} \quad (4.1)$$

( $K$  = absorption coefficient,  $S$  = scattering coefficient,  $R_{\infty}$  = reflectance of a sample of infinite thickness)

Although the Kubelka-Munk function, like the law of Bouguert-Lambert-Beer, is strictly speaking exclusively valid for highly diluted samples, the authors have demonstrated a good agreement of voltammetric and spectrometric data. For the electrochemical oxidation of immobilized silver octacyanomolybdate they have shown validity of Eq. 4.2, a modification of the Kubelka-Munk function connecting the absorbance/reflectance date of the immobilized particles and their Red/Ox ratio.

$$\frac{c_{\text{ox}}}{c_{\text{red}}} = \frac{\frac{(F(R) - F'_{\text{red}})}{(F'_{\text{ox}} - F'_{\text{red}})}}{\left(1 - \frac{(F(R) - F'_{\text{red}})}{(F'_{\text{ox}} - F'_{\text{red}})}\right)} \quad (4.2)$$

( $F'_{\text{ox/red}}$  are the values of the Kubelka-Munk function at 530 nm for  $c_{\text{ox}} = 1$  and  $c_{\text{red}} = 1$ , respectively.  $F(R)$  is the actual value of the Kubelka-Munk function for a certain Red:Ox ratio.)

<sup>12</sup> Kortüm G (1969) Reflexionsspektroskopie. Springer-Verlag, Berlin Heidelberg New York

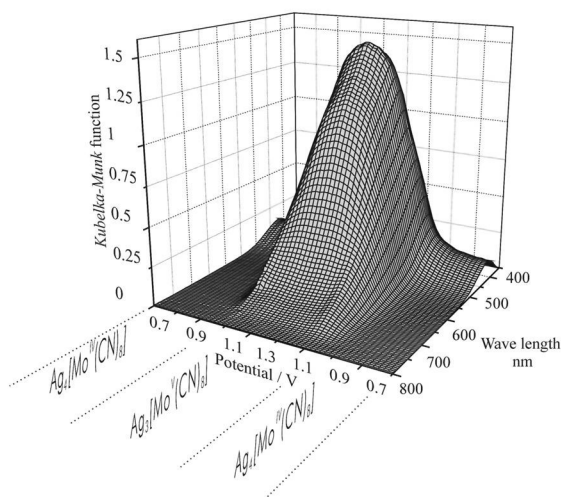


**Fig. 4.5.** Kubelka-Munk function of silver octacyanomolybdate(IV) immobilized on the surface of a paraffin impregnated graphite electrode and immersed in a 0.1 M  $\text{AgNO}_3$  solution. The Kubelka-Munk function was recorded in situ during the cyclic oxidation and re-reduction of the compound [B 136]

The microscopic in situ diffuse reflectance spectroelectrochemistry can also be utilized to interrogate mechanisms of electrochemical reactions of immobilized particles or droplets. As an example, information on the geometric course of the electrochemical redox processes at the deposited silver octacyanomolybdate ( $\text{Ag ocm}$ ) has been derived for the oxidation and reduction of immobilized microparticles of silver octacyanomolybdate (IV)/(V) [B 67]. Based on a comparison of the change of the diffuse reflectance ( $dR/dE$ ) of differently thick patches of silver octacyanomolybdate and the simultaneously recorded cyclic voltammograms (Fig. 4.6a and b) the authors have derived a model of the geometrical course of the electrochemical reaction. They have found that whereas for thin sample layers the voltammetric and the spectrometric curves are virtually identical there is a strong retardation of the  $dR/dE$  curve on the potential scale for the case of a thick sample layer (Fig. 4.6a). In principle, one could suppose that the oxidation of solid silver octacyanomolybdate(IV),  $\text{Ag ocm(IV)}$ , may start either at the graphite-sample interface or at the sample-electrolyte interface. The same applies for the reduction of  $\text{Ag ocm(V)}$ . However, only in the case where the reaction advances from the graphite-sample interface into the compound crystal one can explain the described optical behavior: Upon oxidation, a layer of higher optical density grows from the graphite



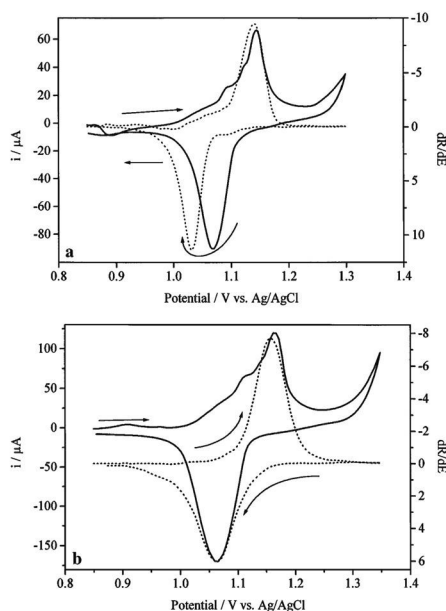


**Fig. 4.6.** Cyclic voltammogram (solid line) of silver octacyanomolybdate (IV/V) in 0.1 M  $\text{AgNO}_3$ , scan rate 1 mV/s; First derivative of the reflectance over the  $dR/dE$  potential (dotted line) versus potential. **a** The reflectance was measured for a sample layer of about 10  $\mu\text{m}$  thickness; **b** The reflectance was measured for a sample layer of about 1  $\mu\text{m}$  thickness [B 67]

octacyanomolybdate (ocm) interface, and the incident light beam can fully penetrate the upper layer of optically less dense Ag ocm(IV) (cf. Fig. 4.7). Thus, the incident light will be less reflected the thicker the Ag ocm(V) layer becomes. If the opposite case was true, i.e., if the optically less trans-

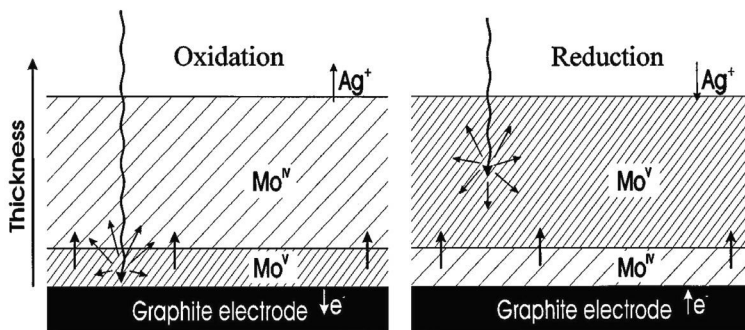


**Fig. 4.7.** Schematic drawing of a model for layer growing and light penetration for the processes of oxidation and reduction of silver octacyanomolybdate immobilized on an electrode surface. This scheme is based on the fact that the absorption coefficient of silver octacyanomolybdate(IV) is much smaller than that of silver octacyanomolybdate(V) [B 67]

parent layer grew from the solution ocm interface downwards, the reflectance would decrease to its minimum before the electrochemical reaction reaches the graphite interface. Obviously, this does not happen. But, upon reduction of the optically dense Ag ocm(V), especially in the case of a thick sample layer, the effect of electrochemical reduction is mirrored by the reflection only with strong retardation. This is the result of a growth of the optically less dense layer from the graphite interface in the direction of the solution interface.

In a later contribution, the same technique has been exploited to unravel the voltammetric responses of crystalline and amorphous sample material of the oxidation and reduction of silver octacyanomolybdate and -tungstate [B 136].

### ***In Situ Transmission Light Microscopy***

The coupling of transmission light microscopy and electrochemistry can be performed for (i) a purely qualitative evaluation, and (ii) for a quantitative analysis of electrochemical reactions of immobilized particles or droplets. Probably due to the delicate surface of ITO electrodes, however, so far it has only been utilized for the study of droplets. Of course, ITO electrodes have been used for decades for the study of electrochemically deposited films of electrochromic compounds, however, such films are not considered here.

Marken and coworkers [B 74] have used the microscopy in order to study redox processes of microdroplets of immobilized microdroplets of *N,N,N',N'*-tetrahexylphenylenediamine (THPD). Marken took advantage of the possibility to visualize the spatial progress of the oxidation of the immobilized THPD droplets. The setup is, in principle, straightforward: an open cell with a counter and a reference electrode was used, and an ITO electrode was located in the optical path of the transmission microscope. A camera, mounted to the microscope, allowed taking images of the electrode surface during the voltammetric experiment. The THPD was deposited on the electrode via evaporation from acetonitrile (Chapter 3.3). The problem with commercial ITO electrodes is a relatively high hydrophilicity of the ITO, which can make the wetting and thus the adherence of droplets of organic liquids difficult. Marken circumvented the problem by siliconizing the ITO surface prior to droplet deposition (Chapter 3.3). The result of the experiment is presented in Fig. 4.8. The photographic images, taken at different stages of the electrochemical oxidation of THPD, gave support to the assumption of an initiation of the reaction at the three-phase bound-

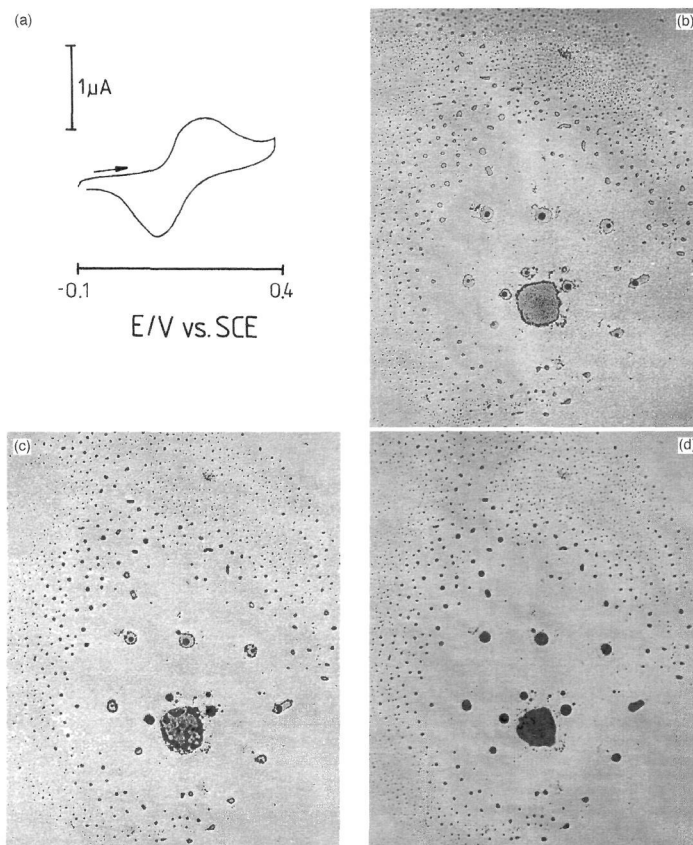


**Fig. 4.8.** **a** Cyclic voltammograms for the oxidation of  $1.24 \mu\text{g}$   $N,N,N',N'$ -tetrahexylphenylenediamine (THPD) deposited on a siliconized ITO electrode immersed in aqueous  $1 \text{ M NaClO}_4$  solution ( $22^\circ\text{C}$ ,  $1 \text{ mV s}^{-1}$ ). **b-d** Photographs of microscopic images of THPD deposited on a siliconized ITO electrode immersed in aqueous  $1 \text{ M NaClO}_4$ . The applied potential has been stepped from  $-0.1$  to  $+0.4 \text{ V vs. SCE}$  for **b** 10 s, **c** 30 s, **d** 5 min (scale  $780 \times 920 \mu\text{m}$ ) [B 74]

ary electrolyte|electrode|droplet, from which the reaction proceeded into the bulk of the droplets. A closer look also revealed a separation of the oxidized and the reduced form of the compound during the reaction.

A quantitative analysis of a microscopic observation can be achieved with a spectroelectrochemical cell as presented in Fig. 4.9, coupled to a microscope and a diode array spectrometer [280]. The cell body, made of acrylic, consists of an ITO plate (working electrode), sandwiched with a glass plate with attached platinum wire (counter electrode). The spacing between the plates is realized with rubber rings of a defined thickness.

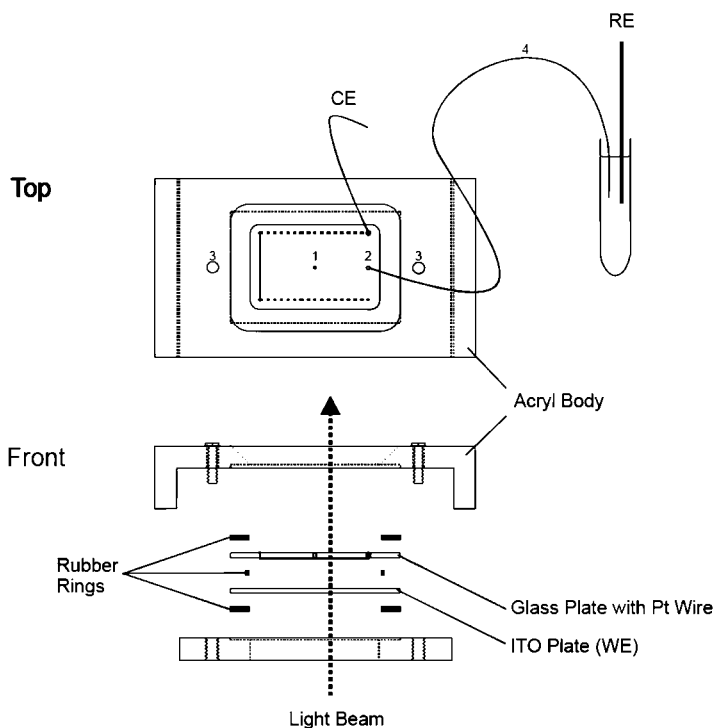


**Fig. 4.9.** Scheme of the spectroelectrochemical cell. CE is the counter electrode, RE is the reference electrode; (1) hole for inserting the nitrobenzene droplet, (2) hole for inserting the electrolyte solution, (3) threads and screws, and (4) tube filled with agar/KCl [B 280]

Two holes enable the injection of the electrolyte solution and of a sample droplet. Komorsky-Lovrić and coworkers have used this setup for studying the ion transfer from water into nitrobenzene at the three-phase junction when decamethylferrocene, dissolved in the nitrobenzene droplet, becomes electrochemically oxidized. By spectrometrically recording the absorbance at different spots of the droplet (see Fig. 4.10) concentration-time plots can be derived which can help to unravel reaction at triple-phase electrodes (Fig. 4.11).

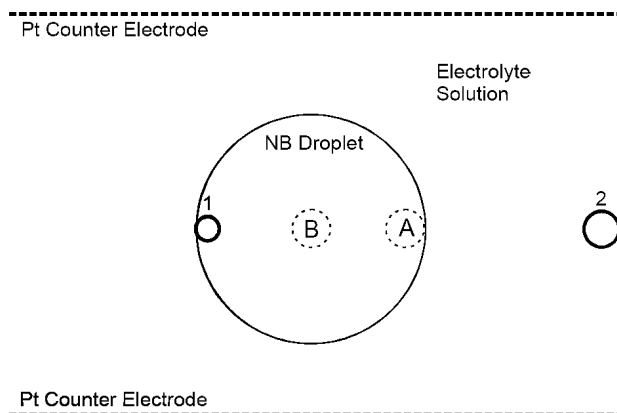


**Fig. 4.10.** Schematic drawing of the spectroelectrochemical cell with locations of the spectrometric measuring points. Spot (A) is located approximately 0.5 mm, and spot (B) approximately 3 mm away from the junction line [B 280]

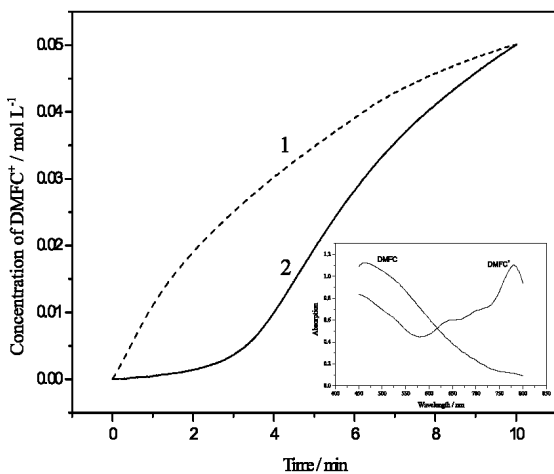


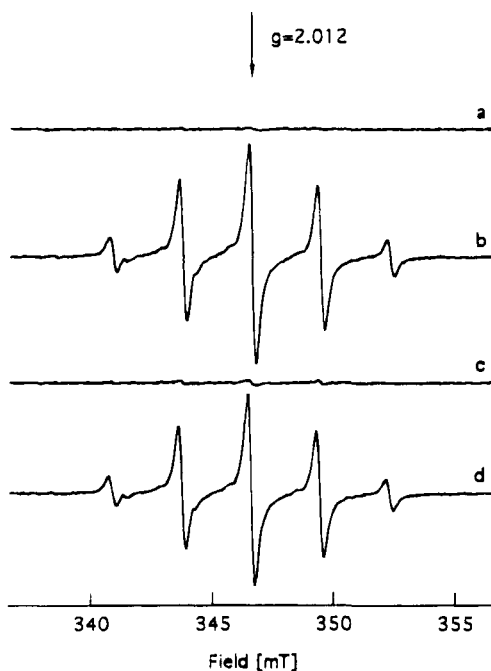
**Fig. 4.11.** The variation of the  $\text{dmfc}^+$  concentration measured close to the three-phase junction line (curve 1) and in the middle of the droplet (curve 2). The concentration of  $\text{dmfc}$  in NB was  $0.05 \text{ mol L}^{-1}$ . The concentration of aqueous  $\text{KNO}_3$  electrolyte solution was  $0.1 \text{ mol L}^{-1}$ . The ITO electrode was polarized at  $0.4 \text{ V}$ . The inset shows the spectra of the completely reduced solution ( $\text{dmfc}$ ) and the completely oxidized solution ( $\text{dmfc}^+$ ,  $\text{ClO}_4^-$ ) [B 280]

### 4.1.3 In Situ Electron Spin Resonance Spectroscopy

Many electrochemical reactions involve the formation of radical species, either as products, or as intermediates. In situ electron spin resonance (ESR) measurements can help identifying these species, give information on their chemical and physical environment and thus help elucidating the mechanism of electrode processes. As an example, in situ ESR can be utilized for distinguishing if an electrochemical oxidation or reduction process of an immobilized compound proceeds as a pure solid-solid conversion or if it proceeds via the solution phase. The first study of this kind was the reduction of solid 7,7,8,8-tetracyanoquinodimethane (TCNQ) and the oxidation of solid organometallic *trans*-Cr(CO)<sub>2</sub>(dpe)<sub>2</sub> (see Fig. 4.12) by Bond and Fiedler [B 70].

In situ ESR can also be applied to the study of immobilized microdroplets. Thus, Marken and coworkers have studied the voltammetry of THPD (tetrahexylphenylenediamine, see Chapter 6.1) immobilized on an electrode surface, or dissolved in acetonitrile [B 74]. The in situ recorded spectra of the electrochemically oxidized compound, THPD<sup>+</sup>, are shown in Figs. 4.13a and 4.13b. The difference between the solution signal and that of the pure redox liquid is clearly visible.

**Fig. 4.12.** In situ electrochemical generation at a platinum electrode of the solution phase ESR spectrum of *trans*-[Cr(CO)<sub>2</sub>(dpe)<sub>2</sub>]<sup>+</sup> by oxidation of *trans*-Cr(CO)<sub>2</sub>(dpe)<sub>2</sub> in a 1:1 mixture of acetonitrile and aqueous K<sup>+</sup>-buffer. **a** Surface attached *trans*-Cr(CO)<sub>2</sub>(dpe)<sub>2</sub> to oxidation; **b** oxidation of *trans*-Cr(CO)<sub>2</sub>(dpe)<sub>2</sub> to *trans*-[Cr(CO)<sub>2</sub>(dpe)<sub>2</sub>]<sup>+</sup>; **c** regeneration of solid *trans*-Cr(CO)<sub>2</sub>(dpe)<sub>2</sub> by electrochemical reduction of *trans*-[Cr(CO)<sub>2</sub>(dpe)<sub>2</sub>]<sup>+</sup>; **d** reoxidation of *trans*-Cr(CO)<sub>2</sub>(dpe)<sub>2</sub> to *trans*-[Cr(CO)<sub>2</sub>(dpe)<sub>2</sub>]<sup>+</sup> after experiment **c** [B 70]



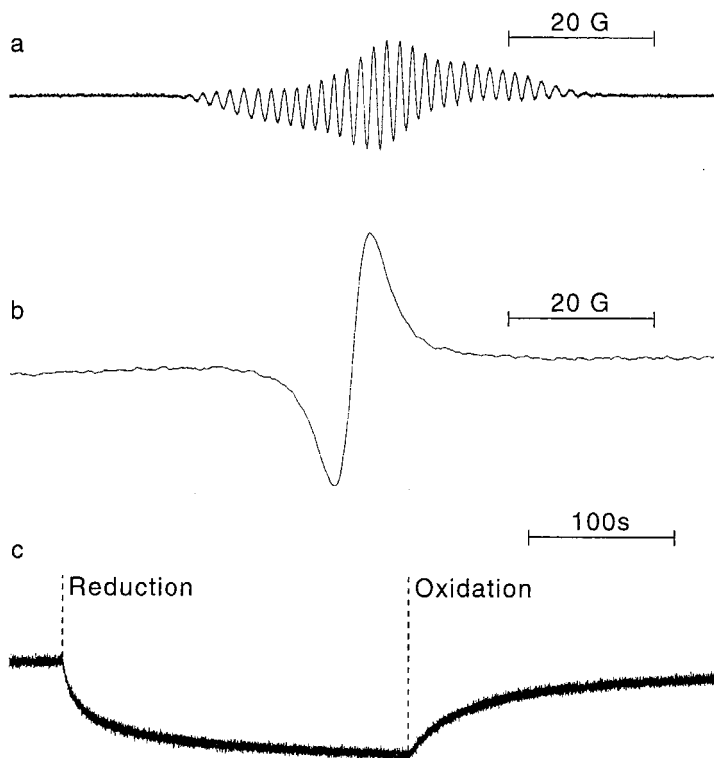


**Fig. 4.13.** **a** ESR signal for  $\text{THPD}^+$  recorded during in situ electrolysis of 0.6 mM THPD in acetonitrile (0.1 M  $\text{NBu}_4\text{PF}_6$ ) at  $E = 0.4$  V vs. SCE. **b** ESR signal for  $\text{THPD}^+$  recorded during in situ electrolysis of 5  $\mu\text{g}$  THPD deposited on a 1.2  $\text{cm}^2$  area gold electrode immersed in aqueous 0.1 M  $\text{NaClO}_4$ . **c** ESR signal intensity vs. time transient for the ESR signal described in **b** when a double potential step between  $E = 0.4$  V and 0 V vs. SCE is applied [B 74]

As demonstrated in Fig. 4.13c, transients of the intensity of the ESR signal versus time can be recorded.

For both studies, which represent examples for the application of in situ ESR for the study of the voltammetry of immobilized microparticles and microdroplets, conventional flat cells<sup>13</sup> have been used.

<sup>13</sup> Piette LH, Ludwig P, Adams RN (1962) *Anal Chem* 34: 916-921

#### 4.1.4 Ex Situ Spectroscopy

Due to the wavelength of the applied radiation many spectroscopic techniques require the experiments to be performed under vacuum conditions. This makes them unsuitable for in situ electrochemical applications. Nevertheless, very often these techniques are of inestimable value for the study of electrochemical reactions. Amongst other things they, for example, allow the determination of the elemental composition of a sample after an electrochemical reaction.

#### ***Scanning Electron Microscopy and X-Ray Electron Probe Microanalysis***

The scanning electron microscopy (SEM) and X-ray probe microanalysis are perfectly suited as a supporting tool for the voltammetry of immobilized microparticles. The value of this combination, i.e., the imaging of the electrode surface by SEM and the subsequent single particle elemental analysis cannot be overestimated.

SEM measurements can be utilized to obtain information on the morphology of the electrode surface and the attached microparticles and their changes as a consequence of a voltammetric experiment. It can also be used to determine size and size distribution of the attached particles. The X-ray microprobe technique, which allows the qualitative and the quantitative surface analysis down to a spatial resolution of less than 1  $\mu\text{m}$  – the usual diameter of the electron beam – is based on the identification and quantification of elements by means of their electron stimulated characteristic X-ray emission. The detection is usually performed with an energy dispersive X-ray detector (EDX). A major limitation of X-ray electron probe microanalysis is its inability to detect lightweight elements.

An example for the utilization of SEM and X-ray electron probe microanalysis is shown in Figs. 4.14 and 4.15. The first figure represents a surface map depicting the distribution of Prussian blue microparticles, mechanically immobilized at a paraffin impregnated graphite electrode. The single particle analysis of immobilized and voltammetrically treated Prussian blue particles is shown in Fig. 4.15. The analysis clearly shows evidence for the insertion of potassium ions upon reduction of Prussian blue, and for the expulsion of potassium upon oxidation.



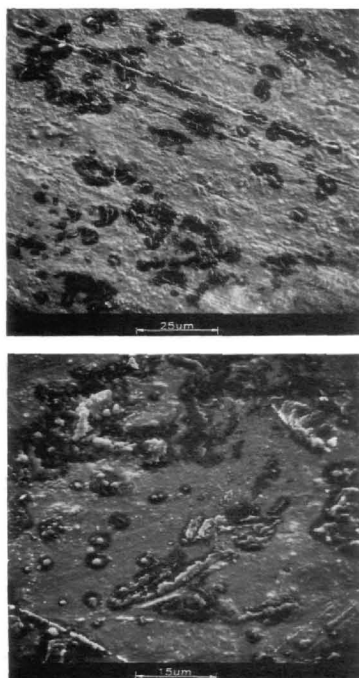


**Fig. 4.14.** SEM micrograph of a paraffin impregnated electrode (top), and SEM micrograph of Prussian blue mechanically attached to a paraffin impregnated electrode (bottom) [B 35]

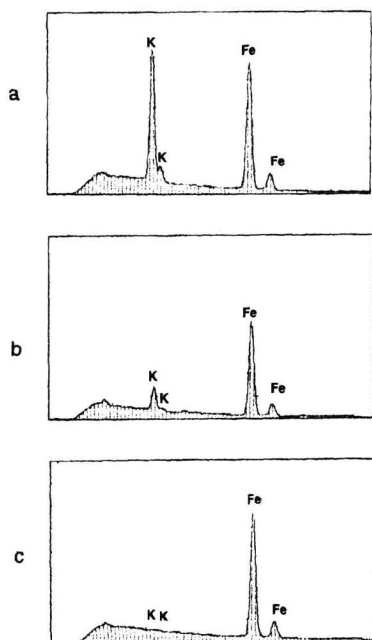


**Fig. 4.15.** Typical examples for single particle electron microprobe analysis of various Prussian blue samples mechanically attached to a paraffin impregnated graphite electrode. **a** Prussian blue electrochemically reduced in 0.1 M  $\text{KNO}_3$  at  $-100$  mV vs. Ag/AgCl for 5 min, **b** without treatment, **c** electrochemically oxidized in 0.1 M  $\text{KNO}_3$  at  $+1100$  mV for 5 min [B 35]

## 4.2 Atomic Force Microscopy and Scanning Tunnelling Microscopy

Atomic force and scanning tunneling microscopy are very useful techniques for direct observation of electrochemical conversions of solid particles immobilized on electrodes. Bond and Marken [B 29] have been the first to apply scanning tunneling microscopy to make visible the deposit of decamethylferrocene on a basal plane pyrolytic graphite electrode before and after the electrochemical reaction. In a later study they used AFM to detect submicrometer deposits of indigo on the same kind of electrodes [B 72]. In case of solid deposits of  $C_{60}$  on the surface of a glassy carbon electrode, electrochemical studies with in situ recording of AFM images allowed showing that the morphology changes indicate nucleation-growth and redistribution processes as well as dissolutions of the solid material [B 119]. The high potential of in situ AFM for the elucidation of electrode reactions of solid particles was also demonstrated in a study of TCNQ: the authors could prove that the electrochemical reduction of TCNQ is associated with the formation of well-formed microcrystals [B 124].

The first case where the reaction front of a solid-to-solid electrochemical transformation could be detected was reported by Hasse and Scholz [B 184]. This was possible when a submicrometer-sized crystal of  $\alpha$ -PbO was subject to a short reduction pulse that did not allow the entire crystal

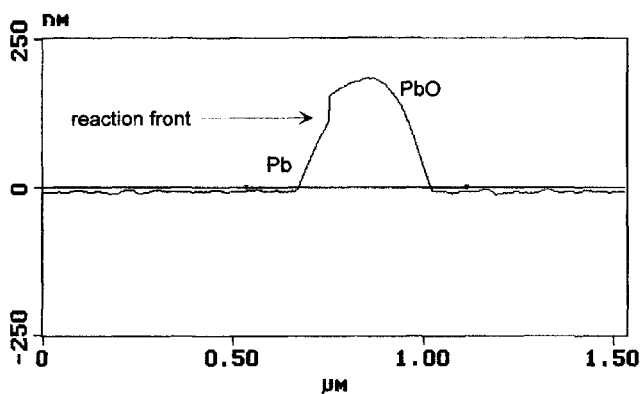


**Fig. 4.16.** Cut through the AFM image of a  $\alpha$ -PbO crystal recorded after a 1 second reduction at 0.695 V vs. Ag/AgCl. The crystal was deposited on a gold electrode and the electrolyte was a 1 M KCl solution [B 184]

to be converted to Pb. Figure 4.16 shows a cut through such a partially reduced crystal where the reaction front appears as a rather steep step.

The electrochemical reductive dissolution of goethite ( $\alpha$ -FeOOH) has been also studied by in situ AFM [B 276]. In this study it could be shown that multidomain and twinned crystals dissolve at less negative potentials than single domain crystals. Further it was possible to follow the dissolution kinetics of single submicrometer-size crystals. Although the kinetics of different crystals varied considerably, the averaged dissolution kinetics agreed very well with what was found earlier in purely electrochemical studies of rather large assemblies of crystals. Figure 4.17 depicts goethite crystals immobilized on the surface of a gold electrode before and after reduction at  $-0.15$  V vs. Ag/AgCl, a potential where only multidomain and twinned crystals dissolve.

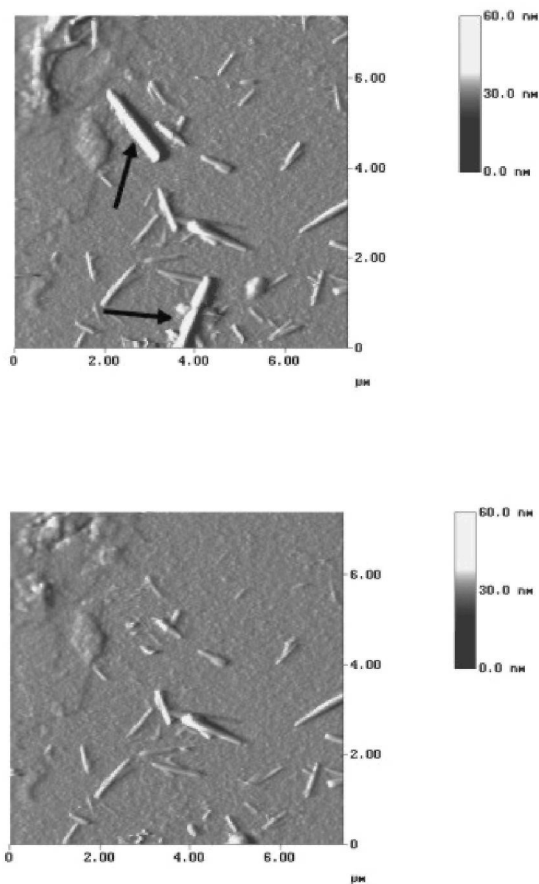


**Fig. 4.17.** AFM images of goethite crystals immobilized on a gold electrode before (top) and after a reduction at  $-0.15$  V vs. Ag/AgCl. The arrows indicate multidomain and twinned crystals [B 276]

AFM studies can also provide direct evidence of the role of the three-phase boundary in an electrochemical reaction. When silver halide crystals, immobilized on a gold electrode, are reduced to silver, this reduction starts at the three-phase boundary gold | silver halide | solution. When the silver halide crystal is only partially reduced during a short reduction pulse, and the remaining silver halide is dissolved with an ammonia solution, a ring of metallic silver is visible in the AFM image right at the place of the three-phase boundary (Fig. 4.18) [B 278]. In this study it has been shown that the reduction of silver halide crystals of submicrometer size proceeds considerably different than the reduction of much larger crystals: in the case of the small size crystals, the reduction converts a surface layer of the silver halide crystals to silver metal. The average thickness of this silver layer is remarkably constant: around 8 nm in case of AgCl, 8.8 nm in case of AgBr, 9.5 nm in case of AgI, and 9.14 nm in case of  $\text{AgBr}_{0.95}\text{I}_{0.05}$ . This corresponds in all cases to the formation of 16 to 21 atomic layers of silver. In no case there has been a filamentous growth of silver for submicrometer-size silver halide crystals, however, this was ob-

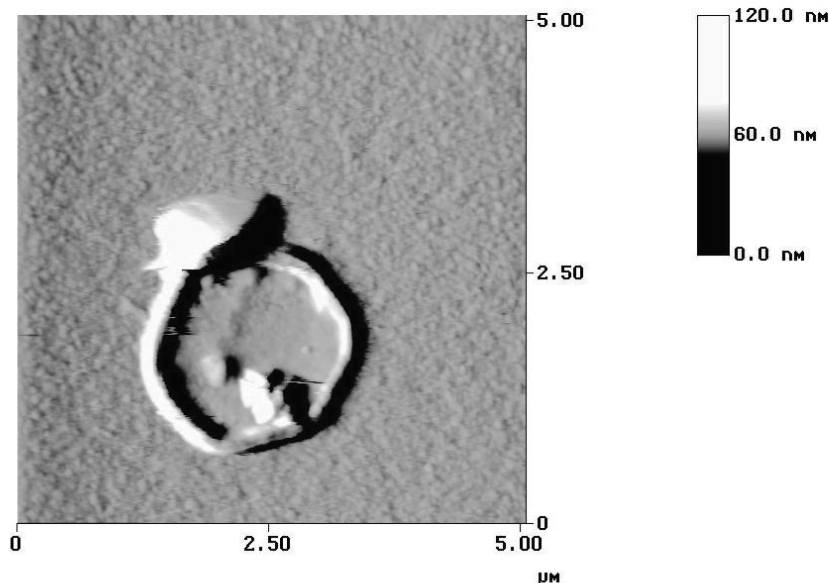


**Fig. 4.18.** Atomic force micrograph of a silver bromide crystal with 5 mol% iodide immobilized on a gold electrode after a reduction at  $-700$  mV vs. Ag/AgCl (3 M KCl) for 20 s and dissolving the remaining silver halide with 5 M ammonia [B 278]

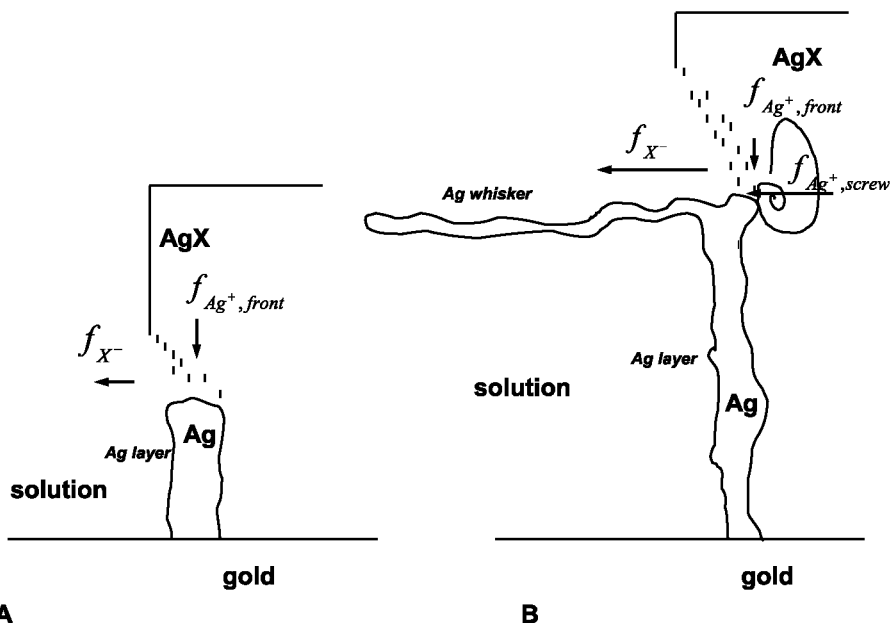


**Fig. 4.19.** Schematic drawing of the reduction of a silver halide crystal to silver: **A** Surface silvering of submicrometer-size crystals (initial stage). **B** Whisker growth following the initial formation of silver near the three-phase junction after prolonged electrolysis of a large crystal. The arrows indicate the transport of silver ions to the silver | silver halide interface [B 278]

served in case of crystals of several micrometer sizes. Of course, the filamentous growth has been known since long to be the typical growth feature in silver halide photographic development. The authors of [B 278] concluded that the “surface silvering” of the submicrometer size crystals is the result of the specific mass transfer conditions: the surface reduction is obviously undisturbed by dislocations on the crystal surface. In the case of large crystals the surface transformation will reach screw dislocations on the crystal surface where the mass transport of silver ions is very fast and the growth pattern changes from a surface layer formation to a whisker growth (see Fig. 4.19).

Very interesting results have also been obtained in studies of the electrochemical oxidation of nanocrystals of silver in an electrolyte solution that contained iodide ions [B 279]. When the AFM image was focused on one single silver crystal, in many cases it disappeared from observation. In a few cases where the crystals did not disappear their volume growth exceeded the theoretically expected value for a reaction in which Ag is oxi-

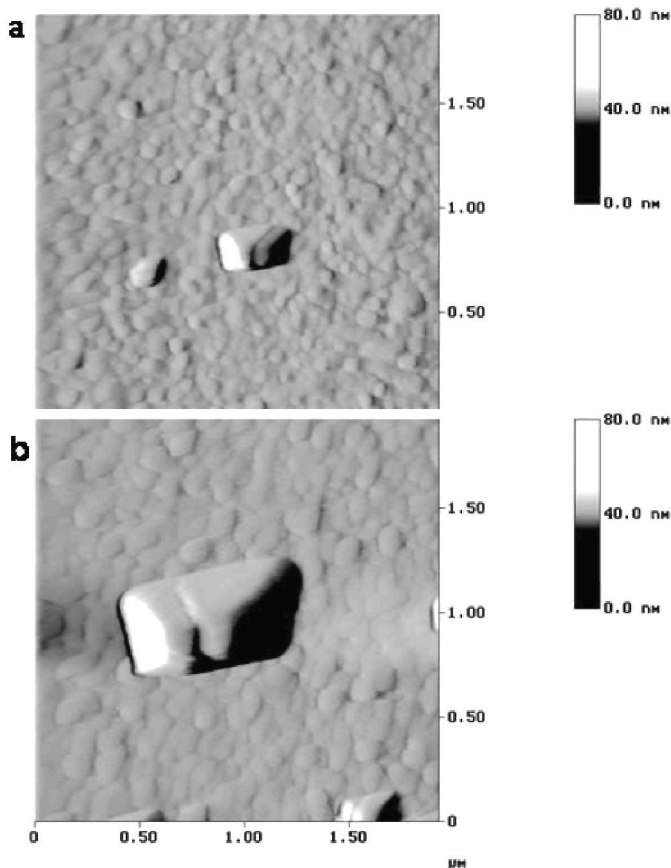


**Fig. 4.20.** **a** Silver nanocrystal immobilized on a gold electrode before oxidation. **b** The resulting silver iodide crystal formed during an oxidation at  $E = 0.15$  V vs. Ag/AgCl for 100 min. Electrolyte solution:  $10^{-4}$  mol L $^{-1}$  KI and 0.1 mol L $^{-1}$  KNO $_3$  [B 279]

dized to AgI by a factor of about 4! Figure 4.20 shows such a silver crystal and the resulting silver iodide crystal. The volume increased by a factor of 14. To understand the phenomenon, the AFM images were recorded in a range to cover many silver crystals. Figure 4.21a shows a gold electrode with an array of silver crystals. When they were oxidized to AgI most of them disappeared and only a small number of AgI crystals grew (cf. Fig. 4.21b). The explanation of this phenomenon is that the oxidation of the silver nanocrystals first produces an oversaturated AgI solution from which only a few but large AgI crystals grow. The number of Ag crystals in Fig. 4.21a was 2036 and the number of AgI crystals in Fig. 4.21b was

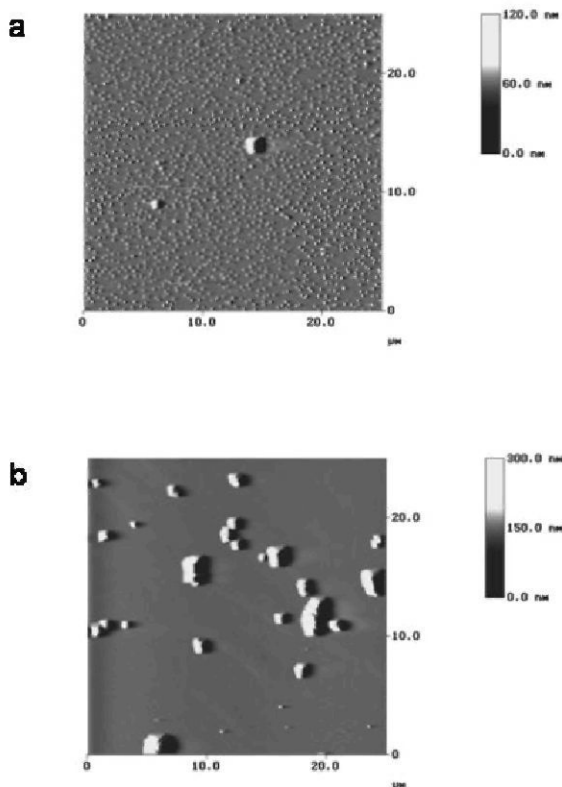


**Fig. 4.21.** **a** Array of immobilized silver nanocrystals before oxidation, and **b** array of the resulting AgI crystals after oxidation of the silver at  $E = 0.15$  V vs. Ag/AgCl for 5 min. Electrolyte solution:  $10^{-4}$  mol L $^{-1}$  KI and 0.1 mol L $^{-1}$  KNO $_3$  [B 279]

only 27! However, when the volumes of all silver crystals and the volumes of all AgI crystals were calculated it turned out that the overall volume increase was 3.8, which is very near to the theoretical value of 3.9. Figure 4.22 shows a similar experiment in which silver nanocrystals have been oxidized to silver bromide. Also in this case the number of AgBr crystals was very much smaller than the initial number of silver crystals, the ratio of the volumes being close to the theoretical value only when integration over all crystals of the image was performed. These in situ AFM studies proved that the oxidation of immobilized silver nanocrystals indeed proceeds via a detectable oversaturated AgI, or AgBr solution, respectively.

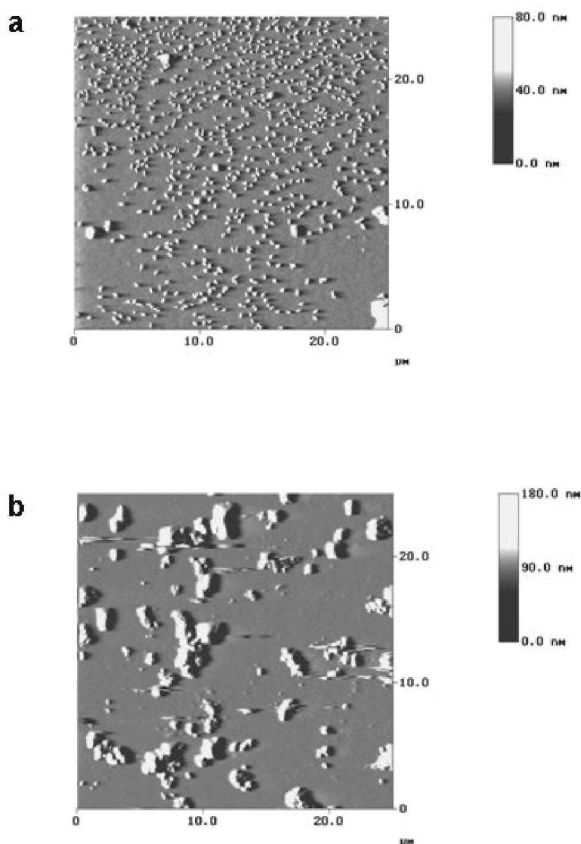


**Fig. 4.22.** **a** Array of immobilized silver nanocrystals before oxidation, and **b** array of the resulting AgBr crystals after oxidation of the silver at  $E = 0.20$  V vs. Ag/AgCl for 5 min. Electrolyte solution:  $10^{-4}$  mol L $^{-1}$  KBr and 0.1 mol L $^{-1}$  KNO $_3$  [unpublished results, Hasse U, Scholz F]

This was the first clear observation of an electrochemical solid-to-solid transformation to proceed via the solution phase.

The above-discussed examples clearly show that AFM/STM can provide extremely important information on the course of solid state electrochemical reactions of microparticles. The main problem of the experiments is certainly the procedure to immobilize the particles on suitable electrode surfaces. Many experiments are usually necessary to find the suitable immobilization technique for a special system. When the crystals are of a size in the range between 50 and 1000 nm, very good results can be obtained



with gold and platinum electrodes that are commercially manufactured by sputtering these metals on a chromium layer on quartz [B 276 and 278]. The optimum immobilization procedure was the evaporation from very dilute suspensions of the crystals in water or organic liquids onto the electrodes. Mostly, the suspensions that did not settle after 5 to 10 minutes contain crystals of a suitable size.

### 4.3. Electrochemical Quartz Crystal Microbalance

One of the most versatile and hence widespread hyphenated techniques for the interrogation of electrode processes is the electrochemical quartz crystal microbalance technique, EQCM. This technique allows to continuously monitor mass changes at an electrode surface with a sensitivity of few nanograms by means of tracking the frequency of the resonator, a gold-coated quartz crystal, which at the same time serves as the working electrode in the electrochemical experiment. EQCM measurements have been widely used for studies of all kinds of monolayer and multilayer depositions and dissolutions, mass transport in polymer films on electrodes, corrosion processes, etc. (see, for instance <sup>14</sup>). Basically, EQCM measurements can easily be applied to the study of microparticles. The method is readily available and does not need special adaptation to the voltammetry immobilized microparticles. The simplest procedure to stick a powder sample onto a quartz crystal electrode is by using a cotton swab and gently rubbing a small amount of the solid onto the electrode. Alternatively, organic compound microcrystals can be attached via evaporation of the dissolved material from a volatile solvent (see Chapter 3.2).

One of the major domains of EQCM in the voltammetry of immobilized particles is the interrogation of electrochemically driven solid-to-solid transformations, which are generally accompanied by the charge-compensating ion transfers between the electrolyte phase and the solid. Here, EQCM helps identifying the nature of the transferred ions. In the first study utilizing EQCM, Shaw and coworkers investigated the electrochemistry of non-conducting microcrystalline particles of *trans*-Cr(CO)<sub>2</sub>(dpe)<sub>2</sub> and [*trans*-Cr(CO)<sub>2</sub>(dpe)<sub>2</sub>]<sup>+</sup> (dpe = Ph<sub>2</sub>PCH<sub>2</sub>CH<sub>2</sub>PPh<sub>2</sub>) attached to gold electrodes [B 53]. From a combination of voltammetric measurements, EQCM experiments (see Fig. 4.23) and EDX data (see Chapter 4.1.3) the authors proved a reaction mechanism involving the in-

---

<sup>14</sup> Buttry DA (1991) Applications of the Quartz Crystal Microbalance to Electrochemistry. In: Bard AJ (ed) Electroanalytical Chemistry, vol 17. Dekker, New York

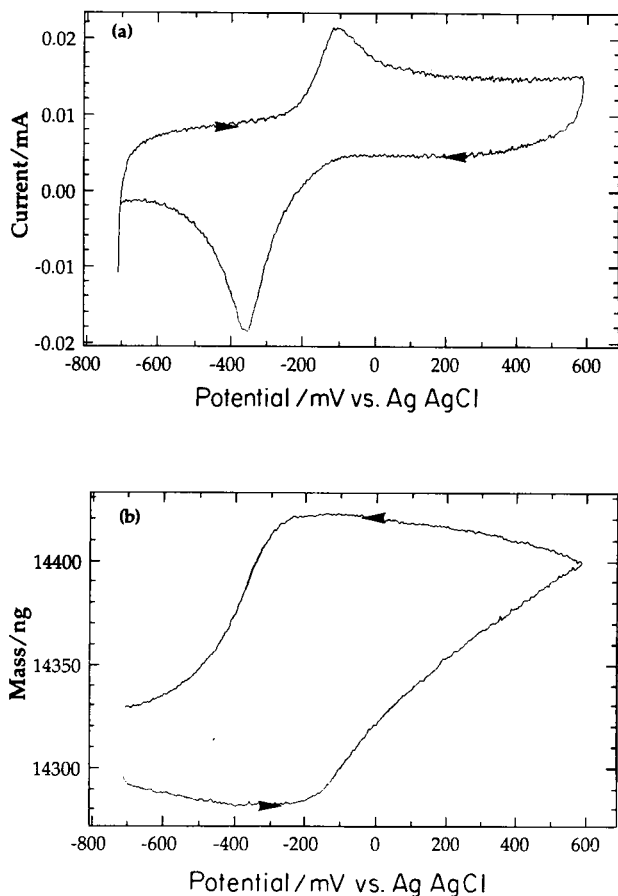


**Fig. 4.23.** **a** Cyclic voltammogram and **b** the corresponding mass change diagram for microcrystalline particles of *trans*-[Cr(CO)<sub>2</sub>(dpe)<sub>2</sub>]<sup>+</sup>Cl<sup>-</sup> attached to a gold quartz crystal which has been placed in 0.1 M KCl aqueous electrolyte [B 53]

corporation of non-solvated anions into the solid upon oxidation and their expulsion upon reduction. EQCM also revealed a rapid ion exchange process when *trans*-[Cr(CO)<sub>2</sub>(dpe)<sub>2</sub>]<sup>+</sup>X<sup>-</sup> salts were immersed into electrolyte solutions containing other anions than that contained in the attached solid.

Since the first application of the EQCM in the voltammetry of microparticles a wealth of studies have been published, including the electrochemical interrogation of tetrathiafulvalene, TTF [B 54], TCNQ [B 101], of C-60 fullerenes [B 154], iodopentacarbonyl chromium(0) [B 65], of solid complex cyanides [e.g., B 33, B 35, B 96, B 136] and of photoactive ruthenium [B 102] and manganese [B 128] complexes. In the latter study the

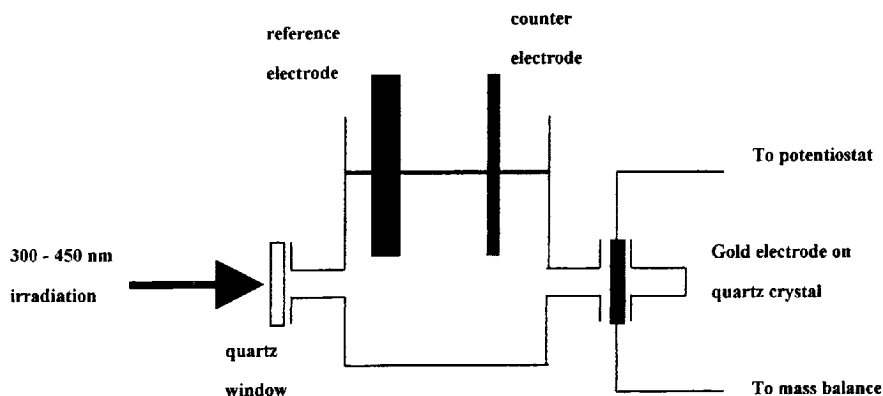


**Fig. 4.24.** Schematic diagram of an EQCM cell used in photochemical experiments [B 128]

authors demonstrate that EQCM measurements can be conveniently combined with photoelectrochemical experiments. For that, an adapted electrochemical cell has been presented as shown in Fig. 4.24.

The application of EQCM for studying immobilized microdroplets is less straightforward. First of all, the viscoelasticity of immobilized droplets does not allow applying the Sauerbrey equation and thus to easily quantify the mass changes at the electrode surface. Especially reactions at immobilized redox liquids – generally accompanied by ion expulsion or uptake – lead to considerable changes of the phase properties like the viscoelasticity of the liquid. Here it is very difficult to distinguish between frequency effects caused by mass changes and those caused by viscoelasticity changes.

#### 4.4 In Situ X-ray Diffraction

In situ X-ray diffraction is a well-established technique for studying the phase transformations in solid state electrochemical reactions. However, due to the following reasons the application to microparticles immobilized on electrode surfaces is not simple: (i) the overall amount of immobilized substance is usually very small, (ii) the electrolyte solution adjacent to the electrode surface diminishes the X-ray intensity, (iii) for technical reasons the X-ray diffraction can be measured only in reflection mode. Until now, there is only one publication in which an in situ X-ray diffraction study has been described with microparticles immobilized on an electrode surface [B 37]. Figure 4.25 shows the cell construction.

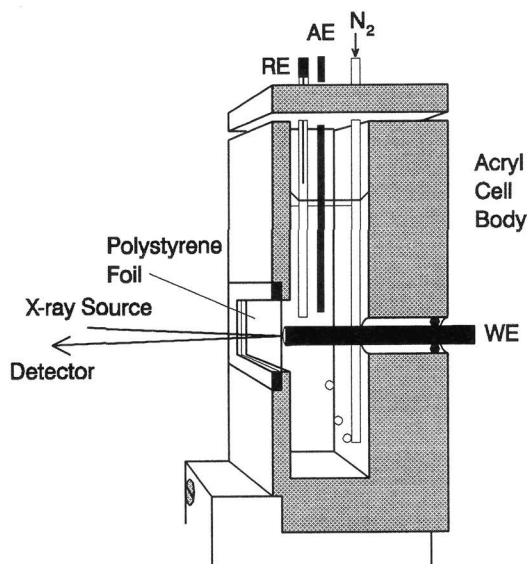


**Fig. 4.25.** Electrochemical cell for in situ X-ray diffraction. AE auxiliary electrode, RE reference electrode, WE working electrode [B 37]

The electrochemical cell was made of polyacrylic with a window made of X-ray amorphous polystyrene foil. The working electrode was a PIGE that was situated in such a way that the circular surface of the electrodes was parallel to the foil and in the axis of the diffractometer. The distance between the foil and the electrode surface must be kept small, because otherwise no X-ray reflections are observed owing to absorption by the electrolyte solution. With the help of this cell the electrochemical reduction of red PbO (litharge) and that of Pb(OH)Cl (laurionite) has been studied by scanning only a very small angle range simultaneously to the electrochemical conversion. Figure 4.26 shows the voltammogram of PbO reduction and the simultaneously recorded reflections of PbO and Pb. The latter prove that, on the time scale of the experiment, there is a simultaneous decrease of PbO reflections and increase of Pb reflections. That means that the reaction does not pass through a range where the metallic lead exists in an X-ray amorphous state. This, however, was evident when Pb(OH)Cl was reduced to lead. Figure 4.27 shows the linear scan voltammogram of Pb(OH)Cl reduction and the corresponding in situ X-ray diffraction signals. The figure proves that the reduction of Pb(OH)Cl proceeds via an

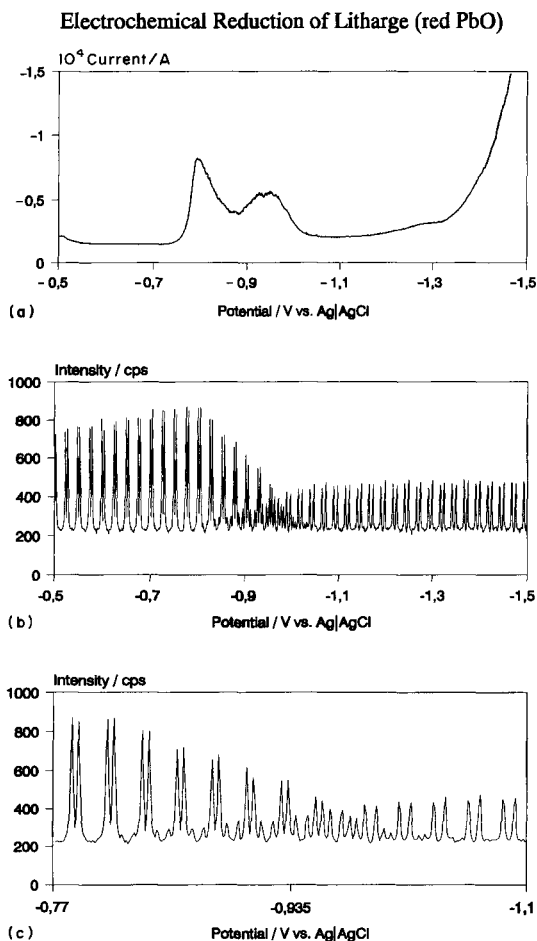


**Fig. 4.26.** Electrochemical reduction of red tetragonal PbO (litharge) in situ coupled with X-ray diffraction. PbO was mechanically attached to the surface of a PIGE, electrolyte  $1 \text{ mol L}^{-1}$  KCl: **a** linear sweep voltammogram (scan rate  $0.1 \text{ mV s}^{-1}$ ); **b** diffraction signal pairs between  $-0.5$  and  $-0.8$  V are due to PbO ( $d = 2.51 \text{ \AA}$ ), signal pairs between  $-1.1$  and  $-1.5$  V are due to Pb ( $d = 2.48 \text{ \AA}$ ); **c** enlarged part of **b** showing the simultaneous decrease in the PbO reflection and the increase in the Pb reflection [B 37]

amorphous phase that slowly recrystallizes. The simultaneous growth of lead crystals in the course of reduction of tetragonal PbO has later also been studied by in situ AFM (see Chapter 4.2) where indeed it was possible to see that this transformation proceeds without disintegration of the crystal.

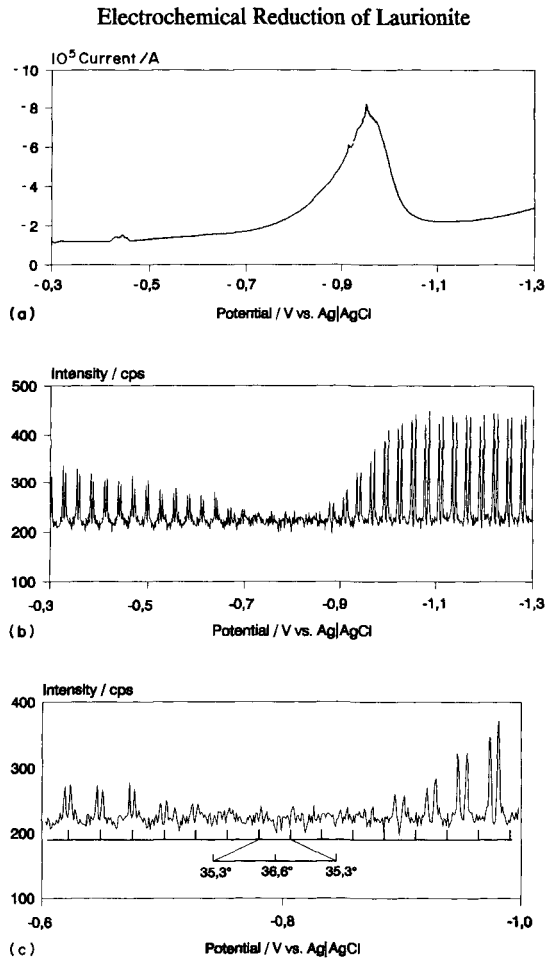


**Fig. 4.27.** Electrochemical reduction of orthorhombic  $\text{Pb}(\text{OH})\text{Cl}$  (laurionite) in situ coupled with X-ray diffraction.  $\text{PbO}$  was mechanically attached to the surface of a PIGE, electrolyte  $1 \text{ mol L}^{-1} \text{ KCl}$ : **a** linear sweep voltammogram (scan rate  $0.1 \text{ mV s}^{-1}$ ); **b** diffraction signal pairs between  $-0.3$  and  $-0.65 \text{ V}$  are due to  $\text{Pb}(\text{OH})\text{Cl}$  ( $d = 2.52 \text{ \AA}$ ), signal pairs between  $-0.9$  and  $-1.3 \text{ V}$  are due to  $\text{Pb}$  ( $d = 2.48 \text{ \AA}$ ); **c** enlarged part of **b** showing a potential (time) range with an amorphous phase [B 37]

The in situ X-ray diffraction of immobilized microparticles has certainly a large potential, provided that high intensity X-ray sources are applied.

## 4.5 In Situ Calorimetry

Calorimetric measurements were the basic experiments to establish the fundamentals of chemical thermodynamics. In the 19<sup>th</sup> and 20<sup>th</sup> centuries, electrochemical thermodynamics was developed and the relations between calorimetric and electrochemical data were discovered. Very often, electrochemical measurements give much more facile and reliable access to thermodynamic data. In theory these are two equally suited methods for obtaining the same information. Hence, one might ask why one should attempt an *in situ* measurement of thermal effects of electrochemical reactions. Historically such measurements were of importance to give experimental proof for the interrelation between electrical and caloric data. But even nowadays there are still reasons for performing *in situ* calorimetry-electrochemistry: in the case of reversible electrochemical reactions, the calorimetric data give unambiguous proof or disproof for the correctness of the electrochemical data. The other good reason for such a combination is the study of irreversible systems, because it makes the irreversible heat effects accessible.

To study the heat effects of electrochemical reactions of immobilized microparticles, special electrodes have had to be developed so that the minute temperature effects, usually in the mK range, can be recorded with sufficient reliability. Figure 4.28 depicts thermistor electrodes that allowed measurements with amounts of  $5 \times 10^{-9}$  up to  $5 \times 10^{-8}$  mol of solid metal hexacyanoferrates.

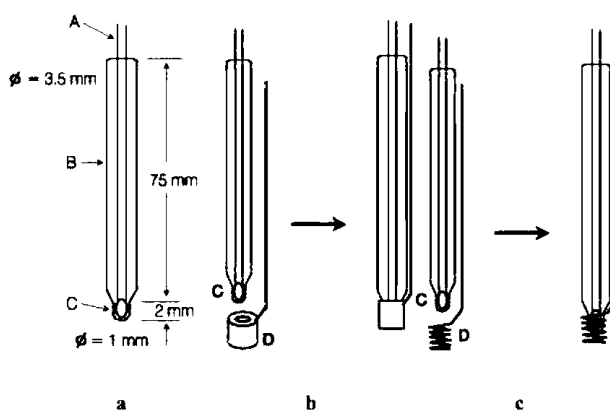


**Fig. 4.28.** **a** The thermistor electrode: A electric wires, B glass tube housing, C thermistor element; **b** the thermistor electrode with graphite cylinder D; **c** the thermistor electrode with gold wire electrode D [B 219]

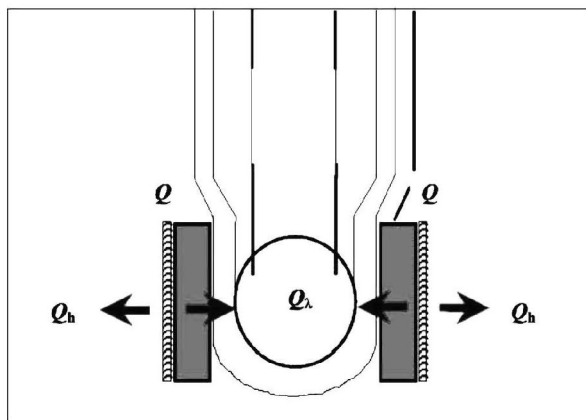


**Fig. 4.29.** The heat  $Q$  produced at the electrode surface is transferred partly to the thermistor element ( $Q_s$ ), and partly to the solution ( $Q_h$ ) [B 219]

The solid microparticles have been immobilized either on a very small graphite cylinder (made from a paraffin impregnated graphite rod) or on a gold wire coil. The graphite cylinder and the gold coil were fitted to the thermistor that was housed in a glass tube. To calibrate the thermistor electrode a Kanthal wire (22.3  $\Omega$ /cm and isolated with a 0.004-mm-thick polyamide film) was wound around the graphite cylinder.

The heat release or absorption occurs at the surface of the electrode, because that is where the electrochemically active compound is immobilized. To quantify this heat it is necessary to understand the relation between the thermal balance and the temperature, as the latter is the measured quantity. For calculating the amount of heat that corresponds to a certain change in temperature, the thermal behavior of the thermistor electrode has to be modeled. Figure 4.29 shows the heat production and dissipation at the electrode. One part of the heat will flow to the thermistor by heat conduction while some other part will be lost to the electrolyte solution, partly by convection. The temperature profile at the electrode can be estimated using the following assumptions: in principle, heat transport from the electrode surface to the solution could occur via free convection. However, an analysis of the hydrodynamic conditions showed that at least 100 times more heat is exchanged by conductance than by convection to the solution. To model the heat transfer at the thermistor electrode it is necessary to calculate the ratio of heat transfer by conduction in the solid parts to the amount of heat transported by conduction into the solution. Because of the very high heat conductivity of the graphite and the low heat conductivity of water, the electrode will be a so-called lumped system, i.e., the temperature in



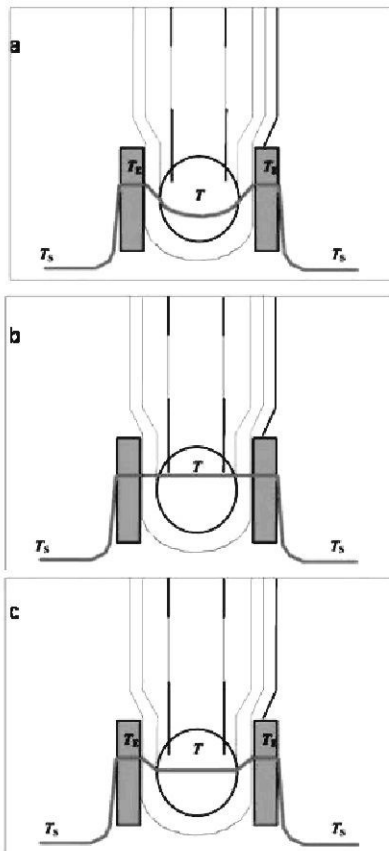


**Fig. 4.30.** a Temperature profile at the thermistor electrode:  $T$  temperature in the thermistor element,  $T_E$  temperature within the electrode,  $T_S$  temperature within the solution. b Assumed temperature profile in Model I.  $T^*$  is the homogeneous temperature in the electrode and the thermistor element and the glass shaft separating both.  $T_S$  is the temperature in the solution. c Assumed temperature profile in Model II.  $T_E$  is the homogeneous temperature in the electrode,  $T$  is the homogeneous temperature in the thermistor element and  $T_S$  is the temperature in the solution [B 219]

the electrode will be uniform. Within the thermistor element a logarithmic temperature drop will occur, as is known to occur for radial heat conduction in cylinders. Figure 4.30a depicts the most probable temperature profile at the thermistor electrode, and Figs. 4.30b and c depict two different models that have been used in the calculations.

Figure 4.30b depicts the assumed temperature profile in model I. In this model the heat balance is:

$$Q_{\text{acc,electrode}} = P - Q_{\text{loss}} \quad (4.3)$$

where  $Q_{\text{acc,electrode}}$  is the heat accumulated in the electrode,  $P$  is the produced heat and  $Q_{\text{loss}}$  is the heat lost via the electric contact and convection. These two values can be calculated as follows:

$$Q_{\text{so,electr}} = mC_p \left( dT^* / dt \right) \quad (4.4)$$

and

$$Q_{\text{loss}} = KT^* \quad (4.5)$$

$T^*$  is the temperature change in respect to the solution temperature ( $T^* = T_T - T_S$ ,  $T_T$  is the temperature of the thermistor and  $T_S$  that of the solution),  $K$  is a global heat transfer coefficient due to conduction and convection,  $mC_p$  is the heat capacity of the thermistor electrode, i.e. the sum of all heat capacities of the different parts of the thermistor electrode. From Eqs. 4.3 to 4.5 a first order differential equation is obtained:

$$mC_p \left( dT^* / dt \right) = P - KT^* \quad (4.6)$$

The solution of this equation for  $T^* = 0$  at  $t = t_0$  is:

$$T^* = \frac{P}{K} \left( 1 - e^{-\frac{K}{mC_p}(t-t_0)} \right) \quad (4.7)$$

$\frac{K}{mC_p}$  is the reciprocal time constant of the temperature response. The parameters of this equation can be determined as follows: when the heat pulse is sufficient to establish a steady state temperature  $T_{st}$ , this value equals  $P/K$ . Since  $P$  is known in a calibration experiment,  $K$  can be easily calculated from  $T_{st}$ . With  $T_{st}$  follows from Eq. 4.7:

$$\ln \left( 1 - \frac{T^*}{T_{st}} \right) = -\frac{K}{mC_p} (t - t_0) \quad (4.8)$$

This equation allows the determination of  $K/mC_p$  from a linear regression. Both constants  $K$  and  $mC_p$  have to be determined for each experiment (each electrode preparation) as minute differences in the electrode assembly will influence their values.

In model II it was assumed that the temperature within the thermistor electrode is not homogeneous, but, due to the lower heat conductivity of glass ( $\approx 1.2$  W/mK), the temperature within the thermistor element will be lower than within the electrode. Figure 4.30c depicts this model. The heat balance was assumed as

$$Q_{\text{acc,electrode}} = P - Q_T - Q_{\text{loss},1} \quad (4.9)$$

where  $Q_{\text{acc,electrode}}$  is the heat accumulated in the electrode,  $P$  is the heat produced,  $Q_T$  is the heat exchanged with the thermistor, and  $Q_{\text{loss}}$  is the heat lost via the electric contact and convection. The heat balance for the thermistor is

$$Q_{\text{acc,thermistor}} = Q_T - Q_{\text{loss},2} \quad (4.10)$$

The differential equations for the two heat balances are:

$$mC_{P,E} \frac{dT_E^*}{dt} = P - K_1(T_E^* - T^*) - K_2 T_E^* \quad (4.11)$$

$$mC_{P,T} \frac{dT^*}{dt} = K_1(T_E^* - T^*) - K_3 T_E^* \quad (4.12)$$

with  $T_E^* = T_E - T_s$  ( $T_E$  is the temperature of the electrode and  $T_s$  the temperature of the solution bulk). In these equations  $K_1$ , and  $K_2$  are the heat transfer coefficients at the thermistor-electrode interface and for the heat loss at the electrode via wires and convection, respectively.  $K_3$  is the coefficient for the heat transfer from the thermistor to the glass, electric wires and loss by convection.  $mC_{P,E}$  and  $mC_{P,T}$  are the heat capacities of the electrode and the thermistor, respectively. All these parameters are unknown. From Eqs. 4.11 and 4.12 the following second order differential equation with three unknowns is obtained:

$$\frac{d^2 T^*}{dt^2} + a_1 \frac{dT^*}{dt} + a_2 T^* = a_3 P \quad (4.13)$$

The new parameters  $a_1$ ,  $a_2$  and  $a_3$  are combinations of the heat capacities and heat transfer coefficients. The solution of Eq. 4.13 is as follows:

$$T^* = T_{\text{st}} + A_1 e^{\alpha_1(t-t_0)} + A_2 e^{\alpha_2(t-t_0)} \quad (4.14)$$

$T_{\text{st}}$  is the steady state temperature,  $\alpha_1$  and  $\alpha_2$  ( $\alpha_1 \neq \alpha_2$ ) are constants depending on  $a_1$  and  $a_2$ , and  $A_1$  and  $A_2$  are constants that have to fulfill the initial conditions. The following equations show the interrelation of these values:

$$T_{st} = \frac{a_3 P}{\alpha_1 \alpha_2} \quad (4.15)$$

$$\alpha_1 = -\frac{a_1}{2} + \sqrt{\frac{a_1^2}{4} - a_2} \quad (4.16)$$

$$\alpha_2 = -\frac{a_1}{2} - \sqrt{\frac{a_1^2}{4} - a_2} \quad (4.17)$$

A comparison of Eqs. 4.14 and 4.7 shows that Eq. 4.14 contains an additional exponential term. Since the thermistor electrode is a system with a finite mass and heat capacity, the initial conditions have been assumed to be  $T^* = 0$  and  $\frac{dT^*}{dt} = \gamma$ . Plotting the experimental data as  $\frac{dT}{dt} = f(t)$  for different electric powers showed that there is a power independent value of  $\frac{dT}{dt}$  at the start of the heating pulse. This can be explained by the fairly high heat conductivity of the graphite electrode. With these experiments an initial value  $\frac{dT}{dt} = \gamma$  was determined that was used for solving the differential equation. Figure 4.31 shows the experimental data and the simulation curve. The latter exhibited a very good fit of the experimentally observed behavior of the thermistor electrode. For the determination of the parameters it is important to use the temperature data before the electrode attains a steady state. Assuming  $n$  layers surrounding the thermistor, the calculation affords a system of differential equations that can be presented as a matrix:

$$d\underline{T}^* / dt = \underline{A}\underline{T}^* + \underline{P} \quad (4.18)$$

where  $\underline{T}^*$  is the vector of temperatures,  $\underline{A}$  is the  $(n \times n)$  matrix of the thermal properties of the layers, and  $\underline{P}$  is the vector of heat production.

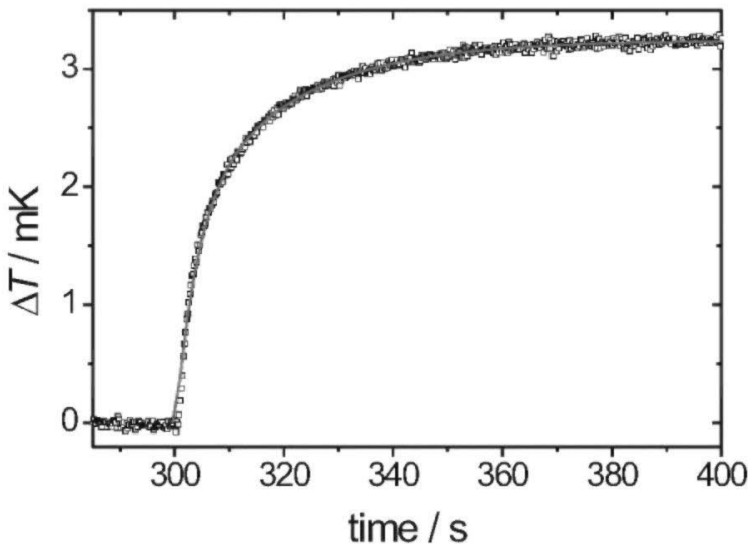


**Fig. 4.31.** Comparison of the experimental temperature-time curve (dots) with the calculated temperature-time curve based on model II. The heat pulse had a power of  $38.08 \mu\text{W}$ , a duration of 300 s and the parameters were estimated as follows:  $\alpha_1/\text{s}^{-1} = -1/3.809$  and  $\alpha_2/\text{s}^{-1} = -1/19.33$  [B 219]

The integral solution is:

$$\frac{T^* - T_s}{T_u - T_s} = 1 - \sum_{i=1}^n a_i \exp\left(-\frac{t}{\tau_i}\right) \quad (4.19)$$

where  $\tau$  is a constant.

Due to the finite amount of electroactive compound immobilized on the thermistor electrode no steady state response is attained and the calculation of heat produced or consumed is more complex. For that it is necessary to use differential equations. Since the power applied in calibration experiments was denoted as  $P$ ,  $Q$  will be used to denote the heat change of an electrochemical reaction. Equations 4.6 and 4.13 have to be solved for the two models. The parameters have been determined in calibration experiments. To calculate the amount of heat associated with the electrochemical reaction, two different methods can be used, i.e., the differential method and the integral method. The differential method based on model I requires the determination of the parameters  $K$  and  $mC_p$ , as well as the first time derivative of temperature, since Eq. 4.6 will be used in the form:

$$Q(t) = KT + mC_p dT / dt \quad (4.20)$$

In the case of model II, the parameters  $a_1$ ,  $a_2$ , and  $a_3$ , as well as the first and second time derivatives of the temperature are necessary, since Eq. 4.13 will be used in the form:

$$Q(t) = \frac{1}{a_3} \frac{d^2T}{dt^2} + \frac{a_1}{a_3} \frac{dT}{dt} + \frac{a_2}{a_3} T \quad (4.21)$$

Application of the differential method is associated with a number of errors, i.e., errors in the determination of the parameters and errors due to the derivations. The advantage of the differential method is that it yields the heat transients. The integral method allows the calculation of the time derivatives of temperature to be avoided. Equations 4.20 and 4.21 can, in principle, be solved with the Runge-Kutta method or by Fourier transformation. However, to obtain a clear insight into the role of the different parameters it is convenient to use the relation  $Q(t) = \frac{dq}{dt}$  in Eqs. 4.20 and 4.21, which allows to write for model I:

$$dq = KTdt + mC_p dT \quad (4.22)$$

and for model II:

$$dq = \frac{1}{a_3} dT' + \frac{a_1}{a_3} dT + \frac{a_2}{a_3} Tdt \quad (4.23)$$

with  $T' = \frac{dT}{dt}$ . Integration of Eqs. 4.22 and 4.23 within certain limits allows the calculation of the heat change within these limits:

$$q = K \int_{t_1}^{t_2} Tdt + mC_p (T_2 - T_1) \quad (\text{model I}) \quad (4.24)$$

$$q = \frac{1}{a_3} (T'_2 - T'_1) + \frac{a_1}{a_3} (T_2 - T_1) + \frac{a_2}{a_3} \int_{t_1}^{t_2} Tdt \quad (\text{model II}) \quad (4.25)$$

From a comparison of these two equations it follows that  $K$  in model I and  $a_2/a_3$  in model II are identical. The heat produced in an electrochemical reaction is the sum of the electrochemical Peltier heat and the irreversi-

bly exchanged heat. The latter is at least the Joule heat and that associated with a possible overvoltage:

$$Q(t) = Q_{\text{Peltier}}(t) + Q_{\text{Joule}} + Q_{\text{overvoltage}} \quad (4.26)$$

$$Q(t) = \frac{\Pi}{zF} I + RI^2 + \eta I \quad (4.27)$$

where  $\Pi$  is the molar Peltier heat,  $R$  the solution resistance (and also the resistance of the solid compound when the current  $I$  flows through it) and  $\eta$  the overvoltage of the electrochemical reaction. There is a simple way to determine the irreversible heat in these experiments because the Peltier heats of the oxidation and reduction must have equal absolute values but opposite signs, whereas the irreversible heat will have the same sign and absolute value. A measurement of the heat associated with the oxidation and subtraction of the heat associated with reduction thus gives the irreversible heat. Of course, small scan rates and small amounts of substance, i.e., small currents will reduce the irreversible heat effects. Experimentally it was shown that the parameters of model I and model II do not depend on the amount of heat released. To quantify the heat of an electrochemical reaction there are two possibilities: the integral method depends only on parameter  $K$  and is applicable to model I and II. For application of model II the value  $a_2/a_3$  was determined as  $K$  using model I. The differential method was not applied to model II because of the severe errors involved in calculating the second time derivative of temperature. Using the differential method and model I, the smaller time constant of model II, i.e.,  $-1/\alpha_1$  was used because  $mC_p/K$ , which is the time constant of model I, is a too bad estimate when relatively fast temperature changes occur.  $mC_p/K$  is a good estimate only for slower temperature changes. (The time constants of the gold coil electrode are about one order of magnitude smaller than those of the graphite electrode. Hence the gold electrode lends itself for studies with faster potential scan rates). Table 4.1 gives electrochemical Peltier coefficients in J/C for the oxidation and reduction of copper(II) hexacyanoferrate(II) immobilized on the graphite surface of the thermistor electrode, using a 0.1 M  $\text{KNO}_3$  electrolyte solution, for different scan rates and calculated with the integral as well as the differential method. The relation between the molar Peltier heat and the Peltier coefficient  $\pi$  is  $\Pi = \pi zF$ . The entropy change follows as  $\Delta S_{\text{reaction}} = \Pi/T$ . The entropy change at an electrode has two sources, the reaction entropy and the transfer entropy of electrons and ions. The transfer entropy was assumed to

**Table 4.1.** Electrochemical Peltier coefficients  $\pi$  for copper(II) hexacyanoferrate(II) as determined at different scan rates. Electrolyte 0.1 M KNO<sub>3</sub> [B 219]

Scan rate / mV s <sup>-1</sup>	Integral method		Differential method	
	$\pi_{\text{Ox}} / \text{J C}^{-1}$	$\pi_{\text{Red}} / \text{J C}^{-1}$	$\pi_{\text{Ox}} / \text{J C}^{-1}$	$\pi_{\text{Red}} / \text{J C}^{-1}$
1	0.1953	0.1910	0.1911	0.1972
2	0.1913	0.1937	0.1934	0.1921
5	0.1904	0.1983	0.1957	0.1945
10	0.1943	0.1927	0.1983	0.1927
20	0.1713	0.1776	0.1943	0.1936
50	0.1478	0.1437	0.1989	0.1924

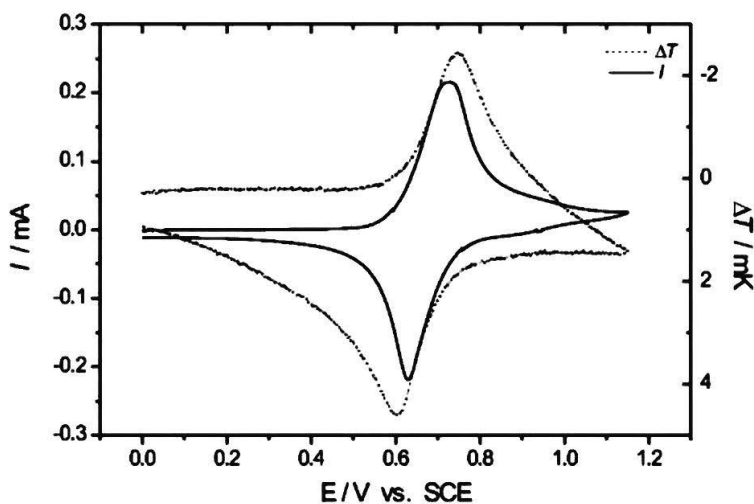


**Fig. 4.32.** Cyclic voltammogram (solid lines) and thermogram (dotted lines) recorded simultaneously at a graphite thermistor electrode with immobilized copper(II) hexacyanoferrate(II). The scan rate was 10 mV s<sup>-1</sup> [B 219]

be zero as a first approximation. From the table it follows that the integral method yields reliable data up to 10 mV s<sup>-1</sup>, whereas at higher scan rates, deviations are serious and the differential method has to be used. It seems that at scan rates above 10 mV s<sup>-1</sup> an overlapping between the released and consumed heat occurs. The data given in Table 4.1 clearly show that the



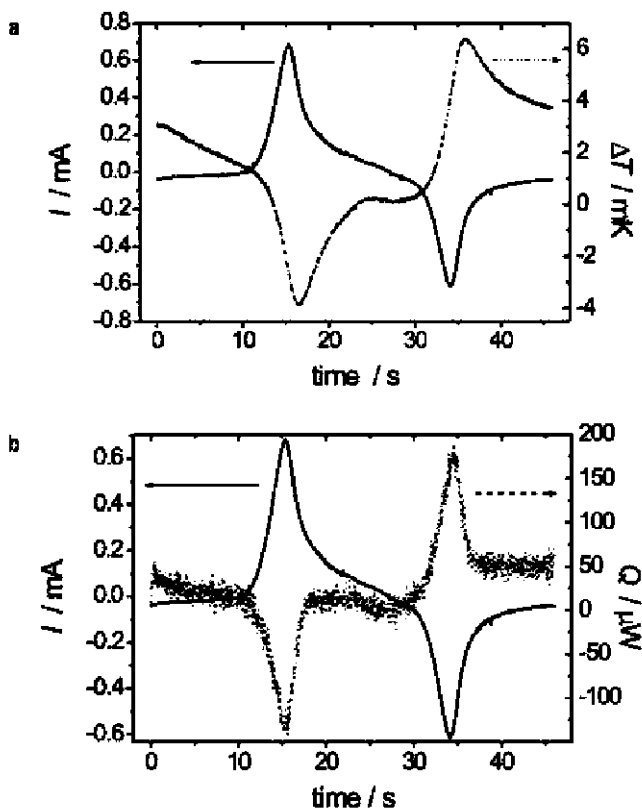


**Fig. 4.33.** **a** Cyclic voltammogram (solid line) and thermogram (dotted line) plotted as function of time for the second cycle of oxidation reduction of copper(II) hexacyanoferrate(II).  $\Delta T$  is the temperature difference between the thermistor and the electrolyte solution. **b** cyclic voltammogram (solid line) and heat versus time curves for the second cycle of oxidation-reduction of copper(II) hexacyanoferrate(II). Electrolyte 0.1 M  $\text{KNO}_3$ , scan rate  $50 \text{ mV s}^{-1}$  [B 220]

irreversible heat must be negligible as the Peltier coefficients for oxidation and reduction are almost identical and show no systematic differences. Figure 4.32 depicts a cyclic voltammogram of a graphite thermistor electrode with immobilized copper(II) hexacyanoferrate(II) and the corresponding thermogram. The two traces, taken together, provide a clear picture of the electrode process. In the cyclic voltammogram the absolute peak currents of oxidation and reduction are equal, indicating reversibility.

**Table 4.2.** Standard reaction entropies of copper(II) and iron(III) hexacyanoferrate as determined with the help of the thermistor electrode and with a temperature variation of a thermostated cell (*hcf* = hexacyanoferrate) [B 220]

Reaction	$\Delta S^\circ / \text{J mol}^{-1} \text{K}^{-1}$ as determined with the help of the thermistor electrode*	$\Delta S^\circ / \text{J mol}^{-1} \text{K}^{-1}$ as determined by temperature variation with the help of the thermostated cell
Fe(III) <i>hcf</i> (III): red. of $\text{Fe}_{\text{is}}(\text{III}), \text{K}^+$ insertion	-41.0	-37.6
Fe(III) <i>hcf</i> (II): oxid. of $\text{Fe}_{\text{is}}(\text{II}), \text{K}^+$ insertion	39.8	-
Fe(III) <i>hcf</i> (II): red. of $\text{Fe}_{\text{hs}}(\text{III}), \text{K}^+$ insertion	-42.1	-
Fe(II) <i>hcf</i> (II): oxid. of $\text{Fe}_{\text{hs}}(\text{II}), \text{K}^+$ insertion	40.8	-
Cu(II) <i>hcf</i> (II): oxid. of $\text{Fe}_{\text{is}}(\text{II}), \text{K}^+$ insertion	40.0	38.6
Cu(II) <i>hcf</i> (II): oxid. of $\text{Fe}_{\text{is}}(\text{II}), \text{Na}^+$ insertion	72.0	-
Ni(II) <i>hcf</i> (II): oxid. of $\text{Fe}_{\text{is}}(\text{II}), \text{K}^+$ insertion	-	32.8
Ni(II) <i>hcf</i> (II): oxid. of $\text{Fe}_{\text{is}}(\text{II}), \text{Na}^+$ insertion	-	72.4
Co(II) <i>hcf</i> (II): oxid. of $\text{Fe}_{\text{is}}(\text{II}), \text{K}^+$ insertion	-	45.3
Co(II) <i>hcf</i> (II): oxid. of $\text{Fe}_{\text{is}}(\text{II}), \text{Na}^+$ insertion	-	66.6

The maximal change in temperature was 3 mK, corresponding to a current of about 0.2 mA for the following reaction:  $\{\text{KCu}[\text{Fe}(\text{CN})_6]\}_s + \text{K}^+_{(\text{aq})} + \text{e}^- \rightleftharpoons \{\text{K}_2\text{Cu}[\text{Fe}(\text{CN})_6]\}_s$ . The subscript *s* denotes the solid phase and the subscript *aq* indicates that this ion is dissolved in the aqueous phase. From Fig. 4.32 it follows that the oxidation is endothermic while the reduction is exothermic. The thermogram allows a rough estimate of the time constant

by measuring the time delay between the current and temperature peaks. This time delay is about 3 s in the example shown.

The described thermistor electrode has been applied for the determination of the standard entropies of insertion electrochemical reactions of solid metal hexacyanoferrates. For that purpose, the standard entropies have been additionally determined by temperature variations of a thermostated cell. Table 4.2 gives the published data. A comparison of the data of different metal hexacyanoferrates and for sodium and potassium ions as inserting ions shows that the desolvation of the inserting ions seems to give the major contribution to the entropies of the overall electrochemical process.

This chapter demonstrates that in situ calorimetric studies of electrochemical reactions of solid microparticles are possible with extremely small amounts of compounds. This is an advantage, because at least in some cases, similar measurements with large quantities of compounds are impossible, since the reaction rate would be much too small to achieve a complete conversion in a reasonable time span. This advantage is obvious from Fig. 4.33, where voltammograms and simultaneous thermograms are shown that were recorded with a scan rate of  $50 \text{ mV s}^{-1}$ , with which a complete conversion of the entire immobilized compound has been achieved.

## 5 Immobilized Particles

The first prerequisite for studying the electrochemistry of particles immobilized on an electrode surface is their insolubility in the used electrolyte solution. Of course, no particle is absolutely insoluble, and so it is a matter of a practical viewpoint what solubility can be tolerated. There is no general answer to this question, however, it makes sense to discuss here only those compounds that do not dissolve to a detectable extent during their electrochemical reactions or only prompted by their electrochemical reactions. What are the general possibilities of electrochemical behavior of an

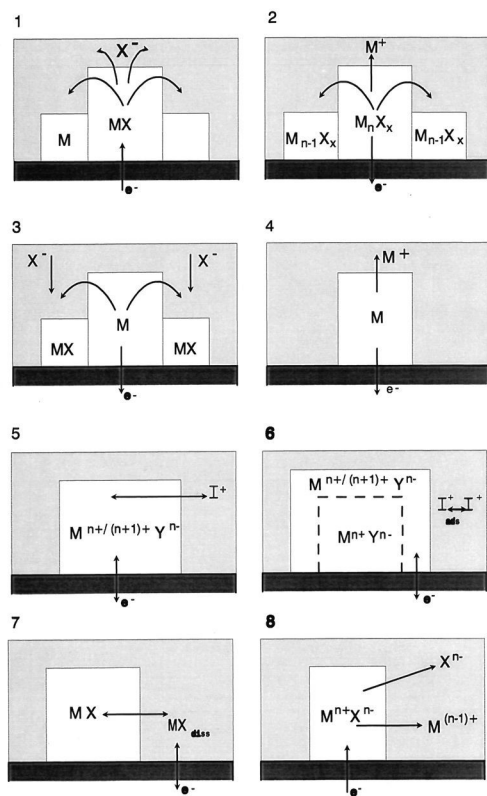


**Fig. 5.1.** Scheme of possible electrochemical reactions of solid particles immobilized on a solid electrode and in contact with an electrolyte solution

immobilized particle? Figure 5.1 depicts some frequently observed cases. Case 1 illustrates the reduction of an insoluble metal salt to the metal, e.g., AgCl to Ag, the released anions diffusing into the bulk of the electrolyte solution. For the reduction of silver halides and also of lead(II) oxide it has been shown that the solid educt is directly transformed to the solid product (see the AFM results discussed in Chapter 4.2). Case 2 is the oxidation of a metal salt with release of metal ions into the electrolyte solution. An example would be the oxidation of copper(I) sulfide to copper(II) sulfide. Case 3 depicts the oxidation of a metal and formation of an insoluble metal compound, e.g., salt, oxide or complex. This reaction can proceed via an oversaturated solution of the compound MX as in the case of silver oxidation to AgBr and AgI (see AFM results given in Chapter 4.2). In case 4 the “simple” anodic oxidative dissolution of a metal particle is considered. Case 5 concerns the insertion electrochemistry of a particle where ions are exchanged between the solid particle and the electrolyte solution when electrons are exchanged between the particle and the electrode. Plenty of examples are discussed in Chapters 5.3, 5.5, and 5.6. Case 6 depicts the case where the electrochemical reaction is confined to the surface layer only. Examples are given in Chapter 5.4. In case 7 it is assumed that the electrochemical reactions occur only via a preceding dissolution of the solid particle (see the electrochemistry of metal dithiocarbamate complexes discussed in Chapter 5.6), and case 8 symbolizes the complete electrochemical dissolution of a particle resulting from its oxidation or reduction. An example of the latter type is the reductive dissolution of iron(III) oxides (see Chapter 5.7).

A special case of immobilization of particles is when a solution layer is sandwiched between the electrode (e.g., graphite) and the particles. For this case it was observed that the electron transfer between the electrode material (glassy carbon) and the immobilized microparticles ( $\text{Cu}_2\text{S}$ ,  $\text{Cu}_2\text{Se}$ ) can be catalyzed by certain ions and compounds (e.g., thiocyanide ions, thiourea) that are already well known as catalysts in electron transfer reactions of dissolved ions (e.g.,  $\text{Ni}^{2+}$ ) [B 60]. Such studies may help understanding also *interparticle* electron transfer processes.

Some general remarks may suffice at this point to explain the specific features of studies of immobilized particles:

- (i) Due to the small amounts of immobilized compounds the electrochemical measurements can be performed on the same time scale as measurements with dissolved species. This feature was elegantly demonstrated by Fiedler et al. for the screening of potential battery materials [B 73, B 86] where measurements could be performed in the  $\text{mV s}^{-1}$  range instead of using  $\mu\text{V s}^{-1}$  for the usual composite electrodes.

- (ii) In general, all solid compounds that can be synthesized can be directly measured. The measurements do require the precipitation of these compounds directly on an electrode surface. Thus, for example, the latter procedure limited very much the number of studied metal hexacyanometalates, whereas it was demonstrated that with the immobilization technique all synthetically accessible compounds of that type can be investigated by electrochemical techniques [e.g., B 33, B 41, B 137, B 247].
- (iii) The mechanical immobilization of particles avoids using liquid binders that may alter the electrochemical response, e.g., by film formation in case of organic binders, and by chemical dis-solutions in case of aqueous electrolyte binders.
- (iv) The immobilization technique allows measurements with very small amounts of compounds, at least down to  $10^{-12}$  mole, and even with single microparticles [B 10, B 78].
- (v) Generally it is difficult to deliberately control the amount of substance immobilized on the electrode, and this seems to be a drawback. However, it is rather simple to deduce the amounts of electrochemically active compound from the electrochemical data, e.g., by integration of voltammograms or by direct coulometry. This is most simple in case of reversible systems. When the characteristic voltammetric potentials, e.g., peak potentials, depend on the amount of electrochemically active compound it is necessary to take this into account by determining these amounts as outlined. Examples are given in Chapter 5.3 [B 57].

## 5.1 Metals and Alloys

The idea of immobilizing microparticles on an electrode surface for the purpose of an electrochemical analysis came to the mind of one of the book's authors (F. S.) from an old gold probe technique where the metal sample was scratched on a special stone and the transferred metal traces were then probed for their stability towards nitric acid. Since voltammetric techniques can detect extremely small currents, caused by oxidations or reductions of invisibly small amounts of substances, it was clear that a mechanical transfer of a solid to an electrode surface must be capable of depositing sufficient amounts of a metal, an alloy or any other solid material on the electrode surface as to detect them electrochemically. The first publication based on that idea reported the analysis of lead-antimony

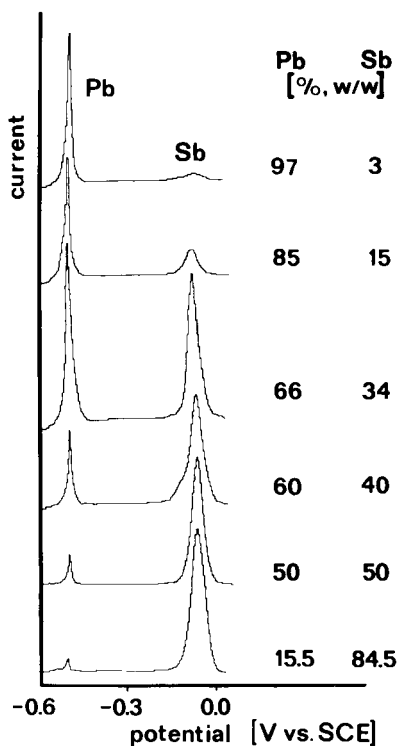


**Fig. 5.2.** Differential pulse voltammograms of the anodic oxidation of traces of Pb-Sb alloys that have been transferred onto a PIGE by mechanical rubbing of the electrode on pieces of the alloys. The electrolyte solution was a 0.1 M oxalic acid [B 1]

alloys [B 1]. Figure 5.2 shows differential pulse voltammograms of the anodic oxidation of Pb-Sb alloy of various compositions. The transfer was accomplished by gently (!) rubbing the lower circular surface of a paraffin impregnated graphite electrode (PIGE) rod on the surface of the alloys. Because of this *abrasive* transfer and deposition of the alloy, in early publications the term *abrasive stripping voltammetry* was coined to be consistent with terms like *adsorptive stripping voltammetry*, where *adsorption* is the process of attaching a compound to the electrode. Later, the more general term *voltammetry of immobilized microparticles* was preferably used. Figure 5.3 depicts the calibration graphs derived from the voltammograms shown in the Fig. 5.2. Since the absolute amounts of alloy traces transferred by rubbing cannot be controlled and vary to some extent from experiment to experiment, the evaluation of the voltammograms was based on the percentage of each peak current in relation to the sum of peak currents.

This first example proved that the idea of an abrasive transfer of traces of a material from a compact sample to an electrode worked quite well and a number of similar publications followed [B 3, B 7, B 8, B 18, B 177, B 193,

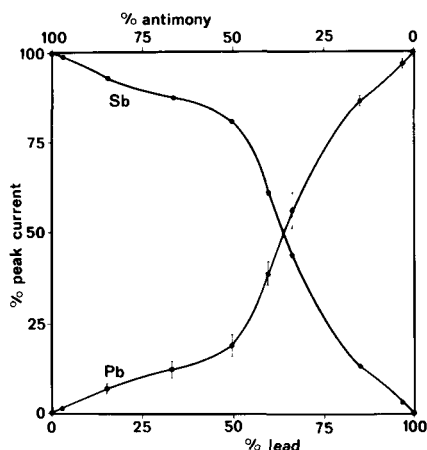


**Fig. 5.3.** Percentage of peak currents for lead and antimony oxidation as a function of the alloy composition. Data derived from the voltammograms shown in Fig. 5.2 [B 1]

B 193, B 261]. The great advantage of performing electrochemical measurements with trace amounts of an alloy is the high resolution that can be achieved at rather high scan rates, due to the complete anodic oxidation and dissolution of the constituents of the alloy without overlapping of the signals. The latter is observed whenever compact pieces of alloys are subjected to an anodic oxidation. Of course, the position of the signals and their shape depend in a complex manner on the thermodynamics of alloys, the thermodynamics of anodic oxidation reactions including complex formation of the metal ions in solution, and on the kinetics of all involved reaction steps. Figure 5.4 shows differential pulse voltammograms of the anodic oxidation of tin-mercury alloys recorded following a mechanical transfer of traces of the alloys to the surface of a PIGE [B 18]. Also shown are the calibration plots. This figure shows the results for two different electrolytes and it is obvious that the electrolyte has a large influence on the shape, position and relative intensities of the signals.

Cepria et al. [B 177] have demonstrated how the mechanical transfer of alloy traces to the surface of an electrode can be used for a quick identification of metal alloys (cf. Fig. 5.5). These authors have used a pyrolytic graphite rod electrode which they impregnated with paraffin as described in Chapter 3.1.

Quantitative analyses have so far been reported only for binary alloys. If there are more than two constituents in an alloy, major complications may primarily arise from intermetallic compounds and phase formation. How-



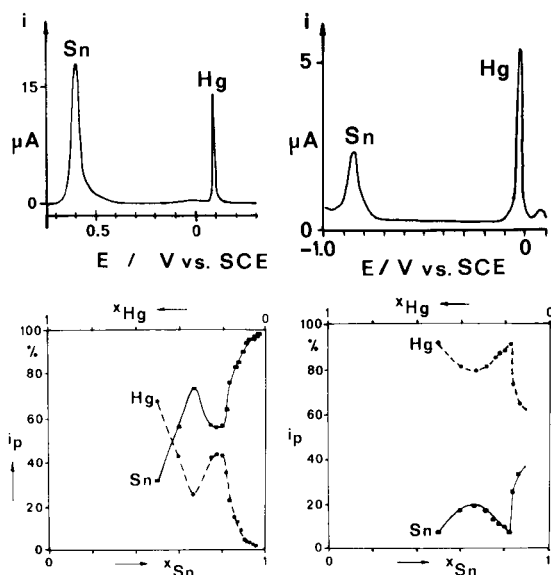


**Fig. 5.4.** Top: differential pulse voltammograms of the anodic oxidation of tin-mercury alloys with 47% tin. Bottom: calibration plots of the percentage peak current of tin and mercury oxidation. Left side: electrolyte  $0.05 \text{ mol L}^{-1} \text{ KCl}$ ,  $0.05 \text{ mol L}^{-1} \text{ oxalic acid}$ . Right side: electrolyte  $1 \text{ mol L}^{-1} \text{ NH}_3$ ,  $1 \text{ mol L}^{-1} \text{ NH}_4\text{Cl}$  [B 18].

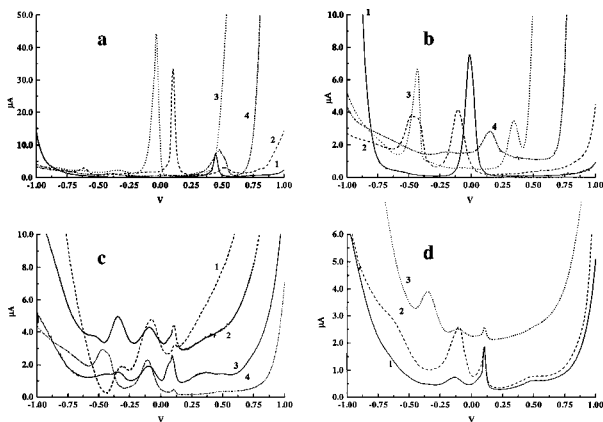


**Fig. 5.5.** Differential pulse voltammograms of anodic dissolution of different metals and alloys. a Silver, b copper, c 1- Ag(91)-Cu(9) alloy, 2- Ag(70)-Cu(30) alloy, 3- Ag(40)-Cu(60) alloy, 4- Ag(10)-Cu(90) alloy d Jewellery items: (1) earring A, (2) earring B, (3) pendant. Electrolytes. a and b 1-  $0.4 \text{ M}$  oxalic acid, 2-  $0.1 \text{ M}$  ammonia buffer, 3-  $0.4 \text{ M}$  thiocyanate solution, 4-  $0.2 \text{ M}$  EDTA. c and d  $0.1 \text{ M}$  ammonia buffer [B 177]

ever, especially this aspect seems to be very interesting to be studied in the future with the technique of immobilizing traces of alloys on electrodes.

Corrosion properties of metals and alloys can be assessed for bulk material and for powders. However, the applicability of the technique to bulk material studies strongly depends on how much the sampling affects the corrosion properties. If the abrasive transfer of alloy traces to an electrode results in alloy patches on the electrode that possess the same or very similar corrosion properties as the compact piece of metal, then there are no objections for an application of this technique. This is obviously the case for many amalgams, the electrochemical corrosion of which has been studied and appeared to be as that known from studies of compact alloy pieces [B 18]. The only, however, very advantageous difference was that the signal resolution was considerably improved in studies of mechanically transferred alloy traces. The detection of the rather corrosion sensitive so-called  $\gamma_2$ -phase in dental amalgams was extremely easy to perform since the presence of this phase produced a well-developed anodic peak. This phase produced just a faint shoulder when compact pieces of that alloy were used as electrodes in anodic oxidation studies. Electrochemical corrosion studies of metal or alloy powders are well known to be difficult to perform for the simple reason of electrode construction. Žežula and Galova have shown that the corrosion potential of iron powder can be determined by immobilizing the powder on a PIGE and performing the usual potentiodynamic measurements [B 108]. As to be expected, the authors observed a small shift in the corrosion potential for repetitive polarizations, most probably due to a reduction of the primarily present oxide layer on the iron particles. The reactivity of iron powders has been assessed by pulsed chronoamperometry [B 307].

## 5.2 Minerals and Pigments

The identification of minerals and pigments is conventionally performed with the help of microscopic techniques, including infrared and Raman spectroscopy, X-ray diffraction, and several microprobe techniques. Here we will show that the voltammetry of immobilized microparticles can be used as a powerful alternative technique, both for the identification of phases as well as for their quantitative analysis. The only prerequisite is electrochemical activity, which, however, is shown by the majority of minerals and pigments.

### 5.2.1 Phase Identification

Generally, solid phases can be identified when a characteristic fingerprint is obtainable by application of a certain analytical technique. It is not necessary to have a complete understanding of the signals of the fingerprint, although this will always be desirable in a truly scientific study.

Voltammetric fingerprints of minerals and pigments can be obtained on the basis of the following measurements: (i) performing a reductive voltammetric scan, provided that the solid phase contains reducible constituents; (ii) performing an oxidative voltammetric scan, provided that the solid phase contains oxidizable constituents; and (iii) performing an oxidative scan after a preliminary reduction of the solid phase. Of course, other approaches are possible as well, however, the published applications all fall into these three categories. Figure 5.6 shows voltammograms exemplifying the three approaches for the case of boulangerite, a lead antimony sulfide mineral  $\text{Pb}_5\text{Sb}_4\text{S}_{11}$  [B 2]. Since lead and antimony are present in the mineral as  $\text{Pb}^{2+}$  and  $\text{Sb}^{3+}$ , it is possible to reduce these ions to the respective metals. Obviously, their reduction occurs at similar potentials and no separate signals are obtained. The reduction signal is not very specific and cannot be used for an unambiguous identification. The same holds true for

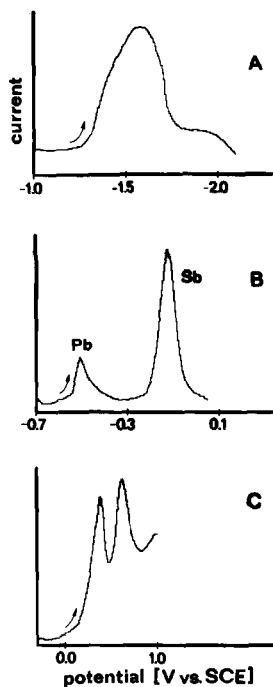
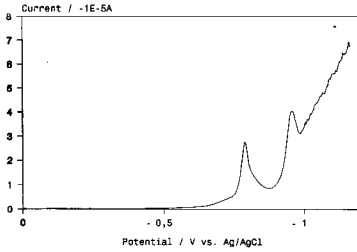


**Fig. 5.6.** Differential pulse voltammograms of boulangerite ( $\text{Pb}_5\text{Sb}_4\text{S}_{11}$ ) obtained after mechanical transfer of traces of the mineral onto the surface of a paraffin-impregnated graphite electrode. **A** Reductive scan; electrolyte: 0.1 M sodium oxalate, pH 5; **B** Inverse voltammogram after reduction at -1.5 V; electrolyte: 0.1 M sodium oxalate, pH 2; **C** Oxidative scan; electrolyte: 0.1 M oxalic acid. [B 2]

the oxidative scan where the sulfide ions are oxidized to yet unidentified products. Much more specific signals can be obtained with approach (iii), i.e., an oxidative scan following a preliminary reduction. In the case of boulangerite, upon reduction at sufficiently negative electrode potential the two metals, lead and antimony, remain on the electrode whereas the sulfide ions escape into the electrolyte solution. In the oxidative scan the two metals give two well-separated signals that are specific for each metal in the used electrolyte solution. Approach (iii) very much resembles that of conventional stripping voltammetry where metals are deposited on an electrode from a solution and oxidatively stripped off during an anodic scan. Figure 5.7 gives further examples for reductive, Fig. 5.8 for oxidative voltammograms of minerals. Both figures illustrate that, although the signals are different, they are not very suitable for unambiguous phase identification. Figure 5.9 shows examples of the highly specific voltammograms that are obtained after a preliminary reduction of the metal ions to metals (approach (iii)). The respective metal signals can be easily identified. A closer look on the voltammograms reveals that the signals of anodic metal oxidation are frequently structured and not as symmetric as in anodic stripping voltammetry using mercury electrodes. The structured signals are due to the fact that the metals are present as solids on the electrode, usually a PIGE. The fact that one and the same metal shows differently structured signals depending on the starting mineral shows that the resulting metal deposits also differ. To avoid such structured signals one can add a small concentration of a Hg(II) salt, e.g.,  $10^{-4}$  mol L<sup>-1</sup> HgCl<sub>2</sub>, to the electrolyte solution. During the preelectrolysis of the minerals a simultaneous plating of mercury occurs and the metals dissolve in the mercury droplets that are deposited on the surface of the PIGE. In this case the anodic dissolution of the metals occurs from the amalgam state and very clean anodic peaks are measured. Figure 5.10 shows anodic differential pulse voltammograms recorded after a preliminary electrolysis of different thallium-tin sulfides using a mercury(II) containing electrolyte [B 32]. The relative heights of the thallium and tin peaks are clearly depending on the stoichiometry of the minerals and they can serve for an unambiguous identification. In Sect. 5.2.3 it will be shown how a quantitative determination of the Tl:Sn ratio can be performed with the help of chronocoulometry. The simplicity of measurements, the extremely small amounts of sample (down to  $10^{-12}$  mole are sufficient), the high mineral specificity and also the elemental specificity, make this analytical approach highly attractive for mineral and pigment identification, both in the laboratory as well as for field analysis [B 17]. Figure 5.11 shows voltammograms of several inorganic pigments [B 25].

$Tl_2As_2SnS_6$

Origin: synthetic  
 Method: differential pulse voltammetry, reduction  
 Electrolyte: 1 M HCl  
 Method parameters:  $E_{pulse} = 0.050$  V  $t_{pulse} = 0.01$  s  
 $E_{step} = 0.0037$  V  $t_{int} = 0.50$  s

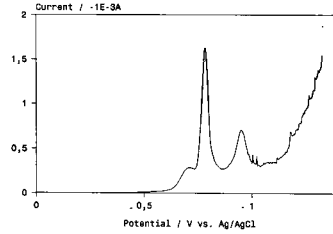


Results of peak search:

	E/ V vs. Ag/AgCl	height / A E - 04	area /AV E - 06	$W_{1/2}$ / V
1	-0.787	-2.172	9.447	0.029
2	-0.952	-1.659	5.266	0.029

$Tl_2As_2Sn_2S_7$

Origin: synthetic  
 Method: differential pulse voltammetry, reduction  
 Electrolyte: 1 M HCl  
 Method parameters:  $E_{pulse} = 0.050$  V  $t_{pulse} = 0.01$  s  
 $E_{step} = 0.0037$  V  $t_{int} = 0.50$  s

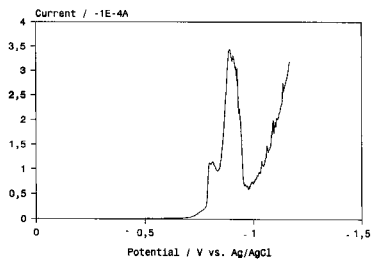


Results of peak search:

	E/ V vs. Ag/AgCl	height / A E - 03	area /AV E - 05	$W_{1/2}$ / V
1	-0.696	—	—	—
2	-0.784	-1.346	5.021	0.029
3	-0.948	-0.424	2.555	0.051

$Tl_2SnS_3$

Origin: synthetic  
 Method: linear sweep voltammetry, reduction  
 Electrolyte: 1 M HCl  
 Method parameters:  $E_{step} = 0.002$  V scan rate = 0.010 V/s

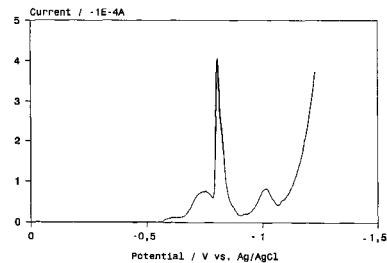


Results of peak search:

	E/ V vs. Ag/AgCl	height / A E - 04	area / C E - 03	$W_{1/2}$ / V
1	-0.793	—	—	—
2	-0.891	-2.573	2.550	0.073

$Tl_2Sn_2S_3$

Origin: synthetic  
 Method: linear sweep voltammetry, reduction  
 Electrolyte: 1 M HCl  
 Method parameters:  $E_{step} = 0.002$  V scan rate = 0.010 V/s



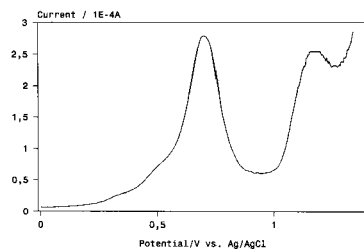
Results of peak search:

	E/ V vs. Ag/AgCl	height / A E - 04	area / C E - 03	$W_{1/2}$ / V
1	-0.730	-0.314	0.211	0.071
2	-0.806	-3.540	1.049	0.027
3	-1.011	-0.481	0.2923	0.059

Fig. 5.7. Reductive voltammograms of several mineral phases [B 46]

**Chalcopyrite (CuFeS<sub>2</sub>)**

*Origin:* Daaden, Altenkirchen  
*Method:* differential pulse voltammetry, oxidation  
*Electrolyte:* 1 M KCl  
*Method parameters:* E<sub>pulse</sub> = 0.050 V t<sub>pulse</sub> = 0.01 s  
 E<sub>step</sub> = 0.004 V t<sub>int</sub> = 0.50 s

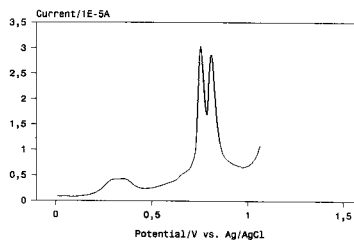


*Results of peak search:*

	E / V vs. Ag/AgCl	height / A E - 04	area / AV E - 05	W <sub>1/2</sub> / V
1	0.703	2.315	4.258	0.146
2	1.187	—	—	—

**Chalcocite (CuSbS<sub>2</sub>)**

*Origin:* Abfattersbach (Austria)  
*Method:* differential pulse voltammetry, oxidation  
*Electrolyte:* 1 M KCl  
*Method parameters:* E<sub>pulse</sub> = 0.050 V t<sub>pulse</sub> = 0.07 s  
 E<sub>step</sub> = 0.005 V t<sub>int</sub> = 0.50 s

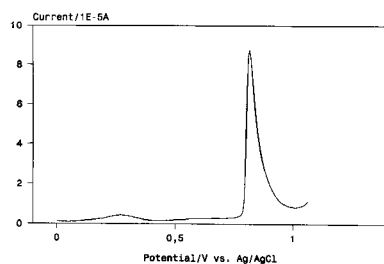


*Results of peak search:*

	E / V vs. Ag/AgCl	height / A E - 05
1	0.303	0.255
2	0.752	2.575
3	0.811	2.344

**Chalcocite (CuSbS<sub>2</sub>)**

*Origin:* synthetic  
*Method:* differential pulse voltammetry, oxidation  
*Electrolyte:* 1 M KCl  
*Method parameters:* E<sub>pulse</sub> = 0.050 V t<sub>pulse</sub> = 0.07 s  
 E<sub>step</sub> = 0.005 V t<sub>int</sub> = 0.50 s

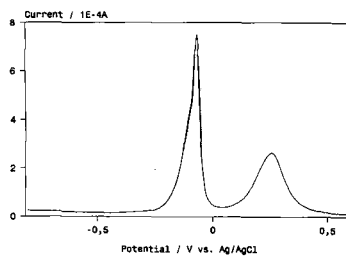


*Results of peak search:*

	E / V vs. Ag/AgCl	height / A E - 05	area / AV E - 06	W <sub>1/2</sub> / V
1	0.269	0.297	0.4633	0.142
2	0.815	8.314	5.1200	0.049

**Cuprite (Cu<sub>2</sub>O)**

*Origin:* Gumerobewak, Ural (Russia)  
*Method:* differential pulse voltammetry, stripping mode  
*Electrolyte:* 1 M KCl  
*Method parameters:* E<sub>pulse</sub> = 0.050 V t<sub>pulse</sub> = 0.01 s  
 E<sub>step</sub> = 0.004 V t<sub>int</sub> = 0.30 s  
 E<sub>dep</sub> = -1.400 V t<sub>dep</sub> = 60 s



*Results of peak search:*

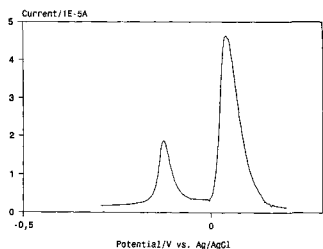
	E / V vs. Ag/AgCl	height / A E - 04	area / AV E - 05	W <sub>1/2</sub> / V
1	-0.068	7.1836	4.8064	0.055
2	0.255	2.3612	3.5910	0.132

**Fig. 5.8.** Oxidative voltammograms of several mineral phases [B 46]

**Stephanite (Ag<sub>5</sub>SbS<sub>4</sub>)**

Origin: Freiberg, Erzgebirge (Germany)

Method: differential pulse voltammetry, stripping mode  
 Electrolyte: 1M HCl  
 Method parameters: E<sub>pulse</sub> = 0.010 V t<sub>pulse</sub> = 0.07 s  
 E<sub>step</sub> = 0.005 V t<sub>int</sub> = 0.50 s  
 E<sub>dep</sub> = -1.200 V t<sub>dep</sub> = 60 s



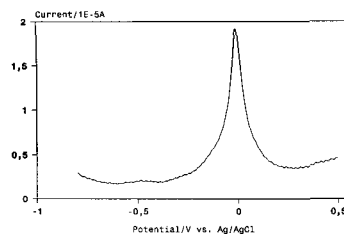
Results of peak search:

	E / V vs. Ag/AgCl	height / A E - 05	area / C E - 06	W <sub>1/2</sub> / V
1	-0.127	1.597	0.712	0.034
2	0.039	4.331	2.650	0.053

**Stibnite (Sb<sub>2</sub>S<sub>3</sub>)**

Origin: Shikoko (Japan)

Method: differential pulse voltammetry, stripping mode  
 Electrolyte: 1 M HCl  
 Method parameters: E<sub>pulse</sub> = 0.050 V t<sub>pulse</sub> = 0.01 s  
 E<sub>step</sub> = 0.004 V t<sub>int</sub> = 0.50 s  
 E<sub>dep</sub> = -1.200 V t<sub>dep</sub> = 60 s



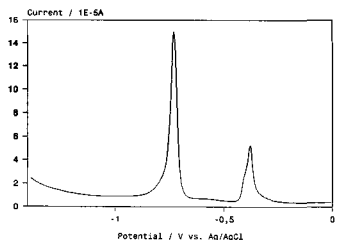
Results of peak search:

	E / V vs. Ag/AgCl	height / A E - 05	area / V E - 06	W <sub>1/2</sub> / V
1	-0.009	1.6125	1.9413	0.077

**Tl<sub>2</sub>As<sub>2</sub>SnS<sub>6</sub>**

Origin: synthetic

Method: differential pulse voltammetry, stripping mode  
 Electrolyte: 1M KCl  
 Method parameters: E<sub>pulse</sub> = 0.050 V t<sub>pulse</sub> = 0.01 s  
 E<sub>step</sub> = 0.004 V t<sub>int</sub> = 0.50 s  
 E<sub>dep</sub> = -1.700 V t<sub>dep</sub> = 60 s



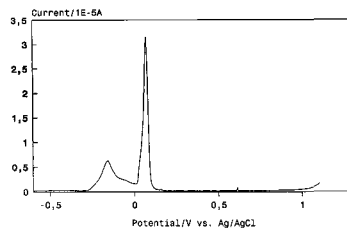
Results of peak search:

	E / V vs. Ag/AgCl	height / A E - 04	area / V E - 06	W <sub>1/2</sub> / V
1	-0.730	1.419	6.483	0.033
2	-0.378	0.476	2.352	0.040

**Pyrrargyrite (Ag<sub>3</sub>SbS<sub>3</sub>)**

Origin: St. Andreasberg, Harz (Germany)

Method: differential pulse voltammetry, stripping mode  
 Electrolyte: 1M KCl  
 Method parameters: E<sub>pulse</sub> = 0.010 V t<sub>pulse</sub> = 0.07 s  
 E<sub>step</sub> = 0.005 V t<sub>int</sub> = 0.50 s  
 E<sub>dep</sub> = -1.200 V t<sub>dep</sub> = 60 s



Results of peak search:

	E / V vs. Ag/AgCl	height / A E - 05	area / C E - 06	W <sub>1/2</sub> / V
1	-0.161	0.5305	0.5415	0.078
2	0.074	3.0474	1.0295	0.029

**Fig. 5.9.** Oxidative voltammograms recorded following to a preliminary reduction of several mineral phases [B 46]

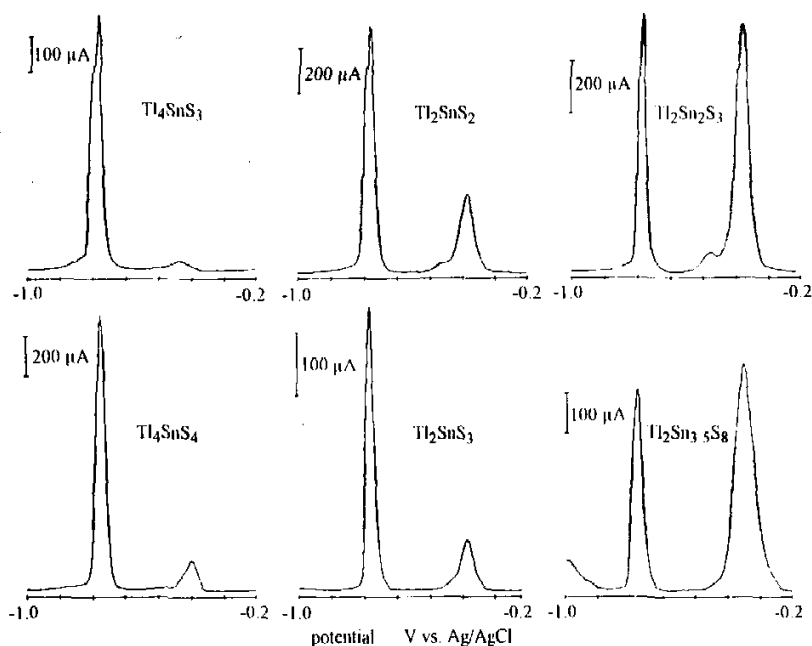


**Fig. 5.10** Anodic differential pulse voltammograms of thallium-tin sulfides of different stoichiometry after a preliminary reduction of the solid phases at  $-1.0$  V vs Ag/AgCl for 60 seconds. The electrolyte solution contained 1 M HCl and  $10^{-4}$  M  $\text{HgCl}_2$ . The scan rate was  $10 \text{ mV s}^{-1}$  [B 32]

Doménech-Carbó et al. [B 143] have studied the Pb(II) and Pb(IV) content in medieval glazes. They used three different techniques for immobilizing the micro-particles obtained after milling small amounts of samples in a mortar: (i) they prepared modified paste electrodes by mixing graphite powder (35 wt%), paraffin oil (35 wt%), and the sample powder (30 wt%). (ii) Aliquots of a dispersion of the sample in a 0.5 wt% solution of Paraloid B 72 in acetone were applied to the surface of a freshly polished glassy carbon electrode to prepare the modified film. (iii) 0.1 mg of the sample powder was mixed with 1 mg graphite powder and the mixture was pressed onto an electrode that was finally covered by a Paraloid B72 coating. Figure 5.12 shows the response of  $\text{PbO}$ ,  $\text{PbO}_2$ , and  $\text{Pb}_3\text{O}_4$  in the film electrodes (preparation (ii)).



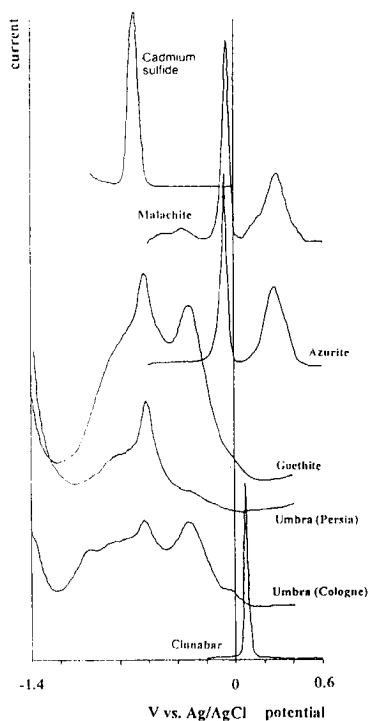


**Fig. 5.11.** Differential pulse voltammograms of pigments (pulse amplitude 10 mV, pulse duration 0.07 s, scan rate  $0.526 \text{ V min}^{-1}$ , preelectrolysis for CdS at  $-1.2 \text{ V vs Ag/AgCl}$ , for all other pigments at  $-1.5 \text{ V vs Ag/AgCl}$ ). The electrolyte solution was a 0.1 M oxalic acid for CdS, and 1 M KCl for all other compounds) [B 25]

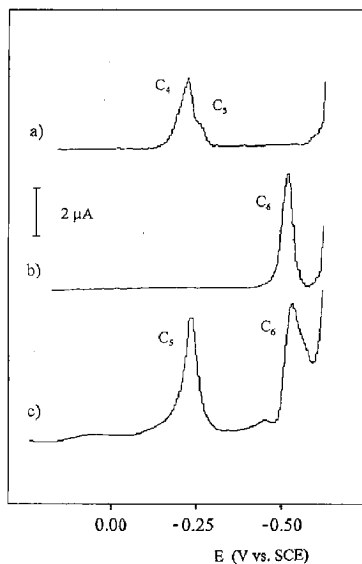


**Fig. 5.12.** Cathodic differential pulse voltammograms for modified film electrodes containing a)  $\text{PbO}$ , b)  $\text{PbO}_2$ , and c)  $\text{Pb}_3\text{O}_4$ . Scan rate  $10 \text{ mV s}^{-1}$ , pulse height: 10 mV [B 143]

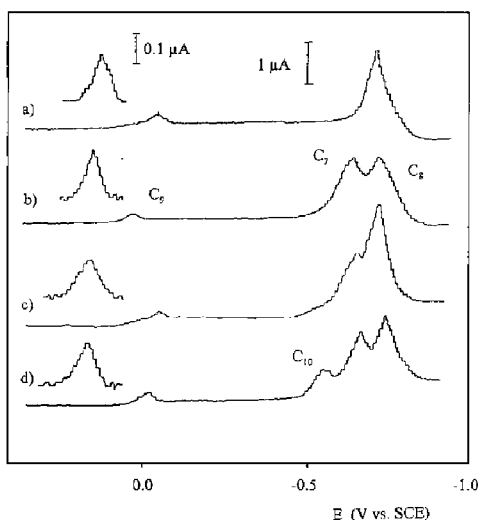


**Fig. 5.13.** Cathodic differential pulse voltammograms for modified film electrodes containing samples of test specimen and archeological samples. Scan rate  $10 \text{ mV s}^{-1}$ , pulse height:  $10 \text{ mV}$ , acetate buffer [B 143]

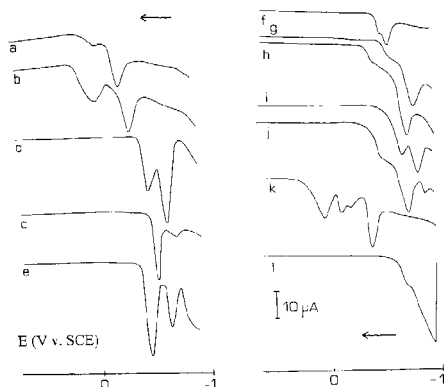


**Fig. 5.14.** Anodic differential pulse voltammograms following a preliminary reduction at  $-1.0 \text{ V}$  in  $1 \text{ M NaCl}$  solution: a malachite, b azurite, c minium, d chrome yellow, e litharge, f lead white, g lead-tin yellow, h chrome orange, i cadmium red, j cadmium yellow, k vermilion, l zinc white [B 146]

Figure 5.13 depicts the responses of medieval glazes. The same authors applied the film electrodes for a wide range of pigments from polychrome sculptures and paintings. Figure 5.14 illustrates very impressively how specific the voltammetric fingerprints are [B 146]. Extensive tables of peak potentials given in this publication support this statement. The film electrodes have also been used studying the canvas painting in a Basilica in Valencia, Spain [B 175] and for the identification of the decomposition products, i.e., alteration products of copper-containing pigments [B 176]. For this purpose the authors have developed a very interesting approach: The pigments verdigris (a basic copper acetate:  $\text{Cu}(\text{C}_2\text{H}_3\text{O}_2)_2 \cdot 2\text{Cu}(\text{OH})_2$ ), azurite (a basic copper carbonate:  $2\text{CuCO}_3 \cdot \text{Cu}(\text{OH})_2$ ), malachite (another

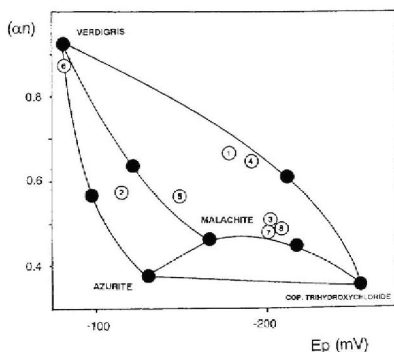


**Fig. 5.15.** Representation of the apparent charge transfer coefficients calculated from the slope of Tafel plots as a function of the peak potential from linear scan voltammograms recorded at 60 mV/s. Black points: samples of the pure pigments and their binary 1:1 mixtures. Circled numbers: samples from a Basilica in Valencia, Spain [B 176]

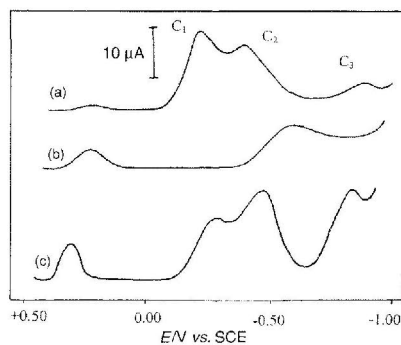


**Fig. 5.16.** Cathodic differential pulse voltammograms of **a** Mars black, **b** Van Dyke brown, **c** Umber raw modified electrodes immersed in 0.1 M HCl [B 195]

basic copper carbonate:  $\text{CuCO}_3\text{Cu}(\text{OH})_2$  and copper trihydroxychloride ( $\text{Cu}_2(\text{OH})_3\text{Cl}$ ) have rather similar reductive voltammograms making their identification difficult, especially in their mutual presence. However, when Tafel plots are constructed from linear scan voltammograms and when the slopes of the Tafel plots are plotted versus the peak potential of reductive dissolution, a two-dimensional diagram is obtained with very clear separation of the pure phases and their binary mixtures. Figure 5.15 shows such a plot including sample spots from green-blue pigments of the Basilica in Valencia. The composition that can be derived from this diagram for the pigment samples was supported by SEM/EDX and FT-IR measurements. In another study Doménech-Carbó et al. [B 189] have identified manganese(IV) centers in archeological glass. The authors studied the relation between the voltammetric responses and the conditions of glass deterioration. The same authors identified iron oxide pigments (green earth, iron oxide red, Mars black, ochre yellow, Sienna raw, umber raw, Van Dyke brown) in microsamples extracted from polychromed sculptures, canvas paintings, wall paintings, altarpieces and panel paintings from Spain, Ethiopia and Italy from the 12<sup>th</sup> to the 20<sup>th</sup> centuries [B 195]. The authors employed a mechanical immobilization of sample particles on the surface of self-made

graphite-polyester electrodes and also modified polyester-graphite electrodes. Figure 5.16 shows the unique shape of cathodic differential pulse voltammograms of three iron oxide pigments. Another example of application of the voltammetry of immobilized microparticles is the detection of Co, Cu, Sb, Mn, Sn, and Fe in archeological samples of Spanish ceramic glazes from the 16<sup>th</sup> to 18<sup>th</sup> centuries [B 217, B 303]. The authors used the mechanical immobilization of microparticles on the surface of a polyester-graphite electrode. Domenech-Carbo et al. have presented an ingenious application of the voltammetry of immobilized particles – the determination of the boron content of minerals [B 118]. Other applications concern the phase identification of iron oxides [B 312], copper and iron oxides [B 314] and cobalt cordierites [B 317].

### 5.2.2 Quantitative Determination of a Phase in a Phase Mixture

In the case that more than one electrochemically active phase is present in a powder mixture it is possible to utilize the voltammetry of immobilized microparticles on the basis of a calibration procedure. This has been shown for two phase mixtures [B 11]. When both phases give an electrochemical signal that is directly proportional to the absolute amount of immobilized substance, however have different slopes (sensitivities), a plot of the percentage peak currents versus the molar ratio of the compounds in the mixture is non-linear (cf. Fig. 5.17). Because it is impossible to immobilize a known amount of the phase mixture on the electrode surface, the percentage peak currents are evaluated for a mixture of phase A and B in the following way:

$$i_{\%,A} = \frac{i_A}{i_A + i_B} 100\% \quad \text{and} \quad i_{\%,B} = \frac{i_B}{i_A + i_B} 100\% \quad (5.1 \text{ and } 5.2)$$

where  $i_A$  and  $i_B$  are the peak currents of the phases A and B, respectively. Figure 5.18 shows calibration plots for mixtures of FeOOH/MnO<sub>2</sub>, HgS/HgO, and PbO/HgO. The standard deviations for the determined powder compositions were in the range of 10 to 20%. These relatively high values were attributed to inhomogeneities of the powder mixtures. It is clear that inhomogeneities play an increasing role the smaller the samples are.

If a solid phase contains a certain concentration of electroactive centers, and if this concentration is to be determined, it is possible to use another electroactive solid phase as inner standard. In solid phases of copper(II) hexacyanoferrate-hexacyanocobaltate only the hexacyanoferrate unit is electroactive. To study the electroactivity of this moiety in solid solutions

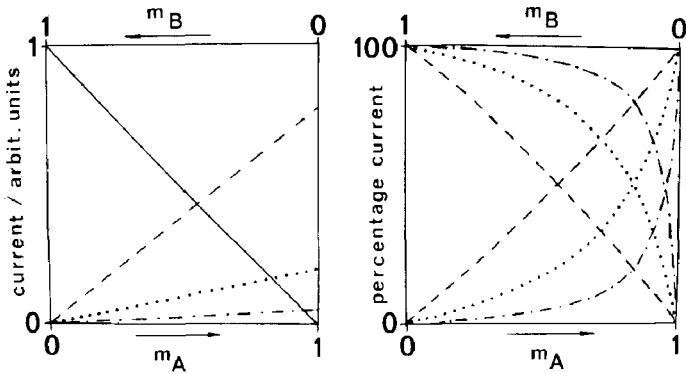


**Fig. 5.17.** Left: Theoretical calibration plots for the absolute peak currents when the amount of mixture is constant for each measurement. Right: Corresponding theoretical calibration plots for the percentage peak currents [B 11]

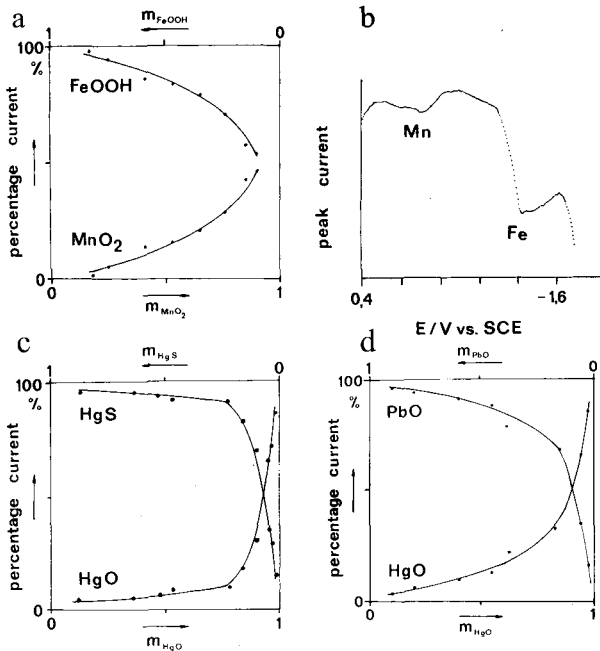


**Fig. 5.18.** Calibration plots of percentage peak currents of the following powder mixtures: a, b MnO<sub>2</sub> /  $\alpha$ -FeOOH, c HgS (black) / HgO (yellow), and d PbO / HgO (yellow) [B 11]

of different composition, i.e., different ratio of hexacyanoferrate to hexacyanocobaltate, this solid phase was mixed in a 1:1 ratio with solid nickel(II) hexacyanoferrate. The latter exhibits a hexacyanoferrate signal well away from that of the solid solutions. In this way it was possible to

evaluate the peak current of the hexacyanoferrate of the solid solution with respect to the constant signal of the nickel(II) hexacyanoferrate [B 247]. The same approach of an inner standard should be applicable to the case where the concentration of an electroactive solid phase has to be determined in the matrix of an electroinactive powder mixture. Indeed this has been done by van Oorschot et al. [B 198] who determined iron(oxy)(hydr)oxides in soils and sediments using pyrolusite ( $\beta$ - $\text{MnO}_2$ ) as inner standard. The authors report this method as being semi-quantitative. In a later publication Grygar et al. reported the determination of ferric oxides in clay with the help of electroactive carbon paste electrodes [B 222]. The paste was a mixture of graphite powder, the sample and an acetate buffer solution. A thin layer of the paste was spread on the surface of a carbon electrode and covered by a foil. The iron oxide was first reductively dissolved and then the iron(II) that must remain in the paste was oxidized to iron(III) ions. The oxidation charge was used to determine the iron content in the samples.

### 5.2.3 Quantitative Analysis of the Composition of a Phase

Here, we understand the term “quantitative analysis of a solid phase” as a determination of either the complete stoichiometry, or at least the determination of one or some phase constituents. Examples for the determination of the complete stoichiometry are:  $\text{Tl}_2\text{S}$ ,  $\text{TlS}$ ,  $\text{Tl}_4\text{S}_3$ , and  $\text{Tl}_2\text{S}_5$  [B 32]. Examples for the determination of the ratios of the metal contents of sample phases are: (i) the  $\text{Tl}:\text{Sn}$  ratio in  $\text{Tl}_4\text{SnS}_4$ ,  $\text{Tl}_2\text{Sn}_{3.5}\text{S}_8$ ,  $\text{Tl}_2\text{SnS}_3$ ,  $\text{Tl}_4\text{SnS}_3$ ,  $\text{Tl}_2\text{Sn}_2\text{S}_3$ ,  $\text{Tl}_2\text{SnS}_2$  [B 32], (ii) the  $\text{Bi}:\text{Cu}:\text{Pb}$  ratio in  $\text{Bi}_{1.8}\text{Pb}_{0.39}\text{Sr}_{1.99}\text{Ca}_{2.06}\text{Cu}_{3.15}\text{O}_{10.5}$  [B 9].

For the quantitative analyses of solid phases it is highly important that the measured charges are caused by strictly defined electrochemical reactions (no side reactions). Any loss of the compounds from the electrode surface has to be prevented during the electrochemical steps. Especially, when solid metal compounds immobilized on the electrode surface are reduced to the metals it can occur that the metal particles do not adhere on the electrode surface. Further, it was found in case of the thallium sulfides [B 32] that the thallium deposit obtained by reduction shows a very peculiar behavior when it is electrochemically oxidized: the oxidation was accompanied by a black cloud that was ejected from the electrode surface. Most probably the thallium deposit was partly lost due to electrostatic charging effects. Of course, such behavior must be circumvented, as well as the early hydrogen evolution on some metal deposits or compound phases. A very appropriate solution for all these problems is the co-deposi-

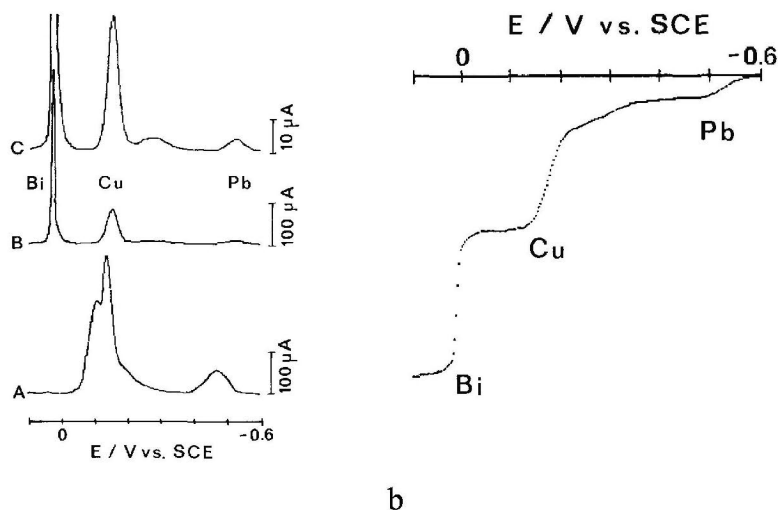


**Fig. 5.19.** **a** Differential pulse voltammograms of the compound  $\text{Bi}_{1.8}\text{Pb}_{0.39}\text{Sr}_{1.99}\text{Ca}_{2.06}\text{Cu}_{3.15}\text{O}_{10.5}$  after a preliminary reduction at  $-1.5$  V vs. SCE for 30 sec, A without calomel, B and C with calomel, **b** integrated curve B of Fig. 5.19a, in arbitrary units [B 9]

tion of metallic mercury. Two alternative approaches have been reported: (i) the solid sample phase can be thoroughly mixed with an excess of calomel ( $\text{Hg}_2\text{Cl}_2$ ) [B 9], or (ii) the electrolyte solution can be spiked with a small concentration of  $\text{Hg}^{2+}$  ions [B 32]. In the case of the high-temperature superconductor  $\text{Bi}_{1.8}\text{Pb}_{0.39}\text{Sr}_{1.99}\text{Ca}_{2.06}\text{Cu}_{3.15}\text{O}_{10.5}$  small amounts of the compound were thoroughly mixed with a 100- to 500-fold excess of solid calomel and a droplet of ethanol. After evaporation of the ethanol the powder mixture was immobilized on a PIGE in the usual way and anodic differential pulse voltammograms were recorded following a preliminary reduction at  $-1.5$  V vs. SCE for 30 seconds (Fig. 5.19a). Figure 5.19b depicts the integrated differential pulse voltammograms. The height of the steps was taken as proportional to the charges consumed for the oxidation of the deposited bismuth, copper and lead. Taking the sum of the charges of the bismuth and lead signals as 100 %, the relative standard deviation of the bismuth signal was as low as 0.5 %, and taking the sum of the charges of the copper and lead signal as 100 %, the copper signal had a relative standard deviation of 1 %. These are very precise determinations, bearing in mind that they were obtained with  $\mu\text{g}$  amounts of the sample on the electrode surface.

In the case of the thallium sulfides  $\text{Tl}_4\text{SnS}_4$ ,  $\text{Tl}_2\text{Sn}_{3.5}\text{S}_8$ ,  $\text{Tl}_2\text{SnS}_3$ ,  $\text{Tl}_4\text{SnS}_3$ ,  $\text{Tl}_2\text{Sn}_2\text{S}_3$ ,  $\text{Tl}_2\text{SnS}_2$  the stoichiometry of the composition can be derived

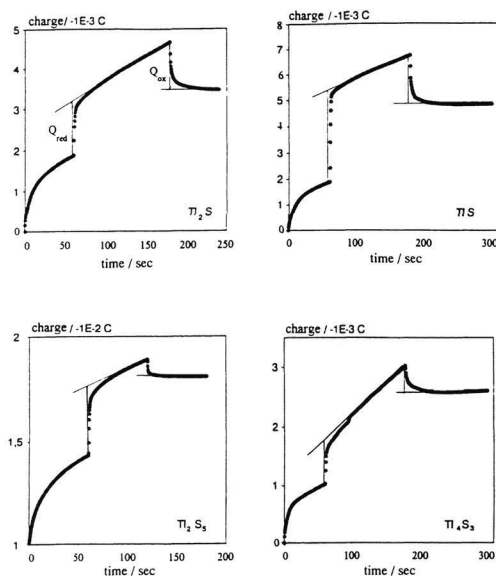


**Fig. 5.20.** Chronocoulograms of thallium sulfides: Electrolyte 2 M NaOH +  $2 \times 10^{-4}$  M HgCl<sub>2</sub>. For details see [B 32]

**Table 5.1** Reactions and ratios of charges necessary for the reduction of a thallium sulfide to the charge for the oxidation of thallium [B 32]

Reduction of the sulfide	Oxidation of thallium	$q_{red} : q_{ox}$ (Theory)	$q_{red} : q_{ox}$ (Experiment)
$Tl_2S + 2e^- \rightarrow 2Tl + S^{2-}$	$2Tl \rightarrow 2Tl^+ + 2e^-$	2:2 = 1	1.18
$TlS + 2e^- \rightarrow Tl + S^{2-}$	$Tl \rightarrow Tl^+ + e^-$	2:1 = 2	2.0
$Tl_4S_3 + 6e^- \rightarrow 4Tl + 3S^{2-}$	$4Tl \rightarrow 4Tl^+ + 4e^-$	6:4 = 1.5	1.65
$Tl_2S_5 + 10e^- \rightarrow 2Tl + 5S^{2-}$	$2Tl \rightarrow 2Tl^+ + 2e^-$	10:2 = 5	4.68

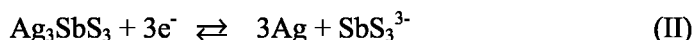
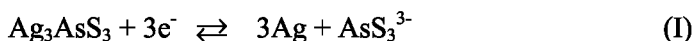
from the determination of the charge necessary to reduce the phases to metallic thallium and the charge necessary for oxidation of the latter. This has been done with the help of triple step chronocoulometry [B 32]. After immobilizing the sample onto the electrode surface, the first potential step was applied to charge the electrode at a potential shortly before the electrochemical reduction. After this, an appropriate reduction potential was applied for 60 s followed by an oxidation potential of -0.5 V vs. Ag/AgCl. The appropriate reduction potential was chosen on the basis of reductive voltammograms. Figure 5.20 depicts some examples of chronocoulograms



and Table 5.1 gives the theoretical and experimental charge ratios for four different compounds. Although the precision of the found charge ratios is certainly too low to be used for high-precision analyses, the ratios can be used to distinguish clearly the otherwise very similar thallium sulfides. It is practically impossible to distinguish them on the basis of simple reductive or oxidative voltammograms.

#### 5.2.4 Determination of Thermodynamic Data of Minerals

In a few cases it has been shown that voltammetric measurements with immobilized microparticles of minerals can give access to the transformation enthalpies of polymorphic forms of minerals [B 24, B 62]. The basis of these measurements is the determination of the reversible potential of the following reactions of the two polymorphs of  $\text{Ag}_3\text{AsS}_3$  xanthoconite and proustite, of  $\text{Ag}_3\text{SbS}_3$  pyrostilpnite and pyrargyrite, and of  $\text{AgAsS}_2$  trechmannite and smithite:



The measurement of the formal potentials of these reactions needs to be performed very fast since the thioanions tend to decompose. It has been shown that square wave voltammograms show all criteria of an electrochemically reversible process. From the differences in the square wave peak potentials, i.e., formal potentials, the difference in the free energy was calculated. The reaction enthalpy of phase transition can be determined according to:

$$\Delta_r G^\circ = \Delta_r H^\circ - T \Delta_r S^\circ \quad (5.3)$$

Assuming a temperature independent entropy (1<sup>st</sup> Uhlich approximation) it follows with

$$\Delta_r S^\circ = \Delta_r H^\circ / T_r \quad (5.4)$$

( $T_r$  is the transformation temperature) that the standard enthalpy is given by:

$$\Delta_r H^\circ = \Delta_r G^\circ / [1 - (T / T_r)] \quad (5.5)$$

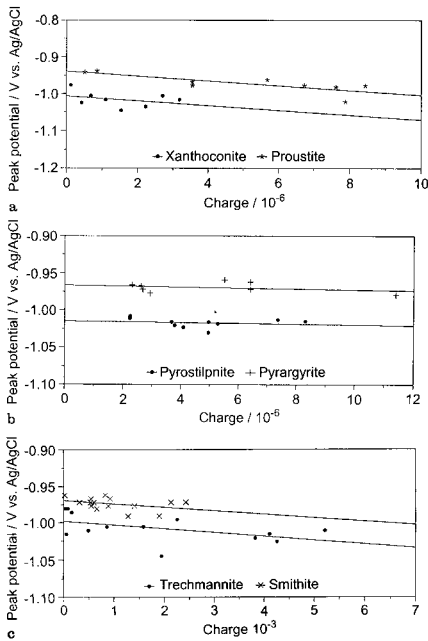


**Fig. 5.21.** Plot of the square wave peak potentials of the three pairs of polymorphic minerals xanthoconite/proustite, pyrostilpnite/yrargyrite, and trechmannite/smithite versus the charge consumed in the electrochemical reactions [B 62]

With the help of the thus determined transformation enthalpies it is possible to calculate the standard formation enthalpy of one polymorphic form when that of the other is known. In the experiments to determine the formal potentials of the polymorphic forms, a small dependence of the square wave peak potentials on the absolute amounts of electroactive mineral reacting on the electrode must be taken into account. This dependence is similar to that discussed in case of solid solutions of  $\text{CuS}_x\text{Se}_{1-x}$  (Chapter 5.3.1). Figure 5.21 shows plots of square wave peak potentials versus the charge underneath the peaks. The variation of charge is just the result of the sampling technique where unavoidably the amounts of mineral transferred to the electrode vary. Like in the case of  $\text{CuS}_x\text{Se}_{1-x}$  (Chapter 5.3.1), the dependencies of the peak potentials on the charge are linear and run parallel for the pairs of polymorphic forms. For the evaluation of the differences of the formal potentials, a linear regression analysis has been used. Because the dependencies are parallel to each other for each pair, the difference of formal potentials is independent on charge. Table 5.2 shows the transformation free energies and enthalpies determined for the three pairs of polymorphic minerals.

**Table 5.2.** Peak potentials, transformation free energies, and enthalpies determined for the three pairs of polymorphic minerals

Mineral pair	$\Delta E_p$ [mV]	$\Delta_r G$ [kJ mol <sup>-1</sup> ]	$\Delta_r H$ [kJ mol <sup>-1</sup> ]
Xanthoconite → Proustite	-68±12	19.7±3.5	54.8±9.6
Pyrostilpnite → Pyrargyrite	-50±7	14.5±20	40.3±5.6
Trechmannite → Smithite	-30±9	2.9±0.9	15.65±1.7

The outlined approach for determining thermodynamic data of minerals is, of course, only applicable when the formal potentials can be measured under reversible conditions.

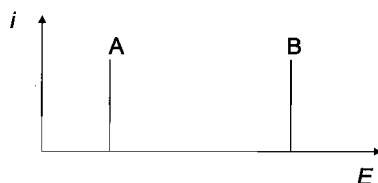
### 5.3 Solid Solutions – Identification and Quantitative Analysis

Solid solutions are of tremendous importance in materials chemistry and physics. Electrochemical measurements can give access to vital information on solid solutions as they are closely linked to thermodynamics. Mixed phase thermodynamics predicts that the electrochemical properties of solid solutions differ in an unambiguous way from that of the pure phases. Therefore it is obvious that from electrochemical measurements two important questions can be answered in a very straightforward way:

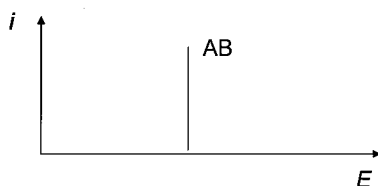
1. Is a certain material a solid solution or is it just a mechanical mixture of two phases?
2. If it is a solid solution, what is its composition?

Figure 5.22 shows the electrochemical signals of two phases A and B and the signal of a solid solution containing A and B in a certain ratio. If a material is a mechanical mixture of the two phases A and B then one will obtain two separate electrochemical signals. These signals may be any kind of characteristic potentials, provided that they are depending on the formal potentials (standard potentials) of the respective systems. Thus it is possible to use peak potentials derived from linear scan voltammetry, from square wave or pulse voltammetry etc., or even the mid-peak potentials of cyclic voltammetry if the system exhibits sufficient reversibility. In any case it will be necessary to have samples of the pure compounds A and B.

Response of the single compounds A and B:



Response of a solid solution AB:



**Fig. 5.22.** Peak positions of single electroactive compounds A and B, and of their solid solution  $A_xB_{1-x}$  [B 204]

When  $E_A$  and  $E_B$  are the characteristic potentials of these pure compounds then it follows that the characteristic potential  $E_{AB}$  of the solid solution

$AB_{(x)}$  with the molar ratio  $x_B = \frac{n_B}{n_A + n_B}$  will shift with the molar ratio as

follows:

$$E_{AB} = E_A + x_B (E_B - E_A) - \frac{RT}{zF} [(x_A \ln x_A + x_B \ln x_B) - x_A x_B \varepsilon] \quad (5.6)$$

The term  $\frac{RT}{zF} (x_A \ln x_A + x_B \ln x_B)$  represents the deviation from linearity caused by the mixing entropy.  $\varepsilon$  is a parameter for the non-ideality<sup>1</sup>. The mixing entropy adds rather little to the non-linearity of the dependence of  $E_{AB}$  on  $x_B$ . It just amounts to 17.7 mV for  $x_B = x_A = 0.5$ ,  $T = 25$  °C and  $z = 1$ . When the reversibility of the electrochemical processes of the pure phases and the mixed phases differ, further deviations from Eq. 6.3.1 must be expected.

<sup>1</sup> Heusler KE (1996) *Electrochim Acta* 41:411-418

### 5.3.1 The Solid Solution System CuS-CuSe

Copper(II) sulfide and selenide form a continuous series of solid solutions. Immobilized on a graphite electrode the pure compounds and the solid solutions can be easily reduced to metallic copper, the sulfide and selenide ions being liberated (Reactions IV and V) and, depending on the pH of the solution, protonated.

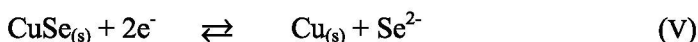
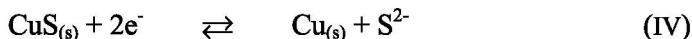
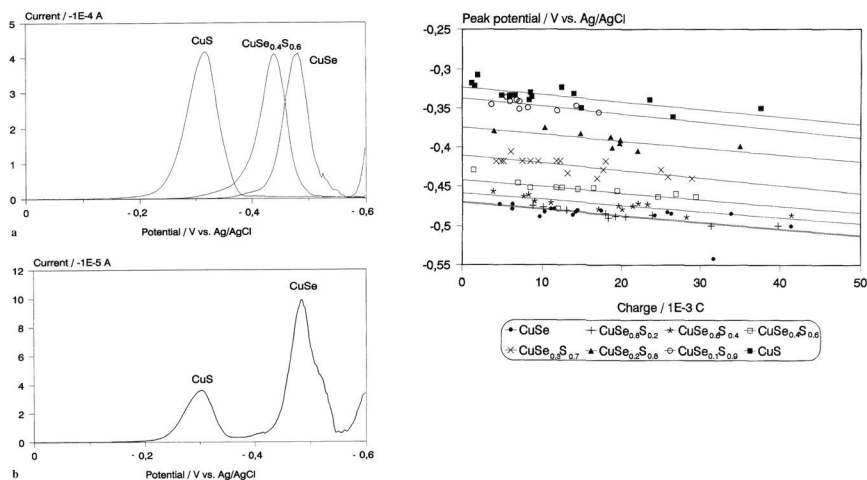
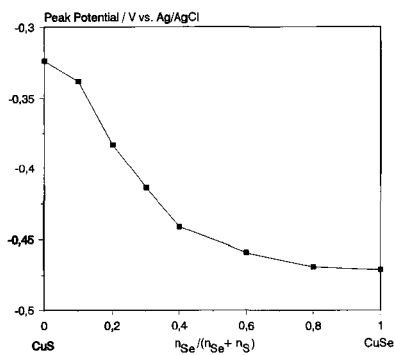


Figure 5.23 depicts the linear sweep voltammograms of the reduction of the pure phases CuS and CuSe, of the solid solution  $\text{CuSe}_{0.4}\text{S}_{0.6}$ , and of a mechanical mixture of CuSe and CuS [B 57]. The voltammogram of the solid solution  $\text{CuSe}_{0.4}\text{S}_{0.6}$  exhibits a single peak in accordance with the expectations from mixed phase thermodynamics. For an exact determination of the composition of the solid solution from a measurement of the peak potential, an empirical calibration is necessary using a set of samples of known composition. Further it is necessary to establish whether the peak potential significantly depends on the amount of particles immobilized on



**Fig. 5.23.** Cathodic voltammograms of **a** CuS, CuSe and  $\text{CuS}_{0.6}\text{Se}_{0.4}$  and **b** a mechanical mixture of CuS and CuSe (1:2). Electrolyte:  $1 \text{ mol L}^{-1} \text{ H}_2\text{SO}_4$ , scan rate  $0.011 \text{ V s}^{-1}$  [B 57]

**Fig. 5.24.** Plot of the peak potential  $E_p$  of different solid solutions  $\text{CuS}_x\text{Se}_{1-x}$  versus charge  $Q$ , consumed in the electrochemical reactions when deliberately varying amounts of the compounds have been immobilized [B 57]



**Fig 5.25.** Plot of standardized peak potentials (extrapolated to values for  $Q = 0$ ) of different solid solutions  $\text{CuS}_x\text{Se}_{1-x}$  versus the molar ratio  $n_{\text{Se}}/(n_{\text{Se}}+n_{\text{S}})$  [B 57]

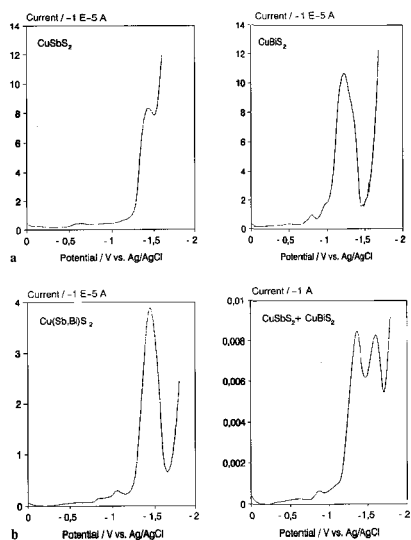


**Fig. 5.26.** Cathodic differential pulse voltammograms of **a**  $\text{CuBiS}_2$  and  $\text{CuSbS}_2$  and **b**  $\text{CuBi}_{0.5}\text{Sb}_{0.5}\text{S}_2$  and a mechanical mixture of  $\text{CuBiS}_2$  and  $\text{CuSbS}_2$ . Electrolyte:  $0.5 \text{ mol L}^{-1}$   $\text{NaOH}$  +  $0.1 \text{ mol L}^{-1}$   $\text{Na-K-tartrate}$ , scan rate:  $6.25 \text{ mV s}^{-1}$ , pulse height:  $25 \text{ mV}$ , and pulse duration:  $0.05 \text{ s}$  [B 57]

the electrode surface. In the case of the copper selenides and sulfides this dependence, which is specific for different immobilized species, has to be taken into account: When each sample is measured several times by trying to deliberately vary the amount and in each case the peak potential is measured and the voltammogram is integrated, one can easily determine the dependence of the peak potentials on the charge, i.e., a value proportional to the amount of reduced substance. Figure 5.24 shows these plots. Interestingly, they are all linear and parallel, and one can extrapolate the peak potentials for zero charge and use them as values standardized for zero amount (any other standardization is suited as well). Plotting these extrapolated peak potentials versus the molar ratio  $x_{\text{Se}}$  yields a smooth curve that can be used as a calibration plot for the analysis of samples of unknown composition (Fig. 5.25). Figure 5.26 shows voltammograms of

$\text{CuSbS}_2$ ,  $\text{CuBiS}_2$  as well as voltammograms of a solid solution of these two compounds and of a mechanical mixture. Again it is obvious that a distinction between a solid solution and a phase mixture is easy to make. For this system no quantification has been made.

### 5.3.2 The Solid Solution System AgCl-AgBr

Silver chloride and silver bromide form a continuous series of solid solutions. The reduction potential of the silver ions shifts as a function of the bromide content of the solid solutions that have been obtained by melting together AgCl and AgBr [B 14]. The dependence (Fig. 5.27) is nonlinear because of a considerable non-ideality of the mixtures.

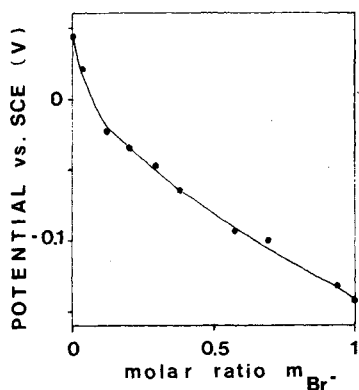


**Fig. 5.27.** Peak potential of differential pulse voltammograms obtained for reduction of solid solution of AgCl-AgBr as a function of the molar ratio of bromide. Electrolyte is  $0.1 \text{ mol L}^{-1}$  oxalic acid [B 14]

### 5.3.3 Solid Solutions of Metal Hexacyanometalates

Prussian blue is the archetype of a large group of metal hexacyanometalates and its electrochemistry has been extensively studied for the following reasons: (i) It can be easily deposited by electrochemical procedures on an electrode surface. (ii) It possesses two different kinds of electrochemically active iron ions, high-spin iron(III) that is nitrogen coordinated, and low-spin iron(II) that is carbon coordinated. (iii) The electrochemistry of both kinds of iron ions is reversible. (iv) The reduction is coupled with a reversible uptake of cations from solution and the oxidation is accompanied by the expulsion of these cations. The ion transfer is possible due to the zeolitic structure of Prussian blue in which ions can be housed in cavities and move along channels. (v) Prussian blue exhibits electrocatalytic properties. (vi) Prussian blue shows electrochromism. (vii) Prussian blue and its oxidized and reduced forms are highly insoluble in aqueous solu-

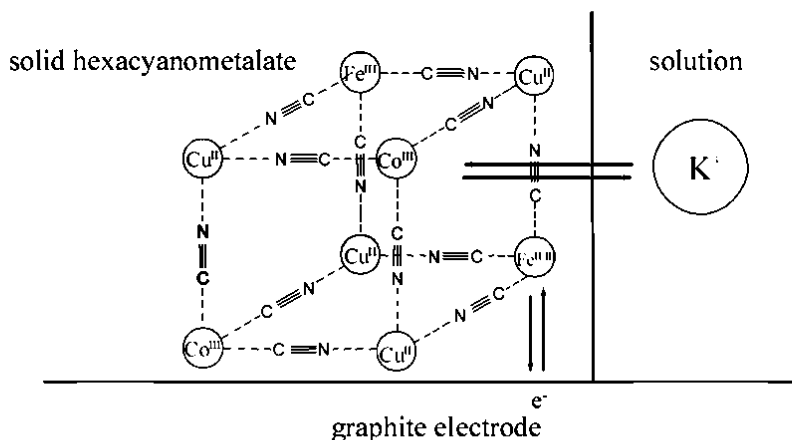


**Fig. 5.28.** Structure of a mixed copper-nickel hexacyanoferrate-hexacyanocobaltate and illustration of its insertion electrochemistry

tions. All these properties made it a favorable compound to be used for electrochemical studies. Since there exist dozens of other very similar metal hexacyanometalates, it was a temptation to study their electrochemistry as well. However, only a relatively small number of these compounds, e.g., copper, nickel, and cobalt hexacyanoferrate and some others, can be precipitated or synthesized on electrode surfaces. The majority of these compounds can be chemically synthesized, but a deposition on electrode surfaces was hampered until introduction of the technique of mechanical immobilization of microparticles.

Figure 5.28 depicts the structure that is representative for the vast majority of the hexacyanometalates. Three kinds of metal ions can be distinguished, and all three positions can be populated by mixtures of ions, provided that their radii fit to each other. Thus it is possible to populate the nitrogen-coordinated sites by Cu<sup>2+</sup> and Fe<sup>3+</sup>, by Cu<sup>2+</sup> and Ni<sup>2+</sup> etc., and the carbon-coordinated sites by Fe<sup>2+/3+</sup> and Co<sup>3+</sup>, etc. The cations in the interstitial cavities can be populated by different alkali metal and also by transition metal ions. Because the cations on this position are mobile and can be exchanged with those in an adjacent solution, such solid solutions do not possess much interest. However, they can be formed in the course of electrochemical reactions with mixed electrolyte solutions. Besides the substitutional solid solutions, metal hexacyanometalates can also form redox mixed solid solutions. Thus a Prussian blue, where one half of the high-spin iron is in the +3 and one half of it is in the +2 oxidation state is a solid solution provided that the redox centers are statistically distributed. This kind of solid solutions will be discussed later. Table 5.3 gives a schematic



**Table 5.3.** Basic types of solid solutions of metal hexacyanometalates

Type of solid solutions	Me'	Me''	Me'''
I	Different ions, e.g., K <sup>+</sup> and Na <sup>+</sup>		
II		Different ions, e.g., Cu <sup>2+</sup> and Fe <sup>3+</sup>	
III			Different ions, e.g., Fe <sup>2+</sup> and Co <sup>3+</sup>
IV	One kind of ions in different oxidation states, e.g., Fe <sup>2+</sup> and Fe <sup>3+</sup>		
V		One kind of ions in different oxidation states, e.g., Fe <sup>2+</sup> and Fe <sup>3+</sup>	
VI			One kind of ions in different oxidation states, e.g., Fe <sup>2+</sup> and Fe <sup>3+</sup>

[Me'] [Me'' -NC- Me''']; Me': interstitial metal ions; Me'': nitrogen-coordinated metal ions; Me''': carbon-coordinated metal ions

overview of the six basic types of solid solutions that can be formed in the case of metal hexacyanometalates. Pure solid solutions of all types are known with the exception of type IV. In many cases higher-order solid solutions are formed, i.e., mixed types of II and III, etc. Type IV seems to exist only as a combination with type I and II [B 111].

Solid solutions in which the nitrogen and carbon coordinated sites are mixed populated are very interesting systems as they give insight into the dependence of the electrochemical properties on the nature of metal ions. Voltammetric measurements on such solid solutions allow an extremely sensitive analysis of the composition of these solid solutions. Nickel(II) and iron(III) hexacyanoferrate(II) form a continuous series of solid solutions [B 49]. In this series, the electroactive high-spin iron(III) ions are continuously diluted by the electro-inactive nickel(II) ions, whereas the electroactive low-spin iron ions remain in place. Therefore, one observes that the peak currents of high-spin iron (III) decrease with increasing nickel content and the formal potential of the low-spin iron system shifts from the value of iron(III) hexacyanoferrate to the value of nickel hexacyanoferrate. This shift is almost linear, although, even in the ideal case, it must be slightly nonlinear because of the mixing entropy. The behavior of solid solutions of copper(II) and iron (III) hexacyanoferrate(II) is very similar [B 137]. Figure 5.29 shows voltammograms of some representative

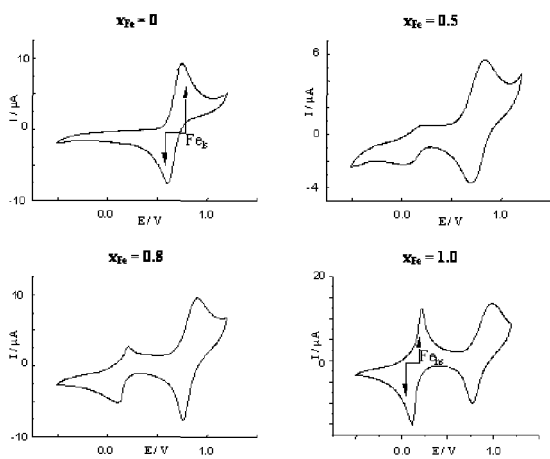


**Fig. 5.29.** Formal potential  $E_f = (E_{p, \text{anodic}} + E_{p, \text{cathodic}})/2$  of the low-spin iron system of the mixed iron-copper hexacyanoferrates as derived from the cyclic voltammograms (scan rate  $0.05 \text{ V s}^{-1}$ ) vs. molar ratio of high-spin iron  $x_{\text{Fe}}$  [B 137]

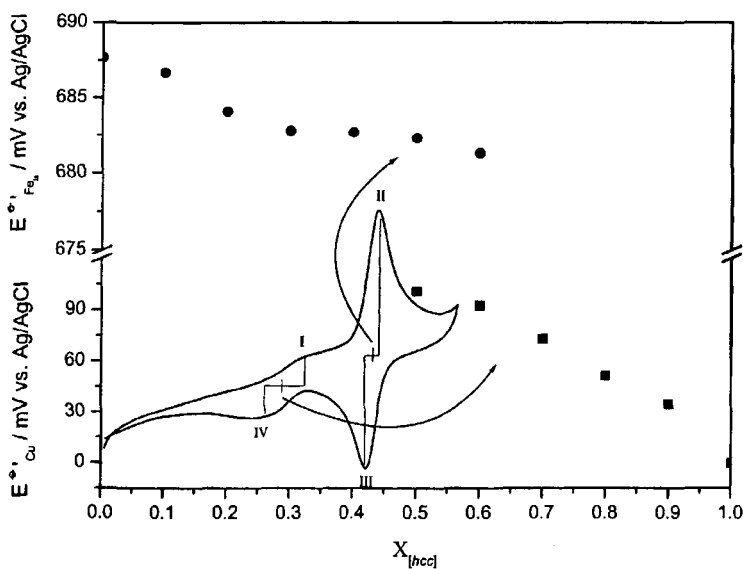


**Fig. 5.30.** Dependence of the formal potential of the Cu(I)/Cu(II) system (peaks I and IV) and of the hexacyanoferrate(II/III) system (peaks II and III) of  $\text{KCu}^{\text{II}}[\text{hcf}]_{1-x}[\text{hcc}]_x$  on the molar ratio of cobalt (hcf: hexacyanoferrate, hcc: hexacyanocobaltate). The inset shows the cyclic voltammogram of  $\text{KCu}^{\text{II}}[\text{hcf}]_{0.3}[\text{hcc}]_{0.7}$  in  $0.1 \text{ M KNO}_3$ , with a scan rate of  $50 \text{ mV s}^{-1}$  [B 247]

examples and Fig. 5.30 depicts the dependence of the formal potential of the low-spin iron system on high-spin iron(III) content in the solid solutions. In the case of cadmium(II) and iron(III) hexacyanoferrate(II) it was observed that solid solutions are formed, too [B 111]. This is rather surprising considering the large difference in ionic radii ( $r_{\text{Cd(II)}} = 109$  pm,  $r_{\text{Fe(III)}} = 78.5$  pm). The formation of solid solutions can be understood when both kinds of iron ions are in the +2 and +3 oxidation states, thus forming both substitutional and redox mixed solid solutions. For the case of metal hexacyanometalates with a mixed population of the carbon coordinated sites, a careful study has been performed with solid solutions of hexacyanoferrates(III)/hexacyanocobaltates(III) [B 247]. Figure 5.30 shows how sensitive the peak potentials of the  $\text{Cu}^{1+/2+}$  and the  $\text{Fe}^{2+/3+}$  systems of mixed copper hexacyanoferrate-hexacyanocobaltates are to the composition of the solid solutions. The iron system shows a relatively small shift because the diluting cobalt ions are rather far away from the iron ions. When the nitrogen coordinated metal ions are continuously substituted by foreign metal ions the effect is much stronger (see Fig. 5.29).

### 5.3.4 Solid Solutions of Oxides

The electrochemical dissolution of solid solutions of metal oxides provides access to information on their composition. Grygar et al. studied the follow-

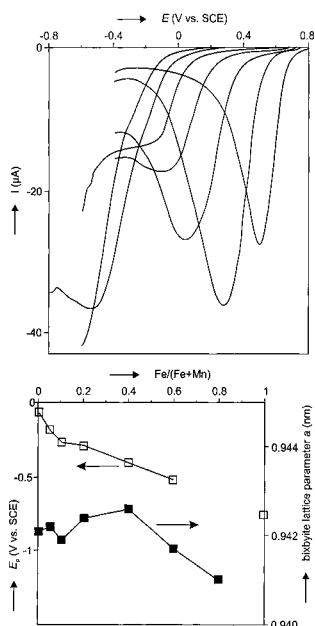


**Fig. 5.31.** Voltammograms (top) of reductive dissolution of  $\text{C-Mn}_2\text{O}_3\text{-}\alpha\text{-Fe}_2\text{O}_3$  solid solutions (electrolyte: acetate buffer at pH 4.4), and plot of peak potential versus molar ratio  $\text{Fe}/(\text{Fe}+\text{Mn})$ . Additionally are given the lattice parameters of the bixbyites [B 181]

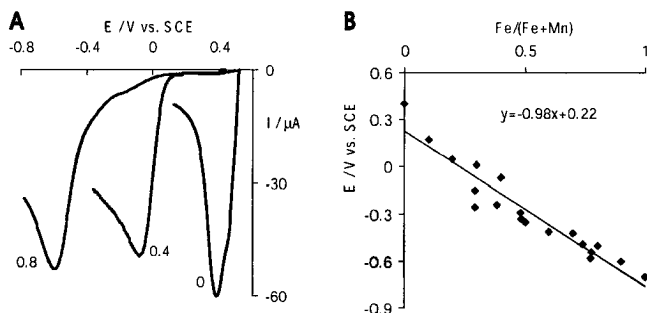


**Fig. 5.32.** **A** Linear-sweep voltammetric dissolution curves of several single-phase Li-Fe-Mn-O spinels (0.2 M acetate buffer: 1:1 acetate:acetic acid; scan rate  $1 \text{ mV s}^{-1}$ ). The numbers denote the value  $\text{Fe}/(\text{Fe}+\text{Mn})$ . **B** Linear-sweep voltammetric peak potentials of single-phase Li-Fe-Mn-O spinels plotted vs.  $\text{Fe}/(\text{Fe}+\text{Mn})$  [B 191]

ing series of solid solutions: (a)  $\text{C-Mn}_2\text{O}_3$  to  $\alpha\text{-Fe}_2\text{O}_3$ , (b)  $\text{LiMn}_2\text{O}_4$  to  $\text{LiFe}_5\text{O}_8$ , (c)  $\text{CaMnO}_3$  through  $\text{Ca}_3(\text{Mn,Fe})_3\text{O}_{8+x}$  to  $\text{CaFe}_2\text{O}_5$ , (d)  $\text{MnO}_x$  to  $\text{FeOOH}$  [B 181], Li-Mn-O and Li-Fe-Mn-O spinels [B 191, B 194, B 311]. When an oxide is electrochemically dissolved by reduction of its metal ions to a lower valence state, this is a highly irreversible process, and the voltammograms are expected to strongly reflect the kinetics of the overall process (see Chapter 5.7). Therefore, it is not expected that the peak potentials of the dissolution voltammograms directly and solely depend on the thermodynamics. More interesting is the observation that the peak potentials show a clear dependence on the composition which makes them useful for analytical applications (see Fig. 5.31 for the system  $\text{C-Mn}_2\text{O}_3$ - $\alpha\text{-Fe}_2\text{O}_3$ ). Figure 5.32 shows how the peak potential of reductive dissolution of a series of Li-Fe-Mn-O spinels shifts with the ratio  $\text{Fe}/(\text{Fe}+\text{Mn})$ .

## 5.4 Organometallics and Organic Compounds

Considering the importance of redox processes of organic and organometallic solids in catalysis, photovoltaics, analysis etc., the voltammetric study of these materials is a highly interesting and rewarding task. In contrast to many inorganic solids, most organic and organometallic compounds are soluble in a suitable organic solvent, making them easily available for solution-phase electrochemical experiments. However, as it will be shown in the following chapter, the solid state electrochemistry of these compounds can be very different than that of the dissolved species,

which makes solid-state electrochemical studies indispensable. The ease of the electrode preparation and the short time scale of the voltammetric experiments (Chapter 3) favor the voltammetry of immobilized microparticles for these studies. In the following sections, an overview is given showing phenomena that are observed when microcrystalline organic and organometallic compounds are attached to an electrode surface and studied voltammetrically. This overview cannot give a complete picture of the work that has been done in the past decades, but by means of examples it shall give an impression of how the voltammetry of immobilized microparticles can be utilized to get access to physical, chemical and mechanistic information on the studied compound.

### 5.4.1 Voltammetry of Organometallic Compounds

Based on their unique redox properties organometallic complexes of the transition metals are of invaluable importance for catalytic and electron mediating processes in nature and in technology. In particular, processes at solid organometallic compounds are not yet fully understood. In the following sections, we will present examples for the study of different kinds of organometallic complexes, their redox properties and reaction mechanisms by means of the voltammetry of immobilized microparticles.

Voltammetric studies of solid metal carbonyl compounds have been performed by Bond and coworkers [B 28, B 31, B 53, B 65, B 90, B 128]. After extensively investigating this class of compounds with respect to their solution electrochemical behavior (Fig. 5.33) [B 77], the authors have devoted their studies to the investigation of the solid compounds. Thus, they have shown that distinct electrochemical responses can be obtained from *cis*-Cr(CO)<sub>2</sub>(dpe)<sub>2</sub> and *trans*-Cr(CO)<sub>2</sub>(dpe)<sub>2</sub> (dpe = Ph<sub>2</sub>PCH<sub>2</sub>CH<sub>2</sub>PPh<sub>2</sub>), mechanically attached to a carbon electrode, and immersed in aqueous electrolytes. The redox processes are reported to be similar to those observed in organic solutions (see Fig. 5.34), the electron

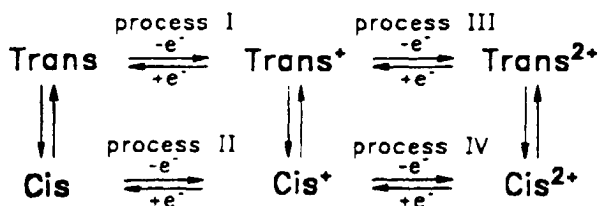
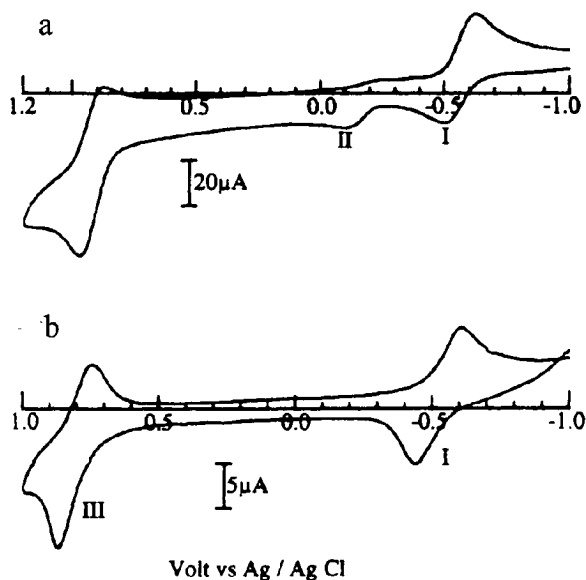


Fig. 5.33. Redox and isomerization reactions of the [Cr(CO)<sub>2</sub>(dpe)<sub>2</sub>]<sup>0/+2+</sup> system [B 31]



**Fig. 5.34.** Cyclic voltammograms obtained at 20 °C at **a** a platinum disk electrode in dichloromethane (0.1 M  $\text{Bu}_4\text{NClO}_4$ ) for a mixture of *cis*- $\text{Cr}(\text{CO})_2(\text{dpe})_2$  and *trans*- $[\text{Cr}(\text{CO})_2(\text{dpe})_2]^+$ . **b** in aqueous (0.1 M  $\text{NaClO}_4$ ) media for solid *trans*- $\text{Cr}(\text{CO})_2(\text{dpe})_2$  mechanically attached to a polished basal plane pyrolytic graphite electrode (scan rate  $50 \text{ mV s}^{-1}$ ) [B 28]

transfer through the crystal being supposedly made possible by electron hopping via self exchange and cross redox reactions with the rate being dependent on the state of the electrode-compound-solution interface and the surface charge [B 28].

The solid state isomerization of *cis*- $[\text{Cr}(\text{CO})_2(\text{dpe})_2]^+$  to *trans*- $[\text{Cr}(\text{CO})_2(\text{dpe})_2]^+$  (Fig. 5.35) has been found to be much slower than in solution, with the effect that the otherwise thermodynamically unstable *cis*- $[\text{Cr}(\text{CO})_2(\text{dpe})_2]^+$  could – for the first time – be spectroscopically identified (see also Chapter 5.5).

The oxidation of *trans*- $\text{Cr}(\text{CO})_2(\text{dpe})_2$  is accompanied by a slow uptake of anions from the aqueous electrolyte solution. By help of electrochemical quartz crystal measurements it has been shown that the anions are transferred into the solid phase in their unhydrated form [B 53]. An interesting phenomenon is that, although the expulsion of the anions during reduction is rapid, this process does not proceed through the entire microcrystal. Fewer anions are released during the reduction scan than were transferred into the solid during oxidation. The conclusion, drawn from the experi-

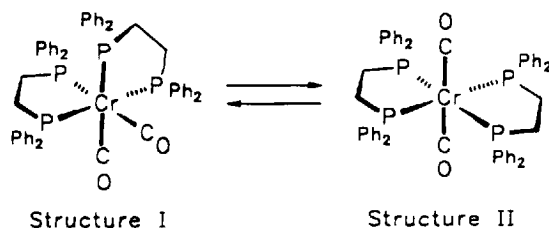


**Fig. 5.35.** Structures of *cis*-Cr(CO)<sub>2</sub>(dpe)<sub>2</sub> (I) and *trans*-Cr(CO)<sub>2</sub>(dpe)<sub>2</sub> (II) [B 31]

ments, is, that the reduction process predominately expels the anions that are situated relatively close to the solid|solution interface.

In solar energy conversion devices, separation of charge in semiconductors occurs upon excitation of an electron from a valence to a conduction band<sup>2</sup>, and this is translated into current flow in an external circuit. In voltammetric studies on solids, charge separation in the crystalline materials usually is generated via application of an external electrical field rather than photolytically. However, the voltammetry of microparticles can also be utilized to probe solid compounds for their photoelectrochemical properties. Thus, Eklund and Bond have examined carbonyl compounds with respect to potential photocatalyzed processes. Based on the photoactivity of *fac*-Mn(CO)<sub>3</sub>(η<sup>2</sup>-Ph<sub>2</sub>PCH<sub>2</sub>PPh<sub>2</sub>)Cl in organic solvents<sup>3</sup>, they have studied the behavior of the immobilized solid compound in an aqueous environment [B 128]. Two possible reaction pathways were subject of discussion: (i) Like in the case of semiconductor electrodes, charge separation occurs within the microcrystalline environment upon radiation, resulting in a current flow and concurrent charge balance through diffusion of ions into the crystalline material. (ii) The material attached to the electrode could undergo a transformation to form a material within the solid environment that can be oxidized or reduced at a different potential from that of the starting material and hence give rise to a photocatalytic reaction.

As it is depicted in Figs. 5.36a and b, the oxidation of immobilized microparticles of *fac*-Mn(CO)<sub>3</sub>(η<sup>2</sup>-Ph<sub>2</sub>PCH<sub>2</sub>PPh<sub>2</sub>)Cl is considerably enhanced upon radiation. Using a special photoelectrochemical cell (see Chapter 4.3, Fig. 4.24) this photoprocess has been studied with the help of the electrochemical quartz crystal microbalance, EQCM. It could be demonstrated

<sup>2</sup> Pleskov YV (1990) Solar Energy Conversion, A Photoelectrochemical Approach. Springer-Verlag, Berlin Heidelberg New York

<sup>3</sup> Compton RG, Barghout R, Eklund JC, Fisher AC, Bond AM, Colton R (1993) J Phys Chem 97: 1661-1664

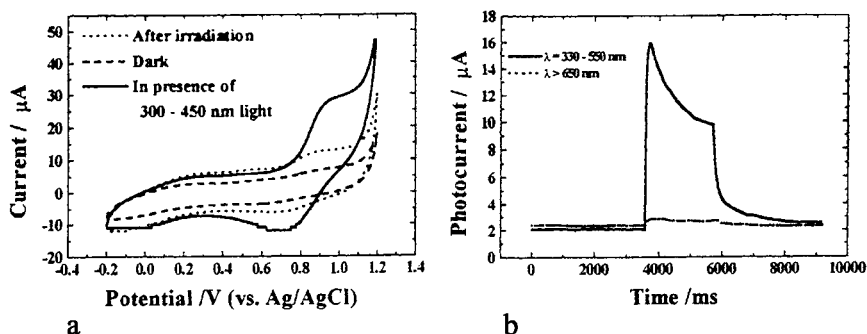


**Fig. 5.36.** **a** Cyclic voltammograms obtained for the oxidation of  $fac\text{-Mn}(\text{CO})_3(\eta^2\text{-Ph}_2\text{PCH}_2\text{PPh}_2)\text{Cl}$  attached to a pyrolytic graphite electrode and placed in contact with 0.1 M NaCl electrolyte (scan rate  $100\text{ mV s}^{-1}$ , irradiation intensity  $10\text{ mW cm}^{-2}$ ). **b** Phototransient response obtained for the oxidation of  $fac\text{-Mn}(\text{CO})_3(\eta^2\text{-Ph}_2\text{PCH}_2\text{PPh}_2)\text{Cl}$  attached to a graphite electrode and placed in contact with 0.1 M  $\text{NaClO}_4$  [B 128]

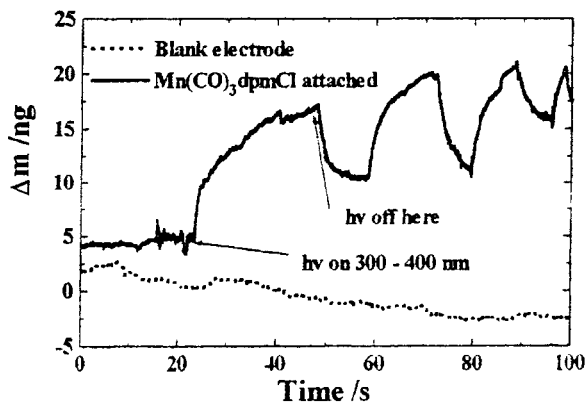


**Fig. 5.37.** EQCM data obtained when solid  $fac\text{-Mn}(\text{CO})_3(\eta^2\text{-Ph}_2\text{PCH}_2\text{PPh}_2)\text{Cl}$ , attached to a gold-coated quartz crystal and placed in contact with aqueous 0.1 M NaCl electrolyte, is irradiated periodically with 300–450 nm light [B 128]

that the photocatalyzed processes at the immobilized  $fac\text{-Mn}(\text{CO})_3(\eta^2\text{-Ph}_2\text{PCH}_2\text{PPh}_2)\text{Cl}$  particles is accompanied by an anion uptake from the surrounding electrolyte solution (Fig. 5.37)

From the combination of voltammetric, EQCM, ex situ electron spin resonance spectroscopy and chemical doping experiments two possible reaction pathways have been proposed: (i) formation of a charge-transfer excited state of the Mn(I) species, which is then rapidly oxidized to a  $fac\text{-Mn}(\text{II})$  cationic species, that can then isomerize to the  $mer^+$  form. (ii)



photoisomerization of *fac*- $\text{Mn}(\text{CO})_3(\eta^2\text{-Ph}_2\text{PCH}_2\text{PPh}_2)\text{Cl}$  to the *mer* form, which is then directly photooxidized to the *mer*<sup>+</sup> cationic form.

Another highly interesting group of organometallic compounds to be studied by voltammetry is the class of metallocenes and their derivatives. The simplest and most studied member of this class is ferrocene (Fc). Ferrocene itself is sparingly soluble in water, its oxidation product, however, is very soluble. This, together with the well defined voltammetry, based on the redox couple  $\text{Fc} / \text{Fc}^+$ , is an ideal basis for the study of the mechanisms of the electrochemistry of immobilized microparticles. In one of the first studies, the voltammetry of ferrocene was studied and compared to other sparingly soluble metal complexes and salts [B 14]. In each case, the electrochemical perturbation generates at least one solution soluble species. For this kind of process a reaction scheme, Fig. 5.38, has been proposed, showing how the electrochemistry is interfered by dissolution and adsorption processes of the involved redox species.

Being much more hydrophobic, decamethylferrocene, dmfc, exhibits a considerably lower solubility in water. This compound can be considered virtually insoluble, and even its oxidized form,  $\text{dmfc}^+$ , is insoluble in water. As for its relative, ferrocene, the voltammetry of the decamethyl compound is based on a one electron oxidation step (Reaction VI).

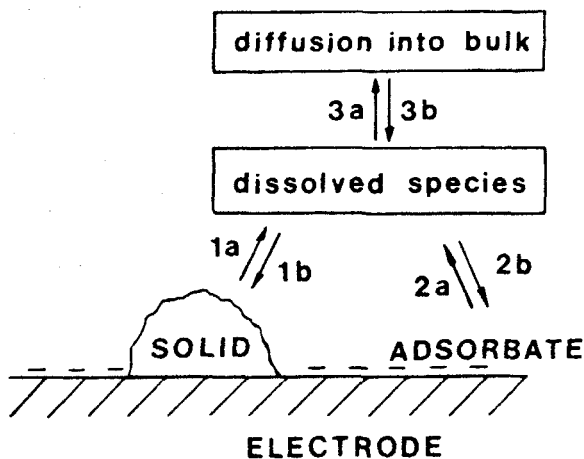
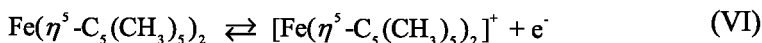
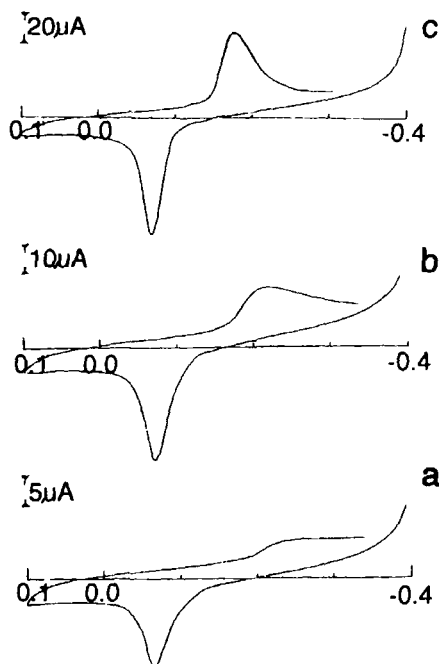


Fig. 5.38. Reaction scheme applying for the electrochemistry of ferrocene and other sparingly soluble solid compounds [B 14]



**Fig. 5.39.** Cyclic voltammograms obtained at a scan rate of  $10 \text{ mV s}^{-1}$  for the oxidation of microcrystalline decamethylferrocene attached mechanically to a basal plane pyrolytic graphite electrode and placed in aqueous medium ( $0.1 \text{ M KPF}_6$ ) at temperatures of **a**  $22 \text{ }^\circ\text{C}$ , **b**  $52 \text{ }^\circ\text{C}$  and **c**  $82 \text{ }^\circ\text{C}$  [B 29]

For charge compensation, the oxidation is accompanied by the uptake of anions ( $X^-$ , Reaction VII) from the electrolyte solution.



The nature of the anion not only has an effect on the shape of the voltammetric signal, it also influences the redox potential of the oxidation process. Thus, the presence of hydrophobic ions in the electrolyte solution leads to an oxidation at lower potentials, whereas the presence of hydrophilic ions, like fluoride, shifts the redox potential of Reaction VII towards more positive potentials. It can be assumed that the Gibbs energy of transfer of the anions from the aqueous into the organic phase is responsible for this phenomenon (see Chapter 6 for more detail). In contrast to the oxidation of ferrocene Reaction VII represents a solid-to-solid transformation. As depicted in Fig. 5.39, it is a kinetically controlled process, and its rate strongly depends on temperature. The increase of the peak currents with temperature is much more pronounced than in solution-phase voltammetry.

The voltammetric study of mechanically immobilized organic or organometallic solids is of considerable importance for compounds that are

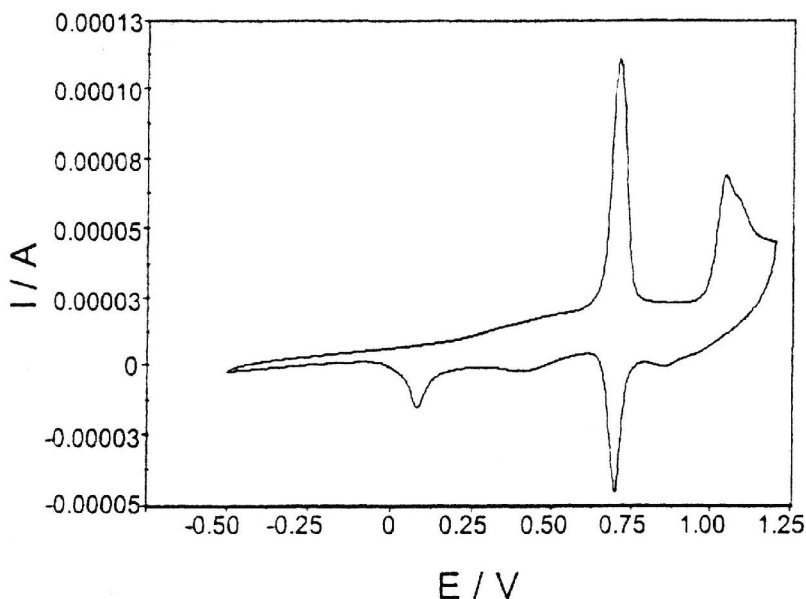
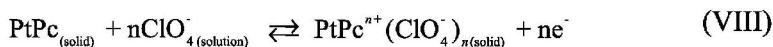


**Fig. 5.40.** Cyclic voltammogram at  $5 \text{ mV s}^{-1}$  for platinum phthalocyanine microcrystals deposited onto a glassy carbon electrode in acetonitrile ( $0.1 \text{ M N}(\text{Bu})_4\text{ClO}_4$ ) [B 138]

insoluble in water and in non-aqueous solvents, as it is the case for many metal phthalocyanines. For example, in a series of studies Kucernak and coworkers have thoroughly investigated the electrochemical behavior of platinum phthalocyanine [B138, B 167, B 185, B 190] – here, the voltammetry of microcrystals offers the simplest and yet a reproducible way of depositing the target compound onto an electrode surface. Well-defined voltammetric responses are obtained for microcrystals in aqueous and in non-aqueous media (Fig. 5.40). The authors suppose that the oxidation, as for many metal phthalocyanine complexes, takes place reversibly on the phthalocyanine ring, and is accompanied by the uptake of anions from the electrolyte solution according to Reaction VIII:



The voltammetry of microparticles is well suitable as a tool to the screening of compounds for desired properties like their electrocatalytic activity towards the oxidation or reduction of a target compound, or for their suitability as electron mediators in biochemical sensors. An example for such a study is the comparative investigation of the electrochemical properties of osmium bipyridyl complexes [B 251]. In contrast to many

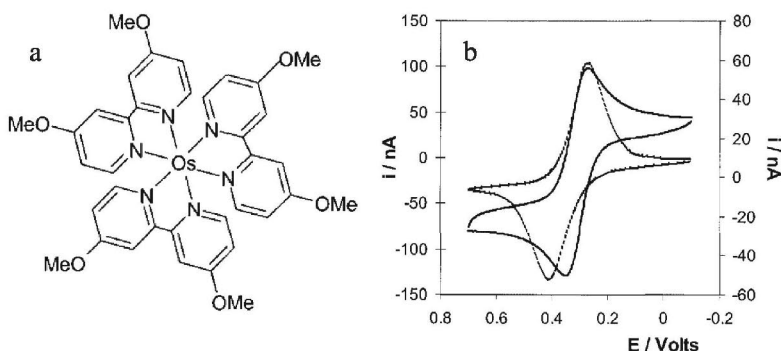


**Fig. 5.41.** **a** Structure of osmium trisdimethoxybipyridyl,  $[\text{Os}(\text{OMe-bpy})_3](\text{PF}_6)_2$  (OMe = 4,4'-dimethoxy; bpy = 2,2'-bipyridyl), **b** Cyclic voltammograms for a 0.8 mM solution of  $[\text{Os}(\text{OMe-bpy})_3]^{2+}$  dissolved in acetonitrile (solid line) and as a solid deposit (dashed line). In both cases, the supporting electrolyte is 0.1 M  $\text{HClO}_4$ , the working electrode is a 25  $\mu\text{m}$  platinum electrode, and the scan rate is 0.1  $\text{V s}^{-1}$  [B 251]

other solid state electrochemical reactions the voltammetry of immobilized osmium trisdimethoxybipyridyl,  $[\text{Os}(\text{OMe-bpy})_3](\text{PF}_6)_2$ , is comparable to its solution-phase voltammetry (see Fig. 5.41). The almost ideally reversible redox switching behavior in the solid state favors this osmium complex as an electron mediator in biosensors. Similar observations have also been made for deposited microcrystals of other osmium bipyridil complexes [B 134, B 155, B 252]; in one case even unusually fast electron and anion transport processes have been observed [B 139].

The extent with which an electrochemical reaction proceeds from the triple phase junction solid | electrode | electrolyte solution into the bulk of an organic or organometallic microcrystal depends on many factors. First, the structure of the solid has to be “electrochemically open”, i.e., it should enable a comparably fast electron hopping between the molecules within the crystal and the diffusion of charge-balancing ions into the crystal. This condition is fulfilled for many complexes, as, for instance, for the above-described metallocenes and chromium carbonyl compounds. In these cases, a fast and exhaustive oxidation or reduction of the deposited solid can be achieved. In other cases, however, as in the case of highly charged complexes like  $[\text{Co}(\text{mtas})_2]^{n+}$  (mtas = bis(2-(dimethylarsino)phenyl)-methylarsine) the voltammetric reaction remains confined to the surface of the microcrystal. Here, the high charge of the complex ( $n = 2$  to 3) leads to ion pair formation with the anions that are transferred into the crystal upon oxidation and thus to an increasing resistivity towards the ion migration within the crystal [B 45].

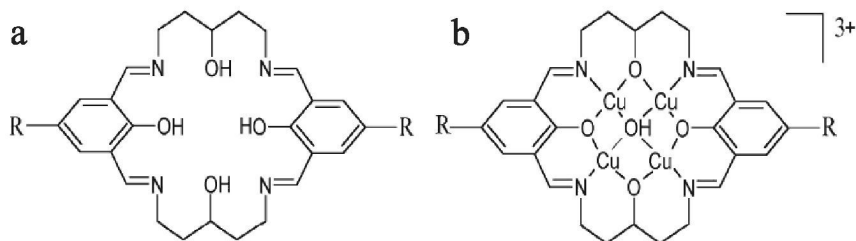


**Fig. 5.42.** Structures of **a** the expanded "Robinson-type" macrocyclic ligand  $H_4L$ , **b** the tetranuclear complex  $[Cu_4(L)(OH)]^{3+}$  [B 260]

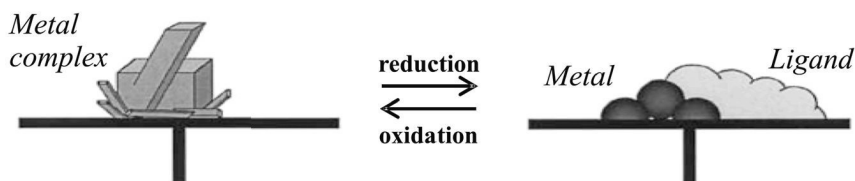


**Fig. 5.43.** Schematic representation of the reversible solid state conversion of metal complex to metal deposit and free ligand [B 260]

As a peculiar phenomenon it has been reported that the voltammetric conversion of immobilized organometallic compounds can lead to a reversible extraction of metals from their complexes. Thus, Marken et al. reported on electrochemically driven reversible solid state metal exchange processes in polynuclear copper complexes [B 260]. These complexes (see the example of the tetranuclear compound, Fig. 5.42), consisting of a "Robinson type" ligand scaffold, can accommodate up to four copper ions that are bridged to each other, as shown in Fig. 5.42. Upon reduction of the immobilized complexes, the copper ions stepwise leave the complex and are reduced at the electrode surface to form a copper deposit. In the first step, two copper ions are extracted from the complex, leaving the di-copper complex behind. In the second step, the water-insoluble ligand is formed, which remains at the electrode surface (see the schematic drawing in Fig. 5.43). Upon oxidation, the formed free copper ions are re-incorporated into the ligand scaffold.

Bond et al. [B 294, B 306, B 308] have demonstrated that the response of microparticles of several organometallic compounds using ionic liquids as electrolyte is indistinguishable from that of the dissolved species. A rapid dissolution of the solids upon electrochemical oxidation of the neutral compounds is held responsible for this observation.

Further, it has been found that small concentrations of organic solvents in the electrolyte solution can induce a catalytic action in the insertion-electrochemical reactions of microparticles [B 295], caused a co-insertion and lattice widening.

### 5.4.2 Voltammetry of Organic Compounds

The voltammetry of immobilized microparticles can be exploited for very different purposes, be it to address mechanistic questions of electrochemical or chemical reactions, to access physical or chemical properties of a target compound, to screen compounds for a desired electrochemical property or behavior (catalysis), or to yield qualitative or quantitative information on a compound. The latter, the qualitative and quantitative determination of organic compounds is nowadays generally a domain for chromatographic and spectroscopic techniques. However, voltammetry, and especially the voltammetry of immobilized microparticles, can be highly useful as a tool for a quick and cheap analysis, without the need of any sample extraction steps. Thus, for example, Komorsky-Lovrić et al. have used the voltammetry of immobilized microparticles for the detection of trace amounts of cocaine powder on contaminated paper money / bills (see Fig. 5.44). Utilizing square wave voltammetry, the authors determined the detection limit for cocaine to be  $0.3 \mu\text{g cm}^{-2}$  surface concentration.

Although due to the limitations caused by the mechanical immobiliza-

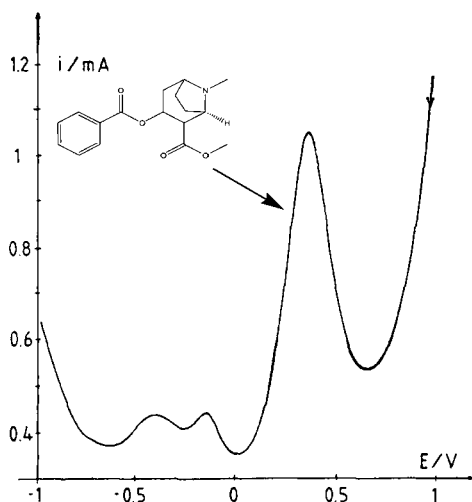
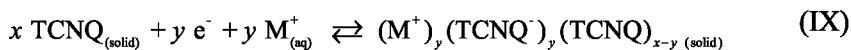


**Fig. 5.44.** Square-wave voltammogram of traces of cocaine powder which was mechanically transferred to a paraffin-impregnated graphite electrode from the surface of contaminated paper money (bills). The frequency was 250 Hz, amplitude 100 mV, step increment 2 mV, starting potential 1V [B 109]

tion of a sample onto an electrode surface the analytical information on a target compound is primarily of qualitative nature, it has been shown for the screening of pesticides on the surface of cucumber and lettuce that by following identical electrode preparation procedures also semiquantitative information can be obtained [B 59]. This fast screening provides information on the presence or absence of a certain pesticide and can thus save labor and costs for unnecessary analysis by, e.g., chromatography.

So far, more emphasis than on the analytical use has been placed on the application of the voltammetry of microparticles for studying the redox properties of organic solids and the mechanisms of their electrochemical reactions. These reactions can proceed under dissolution if the reaction product is soluble or as a solid-to-solid transformation if the product is insoluble in the electrolyte environment. Depending on the properties of the organic microcrystals the latter reaction type can either be purely surface confined, or even confined to the three-phase junction, or it can lead to an exhaustive conversion of the microcrystals. For a given compound, the extent of the reaction depends on a number of properties. First of all, solid-to-solid conversions generally require a charge compensating transfer of ions between the solid and the adjacent electrolyte solution to take place. In order to allow ions to migrate through the molecular solid, the structure of the solid must be "open", i.e., it must provide space to accommodate ions without binding them too strongly (as ion pairs). An example is the reduction of 7,7,8,8-tetracyanoquinodimethane, TCNQ, the reduction of which is accompanied by the uptake of cations from the surrounding electrolyte solution, into its layered structure, Fig. 5.45, following reaction IX.



Of course, the electron transfer within the crystal, in most cases via electron hopping, must be assured, too.

Very often, the structure of the end product of an electrochemically induced solid-to-solid transformation is strongly deviating from that of the starting material, as shown in Fig. 5.45 for the example of TCNQ and its reduction product [B 101], and the structural changes depend on the nature of the intercalating cation. The growing divergence between the oxidized and the reduced form leads to an immiscibility between starting and end product. The effect on the voltammetric response can be seen in Fig. 5.46. Clearly visible is the unusually large separation between the reduction peak and the oxidation peak. This extremely high peak-to-peak separation is caused by a large overpotential of reduction and oxidation, which the authors interpret in terms of a nucleation and growth mechanism (for the thermodynamic interpretation see Chapter 5.11), arising from the fact that

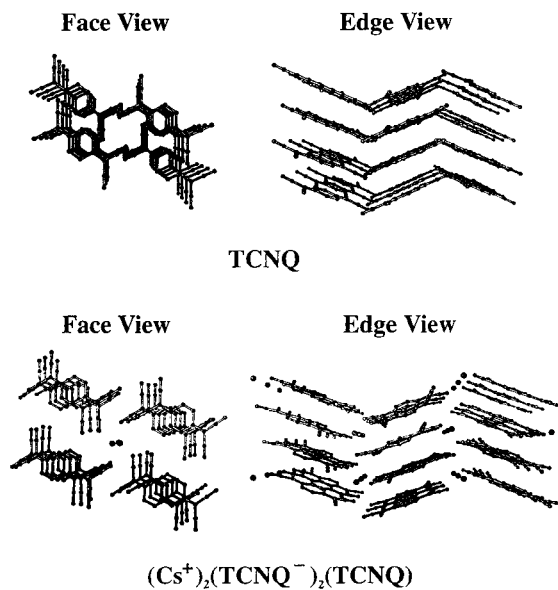


**Fig. 5.45.** Perspective view of the skeletal structure of TCNQ (upper structure) and  $(\text{Cs}^+)_2(\text{TCNQ}^-)_2(\text{TCNQ})$  (below). Hydrogen atoms are omitted for clarity [B 101]

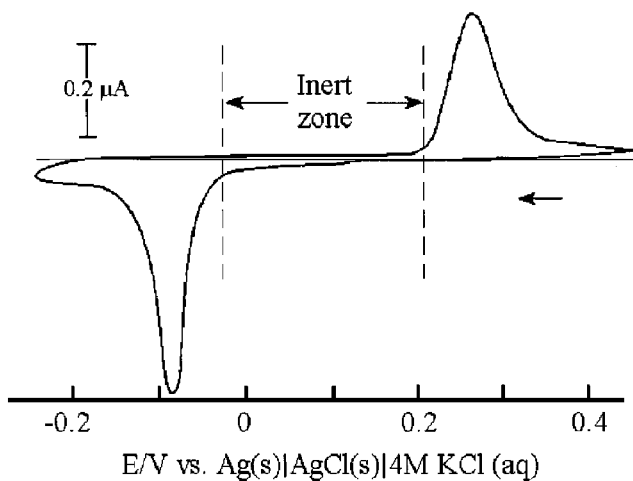


**Fig. 5.46.** Schematic diagram of the voltammetric response for the surface-attached  $\text{TCNQ}^{0/-}$  system when interconversion of TCNQ and the reduced salt occurs by a nucleation-growth mechanism [B 56]



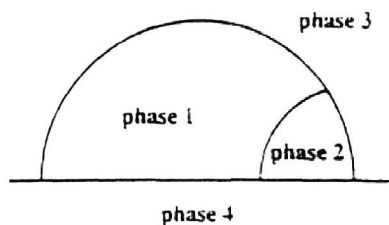


**Fig. 5.47.** Schematic representation of nucleation in the four-phase system electrode (phase 4)/solids (phase 1 and 2) / solution (phase 3) [B 56]

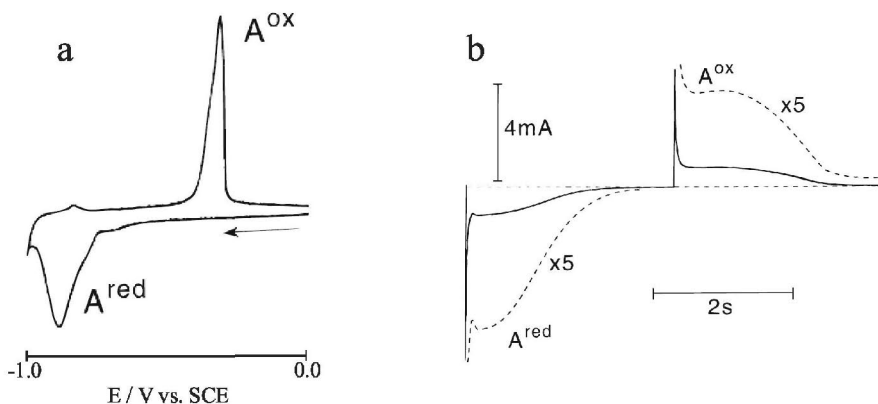


**Fig. 5.48.** **a** Cyclic voltammograms obtained for the reduction and reoxidation of solid  $C_{60}$  mechanically attached to a basal plane pyrolytic graphite electrode immersed in acetonitrile / 0.1 M  $NBu_4PF_6$ . scan rate  $0.02 \text{ V s}^{-1}$ ,  $J = 20 \pm 2 \text{ }^\circ\text{C}$  **b** Chronoamperogram for the reduction and reoxidation of solid  $C_{60}$  mechanically attached to a basal plane pyrolytic graphite electrode and immersed in acetonitrile / 0.1 M  $NBu_4PF_6$ . Potential steps are from 0 to  $-0.85 \text{ V}$  for reduction and  $-0.85 \text{ V}$  to  $-0.205 \text{ V}$  vs. SCE for reoxidation after 10 initial potential cycles between 0 and  $-1.0 \text{ V}$  vs. SCE [B 119]

the electrochemical solid-to-solid conversion does not take place via the formation of a continuous redox solid solution phase, but requires the formation of a separate product phase (as schematically drawn in Fig. 5.47) [B 56, B 296]. The formation of this phase, from the kinetic point of view, obeys the laws of nucleation and growth.

The described effect of the immiscibility of the corresponding redox pairs does not seem to be an exotic behavior. It has been described for other systems too, as for instance for the oxidation of microcrystalline tetrathiafulvalene, TTF [B 54, B 255], which takes place coupled with the intercalation of anions into the TTF lattice.

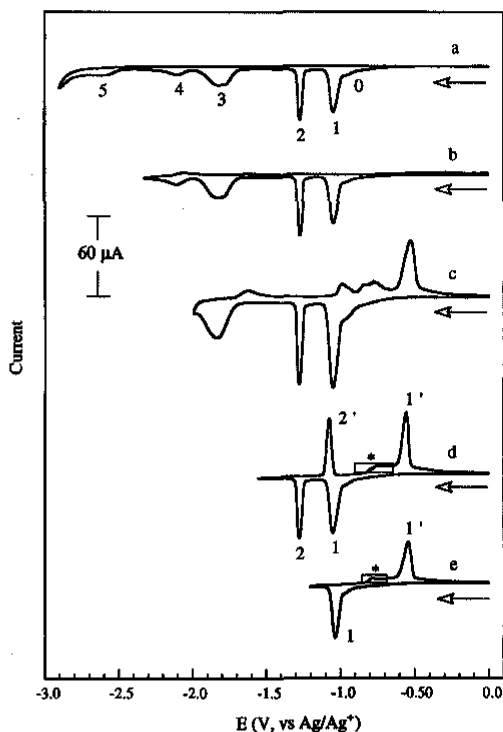


**Fig. 5.49.** Cyclic voltammograms obtained over different potential ranges at a scan rate of  $0.100 \text{ V s}^{-1}$  for reduction of microcrystalline  $(\text{C}_{60})_{1.5}(\text{CTV})$  complex adhered to a 0.10-cm diameter glassy carbon electrode placed in  $\text{CH}_3\text{CN}$  ( $0.10 \text{ mol L}^{-1} \text{ Bu}_4\text{NClO}_4$ ). **a** 0.0 to  $-3.0 \text{ V}$ ; **b** 0 to  $-2.35 \text{ V}$ ; **c** 0 to  $-2 \text{ V}$ ; **d** 0 to  $-1.55 \text{ V}$  and **e** 0 V to  $-1.2 \text{ V}$  vs  $\text{Ag}/\text{Ag}^+$  [B 170]

Evidence for nucleation and growth has also been found for the voltammetric reduction and re-oxidation of the Buckminster fullerene  $\text{C}_{60}$ . The large peak-to-peak separation (Fig. 5.48a) and the typical chronoamperometric curves, showing a “rising” current transient rather than a monotonic decay (Fig. 5.48b) are characteristic and support the proposed reaction mechanism [B 119].

As shown in Fig. 5.49, fullerenes exhibit a well-defined voltammetry. Depending on the applied reduction potential, they undergo a number of reduction steps, as shown in Fig. 5.49 for the example of the  $(\text{C}_{60})_{1.5}(\text{CTV})$  complex (CTV = cyclotrimeratrylene). It can be derived from the voltammetric curves e – a (Fig. 5.49), that the products of the first two reduction steps are still insoluble in the electrolyte solution; the re-oxidation of the compound is thus possible. However, potential sweeps towards more negative potentials lead to the formation of soluble reaction products, visible in the irreversibility of the subsequent reduction.

Organic chemistry, and thus also organic electrochemistry, can generally be much more complex than in the above examples. Thus, the electrochemical oxidation or reduction of an organic compound can be followed

by a chemical reaction of the reaction products. These EC reactions are a research field on their own, and as demonstrated for the example of electrochemically driven polymerization reactions at the mechanically immobilized microparticles [B 211, B 218, B 272] the voltammetry of microparticles is most suited to interrogate them.

The surface identification of carbon particles with organic compounds has been shown to provide interesting new materials for the solution analysis of sulfide ions and pH [B 305, B 309, B 310] when these particles are immobilized on electrode surfaces. Similar results can be achieved by co-immobilization of carbon nanotubes and pH-sensing compounds like 9,10-phenanthraquinone [B 315].

### 5.4.3 Overview of Studied Compounds

#### **Organometallics and Metal Complexes with Organic Ligands**

Compound	Reference (B)
Tris(2,2'-bipyridine)ruthenium(II) hexafluorophosphate	134
<i>cis</i> -Ru <sup>(II)</sup> (dcbpy) <sub>2</sub> (NCS) <sub>2</sub> (dcbpy = 2,2'-bipyridine-4,4'-dicarboxyl acid)	102
[{M(bipy) <sub>2</sub> } {M'(bpy) <sub>2</sub> } (μ-L)](PF <sub>6</sub> ) <sub>2</sub> (M, M' = Ru, Os; L = 1,4-Dihydroxy-2,5-bis(pyrazol-1-yl)benzene	139
Osmium bis(bipyridyl)tetrazine chloride, [Os(bpy) <sub>2</sub> -4-tet-Cl](ClO <sub>4</sub> ) tet = 3,6-bis(4-pyridyl)-1,2,4,5-tetrazine	155
Osmium tris dimethoxy bipyridyl, [Os(OMe-bpy) <sub>3</sub> ](PF <sub>6</sub> ) <sub>2</sub> OMe = 4,4'-dimethoxy; bpy = 2,2'-bipyridyl	251
Triazole bridged osmium dimer, [Os(bpy) <sub>2</sub> Cl 4-bpt Os(bpy) <sub>2</sub> Cl]PF <sub>6</sub>	252
Ruthenium(III) dithiocarbamate	100
Ruthenium(III) diphenyldithiocarbamate	98
[Ru(bpy) <sub>3</sub> ][PF <sub>6</sub> ] <sub>2</sub>	134
[Ru(bpy) <sub>3</sub> ] <sub>3</sub> [P <sub>2</sub> W <sub>18</sub> O <sub>62</sub> ]	303
<i>fac</i> -Mn(CO) <sub>3</sub> (η <sup>2</sup> -Ph <sub>2</sub> PCH <sub>2</sub> PPh <sub>2</sub> )Cl	128
<i>cis</i> -[Mn(CN)(CO) <sub>2</sub> {P(OPh) <sub>3</sub> }(dppm)] (dppm = Ph <sub>2</sub> PCH <sub>2</sub> PPh <sub>2</sub> )	294
<i>cis</i> -[W(CO) <sub>2</sub> (dppe)] (dppe = Ph <sub>2</sub> P(CH <sub>2</sub> ) <sub>2</sub> PPh <sub>2</sub> )	294
<i>cis</i> - <i>trans</i> -[Re(CO) <sub>2</sub> (P-P) <sub>2</sub> ] <sup>+</sup> and <i>trans</i> -[Re(CO)(P-P) <sub>2</sub> ]X P-P = diphosphine ligand, X = Cl, Br	90
<i>trans</i> -Re(Br)(CO)X (X = (dppe) <sub>2</sub> , (dppz)(dppm), (dppe)(dppm) (dppe = Ph <sub>2</sub> P(CH <sub>2</sub> ) <sub>2</sub> PPh <sub>2</sub> , dppm = Ph <sub>2</sub> PCH <sub>2</sub> PPh <sub>2</sub> , dppz = (Ph <sub>2</sub> P) <sub>2</sub> C <sub>6</sub> H <sub>4</sub> )	295
<i>cis</i> , <i>trans</i> -Cr(CO) <sub>2</sub> (dppe) <sub>2</sub> (dppe = Ph <sub>2</sub> P(CH <sub>2</sub> ) <sub>2</sub> PPh <sub>2</sub> )	28, 31, 53, 295
[(C <sub>4</sub> H <sub>9</sub> ) <sub>4</sub> N][Cr(CO) <sub>5</sub> I]	65
Fe(η <sup>5</sup> -C <sub>5</sub> Ph <sub>5</sub> )(η <sup>6</sup> -C <sub>6</sub> H <sub>5</sub> )C <sub>5</sub> Ph <sub>4</sub>	106
1,3,5-tris(3-((ferrocenylmethyl)amino)pyridiniumyl)-2,4,6-triethylbenzene Hexafluorophosphate	306
Bis(η <sup>5</sup> -pentaphenyl-cyclopentadienyl)iron(II)-iron(III)	129

[Co(mtas) <sub>2</sub> ](X) <sub>n</sub> (mtas = bis(2-(dimethylarsino)phenyl)-methylarsine; X = BF <sub>4</sub> <sup>-</sup> , n = 3; X = ClO <sub>4</sub> <sup>-</sup> , n = 2, 3; X = BPh <sub>4</sub> <sup>-</sup> , n = 2)	45
Co and Mn phthalocyanines	43, 63
Pt phthalocyanine	138, 167, 185, 190
Polynuclear copper complexes	260
[Cu <sub>2</sub> (H <sub>3</sub> L)(OH)][BF <sub>4</sub> ] <sub>2</sub> , [Cu <sub>4</sub> L(OH)][NO <sub>3</sub> ] <sub>3</sub> L = O <sub>4</sub> N <sub>4</sub>	
Copper(II) 5,10,15,20-tetraphenyl-21H,23H-porphyrin (H <sub>2</sub> TPP)	135, 159, 178
Azurin	297
Decamethylferrocene	29
Ferrocene / cobaltocene	14, 308
Decaphenylferrocene	295

### Organics

Compound	Reference (B)
Azobenzene	68
Carbazole / polycarbazole	272
Cocaine	109
2,2-diphenyl-1-picrylhydrazyl (DPPH)	114
Diphenylamine (B 197 (droplet))	211, 218
Fullerenes, C <sub>60</sub>	119, 154, 172, 263
C <sub>60</sub> ⊂ L <sub>2</sub> (L = <i>p</i> -benzyl-calix[5]arene) <sub>2</sub> • 8toluene	156
HQBpt (HBpt = 3,5bis(pyridine-2-yl)-1,2,4-triazole; 1,4-hydroquinone H <sub>2</sub> Q)	179
Indigo	72, 126
Lead and mercury dithiocarbamate	13, 14
<i>N,N'</i> -bis(4-Cyanophenyl)-3,4,9,10-perylene-bis(dicarboximide) and	313
<i>N,N'</i> -bis(4-Cyanophe-nyl)-1,4,5,8-naphthalenediimide	
Quinhydrone, acridine	126
Tetraphenylviologen	295
TCNQ	56, 101, 124, 255, 296, 299
1,3,5-Tris[4-[(3-methylphenyl)phenylamino]phenyl]benzene	316
TTF	54, 196, 267
Organic dyes and pigments	302

## 5.5 Electrochemically Initiated Chemical Reactions of Solid Particles

### 5.5.1 Electrochemically Initiated Isomerizations

Similar to the scenario of electrochemical reactions of species in solution, solid compounds can also undergo chemical follow-up reactions. Such systems can be conveniently studied using particles of the solid compound immobilized on an electrode surface. This is very interesting because a comparison can be made between the behavior of a species dissolved and in the solid state. As a first example we shall discuss an isomerization that was well known to occur when iron(II) hexacyanochromate(III),  $\text{KFe}[\text{Cr}(\text{CN})_6]$ , is heated to temperatures around  $100\text{ }^\circ\text{C}$ . Under this condition the cyanide ions turn around to form chromium(III) hexacyanoferrate(II),  $\text{KCr}[\text{Fe}(\text{CN})_6]$ . This isomerization takes place at room temperature when microparticles of  $\text{KFe}[\text{Cr}(\text{CN})_6]$  are immobilized on a graphite electrode and are subjected to potential cycling in a range where the hexa-

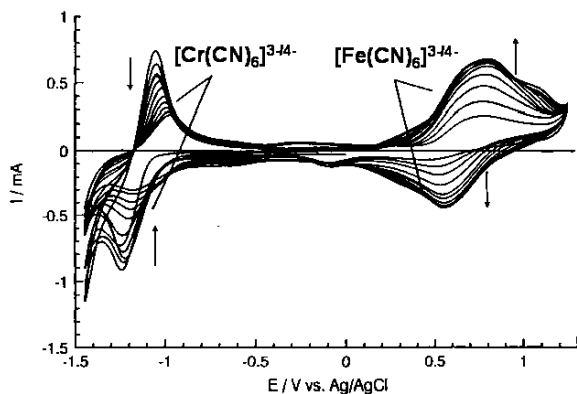


**Fig. 5.50.** Subsequent cyclic voltammograms of iron(II) hexacyanochromate(III) mechanically immobilized on a PIGE. The isomerization to chromium(III) hexacyanoferrate(II) can be deduced from the simultaneous decrease of the hexacyanochromate system accompanied by the growing of the hexacyanoferrate system. Electrolyte:  $0.1\text{ M KCl}$ ; scan rate:  $0.1\text{ V s}^{-1}$  [B 33]

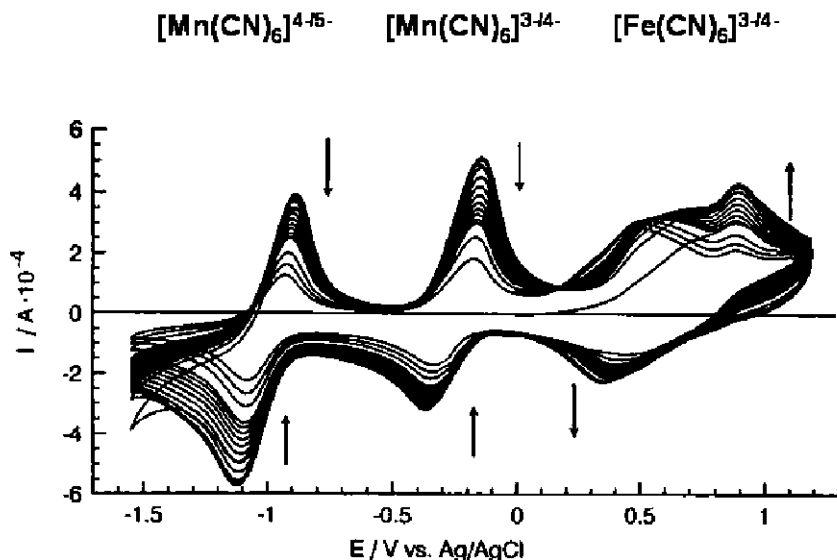


**Fig. 5.51.** Subsequent cyclic voltammograms of iron(II) hexacyanomanganate(III) (*Fe hcm*) mechanically immobilized on a PIGE. The isomerization of *Fe hcm* to manganese(II) hexacyanoferrate (*Mn hcm*) can be deduced from the simultaneous decrease of the hexacyanomanganate signals accompanied by the growing of the hexacyanoferrate signal. Electrolyte 0.1 M KCl; scanrate  $0.1 \text{ V s}^{-1}$  [B 103]

cyanochromate unit is switched between the chromium(III) and chromium(II) states [B 33]. Figure 5.50 depicts the cyclic voltammograms and it is obvious how the hexacyanochromate system decreases simultaneous to the growing of the hexacyanoferrate system. The rate constant of the isomerization was  $4 \times 10^{-9} \text{ mol s}^{-1}$ . The isomerization can be easily understood considering the general inertness of chromium(III) ions against substitution and, on the other hand, a high lability of the ligands of chromium(II) ions. Thus the cyanide ions are labilized in the hexacyanochromate(II) and allowed to turn around, i.e., coordinating on the carbon end to the iron ions. A similar isomerization was observed in the case of iron(II) hexacyanomanganate(III), although in this case the compound could not be synthesized without some amount of the compound having already isomerized, i.e., with some amount of manganese(II) hexacyanoferrate(III) already present when the compound was subjected to potential cycling. Figure 5.51 shows very well how the two voltammetric

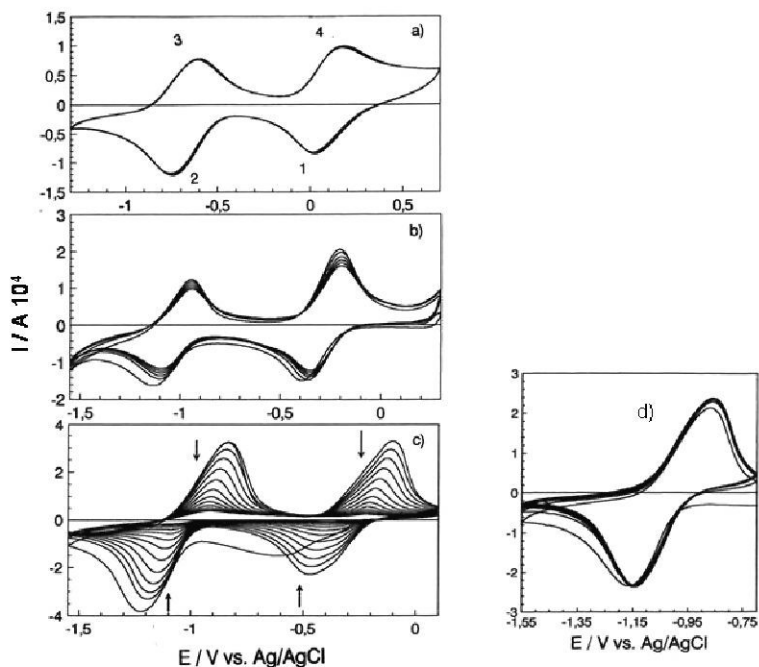


**Fig. 5.52.** Subsequent cyclic voltammograms of immobilized samples of **a** chromium(II) hexacyanomanganate(III), **b** iron(II) hexacyanomanganate(III), **c** manganese(II) hexacyanomanganate(III), **d** as c) but in a limited potential range [B 103]

systems of hexacyanomanganate (III)/(II) and hexacyanomanganate(II)/(I) decrease continuously while the hexacyanoferrate(III)/(II) system grows simultaneously [B 103].

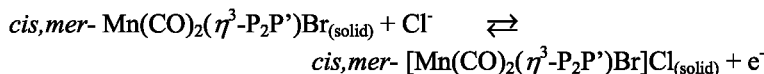
Whether the hexacyanomanganate ion is stable in its reduced or its oxidized state depends both, on the nitrogen-coordinated metal ions, and on the voltage range, i.e., what redox transitions are performed. Figure 5.52 depicts subsequent cyclic voltammograms of three hexacyanomanganates, (a) chromium(II) hexacyanomanganate(III), (b) iron(II) hexacyanomanganate(III), and (c) manganese(II) hexacyanomanganate(III), all measured in the potential range from +0.1 V to -1.55 V vs Ag/AgCl. Comparing Fig. 5.52b with Fig. 6.51 reveals that the iron(II) hexacyanoferrate(III) is rather stable when the electrode is not polarized to potentials where iron(II) is oxidized to iron(III). Figure 5.52a shows that the chromium(II) hexacyanomanganate is even completely stable, whereas the manganese(II) hexacyanomanganate(III) signal quickly deteriorates (Fig. 5.52c). However, when only the system of  $[\text{Mn}(\text{CN})_6]^{4-/5-}$  is measured in the limited po-

tential range from -0.7 to -1.55 V vs Ag/AgCl, then it remains completely stable (Fig. 5.52d).

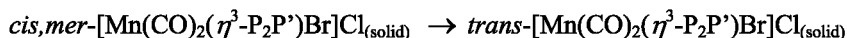
Figures 5.50 to 5.52 are good examples for showing that the voltammetry of immobilized particles yields curves that allow following chemical reactions in the solid state in a straightforward way, very similar to spectroscopic techniques.

Bond et al. [B 75] undertook a thorough study of the electrochemical oxidation of the solid organometallic compounds *cis*, *mer*- and *trans*- $\text{Mn}(\text{CO})_2(\eta^3\text{-P}_2\text{P}')\text{Br}$  ( $\text{P}_2\text{P}' = \{\text{Ph}_2\text{P}(\text{CH}_2)_2\}_2\text{-PPh}$ ), *cis*, *mer*- $\text{Mn}(\text{CO})_2(\eta^3\text{-P}_3\text{P}')\text{Br}$  ( $\text{P}_3\text{P}' = \{\text{Ph}_2\text{PCH}_2\}_3\text{P}$ ), binuclear *cis*, *fac*- $\{\text{Mn}(\text{CO})_2(\eta^2\text{-dpe})\text{Br}\}_2(\mu\text{-dpe})$  ( $\text{dpe} = \text{Ph}_2\text{P}(\text{CH}_2)_2\text{PPh}_2$ ), and of the electrochemical reduction of *trans*- $[\text{Mn}(\text{CO})_2(\eta^3\text{-P}_2\text{P}')\text{Br}]\text{BF}_4$ , *trans*- $[\text{Mn}(\text{CO})_2(\eta^3\text{-P}_3\text{P}')\text{Br}]\text{BF}_4$  and *trans*- $[\{\text{Mn}(\text{CO})_2(\eta^2\text{-dpe})\text{Br}\}_2(\mu\text{-dpe})](\text{BF}_4)_2$ . Aqueous electrolyte solutions have been used in these studies. A major result of this investigation was that isomerizations that were known to occur in the case of organic solutions of these compounds upon electrochemical transformations also occur in the solid state, however, at a markedly slower rate. An example is the following isomerization prompted by oxidation of *cis*, *mer*- $\text{Mn}(\text{CO})_2(\eta^3\text{-P}_2\text{P}')\text{Br}$ :

*Electrochemical oxidation using a chloride containing electrolyte :*

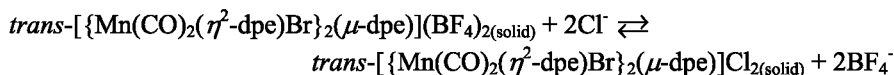


*Slow isomerization:*

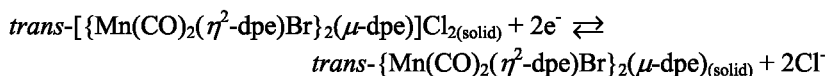


In the case of the solid binuclear complex *trans*- $[\{\text{Mn}(\text{CO})_2(\eta^2\text{-dpe})\text{Br}\}_2(\mu\text{-dpe})](\text{BF}_4)_2$  a single reversible two-electron reduction was observed (cf. Fig. 5.53a), whereas in a dichloromethane solution two one-electron reductions appear. The occurrence of a reversible single two-electron oxidation was attributed to a decreased communication of the metal centers in the solid compound, probably due to less flexibility. When the electrolyte contains chloride ions, an ion exchange reaction precedes the reduction:

*Ion exchange:*



*Electrochemical reduction/oxidation:*





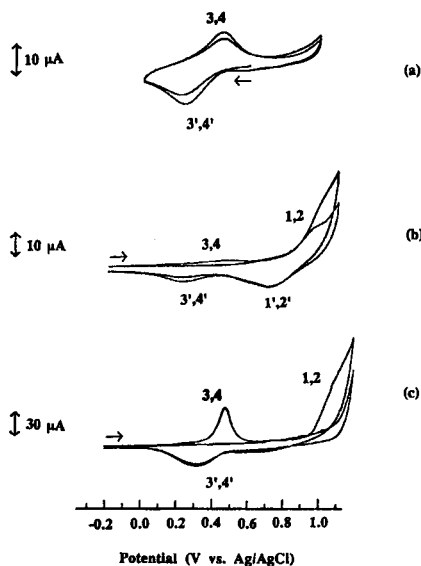


**Fig. 5.53.** Cyclic voltammograms (scan rate,  $200 \text{ mV s}^{-1}$ ) of solid complexes mechanically attached to graphite electrodes and placed in aqueous solution (0.1 M NaCl): **a** *trans*-[ $\{\text{Mn}(\text{CO})_2(\eta^2\text{-dpe})\text{Br}\}_2(\eta\text{-dpe})\}(\text{BF}_4)_2$  at  $20^\circ\text{C}$ , **b** *cis, fac*- $\{\text{Mn}(\text{CO})_2(\eta^2\text{-dpe})\text{Br}\}_2(\mu\text{-dpe})$  at  $20^\circ\text{C}$ , and **c** *cis, fac*- $\{\text{Mn}(\text{CO})_2(\eta^2\text{-dpe})\text{Br}\}_2(\mu\text{-dpe})$  at  $50^\circ\text{C}$  [B 75]

## 5.5.2 Electrochemically Initiated Substitutions

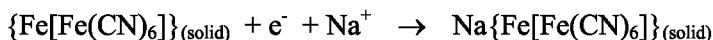
### Solid Metal Hexacyanoferrates

The simplest case of an electrochemically initiated substitution is when a solid contains the cations  $\text{C}^+$ , the electrolyte solution contains the cations  $\text{C}'^+$ , and the solid compound can be oxidized accompanied by a release of  $\text{C}^+$ . When the oxidized form is reduced, the cations  $\text{C}'^+$  will be inserted as the released  $\text{C}^+$  ions have diffused into the solution, provided the time suffices or the solution is stirred. In this way it is easy to pump *out* one sort of cations and to pump *in* another one. The same holds true for anions if their transfer accompanies electrochemical reactions. As an example for cation exchange may serve the electrochemical transformation of potassium containing Prussian blue into sodium-containing Prussian blue:

*Pumping out potassium ions during oxidation of the low-spin iron(II) ions:*



*Pumping in sodium ions during reduction of the low-spin iron(III) ions:*



These reactions have to be carefully taken into account whenever a solid compound is studied that is capable of undergoing chemically reversible

insertion electrochemical reactions. Often, the compound will contain ions from synthesis that differ from those present in the electrolyte solution used for the electrochemical measurements. In such a case the first scan will considerably differ from the following and one should make sure to equilibrate the solid by extended oxidation-reduction cycles. Complete repeated oxidation and reduction and stirring of the solution usually ensures that the final composition of the solid is in equilibrium with the solution composition. This is especially important when scan rate dependencies are recorded. For fast scan rates the layer of converted solid is, of course, much thinner than for slow scan rates. If the solid was not equilibrated before the scan rate dependence is measured, it could happen that at each scan rate a layer of the solid is studied that possesses a different composition compared to the previous (i.e., faster) scan rate. Peak potentials derived from such measurements would be slightly incorrect.

Electrochemically initiated substitutions are not confined to the exchange of counterions, they can also occur with ions more strongly bonded in the framework of the solid compound. Very early it was observed that the high-spin iron ions of Prussian blue can be substituted by cadmium ions when Prussian blue is cyclically oxidized and reduced in a  $\text{Cd}^{2+}$  ions containing electrolyte [B 35]. Later it was shown that analogous substitutions lead to the formation of nickel hexacyanoferrate when Prussian blue is cycled in a  $\text{Ni}^{2+}$  containing solution, and to the formation of cadmium hexacyanoferrate when silver hexacyanoferrate is cycled in a  $\text{Cd}^{2+}$  containing electrolyte [B 55]. Figure 5.54 shows cyclic voltammograms recorded during the electrochemically initiated substitution. It could be shown that the reaction leads not to a simple mixture of the mother and daughter hexacyanoferrate, but it proceeds via bilayered structure. This can be deduced from a scan rate dependence of the ratio of the signals of the mother and daughter hexacyanoferrate as shown in Fig. 5.55 for the cadmium and iron hexacyanoferrate systems. In this figure the ratio of peak currents of signals 4 and 5, Fig. 5.54b, is depicted compared with the voltammograms of a simple powder mixture of the same two hexacyanoferrates (inset of Fig. 5.55). In case of a powder mixture of cadmium and iron hexacyanoferrate both compounds are equally accessible for the electrochemical reactions and both signals increase in the same way upon increasing the scan rate. However, when the daughter hexacyanoferrate forms a layer on the mother hexacyanoferrate that must be crossed by the inserting ions before the mother hexacyanoferrate can react, then the ratio of the peak currents must show a strong scan rate dependence as depicted in Fig. 5.55. A very thorough analysis of this system [B 173] using cyclic voltammetry, impedance spectroscopy and scanning electron microscopy in conjunction with

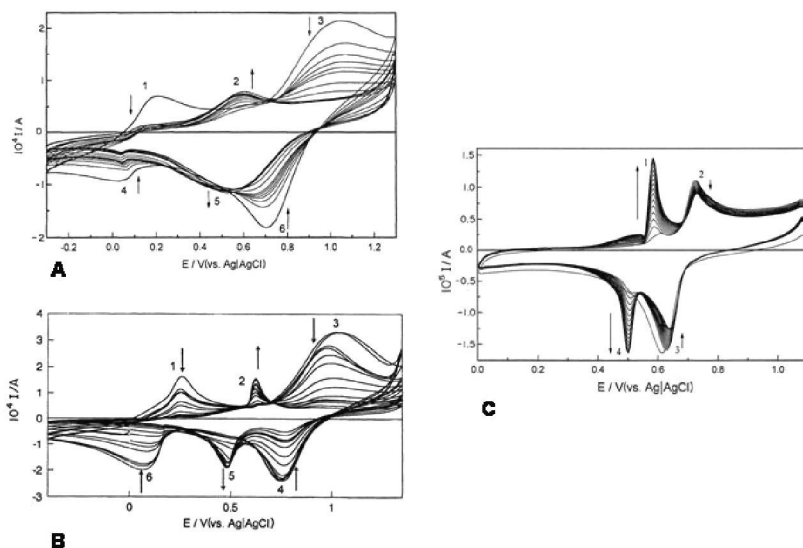


**Fig. 5.54.** Cyclic voltammograms recorded during the conversion of **a** Prussian blue to nickel hexacyanoferrate, **b** Prussian blue to cadmium hexacyanoferrate, and **c** silver hexacyanoferrate to cadmium hexacyanoferrate. Electrolyte solutions: **a**  $0.1 \text{ mol L}^{-1}$  nickel nitrate, **b** and **c**  $0.1 \text{ mol L}^{-1}$  cadmium nitrate. The scan rate was  $0.1 \text{ V s}^{-1}$  [B 55]

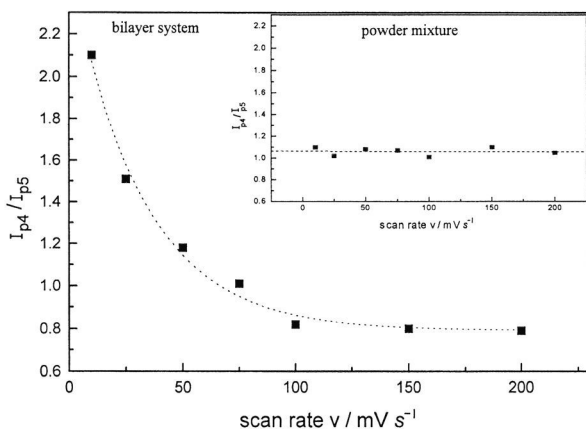
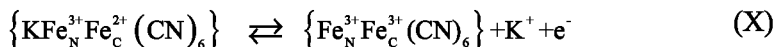
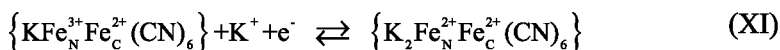


**Fig. 5.55.** Plots of the ratio of peak currents  $i_{p4}/i_{p5}$ , i.e. ratio of cathodic peak current of iron hexacyanoferrate to cathodic peak current of cadmium hexacyanoferrate, as a function of scan rate. The inset shows the same dependence for the case that a powder mixture of these hexacyanoferrates was immobilized [B 55]

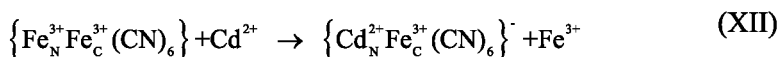
energy dispersive X-ray detection (*ex situ*) confirmed the following reaction mechanism. Prussian blue can be oxidized to Berlin green as follows,



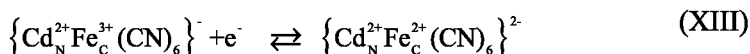
or it can be reduced to Berlin white according to:



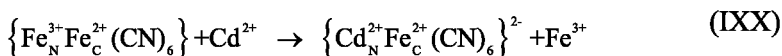
If Prussian blue, or either of its redox congeners, is merely soaked in a solution containing  $\text{Cd}^{2+}$  ions, some of these ions may replace the  $\text{K}^+$  in the cages, but no substantial reaction occurs [B 35]. However, if cyclic voltammetry is carried out on Berlin white microcrystals  $\left\{ \text{K}_2\text{Fe}_N^{\text{2+}}\text{Fe}_C^{\text{2+}}(\text{CN})_6 \right\}$  adhered to graphite in a solution containing both  $\text{K}^+$  and  $\text{Cd}^{2+}$  ions, then an uptake of cadmium ions into the lattice of the metal hexacyanoferrate occurs gradually. It is postulated that the cycling "pumps"  $\text{Cd}^{2+}$  (and  $\text{K}^+$ ) ions in and out of the cages, permitting the substitution reaction



to occur. The twin-process voltammogram described by reactions (X) and (XI) is gradually replaced by a single-process cyclic voltammogram corresponding to the reaction

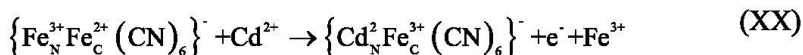


The charge compensating cations are not given in Eqs. XII and XIII because their identity is not exactly known. Depending on time and location  $\text{K}^+$ ,  $\text{Cd}^{2+}$ , and  $\text{Fe}^{3+}$  are possible candidates. Of course, Reactions X, XI, and XIII will also take place under insertion of  $\text{Cd}^{2+}$  into and out of the solid. Even though it is the nitrogen-bound iron atom that undergoes substitution in Reaction XII, the carbon-bound iron atom is also a factor in the process. It is essential that this atom is in the +3 state – then the conceivable reaction

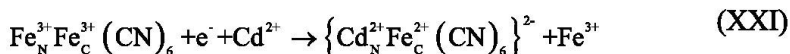


does *not* significantly take place, as evidenced by the observation that cadmium substitution does not occur if the voltammetric cycling is restricted to the range involving only Berlin green and Prussian blue. On the other hand, the reaction cannot be as simple as reaction (XII) suggests, be-

cause the cages of Berlin green are unoccupied, so  $\{\text{Cd}_N^{2+}\text{Fe}_C^{3+}(\text{CN})_6\}^-$  cannot be formed by a pure substitution reaction as implied by Eq. XII. Instead, it may be postulated that substitution and oxidation occur concurrently during the second half of the oxidative scan:



The substitution reaction continues during the reduction of low-spin Fe(III) as long as the latter is still present, that is



One can sum both substitution possibilities defining the following formal exchange reaction with a rate constant  $k_f$ :

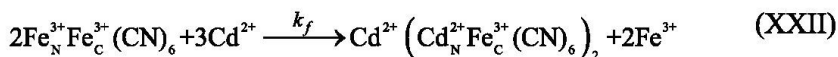
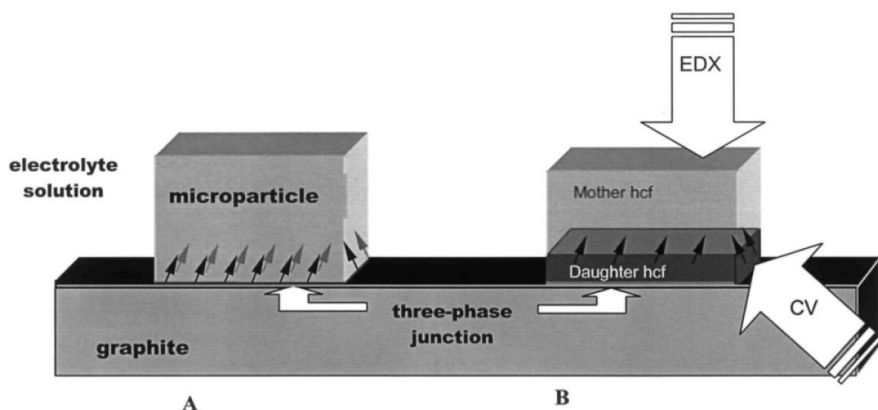


Figure 5.56 schematically shows how the bilayered system is formed and how cyclic voltammetry and EDX mirror the proceeding of the electrochemically induced transformation. See also Sec. 5.11 for the results of theoretical simulations of this substitution reaction.

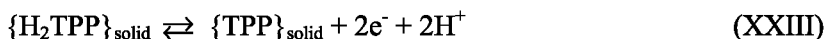


**Fig. 5.56.** Schematic view of the situation when a microparticle of a mother hexacyanoferrate is transformed into a daughter hexacyanoferrate. The scheme visualizes the different perspectives from which cyclic voltammetry (CV) and energy dispersive X-ray analysis sees the reaction. With EDX it takes much longer until the product can be detected, whereas with CV the mother compound will only be seen when slow scan rates are used and the diffusion layer expands within the particles up to the mother compound [B 173]

### Solid Porphyrins

When solid microparticles of 5,10,15,20-tetraphenyl-21*H*,23*H*-porphyrin (H<sub>2</sub>TPP) immobilized on an electrode surface are subjected to reduction-oxidation cycles in a copper(II) containing electrolyte solution, the incorporation of Cu<sup>2+</sup> ions has been observed [B 135, B 159, B 178]. The following mechanism has been proposed:

1. The solid H<sub>2</sub>TPP is oxidized at 0.95 V to solid TPP:



2. The solid TPP is able to incorporate copper(II) ions into the porphyrin ring, presumably accompanied by an association of chloride ions:



3. The porphyrin skeleton of  $\{\text{TPPCu}^{2+}(\text{Cl})_2\}_{\text{solid}}$  is reduced at potentials negative to 0.95 V according to:



4. The solid compound  $\{\text{TPP}^{2-}\text{Cu}^{2+}\}_{\text{solid}}$  undergoes a reversible one-electron reduction-oxidation accompanied by potassium ion transfer at -0.07 V according to (see Fig. 5.57):

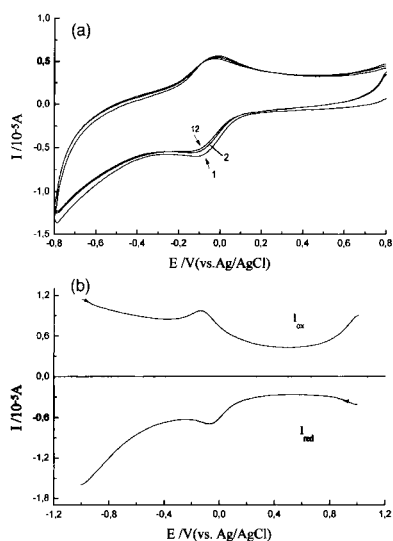


**Fig. 5.57.** a Cyclic voltammograms of an electrode with immobilized H<sub>2</sub>TPP after copper(II) ion incorporation (0.1 M KCl, pH 5.5, scan rate 0.1 V s<sup>-1</sup>). The 1<sup>st</sup>, 2<sup>nd</sup>, and 12<sup>th</sup> cycles are shown. b Square-wave voltammograms of the same electrode [B 135]

While the electrochemical system XXVI has been unambiguously identified, it was not possible to detect the incorporated copper ions with scanning electron microscopy coupled EDX. This can be explained by a very small conversion zone at the three-phase junction so that the electron beam does not access it. The small currents support this idea, suggesting that only a very small fraction of the porphyrin compound is incorporating the copper ions.

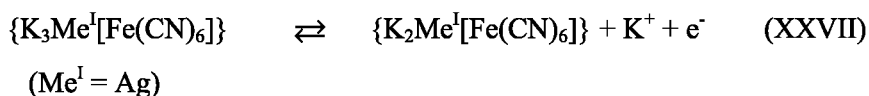
## 5.6 Assessing Structure-Property Relationships

It is the intention of this section to show how systematic studies of certain groups of compounds can be performed with the help of the voltammetry of immobilized particles in order to derive relationships between their structures and their electrochemical properties. Here, we shall discuss some relations between the structure of compounds and their thermodynamic properties.

Any chemically synthesized compounds that are insoluble and electrochemically active can be studied by means of the voltammetry of immobilized particles. For the characterization of these compounds a wealth of analytical tools is available, ranging from elemental analysis to the most sophisticated techniques for structure analysis. This is by far not the case for compounds that are precipitated by electrochemical means as thin films on electrodes. In the latter case the means for analysis are rather limited and the data of these analyses are less reliable. There are also much fewer possibilities to deliberately vary the composition or structure of the synthesized compound.

### 5.6.1 Solid Metal Hexacyanometalates

A first example of a systematic study was the determination of the formal potentials of many metal hexacyanometalates and the search for a correlation of these data with properties of the nitrogen-coordinated metal ions [B 41]. Figure 5.58 depicts the correlation of the formal potentials of the following reactions with the ion potential of the metal ions  $\text{Me}^+$ ,  $\text{Me}^{2+}$ , and  $\text{Me}^{3+}$ :



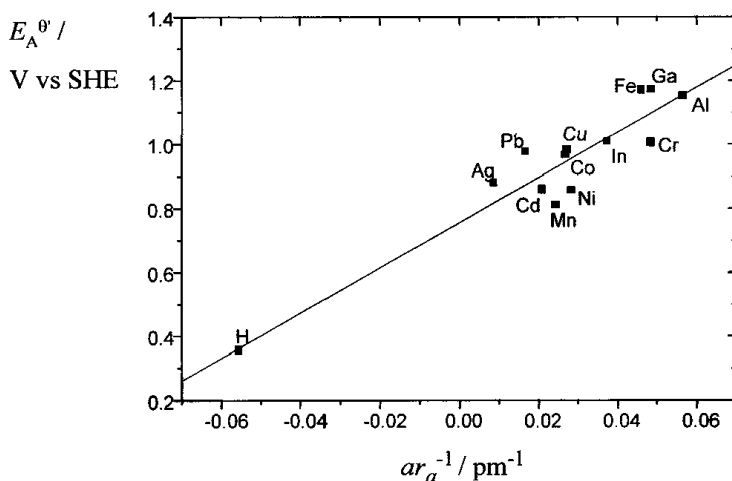
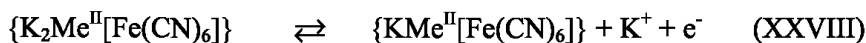
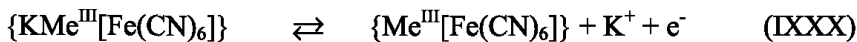


**Fig. 5.58.** Correlation between the formal potentials of the hexacyanoferrate units of the solid hexacyanoferrates and the ion potential (charge/radius) of the nitrogen-coordinated metal ions [B 41, B 209]



( $\text{Me}^{\text{II}} = \text{Cd}, \text{Zn}, \text{Pb}, \text{Mn}, \text{Ni}, \text{Co}$ )



( $\text{Me}^{\text{III}} = \text{Ga}, \text{In}, \text{Al}, \text{Fe}, \text{Cr}, \text{Co}$ ).

All these reactions are typical solid-state insertion electrochemical processes with coupled electron and ion transfers. In Fig. 5.58 included is also the standard potential of the hexacyanoferrate ions in aqueous solution. Very interestingly, there is a rather good correlation between these data, and this is the first example that one and the same correlation bridges the formal potentials of an ion in different solids *and* in aqueous solution. It is reasonable to assume that the protons of the water are the nearest neighbors of the nitrogen atoms of the cyanide ions surrounding the iron, as the metal ions  $\text{Me}^{\text{I}, (\text{II}), (\text{III})}$  ions are the nearest neighbors in the solid. On the basis of elementary thermodynamics it was later possible to derive the following equation for the formal potentials [B 163, B 209]:

$$E_A^{0'} = -\frac{\kappa}{zF} + \frac{\xi}{zF} \frac{a}{r_{\text{Me}}} \quad (5.7)$$

( $\kappa$  and  $\xi$  are constants,  $a$  is the charge of the nitrogen coordinated metal ions  $\text{Me}^{\text{I}, (\text{II}), (\text{III})}$  and  $r_{\text{Me}}$  their radius.)



As can be seen from Fig. 5.58, the experimental data follow this equation. Other examples for systematic studies of the electrochemical and structure data of solid hexacyanometalates concern the dependence of the formal potential of the hexacyanoferrate unit and the ion potential of the inserting metal ions and the correlation between the formal potentials of the hexacyanometalate ions and the lattice constants (the latter correlation includes hexacyanochromates and hexacyanomanganates) [B 41, B 163, B 209].

It has been known for a long time that the formal potential of the hexacyanoferrate system in solid compounds is affected by the nature of the inserting cations. On the basis of simple Born-Haber cycles the following equation was derived for the effect of the ion potential of the inserting cations on the formal potential of the hexacyanoferrate system [B 209]:

$$E_A^{0'} \approx -\frac{\text{const}_3}{zF} - \frac{\Phi}{zF} \frac{b_1}{r_1} \quad (5.8)$$

( $\text{const}_3$  and  $\Phi$  are constants,  $b_1$  is the charge of the inserting metal ions  $\text{Me}^I$  and  $r_1$  its radius).

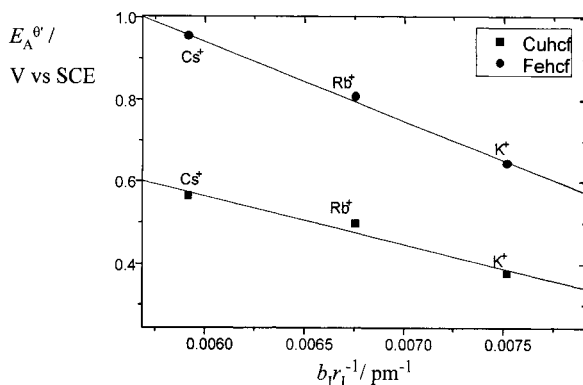
Figure 5.59 gives the experimental proof of the validity of Eq. 5.8. There exists also a relationship between the lattice constant of solid metal hexacyanometalates and the formal potential. This dependence can be experimentally found when the nitrogen-coordinated metal ion and the inserting metal ion is always the same, but the nature of the carbon-coordinated metal ions is varied, i.e., for hexacyanoferrate, hexacyanocobaltate, hexacyanomanganate etc. [B 209]. The equation that has been derived is:

$$E_A^{0'} \approx -\frac{2\Psi}{zF} \left[ \frac{b_C - b_B}{L} \right] - \frac{\omega_1}{zF} \quad (5.9)$$

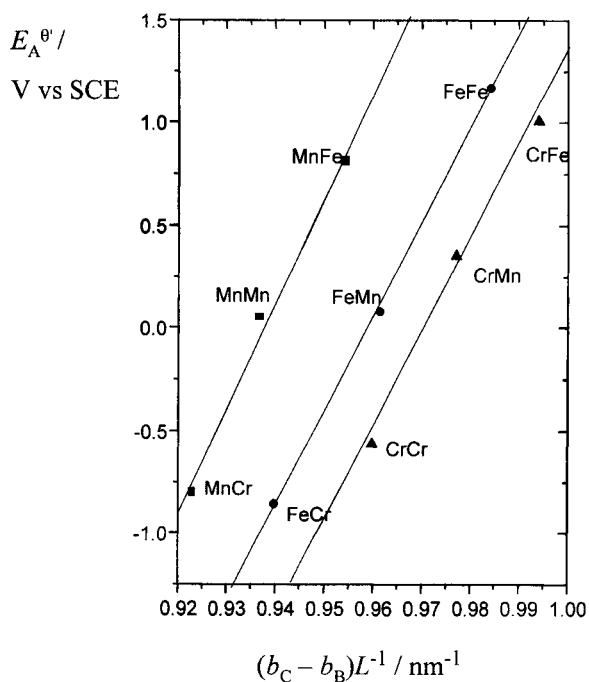
( $\Psi$  and  $\omega_1$  are constants,  $(b_C - b_B)$  is the difference of charges of the oxidized and reduced forms of the hexacyanometalate unit, i.e., it is 1, and  $L$  is the lattice constant of the solid hexacyanometalate).

Figure 5.60 shows that the experimental data are in accordance with this equation.

The results given in Figs. 5.58 to 5.60 show that the technique of immobilizing microparticles of solid compounds on solid electrodes easily allows studying series of related compounds with the aim of understanding how the thermodynamic properties change with certain structure parameters.



**Fig. 5.59.** Correlation between the formal potentials of the hexacyanoferrate units of the solid hexacyanoferrates and the ion potential (charge/radius) of the inserting metal ions [B 41, B 209]

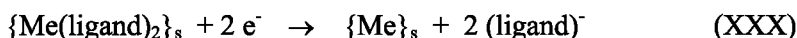


**Fig. 5.60.** Correlation between the formal potentials of the hexacyanometalate units of the solid hexacyanometalates and the inverse lattice constant  $L$  of the solid compounds [B 41, B 209]

### 5.6.2 The Stability Constants of Metal Dithiocarbamate Complexes and their Structure

The electrochemistry of solutions of metal dithiocarbamates in organic solvents has been intensively studied by Alan Bond and his group<sup>4-6</sup>. On this sound basis it was possible to perform a systematic study of the electrochemistry of these highly water-insoluble compounds as immobilized particles on electrodes [B 13, B 14]. All studied mercury(II) and lead(II) dithiocarbamate complexes displayed one redox system in cyclic voltammetry that was characterized by the following features: the response decreased during subsequent cycling, the mid-peak potentials converged against a constant value in subsequent cycles, and the anodic to cathodic peak separation was in most cases below 100 mV. Figures 5.61 and 5.62 show one example for a lead complex and one for a mercury complex.

Eleven differently substituted dithiocarbamate complexes of lead(II) and 17 differently substituted dithiocarbamate complexes of mercury(II) have been studied. For some of them the overall stability constants in water have been known. With the help of these data it was found that the mid-peak potentials of the cyclic voltammograms are determined by these stability constants. Figure 5.63 illustrates the situation on the electrode surface. The solid metal complex is partially reduced to metal and the dissolved ligand ions. This first reaction can be formulated as follows:



In the following cyclic polarizations the dissolution-precipitation equilibrium seems not to establish, perhaps because of a retardation of nucleation. The voltammograms are completely governed by the following electrochemical system involving dissolved complex molecules and ligands:



---

<sup>4</sup> Bond AM, Colton R, Dillon, ML, Moir, JE, Page DR (1984) *Inorg Chem* 23:2883-2891

<sup>5</sup> Bond AM, Colton R, Hollenkamp AF, Hoskins BF, McGregor K (1987) *J Am Chem Soc* 109:1969-1980

<sup>6</sup> Bond AM, Colton R, Hollenkamp AF (1990) *Inorg Chem* 29:1991-1995

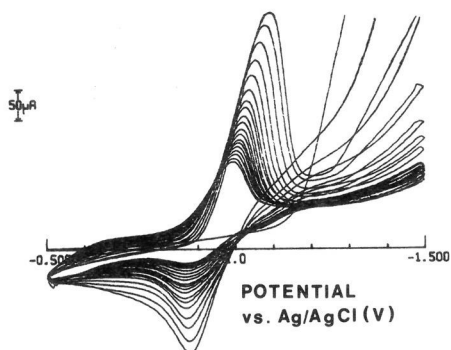


**Fig. 5.61.** First twenty cyclic voltammograms for reduction of  $\text{Pb}(i\text{-Pr}_2\text{dtc})_2$  mechanically attached to a PIGE with aqueous  $0.1 \text{ mol L}^{-1} \text{ KNO}_3$  as electrolyte: scan rate  $100 \text{ mV s}^{-1}$  [B 13]

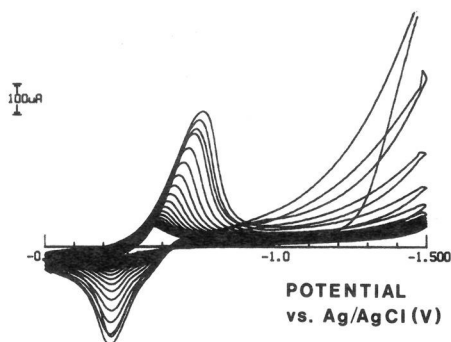


**Fig. 5.62.** Multiple cyclic voltammograms for reduction of  $\text{Hg}(\text{Et}_2\text{dtc})_2$  mechanically attached to a PIGE with aqueous  $0.1 \text{ mol L}^{-1} \text{ KNO}_3$  as electrolyte: scan rate  $100 \text{ mV s}^{-1}$  [B 13]

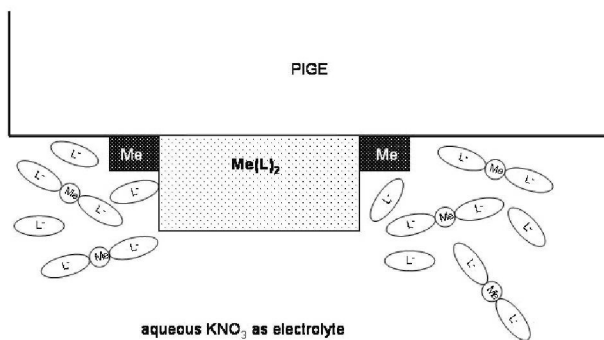


**Fig. 5.63.** Situation at an electrode surface with immobilized  $\text{Pb}(i\text{-Pr}_2\text{dtc})_2$  that is partially reduced to lead metal and dissolved ligands (the ovals)

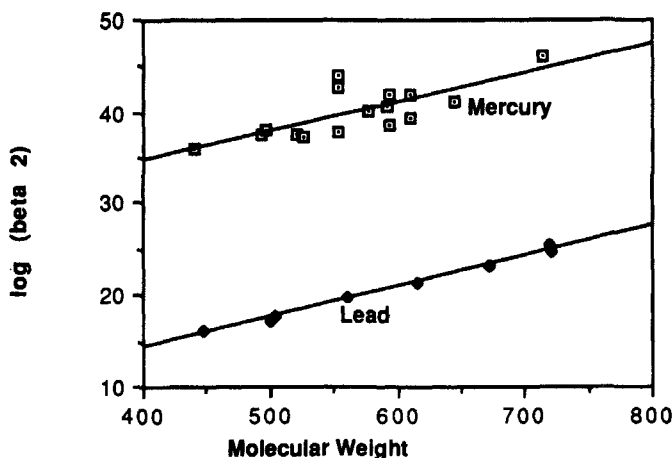


Fig. 5.64. Plot of  $\log \beta_2$  values of mercury and lead dithiocarbamate complexes vs. their molecular weight. The electrolyte solution was  $0.1 \text{ mol L}^{-1} \text{ KNO}_3$  [B 13]

The lead complex of *n*-hexyl-dithiocarbamate crystallizes very slowly, and so several experiments have been performed with attached microdroplets of this compound. Interestingly, the electrochemical response was exactly the same as that of the crystalline compound. These experiments with the oil droplets of this lead compound were obviously the first experiments with attached droplets that further developed so vividly (see Chapter 6).

For the redox system (XXXI) the Nernst equation reads as follows:

$$E = E_{\text{Pb}^{2+}/\text{Pb}}^{\ominus} + \frac{RT}{2F} \ln \beta_2^{-1} + \frac{RT}{2F} \ln \frac{a_{\text{Me}(\text{ligand})_2}}{a_{\text{ligand}}^2} \quad (5.10)$$

The formal potential  $E_c^{\ominus'}$  of the system is:

$$E_c^{\ominus'} = E_{\text{Pb}^{2+}/\text{Pb}}^{\ominus} + \frac{RT}{2F} \ln \beta_2^{-1} + \frac{RT}{2F} \ln \frac{\gamma_{\text{Me}(\text{ligand})_2}}{\gamma_{\text{ligand}}^2} \quad (5.11)$$

Assuming that the activity coefficients are unity, or at least constant at a certain ionic strength, the overall stability constants can be calculated. The intriguing result of this study was that for both series of metal dithiocarbamate complexes the  $\log \beta$  values are linear functions of the molecular weight of the complexes (cf. Fig. 5.64). This is further supported by the fact that the stability constants of the lead complexes of *n*-propyl- and *i*-propyl-dithiocarbamate complexes have exactly the same values, as have

the *i*-butyl and *n*-butyl-substituted complexes. The cyclo-hexyl- and *n*-hexyl-substituted complexes have almost the same stability constants. Following this observation, a search for similar series of metal complexes revealed that there are several other examples for such dependences, although, the number of complexes was much smaller in each series. A prerequisite for these dependencies seems to be that the chelating region of the ligand is electronically not, or only marginally, affected by the substituents of the ligand that increase the molecular weight. A quite similar dependence was also observed for the literature data of  $\text{pK}_a$  values of carboxylic acids on their molecular weight. Until now, there has not been given a theoretical explanation for these correlations. The study of the  $\log\beta$  values is presented here to show how electrochemical measurements of immobilized particles can yield interesting new insight also in cases where dissolution-precipitation processes are coupled to redox and complex equilibria.

## 5.7 Assessing Kinetic Properties of Electrochemical Dissolution Reactions

When solid particles immobilized on an electrode undergo an electrochemical dissolution reaction, the electrochemical measurements should provide information on the size and shape of the particles and on the electrochemical and chemical steps of the reaction. T. Grygar was the first who realized the potential of electrochemical measurements with immobilized particles and who contributed most of the material which is presented in this chapter [B 37, B 40, B 50]. The methodology of these studies was developed using iron(III)-oxides and -hydroxyoxides which undergo reactions as the following:



Reaction XXXII is a proton-assisted reductive dissolution of the solid phase  $\text{FeOOH}$  yielding dissolved iron(II) ions. Grygar applied the general kinetic Eq. 5.12 for reaction rate  $J$  to the special case of electrochemical dissolution of immobilized microparticles of oxides,

$$J = -\frac{dn}{dt} = -kN_0G(c)F\left(\frac{N_t}{N_0}\right) \quad (5.12)$$

where  $k$  is the rate constant,  $N_0$  is the total number of moles of compound to be dissolved,  $N_t$  is the number of moles of compound dissolved until the

time  $t$ , and  $F(N_t/N_0)$  characterizes the dependence of reactivity on the size and shape distribution of the dissolving particles.  $G(c)$  is a function that depends on the composition of the solution phase. If diffusion is controlling the dissolution, this function is simply  $G = c_s - c$  with  $c_s$  being the concentration of the saturated solution and  $c$  being the actual concentration. In the case of reductive dissolution this function depends on the concentration of all reactants and the adsorption capacity of the particles. When all these factors can be kept constant, it may be included in  $k$ . In that case the reaction will be of pseudo-first order and the unit is  $s^{-1}$ . Eq. 5.12 expressed in electrochemical terms reads:

$$I_t = kQ_0G(c)F\left(\frac{Q_t}{Q_0}\right) \quad (5.13)$$

Where  $I_t$  is the current at time  $t$ , and  $Q_t$  and  $Q_0$  are the charges flown until the time  $t$ , and until complete dissolution, respectively. When the solution composition is kept constant, the function  $G(c)$  can be included in the rate constant and for the function  $F(N_t/N_0)$  an experimentally found expression can be used to write Eq. 5.13 as follows:

$$I_t = k'Q_0\left(\frac{Q_t}{Q_0}\right)^g \quad (5.14)$$

The exponent  $g$  has been interpreted as characterizing the heterogeneity of the powder with respect to its reactivity. Grygar has shown that the rate constant  $k'$  in Eq. 5.14 follows a potential dependence that can be written as:

$$k' = k'_0 \exp\left[-\frac{\alpha nF(E - E^0)}{RT}\right] \quad (5.15)$$

Equation 5.15 is limited to growing overpotentials when the subsequent reaction step, the dissolution of  $Fe^{2+}$  compounds, becomes rate limiting. Figure 5.65 depicts experimental plots of  $\ln k'$  versus electrode potential for several iron hydroxyoxides and an oxide, proving that, within the used potential range, the reductive dissolution is charge transfer controlled. Table 5.4 lists rate constants and  $g$ -values as determined from chronoamperometric measurements. From this table and other publications one can see that the rate constants of electrochemical dissolution of  $\alpha$ -FeOOH vary, depending on the electrode potential and electrolyte solution, between  $2.3 \times 10^{-3}$  and  $26 \times 10^{-3} s^{-1}$  [B 40, B 50, B 66]. With the help of in

**Table 5.4.** Values of the  $k'$  and  $g$  parameters in the kinetic Eq. 5.14 for the dissolution of the phases in the 0.1 M oxalate buffer at working electrode potentials of -0.2 and -0.4 V vs. SCE, and the voltammetric half-wave and peak potentials in 0.1 M chloroacetate buffer; scan rate 10 mVs<sup>-1</sup>. The samples designated by A, B, C, etc. were prepared under different experimental conditions [B 40]

Phase	-0.2 V		-0.4 V		$E_{1/2}$ , V
(sample)	$k' \times 10^{-3}$ , s <sup>-1</sup>	$g$	$k' \times 10^{-3}$ , s <sup>-1</sup>	$g$	
Ferrihydrite (A)	45	1.32	>100	-	0.00
(B)	33	1.38	>100	-	-0.10
$\alpha$ -FeOOH (A)	26	1.15	22	1.36	-0.34
(B)	8.0	1.18	15	1.13	-0.49
(D)	3.8	1.18	6.9	1.28	-0.53
(E)	7.1	1.17	5.9	0.93	-0.55
(F)	4.0	1.01	5.6	1.38	-0.50
(G)	3.6	1.38	-	-	-0.47
$\beta$ -FeOOH	4.1	0.88	<sup>a</sup>	-	-0.16 <sup>b</sup>
$\gamma$ -FeOOH	55	1.35	>100	-	-0.01
$\delta$ -FeOOH	43	1.31	>100	-	0.00
Fe <sub>3</sub> O <sub>4</sub>	65	1.98	>100	-	-0.02
$\alpha$ -Fe <sub>2</sub> O <sub>3</sub>	0.6	1.12	2.7	1.04	-0.56
$\gamma$ -Fe <sub>2</sub> O <sub>3</sub>	63	2.62	>100	-	-0.08
Sediments: BRS			15	3.31	c
SLI	16	1.73	16	2.81	c
Fe <sup>3+</sup> (aq) <sup>f</sup>	reduction process obeying Cottrell's equation				-0.08 <sup>d</sup> +0.30 <sup>e</sup>

<sup>a</sup> Chronoamperometric curve is not monotonous; <sup>b</sup> broad peak, slow current decrease after the maximum; <sup>c</sup> no clear maximum, slowly rising wave; <sup>d</sup> clean electrode surface; <sup>e</sup> electrode surface with deposited FeOOH; <sup>f</sup>  $c_{\text{Fe}} = 1 \text{ mmol l}^{-1}$ .

situ AFM the average dissolution rate for seven microcrystals was found to be  $2.0 \times 10^{-3} \text{ s}^{-1}$  [B 276] what is remarkably near to the data with arrays of immobilized microcrystals that have been used in Grygars experiments. In experiments with goethites and Al-substituted goethites Grygar found the exponent  $g$  in a range from 0.8 to 1.2, and interpreted these values as typical for dissolutions that proceed in a shape-conservative fashion [B 66]. Since  $k$  and  $k'$  in Eqs. 5.13 and 5.14 depend on the specific surface area  $\sigma$  of the sample at the start, Eq. 5.15 can be written to describe the peak potential in differential pulse voltammetry, assuming that the DP peak is



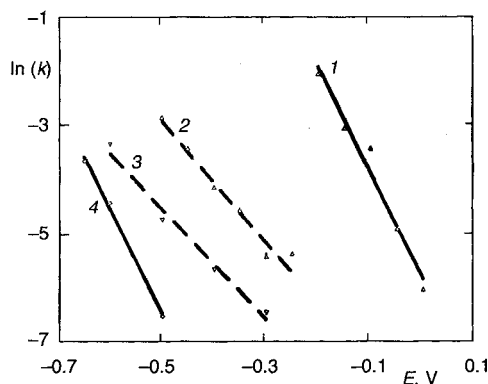


**Fig. 5.65.** Dependence of the logarithm of the electrochemical dissolution rate constant  $k$  on the working electrode potential  $E$ . Curves: 1 ferrihydrite, 0.05 M chloroacetate; 2 goethite, 0.2 M chloroacetate + 0.5 M KCl; 3 goethite, 0.05 M chloroacetate; 4 hematite, 0.2 M chloroacetate [B 40]

shifted from the DC peak by a constant value, in the form:

$$E_{p,DP} = B + \frac{RT}{\alpha nF} \ln \sigma \quad (5.16)$$

It has been shown that such dependencies hold true for the reductive electrochemical dissolution of Ba-hexaferrite, hematite, goethite, maghemite, and magnetite [B 50]. This linear dependence is also obeyed by Li-Mn-O spinels as can be seen in Fig. 5.66 [B 191].

The influence of the parameter  $g$  on the shape of linear sweep voltammograms is depicted in Fig. 5.67. Grygar has derived the following equation for the dependence of the peak current on  $g$ :

$$I_p / Q_0 = \alpha nFv (RT)^{-1} g^{g/(1-g)} \quad (5.17)$$

and has proved that the following equation, that was derived earlier by Brainina for paste electrodes, holds true also for immobilized microparticles:

$$E_p = E^0 - \frac{RT}{\alpha nF} \ln \frac{\alpha nFv}{RT} + \frac{RT}{\alpha nF} \ln \frac{k_E}{d} \quad (5.18)$$

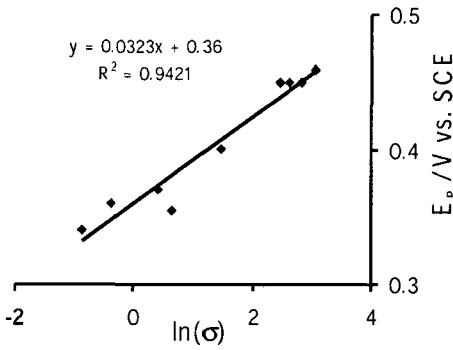


**Fig. 5.66.** Peak potential of reductive dissolution of Li-Mn-O spinels versus natural logarithm of specific surface area [B191]

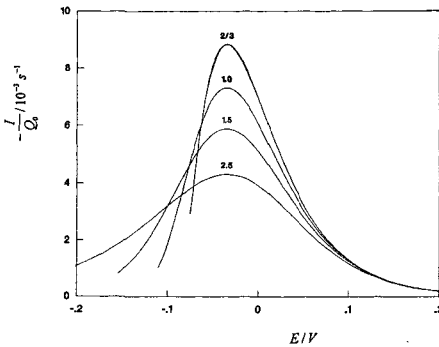


**Fig. 5.67.** The influence of the  $g$  parameter on the shape of the voltammetric curves of the reductive dissolution. The curves were calculated for  $\alpha = 0.5$ ,  $k_0 = 1 \times 10^{-2} \text{ s}^{-1}$  and  $\nu = 1 \text{ mV s}^{-1}$ . The  $g$  values are given at the curves [B 52]

with  $k_E$  being the rate constant of the electrode reaction in  $\text{m s}^{-1}$  at  $E^0$  and  $d$  the particle diameter. Equation 5.17 was approximated by the following equation:

$$\left( \frac{I_p}{Q_0} \right) = 0.37 \frac{\alpha n F}{RT} \nu (1 - 0.47 \ln g) \tag{5.19}$$

that could be observed experimentally for several oxides with only slightly different coefficients [B 52]:

$$\left( \frac{I_p}{Q_0} \right) = 0.2 \frac{\alpha n F}{RT} \nu (1 - 0.5 \ln g) \tag{5.20}$$

For some metal oxides more elaborate models have been developed to describe the electrochemical dissolution. These models take into account an intermediate surface complexation. The general approach was to separate

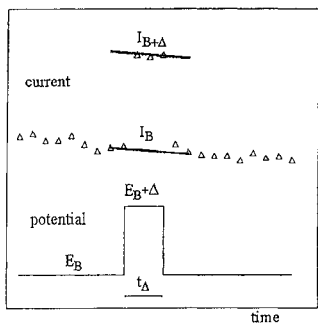


**Fig. 5.68.** Potential time scheme and current response for the determination of formal transfer coefficients according to [B 92]

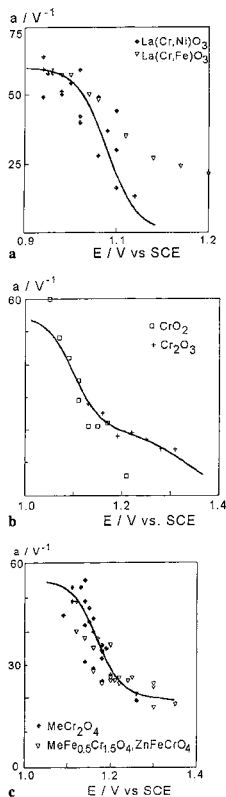


**Fig. 5.69.**  $a_E$  versus potential curves for Cr oxides: **a** perovskites, **b** pure Cr oxides, and **c** spinels. Solid lines are simulated based on a kinetic model [B 92]

the potential and conversion dependent functions that determine the overall kinetics of dissolution. Both contributions have been separated by the combination of potentiostatic and potentiodynamic measurements [B 81]. In a study of the electrochemical oxidative dissolution of chromium oxides, good indications have been found for two one-electron steps preceding the dissolution [B 92]. This result was obtained using a potential pulse technique with which a formal charge transfer coefficient can be determined on the basis of the following equation:

$$a_E = \frac{nF}{RT} \alpha_E = \frac{\ln(I_{B+\Delta}) - \ln(I_B)}{\Delta} \quad (5.21)$$

The meaning of the symbols follows from Fig. 5.68. From the dependence of  $a_E$  on the electrode potential and a fitting of these curves based on kinetic models, the author came to conclusions about the validity of the models. Figure 5.69 depicts these curves for some oxidic compounds. Note the two inflection points in case of the pure chromium oxides indicating two one-electron steps. Similar studies have been performed with the reductive decomposition of manganates(V). From the experiments it was derived that the reduction is controlled by an irreversible one-electron surface reaction, whereas the reduction of  $\text{MnO}_2$  is controlled by a reversible reaction coupled with a discussion in the solid [B 105].

Several similar systems have been studied by Grygar and coworkers with respect to their reactivity under electrochemical conditions [B 104, B 117, B 118, B 125, B 141, B 181, B 191, B 194]. In [B 192] the application of the discussed methodology to the study of the dissolution kinetics of metallic iron particles has been described.

## 5.8 The Electrochemistry of Single Particles

This monograph would be incomplete without a discussion of studies of the electrochemistry of single particles. The use of single particles is, of course, extremely appealing as such studies can, in principle, provide information that is otherwise inaccessible. In case of the AFM investigations discussed in Chapter 4.2, in fact single particles have been imaged and the course of their electrochemical transformations was visualized. This was achieved by immobilizing arrays of particles on an electrode surface and focusing the AFM on a single or just some particles. Of course, the simultaneously recorded electrochemical signals were caused by all immobilized particles.

Here we shall discuss the preparation and immobilization of a single particle on an electrode with the aim of performing the electrochemical measurement with just one particle. This is rather difficult and such measurements will probably be always confined to specialized laboratories.

In 1990 Bursell and Björnbom published an experimental setup that allows contacting agglomerates of particles from 5  $\mu\text{m}$  onwards with the help of a carbon fiber [B 10]. The agglomerate was transferred with a syringe, together with electrolyte solution, onto an electrolyte-soaked separator that was in contact with a reference electrode. Uchida et al. [B 47] have improved the methodology for single particle measurements (see Fig. 6.8.1). These authors have used their equipment for the determination of the diffusion coefficients of hydrogen in  $\text{LaNi}_5$  particles. For this purpose

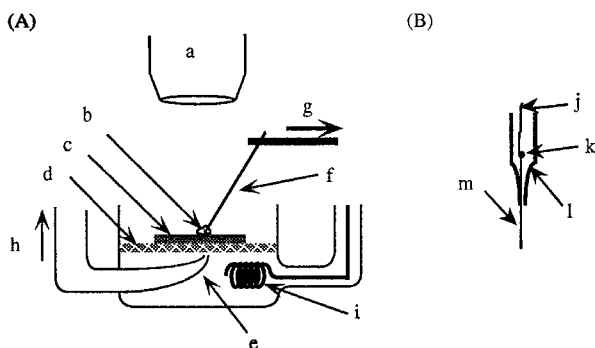


**Fig. 5.70.** Experimental setup for single particle measurements: (A) the measurement system and (B) the carbon fiber microelectrode. **a** microscope; **b** particle to be studied; **c** glass separator; **d** glass frit; **e** Luggin capillary; **f** microelectrode; **g** x-y-z manipulator; **h** reference electrode; **i** counter electrode; **j** lead wire; **k** Ag paste; **l** glass tube; **m** carbon fiber (diameter 10  $\mu\text{m}$ ) [B 47]

they measured the current-time response for the oxidation of hydrogen after a previous loading of the particle. The response was analyzed in a short time and a long time range, as the diffusion regime was supposed to change from semi-infinite planar diffusion to finite diffusion. In the case of  $\text{LaN}_5$  particles the long time response yielded diffusion coefficients that were in agreement with independent NMR data; however, the short time range yielded deviating values that were attributed by the authors to a micro-roughness of the particles. In case of measurements with very smooth spherical Pd particles with a diameter of 520  $\mu\text{m}$  the authors obtained in both time domains diffusion coefficients of hydrogen that were in good agreement.

In a later study, Uchida et al. [B 78] investigated the electrochemistry of single particles of  $\text{LiCoO}_2$  and  $\text{LiMn}_2\text{O}_4$ . The size of the single particles was between 7 and 16  $\mu\text{m}$ . The measured currents were in the nA range. The authors emphasize that cyclic voltammetric measurements of single particles with scan rates between 1-10 mV/s yield information on the cycle performance of these battery materials because the entire volume of the particle is converted.

The same methodology has been applied by Perdicakis et al. [B 80] to study the voltammetric behavior of silver chalcogenide particles, i.e.,  $\text{Ag}_2\text{Se}$ ,  $\text{Ag}_2\text{Te}$ , and  $\text{Ag}_2\text{S}$ .

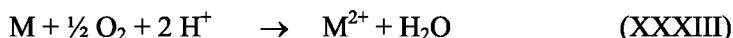
The examples published so far show that the advantages of performing the electrochemical measurement with just one particle are practically the

same as those performed with an array of well-separated particles immobilized on an electrode, as described in all the other parts of Chapter 5. Unfortunately, nobody has yet endeavored to use single particle measurements to study the relation between the shape and the size of single particles and their electrochemical response (see also Chapter 5.11).

## 5.9 Chemical and Enzymatic Conversion of Immobilized Particles

### 5.9.1 In Situ Studies

Electrochemical techniques can also be applied for monitoring chemical or biochemical reactions of powders when the latter are immobilized on an electrode surface. First, we shall discuss the case that a chemical dissolution of metal particles is followed by monitoring the potential of the electrode [B 84]. Let us consider the following dissolution of a metal M by oxygen that is present in the solution:



Assuming that the activity of the solid metal is unity, the so-called *stripping potential* is defined by the equation for an electrode of the first kind. The concentration of metal ions at the electrode surface depends on the flux of  $O_2$ . It can be assumed that for a stirred solution a steady-state is established and that the bulk concentration of metal ions is negligible as well as the concentration of  $O_2$  at the surface of the electrode. The stripping potential  $E_S$  of the diffusion-controlled metal oxidation depends on the bulk concentration of  $O_2$  as follows:

$$E_S = E_M^0 + \frac{RT}{2F} \ln c_{O_2}^* + \frac{RT}{2F} \ln \frac{2D_{O_2} \delta_M}{D_M \delta_{O_2}} \quad (5.22)$$

where  $D_{O_2}$ ,  $\delta_{O_2}$ ,  $c_{O_2}^*$ ,  $D_M$ , and  $\delta_M$  are diffusion coefficients, diffusion layer thicknesses and the bulk concentration of  $O_2$  and the metal ions, respectively. The stripping potential does not depend on the amount of metal immobilized on the electrode surface. Of course, the formation of metal complexes in solution would shift the stripping potential. The amount of immobilized metal determines the time that is necessary to dis-

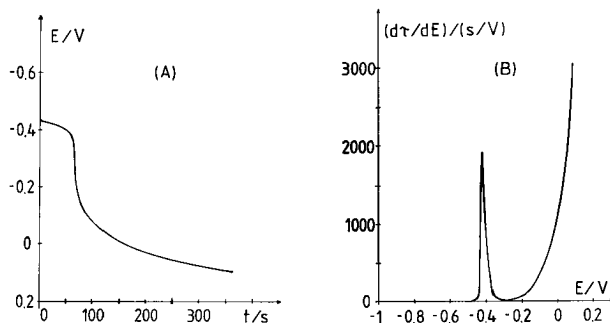


**Fig. 5.71.** Direct (A) and derivative (B) stripping chronopotentiogram of the dissolution of lead microparticles that have been transferred to a PIGE. The electrolyte was a 0.5 M NaClO<sub>4</sub> solution with a pH = 2 (HClO<sub>4</sub>). The oxygen concentration was  $2.6 \times 10^{-4}$  mol L<sup>-1</sup>. The initial potential was -1 V [B 84]

solve the metal in the oxidation reaction. The rate of dissolution depends on the concentration gradient of oxygen according to the equation:

$$\frac{\rho S}{M_M} \left( \frac{dl^*}{dt} \right) = - \frac{2SD_{O_2}c_{O_2}^*}{\delta_{O_2}} \quad (5.23)$$

when it is assumed in a first approximation that the metal forms a thin layer with a thickness  $l^*$  and a surface area  $S$ .  $M_M$  is the molar mass of the metal. The solution of Eq. 5.23 is as follows:

$$\tau = \frac{\rho \delta_{O_2} l^*}{2D_{O_2} M_M c_{O_2}^*} \quad (5.24)$$

$\tau$  is the so-called transition time determined from the potential versus time recording.

Figure 5.71 shows the direct and derivative stripping chronopotentiogram of dissolution of lead traces that have been transferred by the abrasive technique from a piece of lead to a PIGE electrode. Figure 5.72 depicts the dependence of the transition times on the number “rubbing circles” that have been performed to transfer lead from the piece of metal onto the PIGE. The latter correlation is remarkably good. From these experiments one can conclude that such chronopotentiometric measurements are suitable to study the amount of metals that are transferred in mechanical friction experiments. The second example of a study of a chemical conversion of immobilized microparticles concerns the enzymatic oxidation of quinhydrone [B 133]. Quinhydrone microcrystals have been immo-

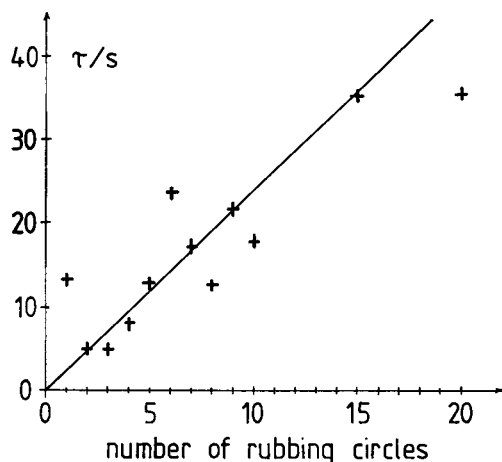


**Fig. 5.72.** Dependence of transition time  $\tau$  on the number of rubbing circles in which the lead was transferred from the piece of lead metal to the PIGE

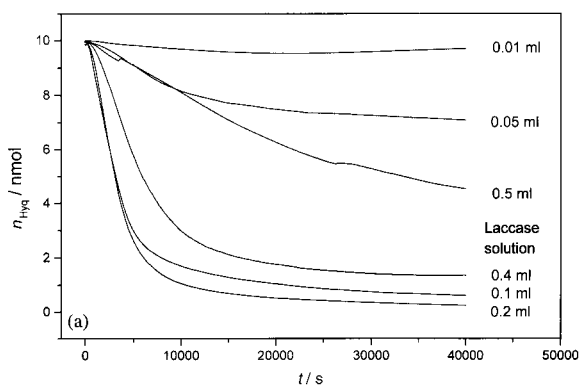


**Fig. 5.73.** The amount of hydroquinone at the electrode surface as a function of time of the enzymatic oxidation of immobilized quinhydrone for different additions of a laccase solution (the laccase solution had an activity of  $0.012 \text{ U ml}^{-1}$ ) [B 133]

bilized onto a gold electrode by evaporation of a solution in ethanol. Laccase, an enzyme isolated from cultures of the fungus *Pycnoporus cinnabarinus*, is capable of catalyzing the oxidation of hydroquinone and thus also that of quinhydrone to quinone. From the potential of the quinhydrone-modified electrode it is easy to calculate the amount of hydroquinone. Figure 5.73 shows the dependence of the amount of hydro-



quinone on the electrode surface as a function of time when the electrode is subjected to a laccase solution that was oxygen saturated. This figure shows that the laccase concentration clearly determines the rate of oxidation of hydroquinone. These two examples show that chronopotentiometry is a powerful technique for monitoring chemical and biochemical reactions of microparticles that are attached to the surface of electrodes.

### 5.9.2 Ex Situ Studies

The third example concerns a chemical reaction between dissolved ions (hexacyanoferrate(II) ions) and an oxide powder (goethite) and of a colloid (Prussian blue) and an oxide (goethite) [B 187]. These reactions are of some environmental interest because there are many places in industrial areas where the soil is contaminated with Prussian blue, esp. from coal gasification plants. To study these reactions, suspensions of goethite have been exposed to hexacyanoferrate(II) ions or Prussian blue colloidal solutions in a well-defined way. The reaction products were isolated and small amounts of the dry powders were immobilized on a PIGE. The electrochemical response of the immobilized microparticles proved that hexacyanoferrate(II) ions are sorbed on goethite. Figure 5.74 shows that the

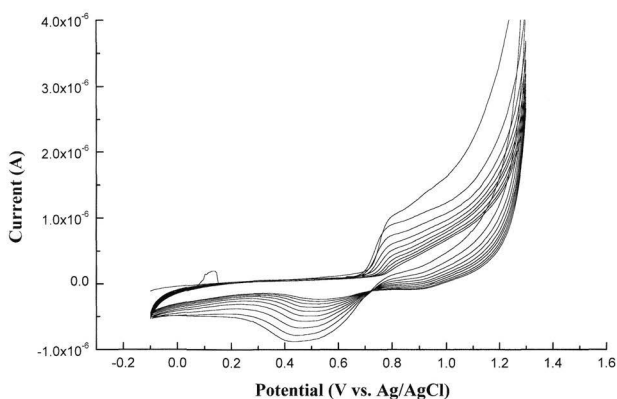


**Fig. 5.74.** Cyclic voltammogram of a goethite sample with a load of 6.05 g  $\text{CN}^-$  (as hexacyanoferrate)/kg goethite. Electrolyte 0.1 M KCl, scan rate  $0.05 \text{ V s}^{-1}$  [B 187]

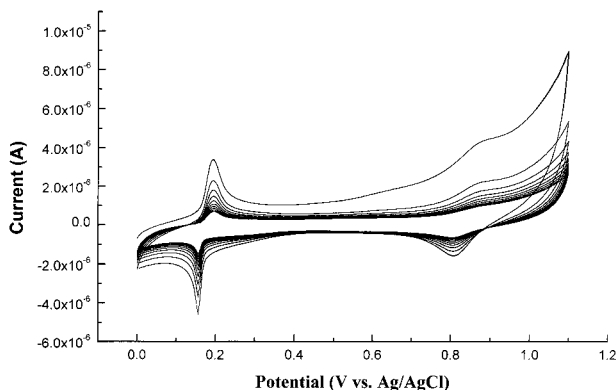


**Fig. 5.75.** Cyclic voltammogram of a goethite sample with a load of 36.7 g  $\text{CN}^-$  (as Prussian blue)/ kg goethite. Electrolyte 0.1 M KCl, scan rate  $0.05 \text{ V s}^{-1}$  [B 187]

goethite particles that were exposed to a hexacyanoferrate(II) solution exhibit a signal of highspin iron, but no signal of lowspin iron. This result is in line with spectroscopic results and indicates that the hexacyanoferrate ions are surface bound. The iron(III) ions on the goethite surface are not electroactive as they are in Prussian blue. Figure 5.75 depicts cyclic voltammograms of goethite powder that was exposed to a Prussian blue colloid. Clearly, the typical Prussian blue response is visible; however, the response decreases upon cycling. This bears witness of a rather low stability of the Prussian blue-goethite surface complex.

## 5.10 The Screening of Electrocatalysts

Electrocatalysts facilitate the electrochemical reduction or oxidation of dissolved compounds on electrodes by decreasing the overpotential, i.e., the activation barrier. Voltammetry of immobilized particles lends itself for the screening of potential electrocatalysts as it allows for a very quick comparison of their effectiveness. Later, the mechanical immobilization of a chosen electrocatalyst may even be used for the modification of working electrodes for analysis. Figure 5.76 shows the results of a search for the most effective electrocatalysts for hydrazine oxidation among many metal hexacyanoferrates.

Table 5.5 gives an overview on the analytical application of electrodes modified by immobilized particles for the sake of electrocatalytic determination of dissolved substrates.

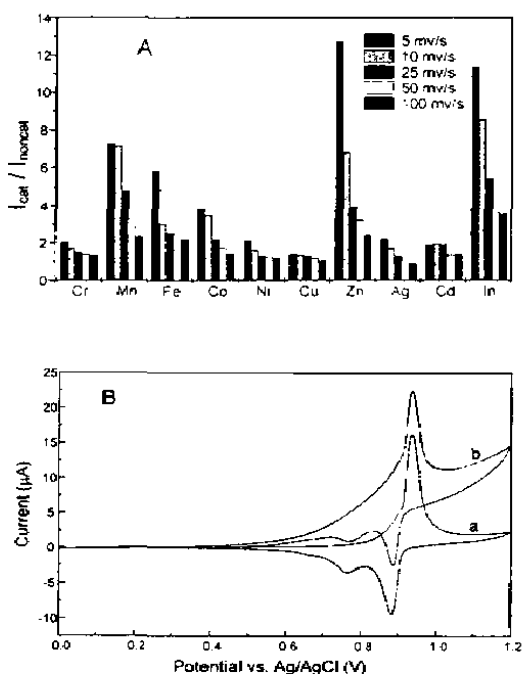


**Fig. 5.76. (A)** Comparison of the catalytic activities of metal hexacyanoferrates for the electrocatalytic oxidation of hydrazine at 700 mV vs. Ag/AgCl (3 M KCl). Electrolyte: 0.1 M  $\text{KNO}_3$ ; pH 6 (phosphate buffer); 1 mM hydrazine. The ratio of the catalytic to the noncatalytic current is given for different scan rates. **(B)** Cyclic voltammograms for the electrocatalytic oxidation of hydrazine (a) without and (b) with zinc hexacyanoferrate [B 113]

Kucernak et al. [B 147, 208, 243] have used the mechanical attachment of nanostructured platinum particles to studying their catalytic activity for hydrogen evolution and the electrooxidation of formic acid. They immobilized the particles on highly oriented pyrolytic graphite and polished gold electrodes. Rolison et al. [B 223] assessed the electrocatalytic properties of several metal and metal oxide particulate materials by immobilizing the compounds on the surface of carbon-wax composite electrodes that consisted of 35 wt.% carbon black (acetylene black) and 65 wt.% wax (eicosane, beeswax, or paraffin wax).

**Table 5.5.** Electrocatalysts applied in the form of particles immobilized on electrodes and substrates to be determined in analyses

Electrocatalyst	Substrate	Reference
metal hexacyanoferrates	hydrazine	B 13, B 202 B 253
ruthenium(III) diphenyldithiocarbamate	sulfhydryl compounds	B 98
copper hexacyanoferrate	cysteine	B 99
ruthenium(III) dithiocarbamate	ascorbic acid	B 100
nickel hexacyanoferrate	thiosulfate	B 130
copper hexacyanoferrate	sulfur dioxide	B 120
copper hexacyanoferrate	ascorbic acid	B 115
nickel hexacyanoferrate	sulfur dioxide	B 160
copper hexacyanoferrate	glutathione	B 199
nickel hexacyanoferrate	thiols	B 201
cobalt hexacyanoferrate	glutathione	B 212

## 5.11 Theoretical Aspects of the Voltammetry of Immobilized Particles

Parallel to the experimental studies, efforts have been made for a deeper understanding of the theoretical basis of electrochemical reactions of immobilized particles. At the beginning of the mathematical modeling the initial conditions and the models have to be defined. Since crystals have finite dimensions, a finite diffusion space has to be considered leading to voltammetric features that differ from those for semi-infinite planar diffusion. For this reason the following section starts with a voltammetric theory for a thin-layer cell.

### 5.11.1 Staircase Voltammetry with Finite Diffusion Space

Due to the digital data processing implemented in all modern voltammetric instrumentation it was necessary to model the theoretical response of a redox system confined to a finite diffusion space in staircase voltammetry. For this purpose a simple redox reaction proceeding in a thin-layer cell has been considered [B 64]:



The diffusion of the reactant and the product of this redox reaction in the space between two parallel planes is defined by the following differential equations:

$$\frac{\partial c_A}{\partial t} = D \frac{\partial^2 c_A}{\partial x^2}; \frac{\partial c_B}{\partial t} = D \frac{\partial^2 c_B}{\partial x^2} \quad (5.25)$$

with the initial and boundary conditions:

$$\begin{aligned} t = 0, 0 \leq x \leq L : c_A &= c_A^*, c_B = 0 \\ t > 0 : \left(\frac{\partial c_A}{\partial x}\right)_{x=0} &= \left(\frac{\partial c_B}{\partial x}\right)_{x=0} = 0; \\ \left(\frac{\partial c_A}{\partial x}\right)_{x=L} &= -\left(\frac{\partial c_B}{\partial x}\right)_{x=L} = -\frac{I}{nFS}; \\ \frac{I}{nFS} &= k_s \exp(-\alpha\varphi)[(c_A)_{x=L} - \exp(\varphi)(c_B)_{x=L}]; \quad \varphi = \frac{nF(E - E^\ominus)}{RT} \end{aligned} \quad (5.26)$$

Here,  $c_A$ ,  $c_B$  and  $c_A^*$  are concentrations,  $t$  and  $x$  are the time and space variables, respectively,  $L$  is the distance between the parallel planes,  $D$  is the diffusion coefficient,  $S$  is the electrode surface area,  $I$  is the current,  $E$  is the applied potential,  $E^\ominus$  is the standard redox potential of the couple A/B,  $k_s$  is the standard rate constant,  $\alpha$  is the electron transfer coefficient, while  $n$ ,  $F$ ,  $R$  and  $T$  have their usual meaning. If Reaction XXXIV is fast and reversible, the dimensionless peak currents of the cyclic staircase voltammograms are a function of the dimensionless thickness parameter  $\omega$  defined as  $\omega = 5L/\sqrt{Dt}$  with  $t = \Delta E/\nu$ ,  $\nu$  being the scan rate and  $\Delta E$  being the potential increment. This dependence has a sigmoidal shape as shown in Fig. 5.77. A characteristic feature of the staircase voltammograms obtained in a cell with  $\log(\omega) < 1.5$  is a decrease of the peak current followed by the vanishing of the voltammetric response for a very thin film. This is a consequence of the current sampling procedure in all staircase techniques. If all redox species inside the cell acquire the Nernst equilibrium before the sampling time, there will be no current to be measured at the end of the potential pulses, i.e., when the current is sampled. When Reaction XXXIV is controlled by the kinetics of charge transfer, the voltammetric features are additionally controlled by the dimensionless kinetic parameter  $\lambda$  defined as  $\lambda = k_s\sqrt{t}/\sqrt{D}$ . The influence of the redox kinetics depends on the cell thickness depicted in Fig. 5.78. For films with moderate thicknesses

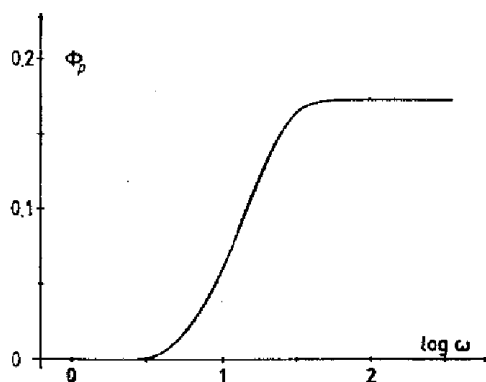


**Fig. 5.77.** Theoretical dependence of the dimensionless peak current  $\Phi_p$  of a reversible reaction on the logarithm of the dimensionless thickness parameter  $\omega$  of the cell. The potential increment was  $\Delta E = 5$  mV [B 64]

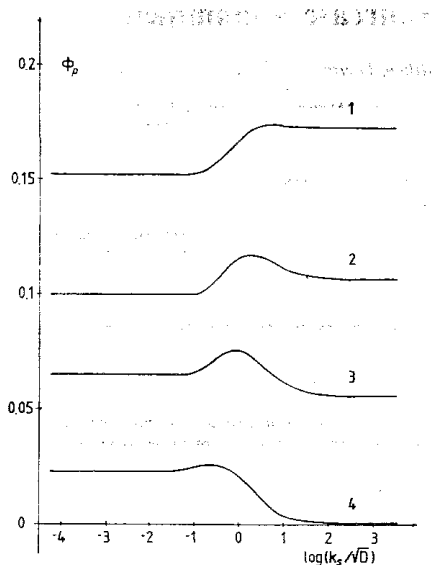


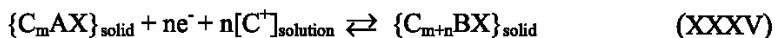
**Fig. 5.78.** Dependence of the dimensionless peak currents on the logarithm of the standard rate constant.  $\Delta E = 5$  mV,  $\nu = 50$  mV/s;  $5LD^{-0.5}/s^{0.5} = 100$  (1), 5 (2), 3 (3) and 1 (4) [B 64]

(curves 2 and 3 in Fig. 5.78) there is a parabolic dependence of the dimensionless peak currents on  $\lambda$ . This feature is well known for surface-confined redox reactions as a so-called quasireversible maximum. It is used for determining the standard rate constant  $k_s$ . The quasireversible maximum, together with the narrower peak-to-peak separation distinguishes the models of finite diffusion space from those with semi-infinite planar diffusion.

### 5.11.2 The Propagation of a Redox Reaction through Microcrystals

A key issue for understanding the voltammetry of microparticles is the propagation of a redox reaction through the microcrystals. It is reasonable to assume that the Nernst equilibrium is initially established at the *three-phase junction*, where the particle, the solution, and the electrode meet. The reaction starts at this junction line and from this locus it may advance along the surface and into the particle.

Chronoamperometry has been considered in a first attempt to theoretically tackle the question of the propagation of a redox reaction through a microcrystal [B 69]. In order to solve the problem of the coupled transport of electrons and ions an infinite crystal attached to an infinite electrode surface has been chosen (cf. Fig. 5.79). The axis  $z$  coincides with the three-phase junction. The electrode surface is located in the  $x$ - $z$  plane, and its body lies in the space for  $y < 0$ . The remaining space ( $y > 0$ ) is divided between the crystal ( $x > 0$ ) and the solution ( $x < 0$ ). It is assumed that the Nernst equilibrium of the insertion electrochemical reaction



is initially established along the axis  $z$ , where both electrons and ions are immediately available. Thereafter, the current is conducted along the crystal surface. This surface redox reaction creates a gradient of electrochemical potential and defines the initial conditions for the diffusion of ions into the crystal. The fluxes of electrons and ions inside the solid particle are perpendicular to each other. The surface diffusion of the electrons is described by the differential equation of Eq. 5.27.

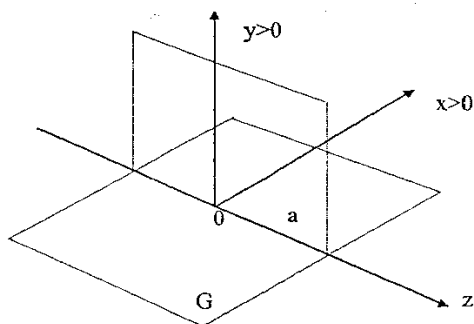


Fig. 5.79. Coordinate system with a part of the crystal|solution interface (a) and a part of the electrode graphite surface (G) [B 69]

$$\frac{\partial \Gamma_B}{\partial t} = D_e \frac{\partial^2 \Gamma_B}{\partial y^2} \quad (5.27)$$

with the following initial and boundary conditions:

$$\begin{aligned} t = 0, y \geq 0 : \Gamma_B = 0, \Gamma_A = \Gamma; \quad t > 0, y \rightarrow \infty : \Gamma_B \rightarrow 0, \Gamma_A \rightarrow \Gamma; \\ y \geq 0 : \Gamma_A + \Gamma_B = \Gamma; \quad y = 0 : \Gamma_{A,y=0} = \Gamma_{B,y=0} \exp(\varphi); \\ \varphi = \frac{nF(E - E_c^{st})}{RT}; \quad \frac{I_s}{nFbD_e} = -\left(\frac{d\Gamma_B}{dy}\right)_{y=0} \end{aligned} \quad (5.28)$$

where  $\Gamma_A$  and  $\Gamma_B$  are the surface concentrations of ions A and B, and  $\Gamma$  is the total surface concentration.  $D_e$  is a diffusion coefficient of the electrons,  $I_s$  is the surface component of the current and  $b$  is the length of the contact between the electrode, the crystal and the solution. In chronoamperometry the solution for the *surface current* is given by:

$$I_s = nFb\Gamma[1 + \exp(\varphi)]^{-1} \sqrt{\frac{D_e}{\pi t}} \quad (5.29)$$

Equation 5.29 implies that the *surface current* depends of the diffusion coefficient of the electrons, and it decreases with the square-root of time. Within the solid particle, the diffusions of electrons (i.e., here the propagation of electrons by hopping) and ions are coupled. The advancement of electrons is slower than at the surface since they must wait for ions (supposed that ion diffusion is slower than electron self-exchange). The diffusion of ions is described by the following differential equation:

$$\frac{\partial c_B}{\partial t} = D_C \frac{\partial^2 c_B}{\partial x^2} \quad (5.30)$$

which was solved for the following initial and boundary conditions:

$$\begin{aligned} t = 0, x \geq 0 : c_B = 0, c_A = \rho_d; \\ t > 0, x \rightarrow \infty : c_B \rightarrow 0, c_A \rightarrow \rho_d; \quad x \geq 0 : c_A + c_B = \rho_d; \\ y = 0 : x = 0 : (c_A)_{x=0,y=0} = (c_B)_{x=0,y=0} \exp(\varphi); \\ x = 0 : (c_B)_{x=0} = \rho_d [1 + \exp(\varphi)]^{-1} \operatorname{erfc}[0.5y(D_e t)^{-0.5}] \\ \frac{dI_c}{dS} = -nFD_C \left(\frac{\partial c_B}{\partial x}\right)_{x=0}; \quad dS = bdy \end{aligned} \quad (5.31)$$



Here,  $D_C$  is the diffusion coefficient of the ions,  $I_c$  is a volume component of the current, while  $S = by$  is the surface area of the crystal which is exposed to the solution and  $\rho_d$  is a common density ( $\text{mol}/\text{cm}^3$ ). The concentration of the product B and the current within the crystal are obtained as follows:

$$c_b = \frac{\rho_d}{1 + \exp(\varphi)} \operatorname{erfc}([0.5x(D_C t)^{-0.5}] + [0.5y(D_C t)^{-0.5}]) \quad (5.32)$$

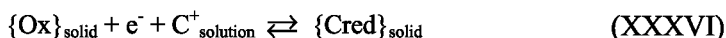
$$\frac{dI_c}{dS} = \frac{nF\rho_d\sqrt{D_C}}{1 + \exp(\varphi)} \frac{1}{\sqrt{\pi t}} \exp\left(-\frac{y^2}{4D_C t}\right) \quad (5.33)$$

Equation 5.32 shows that the product of Reaction XXXV appears primarily near the two crystal surfaces: the one which faces the solution ( $x = 0$ ) and the one which is in contact with the electrode ( $y = 0$ ). In both planes the concentration of the product decreases with the distance from the three-phase boundary, i.e., it propagates through the body of the crystal. Equation 5.33 shows that the current density is highest at the contact line  $b$ , where  $y = 0$ , and decreases along the crystal surface. Equations 5.27 and 5.30 have also been solved for conditions of single scan and cyclic voltammetry. In both cases the solutions give a steady-state current because of the infinite volume of the crystal. Since Eq. 5.32 implies that Reaction XXXV propagates through the crystal, a term of the *advancing front* has been introduced to depict this propagation. In the case that both the surface and the bulk (volume) reaction proceed at comparable rates, the reaction front expands from the three-phase boundary as a space with exponential borderlines in the  $x$  and  $y$  directions. Generally, the total current is the sum of the surface and the volume current. The reaction will be surface confined when the diffusion of the ions inside the crystal is hindered, and the surface current will be negligible when the volume reaction is dominating. *In any case, the three-phase junction is the starting point for the reaction front independent of the geometry of the particle and its conductivity.* Qualitatively, the same results have been obtained by using a rigorous model for the coupled diffusions of electrons and ions in two directions by using the lattice-gas concept without interactions [B 107]. By that model, it has been shown that the surface and the volume currents depend on Wagner's thermodynamic factor ( $W$ ) of electrons and ions. The Wagner factor is defined as  $W = 1 + \partial \ln(\gamma) / \partial \ln(c)$  where  $\gamma$  is the activity coefficient and  $c$  is the concentration. The transport in direction perpendicular to the electrode surface depends on the Wagner factor of electrons, while the transport parallel to the electrode surface depends on the Wagner factor of ions.

The final mathematical solutions of both models under conditions of chronoamperometry, single scan and cyclic voltammetry are given elsewhere [B 69 and 107] and can be applied directly in any appropriate mathematical program.

### 5.11.3 The Effect of the Electrolyte Concentration on the Voltammetric Response of Insertion Electrodes

In the previous model of insertion electrochemical reactions with coupled ion and electron transfer the solution side has been neglected. However, under certain conditions that may not be justified. Therefore, the following model has been developed: a conductive cylinder of the solid compound is embedded in the surface of the electrode in a way that only a circular surface of the cylinder is exposed to the solution. This surface is positioned at  $x = 0$ ,  $x$  being positive inside the crystal and negative inside the solution. Assuming the insertion electrode to be of the type [B 87]



in which cations can diffuse through the crystal surface along the longitudinal axis of the cylinder, the mass transport can be described by planar semi-infinite diffusion of cations in two media, the solution ( $x \leq 0$ ) and the crystal ( $x \geq 0$ ). This will be valid only if the longitudinal axis in the crystal is longer than the diffusion layer in the particle. By solving the differential equation

$$\frac{\partial c}{\partial t} = D \frac{\partial^2 c}{\partial x^2} \quad (5.34)$$

where  $D = D_{\text{aq}}$  and  $c = [\text{C}^+]$  if  $x \leq 0$ , and  $D = D_{\text{ss}}$  and  $c = [\text{C}_{\text{red}}]$  if  $x \geq 0$ .  $D_{\text{aq}}$  and  $D_{\text{ss}}$  are the diffusion coefficients of the cations in aqueous solution and in the crystal, respectively. The starting and the boundary conditions for Eq. 5.34 are:

$$\begin{aligned} t = 0, x \geq 0 : [\text{Cred}] = 0, [\text{Ox}] = \rho; \quad x \leq 0 : [\text{C}^+] = [\text{C}^+]^* \\ t > 0, x \rightarrow -\infty : [\text{C}^+] \rightarrow [\text{C}^+]^*; \quad x \geq 0 : [\text{Cred}] + [\text{Ox}] = \rho; \\ x \rightarrow \infty : [\text{Cred}] \rightarrow 0; [\text{Ox}] \rightarrow \rho; \quad x = 0 : \frac{I}{D_{\text{ss}}FS} = - \frac{\partial [\text{Cred}]}{\partial x}; \end{aligned} \quad (5.35)$$

$$\frac{I}{D_{\text{aq}}FS} = - \frac{\partial [\text{C}^+]}{\partial x}; [\text{Ox}] = [\text{red}^-] \exp\left[\frac{F(E - E^{\ominus})}{RT}\right]; \quad K = \frac{[\text{Cred}]}{[\text{red}^-][\text{C}^+]}$$

where  $[C^+]$ \* is the concentration of cations in the bulk of the solution, and the meaning of the other symbols is as in the previous models.  $K$  is the equilibrium constant for  $\{\text{red}\}_{\text{solid}} + C^+ \rightleftharpoons \{\text{Cred}\}_{\text{solid}}$ . In the mathematical solution of the differential Eq. 5.34 two important parameters containing the term of  $[C^+]$ \* appear, i.e., the formal potential  $E_c^{\ominus}$  and the mass transfer parameter  $z$ , defined as:

$$E_c^{\ominus} = E_{\text{Ox/red}}^{\ominus} + \frac{RT}{F} \ln K + \frac{RT}{F} \ln [C^+]* \quad (5.36)$$

$$z = \sqrt{\frac{D_{\text{ss}}}{D_{\text{aq}}}} \frac{\rho}{[C^+]*} \quad (5.37)$$

Cyclic voltammograms obtained from this model depend on the mass transfer parameter  $z$ . The dependence of cathodic and anodic peak potentials and of their median on  $\log(z)$  are depicted in Fig. 5.80, while in Fig. 5.81 is given the dependence of the cathodic and anodic peak currents as a function of the same parameter.

For  $z < 0.1$  the voltammograms are independent of the mass transfer in solution. In that case the median of the peaks is equal to the formal potential, i.e.:

$$\bar{E} = E_{\text{Ox/red}}^{\ominus} + \frac{RT}{F} \ln K + \frac{RT}{F} \ln [C^+]* \quad (5.38)$$

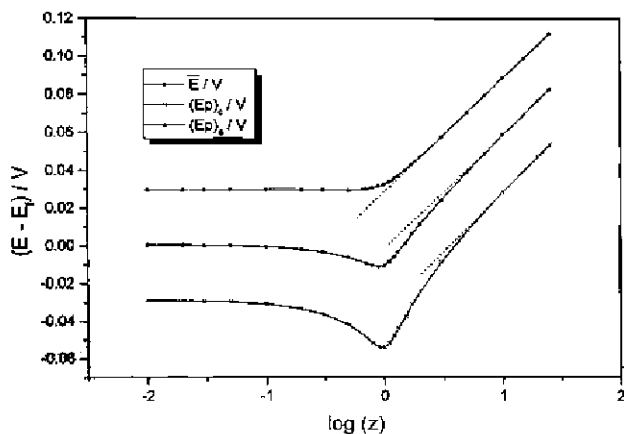


**Fig. 5.80.** Dependence of the anodic and cathodic peak potentials  $(E_p)_a$  and  $(E_p)_c$ , respectively, and their median  $\bar{E}$  on the logarithm of the mass transfer parameter  $z$  [B 87]

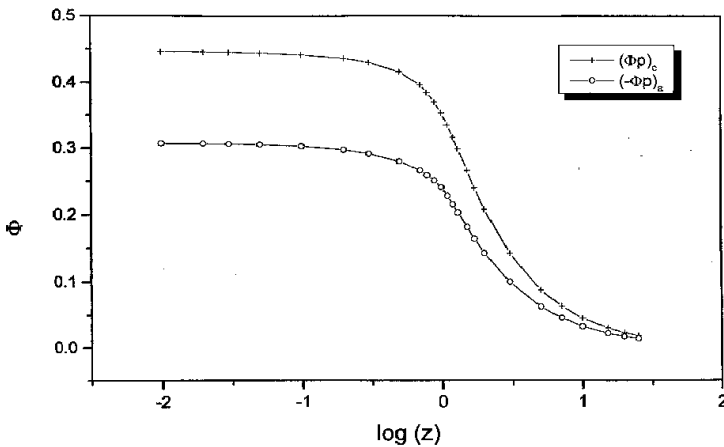


**Fig. 5.81.** Dependence of the absolute values of dimensionless anodic peak currents  $(\Phi_p)_a$  and cathodic peak currents  $(\Phi_p)_c$  on the logarithm of the mass transfer parameter  $z$  [B 87]

Under experimental conditions, such a situation exists if the concentration of the cations in the aqueous solution exceeds  $1 \text{ mol L}^{-1}$ . If  $z > 10$ , the median depends linearly on  $\log(z)$  with a slope of 59 mV and the intercept is equal to:

$$E - E_c^{\ominus'} = 2.3 \frac{RT}{F} \log z \quad (5.39)$$

Then, the median does not depend on  $[C^+]^*$  and is given by:

$$\bar{E} = E_{\text{Ox/red}}^{\ominus} + \frac{RT}{F} \ln K + \frac{RT}{F} \ln \rho + \frac{RT}{2F} \ln \frac{D_{\text{ss}}}{D_{\text{aq}}} \quad (5.40)$$

Equation 5.40 has been obtained by combining the Eqs. 5.36–5.39. However, if  $z > 10$ , the voltammograms vanish. The dependencies given in Fig. 5.81 can be used for the determination of  $D_{\text{ss}}$  [B 95]. The described theory has been successfully applied to decide whether the diffusion of  $\text{OH}^-$  in solution or in a  $\text{RuO}_2\text{-PVC}$  film electrode controls the rate of the electrode process<sup>7</sup>.

<sup>7</sup> Dharuman V (2001) A study of reaction mechanisms at  $\text{RuO}_2\text{-PVC}$  and  $\text{RuO}_2\text{-NAFION}$  film electrodes: Electrooxidation of glucose, catechol and L-dopa. PhD thesis, University of Madras, Madras

### 5.11.4 Solid State Voltammetry at a Three-Phase Junction

Oldham has mathematically modeled the processes occurring at microparticle modified electrodes [B 88]. He developed a model to address such important issues, as the possible magnitude of currents and the shape of voltammograms that can be expected when the electrochemical reaction is *exclusively* confined to the three-phase junction. The author has not considered the intriguing and important question of how the cations spread inside the crystal, once they have entered it via the three-phase junction. This spreading has been assumed to be so rapid that their concentration is always uniform throughout the crystal. This is more a limiting case than a realistic description of real experiments. It is, however, of interest to determine the extent to which diffusion can supply ions to, or remove them from a three-phase junction. The key question is whether the bottleneck three-phase junction will allow obtaining measurable voltammetric responses.

For this, the insertion electrochemical Reaction XXXV has been considered. The diffusion has been supposed to occur under cylindrical conditions and therefore the cylindrical version of the differential equation of Fick's second law

$$\frac{\partial^2 c}{\partial r^2} + \frac{1}{r} \frac{\partial c}{\partial r} = \frac{1}{D} \frac{\partial c}{\partial t} \quad (5.41)$$

has been solved for the two cases: a) assuming a constant concentration of cations at the three-phase junction, and b) assuming a variable concentration of cations at the three-phase junction line. In both cases qualitatively similar results have been obtained.

The current density  $i$  obtained by solving Eq. 5.41 has the form:

$$i = \frac{-\pi F D (c^b - c^j)}{\ln \left\{ \frac{\eta \sqrt{D t}}{a} \right\}} \quad (5.42)$$

where  $c^j$  is the concentration of the cations at the three-phase junction line,  $c^b$  is the bulk concentration of cations in the solution,  $a$  is the distance of the three-phase junction at which a diffusing species has reached the three-phase junction ( $a$  has a magnitude of atomic dimensions), and  $\eta$  is defined as  $\eta = 2 \exp(-\gamma) = 1.123\dots$ , where  $\gamma$  is the Euler constant,  $\gamma = 0.57722$ . The meaning of other symbols is as usual. The weak inverse logarithmic dependence of the current density on time, for all periods of voltammetric significance, implies that the current is almost steady-state throughout any practicable experiment. In order to apply Eq. 5.42 to voltammetric pur-

poses, one needs to estimate the length of the three-phase junction. If a total volume of the electroactive solid is  $V$ , and if it consists of isolated, uniformly sized cubes of edge length  $L$ , each cube resting on the electrode via one of its faces. Then, the number of the cubes will be  $VL^{-3}$ , while the total length of the three-phase junction is  $4VL^{-2}$ . By multiplying this term with Eq. 5.42, one obtains the following equation for the current as a function of the length of the cube edges:

$$I = \frac{-2\pi F D V (c^b - c^j)}{L^2 \ln \left\{ \frac{\eta \sqrt{D t}}{a} \right\}} \quad (5.43)$$

This equation shows that after subdivision of the solid crystal, the three-phase junction length is a predominant parameter determining the magnitude of the total current. Using the constant values for the other parameters in Eq. 5.43, the values of the current estimated for different values of  $L$  are given in Table 5.6. The column headed by “#” represents the number of the cubes according to this model. Table 5.6 confirms that significant currents can flow into an adherent electroactive solid via the three-phase junction line, especially when the crystals are sufficiently small and numerous. The parameter  $t_{\min}$  in Table 5.6 is very important since it represents the minimum time in which total reduction can be achieved. Typical times corresponding to voltammetric experiments are encountered for  $L$  being a few micrometers.

**Table 5.6.** Dependence of the current  $I$  on the edge length  $L$  of the crystal cubes.  $L$  is the edge length of cubes, # denotes the number of cubes,  $I$  is the overall steady state current, and  $t_{\min}$  is the time necessary for total reduction [B 88]

$L/\mu\text{m}$	#	- $I$	$t_{\min}/\text{s}$
464	1	1.2 nA	$3.4 \times 10^6$
215	10	5.6 nA	$7.4 \times 10^5$
100	100	26 nA	$1.6 \times 10^5$
46	$10^3$	0.12 $\mu\text{A}$	$3.4 \times 10^4$
22	$10^4$	0.56 $\mu\text{A}$	$7.4 \times 10^3$
10	$10^5$	2.6 $\mu\text{A}$	$1.6 \times 10^3$
4.6	$10^6$	12 $\mu\text{A}$	340
2.2	$10^7$	56 $\mu\text{A}$	74
1.0	$10^8$	0.26 mA	16
0.46	$10^9$	1.2 mA	3.4
0.22	$10^{10}$	5.6 mA	0.74
0.10	$10^{11}$	26 mA	0.16

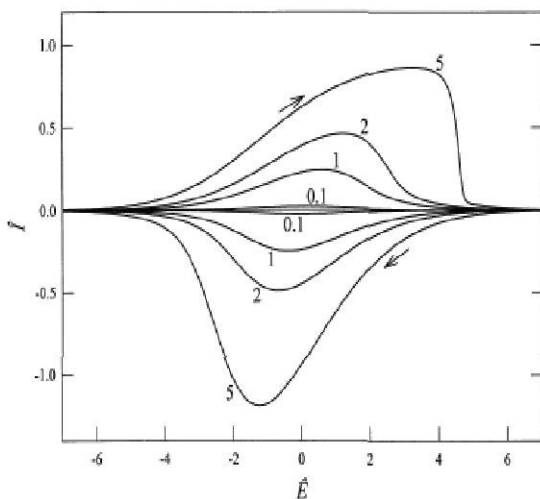


**Fig. 5.82.** Cyclic voltammograms obtained for several rather slow scan rates [B 88]

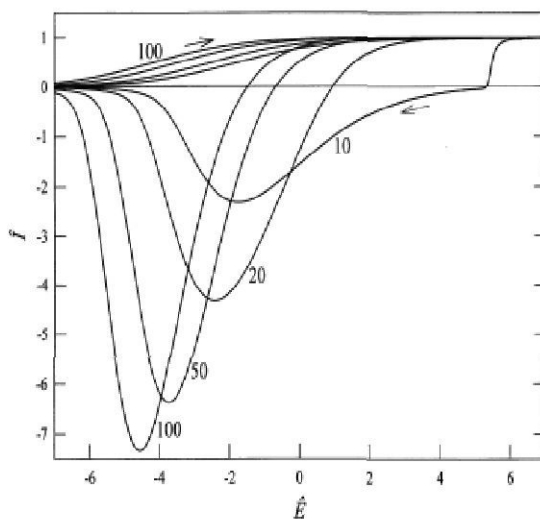


**Fig. 5.83.** Cyclic voltammograms obtained for scan rates one range of magnitude faster than that presented in Fig. 5.82 [B 88]

Applying the solution of Eq. 5.41 under conditions of cyclic voltammetry, the scan rate is the major parameter that determines the shape of the cyclic voltammograms. Two types of theoretical voltammograms obtained with slow and fast scan rates are depicted in Figs. 5.82 and 5.83, respectively. Their shape considerably differs from what is common in solution electrochemistry. At the slowest scan rates (see Fig. 5.82) the cyclic voltammograms have inversion symmetry about the origin and resemble their counterparts for reversible thin-layer voltammetry. Another similarity to thin-layer cyclic voltammetry is in having peak heights proportional to the scan rate. These similarities are expected since in both cases there is a limited amount of material, which can exhaustively be reduced. In the voltammo-

grams obtained at rather low scan rates the current is close to zero at the right-hand side of each plot, since at these positive potentials the solid is totally oxidized. When the dimensionless scan rate is as large as 10, the total reduction is delayed until after reversal (cf. Fig. 5.83). At faster scan rates the total reduction is never approached under CV conditions. Considerably higher anodic currents are flowing, but for shorter periods. The reason for that is that the junction concentration  $c^j$  can decrease to zero upon reduction, but can exceed  $c^b$  many-fold during anodization. This is equivalent with the idea that the ions can escape from the crystal through the three-phase junction much faster than they can enter the crystal from solution. The model has been solved also for the conditions of chronoamperometry (at constant potential). The main result obtained in this study is that the diffusion to a three-phase junction can provide an adequate supply of ions to permit classical voltammetric techniques to be applied within the time and current ranges traditionally used. The supply of ions to the three-phase junction seems to be in a quasi steady-state during the electrochemical experiments. If the voltammetry is reversible, the response is predicted to be very dependent on the degree of subdivision of the crystals. Depending on the crystal size and scan rate, cyclic voltammograms may mimic solution phase voltammograms of classical thin-layer experiments or typical stripping experiments. This model, despite of its limitations, clearly demonstrates that the role of the three-phase junction must not be overlooked in modeling the voltammetry of solids.

### 5.11.5 The Effect of Crystal Size and Shape on Electrochemical Signals

The electrochemical reduction of a microcrystal attached to an electrode has been theoretically described by the help of two- and three-dimensional models [B 142]. An electrochemically reversible reduction of redox centers in a crystal followed by insertion of cations from the adjacent aqueous phase can be described by Reaction XXXVI [B 69]. The authors have considered a model where the simultaneous uptake of electrons and cations starts at the three-phase junction line. They have utilized two- and three-dimensional models to simulate the diffusion of cations and electrons and the current flow in response to the applied potential. A scheme of the two-dimensional matrix used in the simulations is given in Fig. 5.84. The total flux of electrons and cations is a function of the concentration gradients between each box ( $k$ ,  $m$ ) and its two neighbor boxes. Both fluxes follow Fick's first diffusion law (Eq. 5.44), where  $\Delta N$  represents the change of the



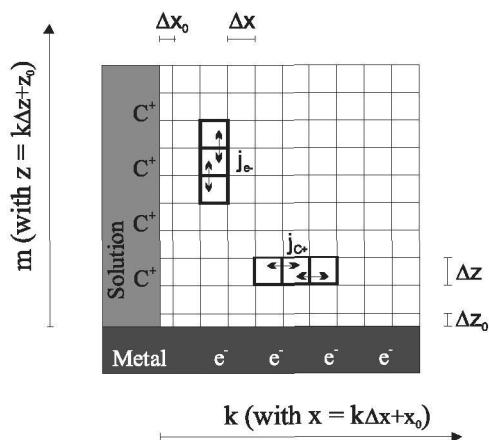


**Fig. 5.84.** Two-dimensional matrix of discrete boxes with  $\Delta x \Delta z$  being the size of the bulk boxes,  $\Delta x_0 \Delta z$  and  $\Delta x \Delta z_0$  being the size of the surface boxes and  $\Delta x_0 \Delta z_0$  representing the three-phase junction [B 142]

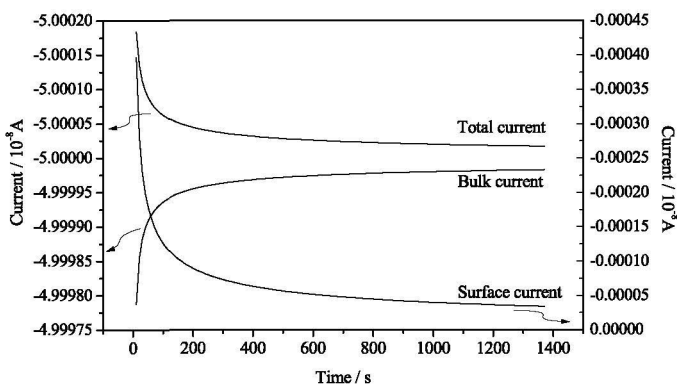


**Fig. 5.85.** Chronoamperogram for a potential step of a value 200 mV more negative than the formal potential of Reaction XXXVI.  $D_{e^-} = D_{C^+} = 5 \times 10^{-8} \text{ cm}^2 \text{ s}^{-1}$ ;  $\Delta x_0 = \Delta z_0 = 10^{-4} \Delta x$  [B 142]

$$j_{C^+} = \frac{1}{Y \Delta z} \frac{\Delta N}{\Delta t} \quad (5.44)$$

$$j_{e^-} = \frac{1}{Y \Delta x} \frac{\Delta N}{\Delta t} \quad (5.45)$$

moles of cations or electrons and  $Y$  is the length of the infinite three-phase junction, defined similarly as given in Fig. 5.84. Equations 5.44 and 5.45 imply that both currents, i.e., the surface (due to the electron diffusion) and bulk (or volume) currents (due to the cations diffusion) are considered

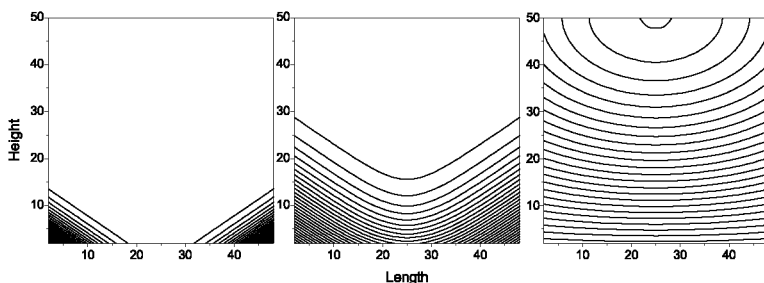


**Fig. 5.86.** Concentration profiles of a partially converted two-dimensional microcrystal at different times after a potential step A) 3 s, B) 10 s and C) 40 s.  $D_{e^-} = 5 \times 10^{-9} \text{ cm}^2 \text{ s}^{-1}$ ;  $D_{C^+} = 10^{-8} \text{ cm}^2 \text{ s}^{-1}$  [B 142]

separately in this model. The two- and three-dimensional models have been solved for the conditions of chronoamperometry by considering a semi-infinite diffusion space as well as a finite diffusion space. The main feature of the chronoamperometric plot is for the two-dimensional model and semi-infinite diffusion that the total current approaches a steady-state value (see Fig. 5.85). The time dependence of the total current is:

$$I(t) = \frac{FY}{V_m} \left\{ \frac{1}{1 + \exp(-\varphi)} \right\} \left[ \left( \frac{\Delta x_0 \sqrt{D_{e^-}} + \Delta z_0 \sqrt{D_{C^+}}}{2\sqrt{\pi t}} \right) + \sqrt{D_{C^+} D_{e^-}} \right] \quad (5.46)$$

Here,  $V_m$  is the molar volume, while  $\varphi$  is the dimensionless potential of the Nernstian equation representing the thermodynamic equilibrium of Reaction XXXVI.  $D_{e^-}$  and  $D_{C^+}$  are the diffusion coefficients of electrons and cations inside the crystal. The increasing of the bulk current in Fig. 5.85 can be ascribed to the growing of the reaction zone as shown in Fig. 5.86A.

The semi-infinite diffusion model applied to the three-dimensional model is more realistic since for real cuboid crystals the three-phase junctions of these objects include the edges of the rectangular base. The consequence of this is that the cations in the real three-dimensional system can enter the crystal from different directions. The total current in this three-dimensional model has the following form:

$$I(t) = \frac{F}{V_m} \left\{ \frac{1}{1 + \exp(-\varphi)} \right\} \left[ Y \left( \left( \frac{\Delta x_0 \sqrt{D_{e^-}} + \Delta z_0 \sqrt{D_{C^+}}}{2\sqrt{\pi t}} \right) + \sqrt{D_{C^+} D_{e^-}} \right) - D_{C^+} \sqrt{2t D_{e^-}} \right] \quad (5.47)$$

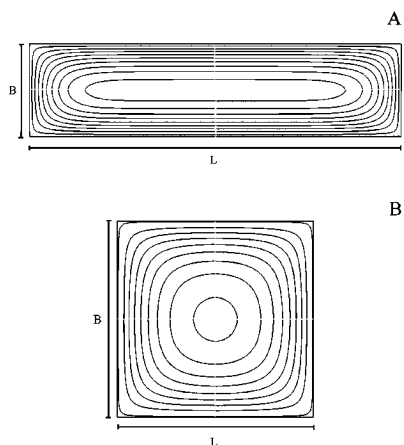


**Fig. 5.87.** Concentration profile inside partially (10 %) converted crystals: cross-section through  $x$ - $y$  plane at half height; **A** crystal of  $L = H = 10 \mu\text{m}$ ,  $B = 40 \mu\text{m}$  and **B**  $L = B = H = 10 \mu\text{m}$  size [B 142]

Compared to the expression of the current in the two-dimensional model (Eq. 5.46) the three-dimensional model (Eq. 5.47) has an additional subtractive term. This has been interpreted as an “edge effect” describing the overlapping of the cation diffusion (which now proceeds in  $x$  and  $y$  directions) near the corner and thereby its influence on the entire diffusion process. Equations 5.46 and 5.47 are a consequence of the diffusion of electrons and cations into a semi-infinite space. This diffusion is accompanied by the growing of the reaction zone and it is not exclusively confined to a real semi-infinite diffusion space, but can also be expected to apply to the beginning of the conversion of a crystal of limited size. Since the crystal considered in the simulation has a very small size (some  $\mu\text{m}$ ) and a time scale was assumed where total conversion of material may take place, an unhindered diffusion is expected only for the initial period of the reaction. Now, the most important question is: how do the diffusion barriers given with the crystal size and shape determine the advancement of the electrochemical conversion through the crystal? For a certain geometry (cube or cuboid) of the microcrystal, the ratio  $D_e/D_{C+}$  determines the spatial course of the development of the reaction zone and thereby the resulting current-time functions. In Fig. 5.87, the isoconcentration lines along the  $(x, y)$  plane at half height are depicted for two differently shaped cuboids after a partial reduction of the particle. The progress of the reaction zone in such situation follows different geometries, causing tremendous changes in the chronoamperometric curve. This is also obvious from the different shapes of the cyclic voltammograms given in Fig. 5.88. The voltammograms are a result of a cyclic oxidation and reduction of differently shaped cuboids of a uniform volume. Depending on the ratio of crystal height to length and width, different diffusion regimes dominate and determine the time for

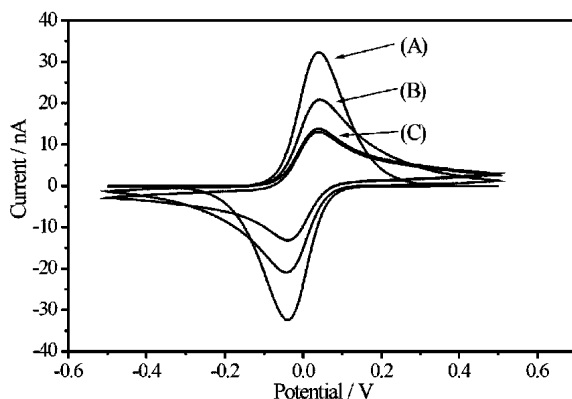


**Fig. 5.88.** Cyclic voltammograms of differently shaped cuboid particles of constant volume with a square base of different size; Concentration profile inside partially (10 %) converted crystals: cross section through x-y plane at half height;  $D_e = D_{C^+} = 10^{-8} \text{ cm}^2 \text{ s}^{-1}$ ,  $V_m = 153.8 \text{ cm}^3 \text{ mol}^{-1}$ ; (A) crystal of  $L = B = 28 \text{ }\mu\text{m}$ ,  $H = 10 \text{ }\mu\text{m}$ , (B)  $L = B = H = 20 \text{ }\mu\text{m}$ ; (C)  $L = B = 16 \text{ }\mu\text{m}$ ,  $H = 31 \text{ }\mu\text{m}$  [B 142]

the total conversion of the solid. The geometry of the spatial development of the reaction zone additionally depends on the ratio of the diffusion coefficients of the electrons and cations. Due to the different values of diffusion coefficients of electrons and cations, the reaction at the three-phase boundary only initially determines the course of the reaction. During the initial three-phase reaction, the faster process leads to an exhaustive conversion along the corresponding interface either the crystal|electrode, or the crystal|solution interface. The further course of the conversion is determined by the slowest diffusion process. In principle, the results of this study [B 142] can be utilized for determining the diffusion coefficients from experimental data and to derive the geometric parameters of the attached crystals. This, however, would require experiments with single size and single shaped crystals. In reality there will always be a size and shape distribution for which a theory still needs to be developed.

### 5.11.6 Redox Mixed Phases and Miscibility Gaps

In all previously considered reactions of type XXXVI it was assumed that the solid phase transforms in a series of completely miscible solid solutions from {ox} into the final form { $C_n$ red}. In fact, in intercalation electrochemistry there are known many examples in which a continuous series of mixed crystals exists between the oxidized and reduced forms. Several hexacyanometalates are discussed as examples in Chapter 5.3. The phase

transformation of {ox} to {C<sub>n</sub>red} via {ox<sub>x</sub>(C<sub>n</sub>red)<sub>1-x</sub>} gives an opportunity to describe these processes on the basis of mixed phase thermodynamics. The model of *redox* mixed phases (*redox* solid solutions) allows treating also cases with miscibility gaps that frequently occur in solid systems. Considering only the thermodynamic conditions in the solid phases, Reaction XXXVI can be defined as follows:

$$c_{\text{ox}} + c_{\text{red}} = \rho; c_{\text{ox}} = c_{\text{red}} \exp(\varphi); \varphi = \frac{nF}{RT} (E - E_c^{\theta'}) \quad (5.48)$$

In the case of partial miscibility of {ox} and {C<sub>n</sub>red}, the formal concentrations  $c_{\text{ox}}$  and  $c_{\text{red}}$  are linked to the molar fractions of the corresponding compounds via the following relations:

$$c_{\text{ox}} = \frac{m_{\text{ox}}}{m_{\text{ox}} + m_{\text{red}}}; c_{\text{red}} = \frac{m_{\text{red}}}{m_{\text{ox}} + m_{\text{red}}} \quad (5.49)$$

where  $m_{\text{ox}}$  and  $m_{\text{red}}$  are mole numbers of {ox} and {red}, respectively. If the mutual solubility is limited, the concentrations (or more precisely activities) of both components can be changed only within a restricted range. Consequently, the Nernst equilibrium (Eq. 5.48) will not be satisfied at all potentials. This will lead to an immiscibility polarization as shown in Fig. 5.89. If {ox} is gradually reduced to {C<sub>n</sub>red}, the activity of {C<sub>n</sub>red} may increase up to a certain limiting value  $Z_{\text{red/ox}} = m_{\text{red}}/(m_{\text{red}} + m_{\text{ox}})$ , which depends on the maximal solubility of {C<sub>n</sub>red} in {ox}. In that case, the potential of the saturated mixed crystal is given by:

$$E_{C,1} = E_c^{\theta'} + 2.3 \frac{RT}{nF} \log \left( \frac{1 - Z_{\text{red/ox}}}{Z_{\text{red/ox}}} \right) \quad (5.50)$$

where  $Z_{\text{red/ox}}$  is the maximal solubility of {C<sub>n</sub>red} in {ox}. The second critical potential ( $E_{C,2}$ ) depends on  $Z_{\text{ox/red}} = m_{\text{ox}}/(m_{\text{red}} + m_{\text{ox}})$ , that is the maximal solubility of {ox} in {C<sub>n</sub>red}:

$$E_{C,2} = E_c^{\theta'} + 2.3 \frac{RT}{nF} \log \left( \frac{Z_{\text{ox/red}}}{1 - Z_{\text{ox/red}}} \right) \quad (5.51)$$

The ratio  $a_{\{\text{ox}\}}/a_{\{\text{C}_n\text{red}\}}$  in the crystal can be changed continuously for  $E > E_{C,1}$  and  $E < E_{C,2}$ , but between  $E_{C,1}$  and  $E_{C,2}$  it will remain constant as shown in Fig. 5.89.

The miscibility gap can be also explained in terms of differences in the Gibbs energies of the two solid phases. Let us first assume that the reduction of {ox} to {C<sub>n</sub>Red} forms mixed crystals of the type {ox<sub>x</sub>(C<sub>n</sub>red)<sub>1-x</sub>}

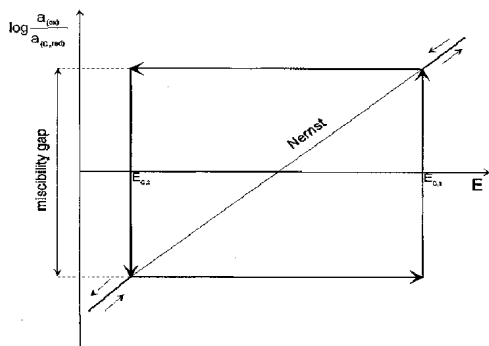


**Fig. 5.89.** Schematic plot of the logarithm of the activity ratios of the oxidized to the reduced form in the solid state as a function of the applied potential [B 79]

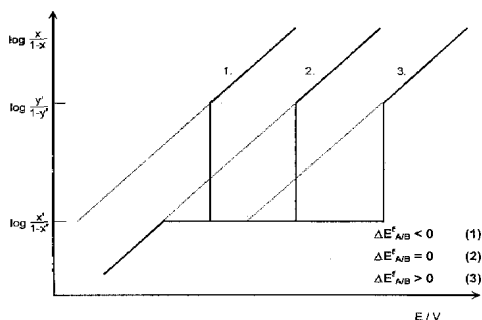


**Fig. 5.90.** Plot of  $\log(x/1-x)$  for a solid solution system  $\{ox_x(C_n red)_{1-x}\}$  vs. potential [B 158]

until the maximum solubility of  $\{C_n Red\}$  in  $\{ox\}$  is reached. The mixed crystal with this maximum concentration of  $\{C_n Red\}$  may be written as  $\{ox_{x'}(C_n red)_{1-x'}\}$ . Then there might exist a solubility gap between the composition  $\{ox_{x'}(C_n red)_{1-x'}\}$  and  $\{ox_{y'}(C_n red)_{1-y'}\}$  ( $x'$  is much bigger than  $y'$ ). The mixed crystal  $\{ox_{y'}(C_n red)_{1-y'}\}$  can be further reduced until  $\{C_n Red\}$  is reached. The mixed phase  $\{ox_{x'}(C_n red)_{1-x'}\}$  has a structure  $\alpha$ , and the mixed phase  $\{ox_{y'}(C_n red)_{1-y'}\}$  a structure  $\beta$ .  $\alpha$  and  $\beta$  are so different that a miscibility gap arises. The difference in the Gibbs free energies  $\Delta G_{A/B}$  of the two phases  $\alpha$  and  $\beta$  is equivalent to the difference in the formal potentials of both systems, and it can be split in two terms, i.e.,  $\Delta G_{A/B} = \Delta G_{red/ox} + \Delta G_{lattice}$ , where  $\Delta G_{lattice}$  is the difference in the free energies due to the different structures of the lattice of phases  $\alpha$  and  $\beta$ . Generally,  $\Delta G_{lattice}$  may have very different values. If  $\beta$  is much more stable than  $\alpha$ , this will shift the formal potential of the redox system in this phase so much in comparison to its value in phase  $\alpha$  that within the miscibility gap the phase  $\beta$  will be formed at the expense of  $\alpha$  until  $\alpha$  is converted into  $\beta$  (line 1 in Fig. 5.90). An interesting situation arises when  $\Delta G_{lattice}$  is much smaller than  $\Delta G_{red/ox}$ . In such a case, we can say that  $\Delta G_{A/B} = \Delta G_{red/ox}$ ,

which would mean that the formal potentials of the redox systems in  $\alpha$  and  $\beta$  are the same (line 2 in Fig. 5.90). This leads to the situation that, within the miscibility gap, there is no sufficient stabilization of  $\beta$  for phase segregation. In other words, within the miscibility gap the potential corresponds to the composition neither of  $\alpha$  nor of  $\beta$ . Thus, no net oxidation of  $\alpha$  to form  $\beta$  can take place. In that case the miscibility gap is simply an inert zone where no reaction can proceed. A third case is possible when the phase  $\alpha$  is much more stable than  $\beta$ . It follows that the formal potential of ox/red in  $\alpha$  is more negative than in  $\beta$ . This again will lead to a separation of the potential ranges in which reduction of ox can occur. After completing the reduction of  $\{\text{ox}\}$  to the composition  $\{\text{ox}_x(\text{C}_n\text{red})_{1-x}\}$ , there will appear an inert zone until the formation of  $\{\text{ox}_y(\text{C}_n\text{red})_{1-y}\}$  may take place. This inert zone is bigger than the miscibility gap by the difference in formal potentials of ox/red in  $\alpha$  and  $\beta$  (see line 3 in Fig. 5.90).

The mathematical modeling was considered identically as in [B 87] using the differential Eq. 5.34 under the initial and boundary conditions given in Eq. 5.35. The numerical solution has been applied to cyclic staircase voltammetry and linear scan voltammetry [B 79]. The influence of the volume of the substance and of the redox kinetics on the voltammetric features have been investigated, too. The influence of the limited miscibility of redox components of the mixed crystal on staircase cyclic voltammograms simulated for semi-infinite diffusion is depicted in Fig. 5.91. Curve A is the voltammogram for complete miscibility, while curve B shows the case of a miscibility gap assuming  $Z_{\text{red/ox}} = Z_{\text{ox/red}} = 0.3$ . It can be seen that the miscibility gap causes a splitting of the voltammogram into two peaks. The first peak appears when the surface of the crystal is charged to the first critical potential  $E_{C,1}$ . Though the potential of the electrode is continuously changed, the ratio of the oxidized to the reduced form remains constant and equal to the value of  $E_{C,1}$ , until the value of the second critical potential  $E_{C,2}$  is reached. When the potential is equal to  $E_{C,2}$ , at this moment the composition of the crystal suddenly changes from 30 %  $\{\text{C}_n\text{red}\}$  and 70 %  $\{\text{ox}\}$  to 70 %  $\{\text{C}_n\text{red}\}$  and 30 %  $\{\text{ox}\}$ . This sudden reduction of 40 % of  $\{\text{ox}\}$  prompts a sharp peak to appear in the cathodic branch of the voltammogram. Under anodic polarization, a second sharp peak appears. The separation between these two peaks increases as the miscibility of the components decreases (see Fig. 5.92).

The influence of the finite crystal volume on the staircase voltammogram is shown in Fig. 5.93. The miscibility parameters are the same as those in Fig. 5.92, but the results in Fig. 5.93 are calculated for a very

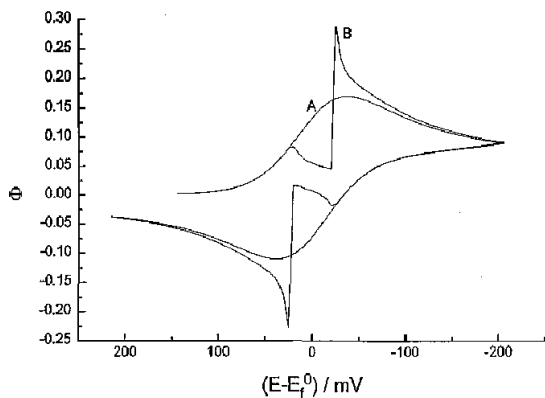


**Fig. 5.91.** Staircase cyclic voltammograms of ideally miscible A and partly immiscible B solid redox components. Miscibility limits:  $Z_{\text{red/ox}} = Z_{\text{ox/red}} = 0.5$  (A) and 0.3 (B). Reversible redox reaction,  $\Delta E = 5 \text{ mV}$  [B 79]

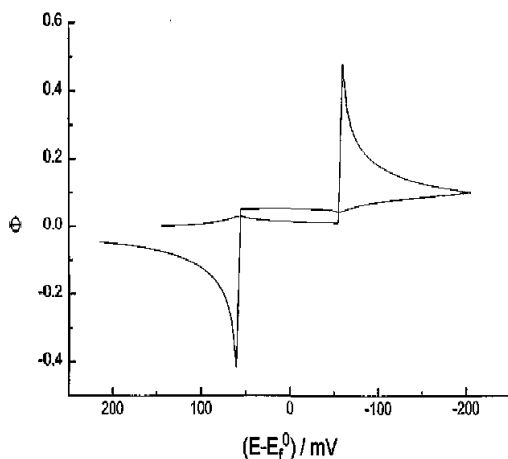


**Fig. 5.92.** Staircase cyclic voltammetry of a reversible solid-state redox reaction influenced by the limited miscibility of the components:  $Z_{\text{red/ox}} = Z_{\text{ox/red}} = 0.1$  [B 79]

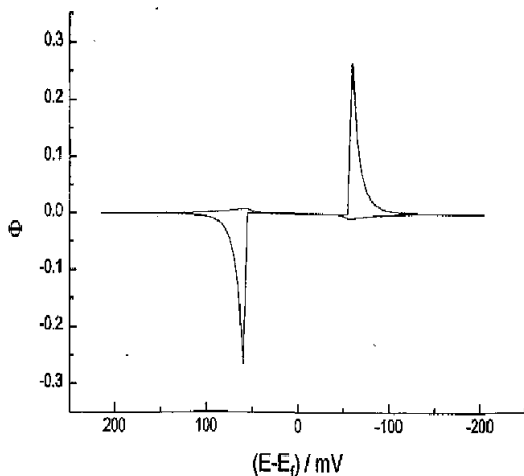


**Fig. 5.93.** Staircase cyclic voltammetry of hemispherical solid electroactive microparticle with a dimensionless radius  $5r_0v^{0.5}(D\Delta E)^{-0.5} = 20$ . Reversible redox reaction influenced by the limited immiscibility of the components  $Z_{\text{red/ox}} = Z_{\text{ox/red}} = 0.1$  [B 79]



small hemispherical particle with the dimensionless radius  $5r_0\nu^{0.5}(D\Delta E)^{-0.5} = 20$ . The major difference between Figs. 5.92 and 5.93 is that such small particles can be electrolyzed completely within a single potential scan. Thus, the peaks are narrower, containing no diffusion “tails”, and the current between cathodic and anodic peaks tends to zero.

An integral study which contains also results for the influence of the charge transfer kinetics can be found elsewhere [B 79]. The outlined treatment of the effect of a miscibility gap on voltammograms is a purely thermodynamic treatment. However, when a phase transformation occurs due to a miscibility gap, a more or less pronounced nucleation process must be observed. Therefore, it is not surprising that voltammograms that resemble very much those simulated for systems with miscibility gaps have been observed experimentally for the reduction of TCNQ (7,7,8,8-tetracyanoquinodimethane) [B 56 and B 101] under conditions of immobilized microparticles. Figure 5.94 shows cyclic voltammograms for the reduction of TCNQ to different alkali salt  $\text{Cat}^+(\text{TCNQ})^-$ . The authors of these papers could show that the electrochemical transformation of TCNQ to the salts exhibits the typical features of nucleation growth kinetics. The essential prerequisite for the occurrence of the nucleation phenomenon is a miscibility gap and the authors have shown that the crystallographic structures of the educts and products are indeed very different [B 101].

In a further paper [B 158] on the theoretical effects of miscibility gaps the focus was on the influence of the structure of the interface of the two

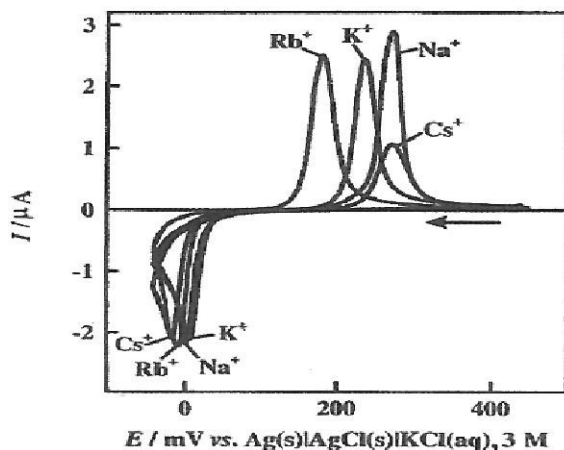


**Fig. 5.94.** Cyclic voltammograms of TCNQ microcrystals in  $0.1 \text{ mol L}^{-1}$  aqueous solutions of NaCl, KCl,  $\text{RbNO}_3$  and CsCl. Scan rate is  $\nu = 50 \text{ mV s}^{-1}$  [B 101]

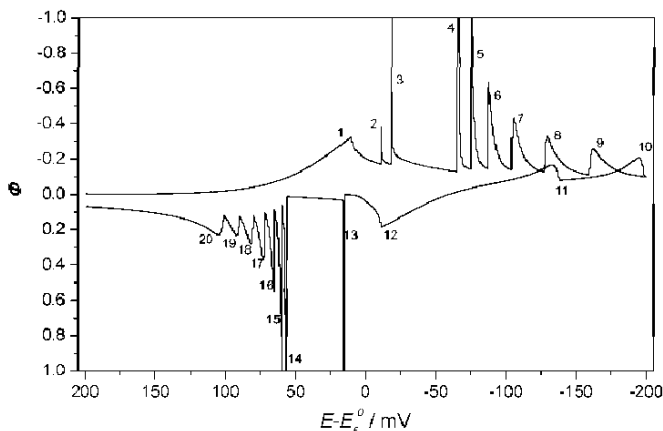


**Fig. 5.95.** Cyclic voltammograms of partly immiscible solid redox compounds. Reversible redox reaction. Miscibility limits:  $Z_{\text{Cred/ox}} = Z_{\text{ox/Cred}} = 0.4$ ,  $d = 0.4$ ,  $\Delta E = 0.2$  mV. No transition zone was assumed [B 158]

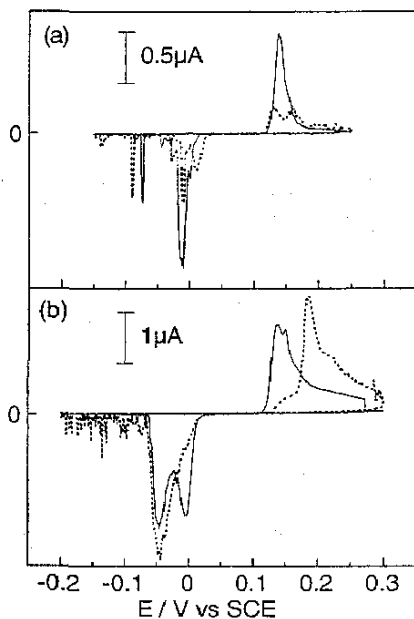


**Fig. 5.96.** Staircase cyclic voltammograms of 1-1 OHSQ/HOPG electrodes (dipping mode) in  $0.1 \text{ mol L}^{-1}$  aqueous solution of LiCl. In each panel, the first scan (dotted line) and the eleventh **a** or tenth **b** scan (solid line) for two different samples are shown. Scan rate  $\nu = 10 \text{ mV s}^{-1}$  [B 169]

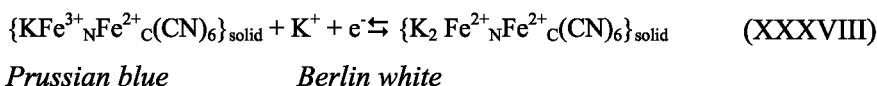
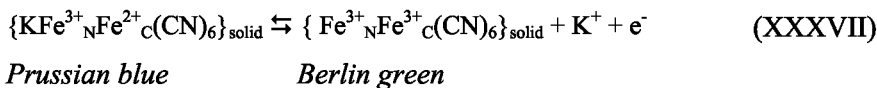
immiscible solid phases. When an interfacial *interphase* is assumed to exist at the place where the two structures transform, a smooth voltammetric response is expected. However, when a rather sharp interface exists, con-

concentration barriers are build up that lead to very unusual voltammetric spikes as depicted in Fig. 5.95.

Shortly after the publication of these theoretical results [B 158], Parkinson et al. [B 169] published voltammograms of electrodes covered with the solid compound (4-dimethylamino-2-dihydroxyphenyl)squaraine that exhibit such curious spikes in addition to the typical feature of a miscibility gap (cf. Fig. 5.96).

### 5.11.7 Electrochemically Driven Formation of Bilayered Systems

In Chapter 5.5 the electrochemically initiated substitution of the high-spin iron ions of Prussian blue by foreign metal ions has been discussed from an experimental point of view (see Figs. 5.54 to 5.55). This substitution reaction has been simulated on the basis of a theoretical model considering semi-infinite planar diffusion applied to a particle cylinder [B 173]. In a solution containing  $K^+$  as the sole cation, Prussian blue microcrystals adhering to a graphite electrode (see Fig. 5.97) can be both reduced and oxidized in cyclic voltammetry:



( $\text{Fe}^{3+}_N$  and  $\text{Fe}^{2+}_C$  denote the N-coordinated high-spin and the C-coordinated low-spin iron ions, respectively). If these reactions are reversible, the following equations govern the concentration ratios:

$$\frac{c_0}{c_1} = \exp\left\{\frac{F(E - E_1)}{RT}\right\}; \quad x = 0, t \geq 0;$$

$$\frac{c_1}{c_2} = \exp\left\{\frac{F(E - E_2)}{RT}\right\}; \quad x = 0, t \geq 0 \quad (5.52)$$

where  $c_0$ ,  $c_1$  and  $c_2$  are the concentrations of Berlin green, Prussian blue, and Berlin white, respectively. The sum of all three concentrations is equal to  $c^*$ . Both, the electron transfer and the mass transfer of the intercalated compounds by Reaction XXXVII and XXXVIII are given by the corresponding diffusion equations:

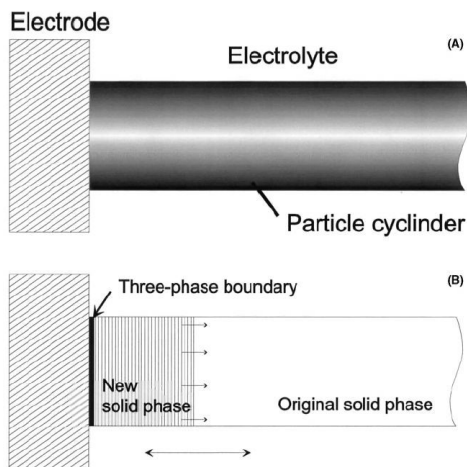
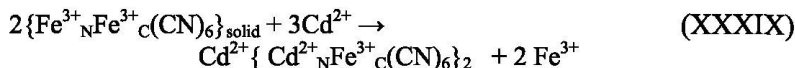


**Fig. 5.97.** Model of the semi-infinite planar diffusion applied to a particle cylinder attached to a solid electrode and in contact with an electrolyte solution **A**. Initiated at the three-phase junction, the new solid phase advances into the bulk particle, following the diffusion of cations **B** [B 173]

$$\frac{\partial c_i}{\partial t} = D \frac{\partial^2 c_i}{\partial x^2}; \quad x \geq 0, t \geq 0 \quad (5.53)$$

Equation 5.53 has been solved by the standard finite difference method for all species in Reactions XXXVII and XXXVIII.

When the electrochemical transformation of iron hexacyanoferrate into cadmium hexacyanoferrate takes place, the following reaction occurs:



This reaction is characterized by  $k_f$ , the rate constant of the electrochemical transformation (or substitution). In order to quantify the progress of the reaction, a parameter  $w$  is defined as  $w = \Phi_{\text{Cd}^{2+}}^{\text{ox}} / (\Phi_{\text{Cd}^{2+}}^{\text{ox}} + \Phi_{\text{Fe}^{3+}}^{\text{ox}})$ . This is the ratio of the oxidation currents of cadmium hexacyanoferrate to the sum of the oxidation currents of cadmium hexacyanoferrate and iron hexacyanoferrate. The dependences of the  $w$  on the number of the potential cycles for several simulations assuming different values of  $k_f$ , and the same plot with the experimental values obtained under the same conditions as in the simulation, are given in Fig. 5.98. Assuming a dimensionless rate constant  $k_f = 0.5$  of Reaction XXXIX provides the best fit of the experimental results. Simulated cyclic voltammograms based on this dimensionless rate constant are depicted in Fig. 5.99. Figure 5.100 depicts the dependence

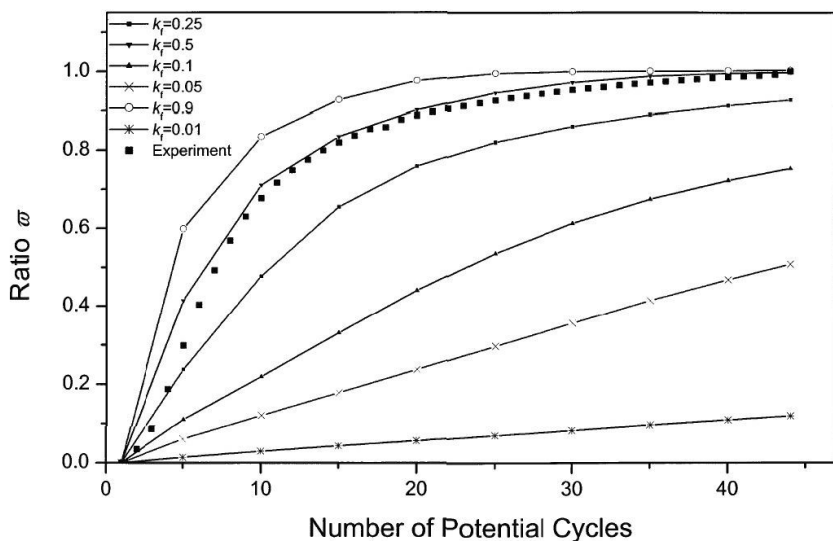


**Fig. 5.98.** Dependence of the ratio  $\varpi$  on the number of potential cycles for a couple of simulations assuming different values of the kinetic contribution  $k_{\tau}$ , and for the real experiment [B 173]

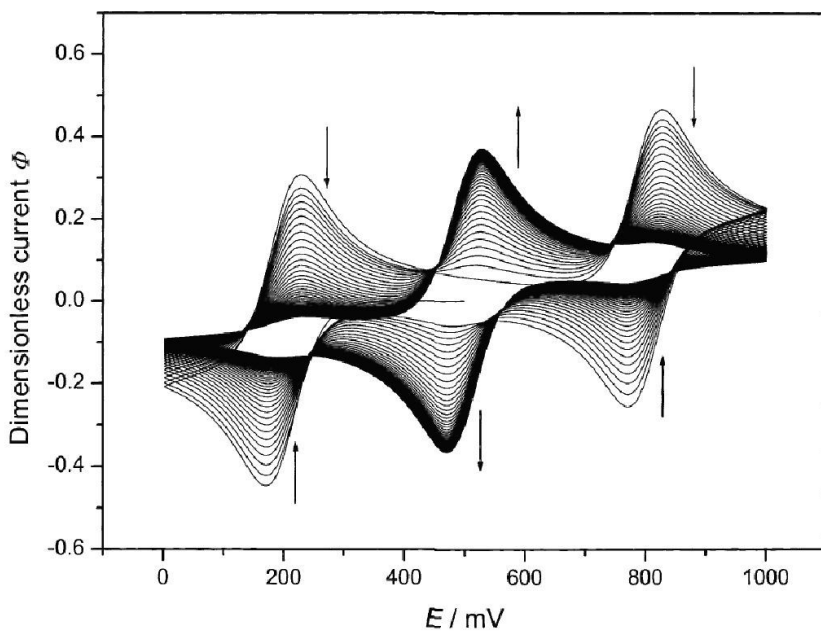


**Fig. 5.99.** Simulated multiple cyclic voltammograms for the solid state conversion of Prussian blue (first and third redox couple) to cadmium hexacyanoferrate (second redox couple).  $\nu = 100 \text{ mV s}^{-1}$ ,  $k_{\tau} = 0.25$ ,  $dE = 2 \text{ mV}$  [B 173]

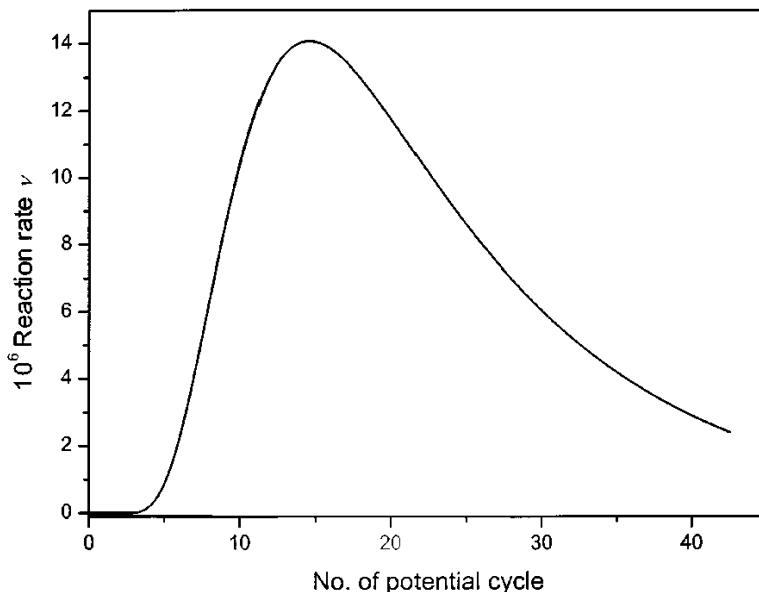


**Fig. 5.100.** Dependence of the reaction rate on the number of the potential cycle during the solid-state conversion of Prussian blue to cadmium hexacyanoferrate. Simulated data are the same as in Fig. 5.99 [B 173]

of the rate of the substitution reaction on the number of potential cycles. As can be seen in Fig. 5.100, after an induction period of 4-6 potential cycles, the rate of substitution is increasing to reach a maximum at around 15 cycles, corresponding to the increased amount of inserted ions, and then it is decreasing due to the decreasing concentration of starting material available for substitution.

## 6 Immobilized Droplets

In principle, the voltammetry of immobilized droplets is in many respects very similar to the voltammetry of immobilized microparticles. However, the fluidity of droplets in contrast to the rigidity of solids, leads to specific features which have to be discussed before the details of electrochemical studies can be presented.

Although the adhesion of a liquid droplet to a solid electrode surface in the presence of a third liquid phase, usually the electrolyte solution, is, from a physical point of view, not fundamentally different to that of solid particles, the magnitude of forces keeping the droplet adhering are different. In addition, the fluidity of the droplet allows a fast establishment of the equilibrium of forces, which is not the case with solid particles.

Figure 6.1 depicts the situation when a three-phase electrode is composed of a droplet of liquid, phase II, immobilized on a solid electrode surface (phase I) and immersed in an electrolyte solution (phase III). The

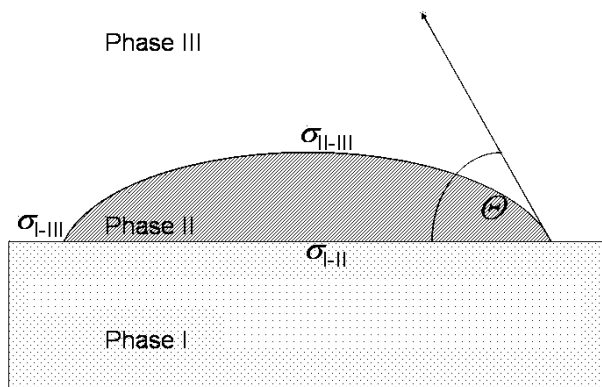


**Fig. 6.1.** Three-phase electrode with an immobilized droplet (phase II) attached to a solid electrode (phase I) and in an electrolyte solution (phase III).  $\theta$  is the contact angle and  $\sigma$  is the interfacial tension between the phases indicated in the subscripts

relation between the interfacial tensions between the three phases and the contact angle is described by the Young<sup>1</sup> equation:

$$\cos \theta = \frac{\sigma_{\text{I-III}} - \sigma_{\text{I-II}}}{\sigma_{\text{II-III}}} \quad (6.1)$$

From this equation follows that the shape of the droplet is a function of the interfacial tensions between the phases I and II, II and III, and I and III. When the contact angle is very small or even going to zero, the liquid II would form a film on the solid, what is clearly not desirable in the experiments that we are discussing, because the three-phase junction would be lost. On the other side, a too large contact angle would destabilize the droplet or, for  $\theta$  approaching  $180^\circ$  even detach the droplet immediately. The consequences of electrode potentials for the adhesion of oil droplets<sup>2</sup>, and of liposomes<sup>3</sup> suspended in an electrolyte solution has been demonstrated with mercury electrodes.

In electrochemistry, another complication arises from the well known relation between the electrode potential and the interfacial tension:

$$\sigma = -\frac{1}{2} C_d E^2 + \text{const.} \quad (6.2)$$

where  $C_d$  is the differential double layer capacity and  $E$  the electrode potential. This means that changing the electrode potential will alter in any case the interfacial tensions  $\sigma_{\text{I-II}}$  and  $\sigma_{\text{I-III}}$ . Consequently - as the interface between the two liquid phases II and III is in series with interface I-II, the interfacial tension  $\sigma_{\text{II-III}}$  changes too, provided the droplet has a sufficient ionic conductivity. If the conductivity of the droplet is high in all its volume elements the entire interface II-III will be affected by the electrode potential, whereas in case that only the edge of the droplet acquired ionic conductivity (by natural partition of the electrolyte from phase III, or by an electrochemical reaction) there will even be an anisotropy of the interfacial tension between II and III from the edge to the apex of the droplet (see Fig. 6.2.2 in Chapter 6.2). Further complications may arise from the fact that the electrochemical reaction will change the composition of the droplet phase, and possibly also of the electrolyte phase near the three-phase junction and near the droplet surface. A change of composition will always affect the interfacial tension, and this parameter may even become strongly

<sup>1</sup> Young Th (1805) Philos Trans 65-87

<sup>2</sup> Ivošević N, Žutić V (1998) Langmuir 14:231-234

<sup>3</sup> Hellberg D, Scholz F, Schauer F, Weitschies W (2002) Electrochem Commun 4:305-309

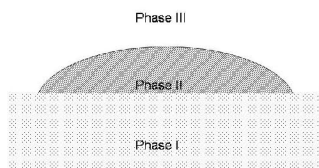


anisotropic over the interface. This could deform the interface, and it may induce the so-called Marangoni <sup>4</sup> streaming. The latter is an effect of an induced flowing of a liquid along an interface from places with low interfacial tension to places with a higher interfacial tension. This way a convective mass transport may act at a three-phase electrode. The feedback effects between electrode potential, interfacial tension, mass transport, electrode reaction, etc., are certainly very complicate. Fortunately, the changes of interfacial tensions caused by the electrode potential are in many cases practically negligible; esp. when lipophilic droplets are attached to rather lipophilic surfaces like that of graphite electrodes, or even better for the paraffin impregnated electrode (PIGE). In these cases, the value of the interfacial tension between the droplet and the underlying base material is such that there is hardly any shape change detectable upon potential variations. However, when an organic liquid droplet is attached to a metal electrode, platinum or gold perhaps, it is impossible to keep the droplet stable in voltammetric experiments. The alteration of the interfacial tensions by potential scanning leads to a rapid movement of the droplet on the surface, to spreading or detachment, i.e., to irreproducible conditions at the electrode surface. The situation is slightly better when an aqueous droplet is attached to a platinum electrode since the latter is rather hydrophilic. Ulmeanu et al. [B 180] reported experiments with a very small aqueous electrolyte droplet attached to a platinum microelectrode in a Teflon holder.

The mechanisms of electrode reactions observed at three-phase electrodes with immobilized droplets resemble those observed with immobilized particles. Table 6.1 gives an overview of some frequently observed cases. There are certainly more possible cases, and especially catalytic reactions at such three-phase electrodes are not considered here. Examples for these reactions are discussed in the following chapters. The first case listed in Table 6.1 is when an oxidizable non-ionic compound X is dissolved in a polar organic solvent. The oxidation to  $X^+$  may be accompanied by the transfer of anions  $B^-$  from the aqueous to the organic phase (case 1a) if the free energy for that transfer is smaller than that for the transfer of  $X^+$  to the aqueous phase (case 1b). When a nonpolar solvent is used, the transfer of  $X^+$  to the aqueous phase is the most probable reaction (case 2). When a reducible non-ionic compound X is dissolved in a polar organic solvent, the reaction to  $X^-$  may be followed by the transfer of cations  $A^+$  to the organic phase (case 3a) or by the transfer of  $X^-$  to the aqueous phase (case 3b). Again, the free energies of the ion transfer of  $X^-$

---

<sup>4</sup> Marangoni CGM (1871) Ann Phys Chem (Poggendorf) 143:337-354

**Table 6.1.** Overview of possible reaction mechanisms at three-phase electrodes with immobilized droplets

	Phase II	Phase III	Mechanism	Ref.
1	Polar organic solvent O with dissolved non-ionic oxidizable compound X	Aqueous electrolyte A <sup>+</sup> B <sup>-</sup>	1a) X <sub>o</sub> + B <sub>aq</sub> <sup>-</sup> ⇌ X <sub>o</sub> <sup>+</sup> + B <sub>o</sub> <sup>-</sup> + e <sup>-</sup> 1b) X <sub>o</sub> ⇌ X <sub>aq</sub> <sup>+</sup> + e <sup>-</sup>	[B 132]
2	Nonpolar organic solvent O with dissolved non-ionic oxidizable compound X	Aqueous electrolyte A <sup>+</sup> B <sup>-</sup>	X <sub>o</sub> ⇌ X <sub>aq</sub> <sup>+</sup> + e <sup>-</sup>	[B 132]
3	Polar organic solvent O with dissolved non-ionic reducible compound X	Aqueous electrolyte A <sup>+</sup> B <sup>-</sup>	3a) X <sub>o</sub> + e <sup>-</sup> + A <sub>aq</sub> <sup>+</sup> ⇌ X <sub>o</sub> <sup>-</sup> + A <sub>o</sub> <sup>+</sup> 3b) X <sub>o</sub> + e <sup>-</sup> ⇌ X <sub>o</sub> <sup>-</sup>	[B 271]
4	Organic oxidizable liquid O	Aqueous electrolyte A <sup>+</sup> B <sup>-</sup>	4a) O <sub>o</sub> + B <sub>aq</sub> <sup>-</sup> ⇌ O <sub>o</sub> <sup>+</sup> + B <sub>o</sub> <sup>-</sup> + e <sup>-</sup> (O <sub>o</sub> <sup>+</sup> + B <sub>o</sub> <sup>-</sup> form an ionic liquid) 4b) O <sub>o</sub> ⇌ O <sub>aq</sub> <sup>+</sup> + e <sup>-</sup> (follow-up precipitation of [O <sup>+</sup> B <sup>-</sup> ] is possible)	[B 166]
5	Organic reducible liquid O	Aqueous electrolyte A <sup>+</sup> B <sup>-</sup>	O <sub>o</sub> + e <sup>-</sup> + H <sub>aq</sub> <sup>+</sup> ⇌ OH <sub>o</sub> (the organic liquid remains non-ionic)	[B 273]

to the aqueous phase and of A<sup>+</sup> to the organic phase decide what will happen. The case of a reducible compound in a nonpolar organic solvent is not listed. Of course, the transfer of X<sup>-</sup> to the aqueous phase would be the most probable reaction path. Case 4 in Table 6.1 concerns oxidizable organic liquids. The oxidation can result as in case 1a to the transfer of anions B<sup>-</sup> from the aqueous to the organic phase, however, now the organic liquid is converted to an ionic liquid (in principle, also a precipitation of the salt [O<sup>+</sup>B<sup>-</sup>] in the organic liquid may occur). Alternatively, the cations O<sup>+</sup> can be transferred to the aqueous phase, where they remain dissolved, or they may form a precipitate [O<sup>+</sup>B<sup>-</sup>] with the anions. Again the free energies of

ion transfer determine the pathway. Case 5 in Table 6.1 describes the reduction of an organic liquid O to the organic liquid OH that results from a transfer of electrons from phase I to phase II and a proton transfer from phase III to phase II. Also this case has been verified experimentally to exist.

The very simplified Table 6.1 shows already the diversity of possible reaction mechanisms, but it also suggests that the underlying principles are rather general. It is hoped that this table gives an orientation for further investigations. Detailed explanations are discussed on the following pages.

## 6.1 The Electrochemistry of Redox Liquids

The first report that involved the voltammetry of immobilized redox liquids was a study of the *n*-hexyldithiocarbamate complex of lead(II) [B 13]. It was found that the voltammetry of the immobilized droplets of this compound was the same as that of its microcrystals. Initiated by the idea of studying electrochemical processes in biphasic media such as emulsions, Marken et al. has undertaken the first intentional investigations involving immobilized microdroplets of redoxactive liquids [B 74]. The immobilization of droplets was meant to provide a controlled environment to separately elucidate processes involving the direct and simultaneous contact of immiscible liquids to an electrode surface and to an aqueous solution. Since then a wealth of information regarding electron transfer and ion transfer processes as well as chemical reactions of the deposited redox liquids has been gathered. As it is presented in the latest review on the field by Banks et al. [B 285], the *N,N,N',N'*-tetraalkylphenylenediamines, TRPDs (R = alkyl), are the by far the most investigated redox liquids (see Fig. 6.2 and Table 6.2).

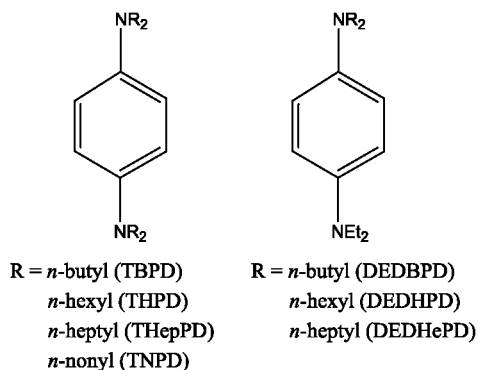


**Fig. 6.2.** Structure of the *N,N,N',N'*-tetraalkyl-*para*-phenylenediamines (*p*-TRPD) and the *N,N*-diethyl-*N',N'*-dialkyl-*para*-phenylenediamines (*p*-DEDRPD)

**Table 6.2.** Redox liquids that have been studied voltammetrically as microdroplets immobilized on basal plane pyrolytic carbon electrodes (reproduced from B 285)

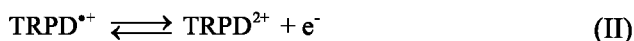
Redox liquid	Reference (B)
<i>N,N,N',N'</i> -Tetrahexyl- <i>para</i> -phenylenediamine ( <i>p</i> -THPD)	74, 97, 149, 150, 166, 168, 171, 182, 230, 254, 284, 287, 288
<i>N,N,N',N'</i> -Tetrahexyl- <i>meta</i> -phenylenediamine ( <i>m</i> -THPD)	166
<i>N,N,N',N'</i> -Tetrabutyl- <i>para</i> -phenylenediamine ( <i>p</i> -TBPD)	230, 254, 284
<i>N,N,N',N'</i> -Tetraheptyl- <i>para</i> -phenylenediamine ( <i>p</i> -THePD)	230, 254, 284
<i>N,N,N',N'</i> -Tetraoctyl- <i>para</i> -phenylenediamine ( <i>p</i> -TOPD)	213, 214, 254
<i>N,N,N',N'</i> -Tetranonyl- <i>para</i> -phenylenediamine	230, 284
<i>N,N</i> -Diethyl- <i>N',N'</i> -dibutyl- <i>para</i> -phenylenediamine ( <i>p</i> -DEDBPD)	284
<i>N,N</i> -Diethyl- <i>N',N'</i> -dihexyl- <i>para</i> -phenylenediamine ( <i>p</i> -DEDHPD)	284
<i>N,N</i> -Diethyl- <i>N',N'</i> -diheptyl- <i>para</i> -phenylenediamine ( <i>p</i> -DEDHePD)	284
<i>N,N,N',N'</i> -Trihexyl- <i>para</i> -phenylenediamine ( <i>p</i> -TriHPD)	171
<i>N,N,N',N'</i> -Tetrakis(6-methoxyhexyl)- <i>para</i> -phenylenediamine ( <i>p</i> -TMHPD)	166
<i>N<sup>t</sup></i> -[4-(Dihexylamino)phenyl]- <i>N<sup>t</sup>,N<sup>t</sup>,N<sup>t</sup></i> -trihexyl-1,4-phenylenediamine (DPTPD)	289
3-Methylthiophene	197
<i>n</i> -Butylferrocene	241
4-Nitrophenyl nonyl ether	286
Vitamin K1	273, 287

<sup>a</sup> Studied as single millimetric drop immobilized on a PIGE.

These compounds combine an extremely low miscibility with water, a suitable oxidation potential, the formation of colored radical species and the possibility to tailor their physical and chemical properties by changing the

the length and the nature of the alkyl chains. In contrast to the solid, water-soluble tetramethylphenylenediamine, TMPD, the long-chain compounds are liquids that remain extremely insoluble in water even after oxidation and the formation of the radical cationic form. The long alkyl chains not only ensure the low solubility and the highly lipophilic character of the compound, they also hinder regular packing of the molecules and thus prevent crystallization. That all makes the TRPDs very well suited as model compounds for the study of the voltammetry of immobilized redox liquids.

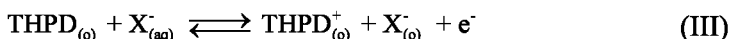
The tetra-*N*-alkylated phenylenediamine backbone can be reversibly oxidized in two one-electron transfer steps, the first, which involves the formation of the radical cation, being by far the most intensively studied reaction:



The electrochemical oxidation of TRPD in the biphasic system of the immobilized microdroplets has been studied from very different viewpoints including the electrochemically and chemically facilitated ion transfer reactions, reactive chemistry, photochemistry and catalysis. In the following sections these different aspects will be appreciated, demonstrating the potential of the voltammetry of immobilized microdroplets as a simple and yet powerful electrochemical tool.

### 6.1.1 Electrochemically Driven Ion Transfer Reactions

*N,N,N',N'*-tetrahexyl-*para*-phenylenediamine, THPD, was the first compound of the phenylenediamine family to be studied in detail [B 74, B 97]. The authors have compared the electrochemistry of THPD, dissolved in acetonitrile, and the electrochemistry of immobilized microdroplets of the compound in contact to an aqueous electrolyte solution. They have found that the oxidation of the immobilized droplets was essentially connected with the uptake of anions from the surrounding electrolyte solution in order to maintain electroneutrality within the droplets:



The authors also observed that the mid-peak potential of this reaction and the shape of the voltammetric signals (see Fig. 6.3) depend on the nature of the electrolyte anion, whereas the nature of the cations did not contribute

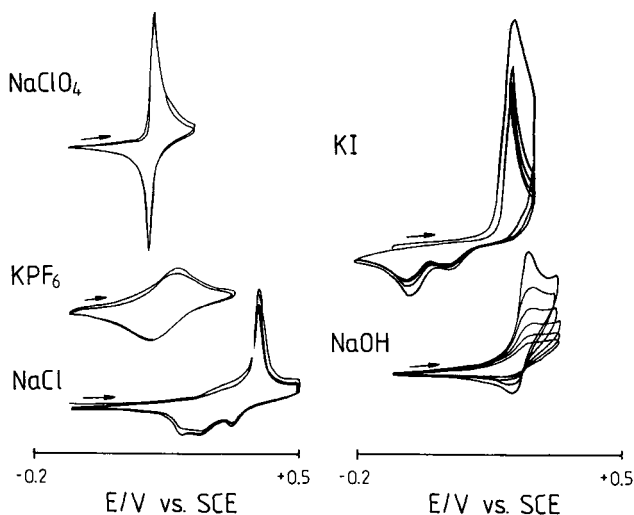


**Fig. 6.3.** Multicycle voltammograms for the oxidation of 1.24  $\mu\text{g}$  THPD deposited on a 4.9-mm diameter basal plane pyrolytic carbon electrode and immersed in aqueous solutions of different electrolyte salts (electrolyte concentration 0.1 M, 6 cycles, 22  $^{\circ}\text{C}$ , scan rate 10  $\text{mV s}^{-1}$ ) [B 74]

significantly. As a consequence, the authors suggested utilizing this effect, which they attributed to specific interactions between the phenylenediamine cation and the inserted anion, for the detection of anions in aqueous solutions [B 74].

Initiated by these studies a series of papers have appeared dedicated to the systematic investigation of the voltammetry of differently substituted phenylenediamines. Thus, the anion insertion and chemical reactions in microdroplets of *para*-tetrakis(6-methoxyhexyl)phenylenediamine, *para*- and *meta*-tetrahexylphenylenediamine (Fig. 6.4) has been compared [B 166]. In this study the effects of the altered molecular structures of the liquid precursors were investigated. The authors observed dramatic changes in the voltammetric behavior of the liquids, which they interpreted in terms of changes in the interaction between the TRPD radical cation and the transferred anion within the organic liquid as a function of the chain length of the phenylenediamine and the position of the amine groups at the benzene unit. Due to the high density of the redox centers within the redox liquids, very much in contrast to the electrochemistry of compounds dissolved in droplets of inert solvents, such specific and none-specific interactions between the constituents in the liquids are very likely. The very narrow peak shape that was found for the oxidation of THPD microdroplets

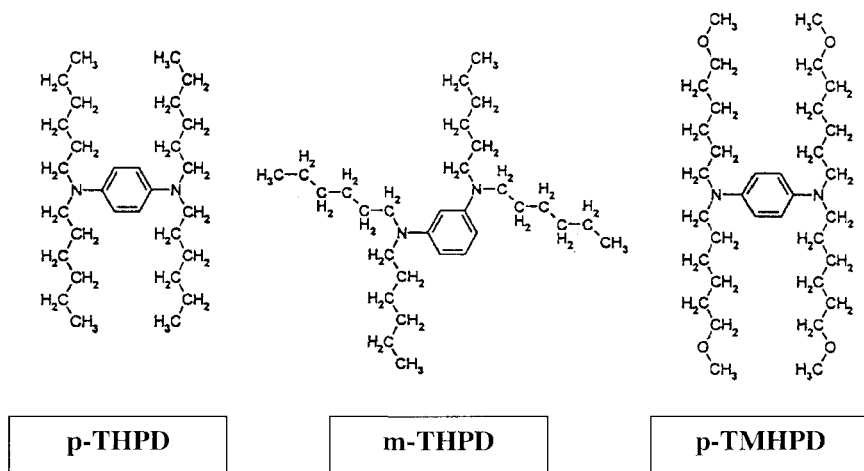


**Fig. 6.4.** Structures of *para*-*N, N, N', N'* tetrahexylphenylenediamine (*p*-THPD), *meta*-*N, N, N', N'* tetrahexylphenylenediamine (*m*-THPD) and *para*-tetrakis(6-methoxyhexyl) phenylenediamine (*p*-TMHPD) [B 166]

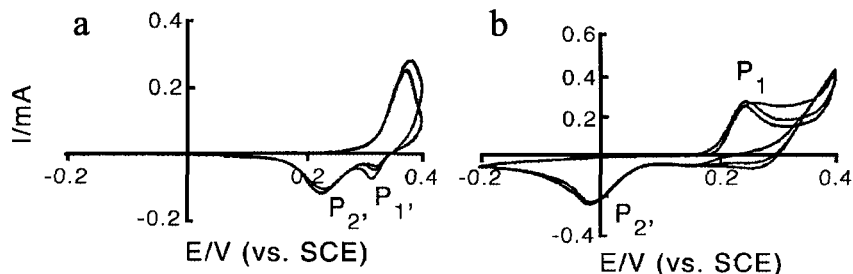


**Fig. 6.5.** Cyclic voltammograms (first three scans) recorded at  $100 \text{ mV s}^{-1}$  for the oxidation of  $5.3 \times 10^{-9} \text{ mol } p\text{-THPD}$  deposited by solvent evaporation onto a 4.9 mm diameter basal plane pyrolytic carbon electrode immersed in **a** 0.1 M NaBr, and **b** 0.1 M KI [B 166]

[B 74] supports this assumption. Very interesting voltammetric features have been reported for the insertion of halides into the redox liquids (Fig. 6.5). Upon oxidation in the presence of bromide and iodide ions THPD showed an additional reduction signal connected with a large peak-to-peak separation. The occurrence of this reduction signal was found to be fully chemically reversible, and in the case of bromide it disappeared at elevated temperature ( $40 \text{ }^\circ\text{C}$ ). To interpret this behavior the authors have presented

a number of possible explanations that comprise (i) possible crystallization processes upon oxidation, and (ii) the co-insertion of water into the organic liquid.

The search for the relationship between the nature of the electrolyte ions transferred across the phenylenediamine | water interface and the characteristics of the voltammetric signals has always been a key issue in the published studies. Generally, the authors have found correlations between the measured formal potential, the lipophilicity of the inserted ions and the lipophilicity of the redox liquid (see Table 6.3). Thus, increasing the number of carbon units in the alkyl chains of the TRPD, for a given anion, leads to a shift of the midpoint potentials towards more positive values, *viz* DEDBPD < TBPD < DEDHPD < DEDHePD < THPD < THePD < TOPD < TNPD [B 284]. Also, increasing the hydrophilicity of the supporting electrolyte anion leads to more positive midpoint potentials. Inspired by a new approach to access thermodynamic quantities of electrochemically driven ion transfer reactions at nitrobenzene droplets (B 132, see Chapter 6.2), the voltammetry of immobilized redox liquids has been compared with experimental data achieved when droplets of TRPD dissolved in nitrobenzene were used instead of the pure redox liquid.

**Table 6.3.**  $E_{\text{mid}}$ /mV data<sup>a</sup> obtained from cyclic voltammograms<sup>b</sup> for the oxidation of DEDRPD and TRPD oils<sup>c</sup> [B 284]

	DEDBPD	TBPD <sup>d</sup>	DEDHPD	DEDHePD	THPD <sup>d</sup>	THePD <sup>d</sup>	TNPD <sup>d</sup>
PF <sub>6</sub> <sup>-</sup>	-30 <sup>i</sup>	-20 <sup>i</sup>	3 <sup>i</sup>	18 <sup>i</sup>	26 <sup>i</sup>	41 <sup>i</sup>	64 <sup>i</sup>
ClO <sub>4</sub> <sup>-</sup>	45 <sup>ii</sup>	63 <sup>i</sup>	86 <sup>i</sup>	91 <sup>i</sup>	109 <sup>i</sup>	126 <sup>i</sup>	146 <sup>i</sup>
SCN <sup>-</sup>	105 <sup>ii†</sup>	129 <sup>ii</sup>	141 <sup>i</sup>	153 <sup>i</sup>	178 <sup>i</sup>	188 <sup>i</sup>	201 <sup>i</sup>
Br <sup>-</sup>	125 <sup>ii</sup>	185 <sup>ii</sup>	259 <sup>ii‡</sup>	269 <sup>*</sup>	296 <sup>i</sup>	318 <sup>i</sup>	324 <sup>i</sup>
NO <sub>3</sub> <sup>-</sup>	117 <sup>ii‡</sup>	180 <sup>ii‡</sup>	245 <sup>*‡</sup>	253 <sup>*</sup>	298 <sup>i</sup>	313 <sup>i</sup>	327 <sup>i</sup>
OCN <sup>-</sup>	117 <sup>ii‡</sup>	188 <sup>ii</sup>	265 <sup>ii‡</sup>	290 <sup>ii</sup>	365 <sup>ii</sup>	381 <sup>ii</sup>	385 <sup>ii</sup>
Cl <sup>-</sup>	126 <sup>ii</sup>	193 <sup>ii</sup>	266 <sup>ii‡</sup>	310 <sup>i</sup>	371 <sup>ii</sup>	383 <sup>ii</sup>	383 <sup>i</sup>
SO <sub>4</sub> <sup>2-</sup>	135 <sup>ii</sup>	203 <sup>ii</sup>	281 <sup>ii</sup>	318 <sup>ii</sup>	444 <sup>†</sup>	467 <sup>†</sup>	481 <sup>ii</sup>
F <sup>-</sup>	113 <sup>ii</sup>	198 <sup>ii</sup>	274 <sup>ii</sup>	330 <sup>ii</sup>	465 <sup>†</sup>	489 <sup>†</sup>	513 <sup>ii</sup>
IO <sub>3</sub> <sup>-</sup>	134 <sup>ii</sup>	238 <sup>ii</sup>	268 <sup>ii</sup>	336 <sup>ii</sup>	470 <sup>ii</sup>	481 <sup>ii</sup>	501 <sup>ii</sup>

<sup>a</sup> All data are reported in mV vs SCE; error = 5 mV. <sup>b</sup> Oil (5 nmol) was deposited as microdroplets on a 4.9-mm diameter basal plane pyrolytic carbon electrode and immersed into 0.1 M aqueous electrolyte. The data were obtained using a scan rate of 100 mV s<sup>-1</sup>. <sup>i</sup> indicates that the oxidation follows Reaction I, <sup>ii</sup> indicates that the oxidation follows Reaction III; <sup>\*</sup> indicates that the voltammetric behavior is case (i) at fast scan rates but case (ii) at slow scan rates; <sup>†</sup> indicates this case is effectively type (ii) behavior, only with very fast kinetics; <sup>‡</sup> indicates those systems that give rise to split waves at slow scan rates. <sup>d</sup> Data taken from [B 230 and B 254]



Although the basic methodology of both approaches, the voltammetry of compounds dissolved in inert solvents, and the voltammetry of unsupported redox liquids is practically identical, and it can be expected that their basic features are comparable, there are fundamental differences: Performing voltammetric measurements at droplets of inert solvents that contain an electro-active species generally means that the concentration of the electro-active species within the droplet is significantly lower than the concentration of the solvent. Due to the low concentration, interactions between the molecules of the active compound are very often insignificant. Oxidation or reduction processes of the dissolved species, connected with an ion transfer between the droplet and the adjacent aqueous solution, generally do not completely change the physical and chemical phase characteristics of the organic droplet. An exception is the change of the ionic conductivity due to the formation or consumption of ionic species and their transfer into or out of the organic phase. However, increasing the concentration of the redox active species at the expense of the solvent gradually raises the impact of the reaction at the droplet phase. The end of this line is marked by the voltammetry of redox liquids, or, if the target compound is solid, by the voltammetry of immobilized microparticles. Here, chemical or electrochemical reactions will not only cause changes on the molecular level, but they will also alter the properties of the entire organic phase. Thus, an entirely new phase evolves, in some cases even accompanied by a crystallization or precipitation [B 213]. Additionally to the phase transition, the high density of redox centers increases the impact of intermolecular interactions on the electrochemical behavior [B 74].

In a comparative study the electrochemically driven ion transfer processes across liquid | liquid interfaces of droplets of *para-N, N, N',N'* tetraalkylphenylenediamines and of the same compounds diluted in droplets of nitrobenzene has been elucidated [B 254]. As expected, the voltammetric responses of the two redox steps of the diluted compound are electrochemically fully reversible; peak shape and virtually zero peak separation showing ideal thin film behavior (Fig. 6.6b). The voltammograms of the undiluted compound deviates from that behavior. Beside the narrow peak shape of the first oxidation process additional voltammetric features are found for the THPD<sup>+</sup>/THPD<sup>2+</sup> redox couple. At slow scan rates the reduction of THPD<sup>2+</sup> in the pure redox liquid is characterized by a large overpotential (peak P<sub>2</sub>, Fig. 6.6a). At elevated temperature, however, and at high scan rates (above 100 mV s<sup>-1</sup>) this peak vanishes and is replaced by a new signal, P<sub>1</sub>. This signal can be assigned to the reversible reaction



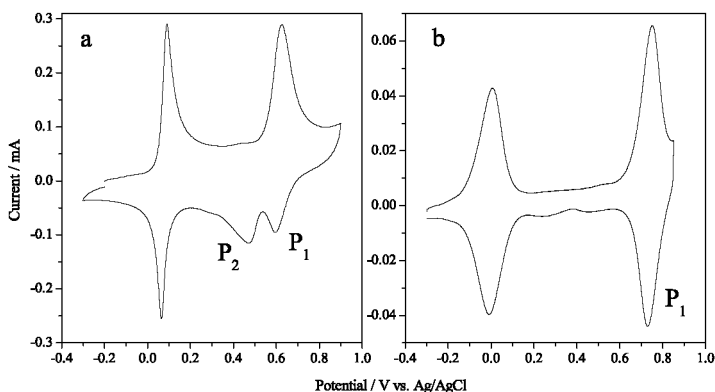


**Fig. 6.6.** **a** Cyclic voltammogram for the oxidation of 3.5 nmol THPD deposited on a 4.9-mm diameter basal plane pyrolytic graphite electrode and immersed in a 0.1 M NaClO<sub>4</sub> electrolyte solution,  $\theta = 42$  °C; **b** Cyclic voltammogram for the oxidation of THPD dissolved in microdroplets of nitrobenzene ( $c_{\text{THPD}} = 25$  mM), deposited at a basal plane pyrolytic graphite electrode and immersed in a 0.1 M NaClO<sub>4</sub> electrolyte solution; scan rate = 100 mV s<sup>-1</sup> [B 254]

as it has been observed for the THPD<sup>+</sup> oxidation in nitrobenzene droplets (Fig. 6.6b). The authors attributed the occurrence of the two chemically reversible reduction processes P<sub>1</sub> and P<sub>2</sub> to a phase transition of the THPD<sup>2+</sup>(ClO<sub>4</sub>)<sub>2</sub> ionic liquid phase towards a higher packing density caused by geometrical configuration changes of the THPD scaffold upon oxidation. Naturally, such a reorientation would not be expected to take place in the diluted system.

Apart from these differences, however, the thermodynamics of the voltammetric reactions of the immobilized tetraalkylphenylenediamines has been found to be very similar to that of the compounds dissolved in nitrobenzene. The authors have shown that for lipophilic anions (section (i) in Fig. 6.7) the formal potentials of Reaction III is strongly correlated to the Gibbs free energy of the ion transfer across the water | nitrobenzene interface. So, despite of the differences in the appearance of the voltammetric signals the redox processes are predominately ruled by the Gibbs free energy of the transfer of the electrolyte anions across the water | redox liquid interface,  $\Delta\varphi_{\text{aq}, X}^{\circ}$  (see Eq. 6.3).

$$E = E^{\circ} + \Delta\varphi_{\text{aq}, X}^{\circ} - \frac{RT}{F} \ln a_{X(\text{aq})} + \frac{RT}{F} \ln \frac{a_{\text{TRPD}^{\circ}} a_{X(\text{o})}}{a_{\text{TRPD}(\text{o})}} \quad (6.3)$$

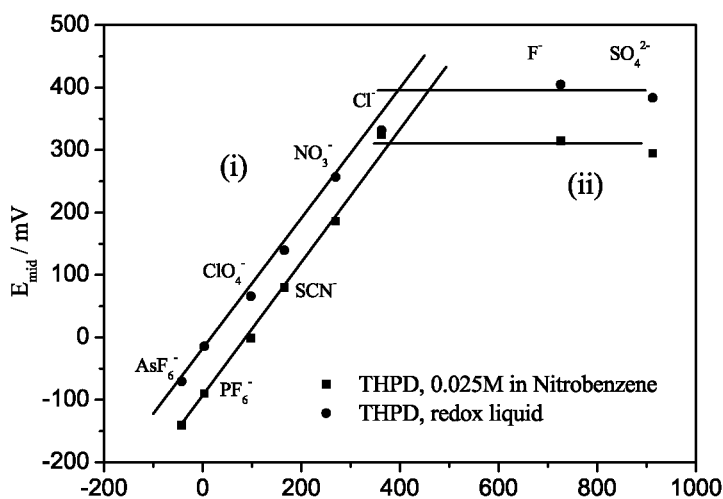


**Fig. 6.7.** Plot of the formal potentials of the first oxidation step (Reaction III) for THPD dissolved in nitrobenzene, and for the pure redox liquid measured in the presence of different electrolyte anions versus the standard membrane potentials of the electrolyte anions at the water/nitrobenzene interface; pH = 9; oxidation of THPD in section (i) follows Reaction (III); in section (ii) it follows Reaction V [B 254]

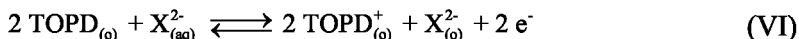
The extremely high hydrophilicity (high values of the Gibbs energy of transfer) of small anions like  $\text{F}^-$  or highly charged ions like sulfate makes the transfer of these ions energetically unfavorable. Instead, upon oxidation, the transfer of the oxidation product, the radical cation  $\text{TRPD}^+$ , takes place from the organic phase into the aqueous solution (Reaction V; see also section (ii) in Fig. 6.3):



$$E = E^\circ - \Delta\phi_{\text{aq, TRPD}^+}^{\circ \circ} + \frac{RT}{F} \ln \frac{a_{\text{TRPD}^+(\text{aq})}}{a_{\text{TRPD}(\text{o})}} \quad (6.4)$$

According to Eq. 6.4, the redox potential does not anymore depend on the Gibbs free energy of transfer of the electrolyte anions,  $\Delta\phi_{\text{aq, X}^-}^{\circ \circ}$ , but on that of the TRPD radical cation,  $\Delta\phi_{\text{aq, TRPD}^+}^{\circ \circ}$ . This process is chemically irreversible. It leads to the dissolution of the redox liquid.

In order to electrochemically drive the transfer of strongly hydrophilic anions from the aqueous into the organic phase by means of the voltammetry of immobilized microdroplets the redox liquid is required to be extremely hydrophobic even in its cationic form. Marken et al. have been the first to report the transfer of sulfate into droplets of *para*-tetrakis(6-methoxyhexyl)phenylenediamine (TMHPD), which, however, was accompanied by dimerization and oligomerization reactions of the formed TMHPD<sup>•+</sup> radical cation [B 166]. In a later study the same authors have reported the reversible insertion of sulfate, chromate and dichromate into microdroplets of *para*-*N,N,N',N'*-tetraoctylphenylenediamine, TOPD [B 214], following Reaction VI:



The authors determined the mid-peak potential of the TOPD oxidation in the presence of a 0.1 M Na<sub>2</sub>SO<sub>4</sub> solution with  $E_{\text{mid}} = 0.428 \text{ V}$  (vs. Ag/AgCl). However, in a similar study Wadhawan et al. could not confirm these results [230]. They systematically examined the electrochemically induced ion insertion and expulsion processes at microdroplets of TRPDs with R = *n*-butyl, *n*-hexyl, *n*-heptyl, and *n*-nonyl. In contrast to the *n*-octyl-substituted compound examined by Marken they interpreted the voltammetric response, recorded for the oxidation of the long-chain TRPDs in the presence of sulfate, by means of Reaction V, the expulsion of the radical cation from the organic phase into the aqueous solution. This assumption seems very reasonable since due to the high value of the Gibbs energy of transfer between water and nonpolar solvents ( $\Delta_r G_{\text{SO}_4^{2-}}^\circ = 88 \text{ kJ mol}^{-1}$ , for the water to acetonitrile transfer<sup>5</sup>), the oxidation of the TRPDs, connected with the uptake of sulfate, would have to be expected to proceed at considerably higher potential values than those found for TOPD.

Recently, Marken et al. have also claimed the insertion of extremely hydrophilic anions such as phosphate and arsenate into microdroplets of *para*-*N, N, N', N'* tetraoctylphenylenediamines [B 213]. Upon oxidation, the redox liquid transformed into a crystalline compound, forming needle structures on the electrode surface (Fig. 6.8). It can be supposed that again a transfer of TOPD cations to the aqueous phase takes place with a follow-up precipitation of the salts at the electrode surface.

<sup>5</sup> Marcus Y (1997) Ion properties. Marcel Dekker, New York, Basel

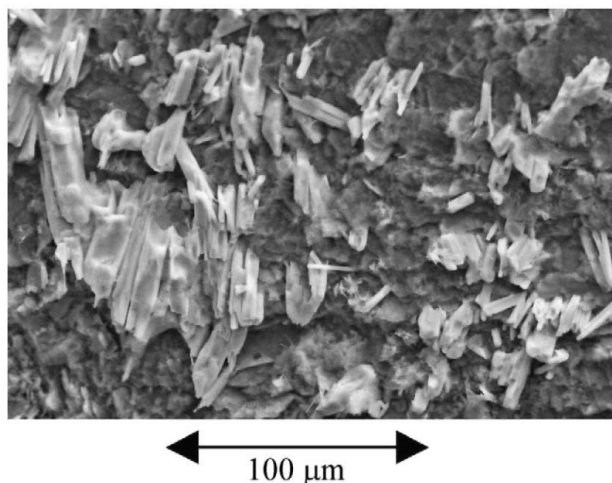


**Fig. 6.8.** Field emission gun scanning electron microscopic image of a deposit of  $6.5 \mu\text{g}$  TOPD on a  $1\text{-cm}^2$  basal plane pyrolytic graphite electrode after 30 s immersion in aqueous  $2.0 \text{ M}$  phosphate buffer at pH 2.3 with a potential of  $0.5 \text{ V}$  vs. SCE applied [B 213]

### 6.1.2 Voltammetric Study of Chemically Facilitated Ion Transfer Processes across the Liquid | Liquid Interface

Due to the generally very low solubility of inorganic salts in the studied redox liquids the extent of the partitioning of ionic species from water into the organic phase can be considered to be extremely low. The partitioning can, however, be facilitated by chemical processes like acid-base reactions of the organic compound.

Theoretically, due to their basicity it should be possible to protonate both amine groups of the phenylenediamine backbone of a TRPD. However, the delocalization of charge via the conjugated  $\pi$ -system of the phenylene ring leads to a decreased electron density, hence to a considerably decreased basicity of the second amine group after the protonation of the first amine group. That means that under mild pH conditions, i.e.,  $\text{pH} \geq 0$ , generally only one amine group can be protonated.

Being performed in the biphasic oil | water system the protonation reaction requires the uptake of protons from the surrounding aqueous into the organic phase. In order to maintain charge neutrality the transfer is accompanied by the transfer of an equivalent number of anions (Reaction VII).

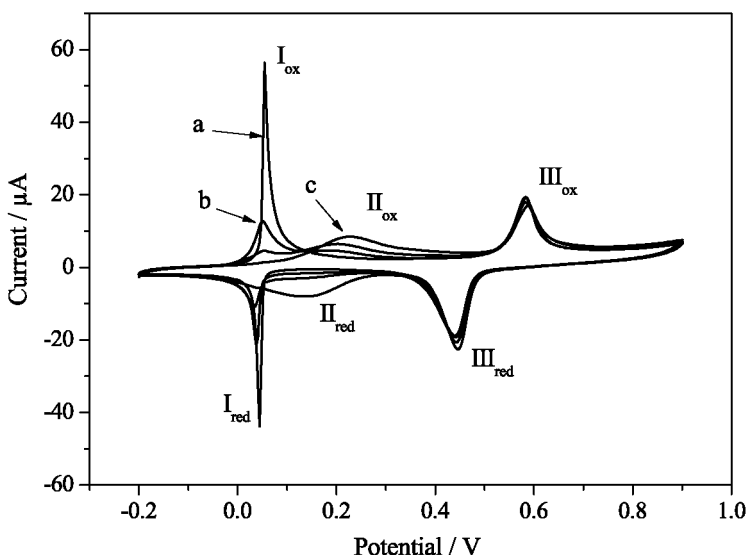


**Fig. 6.9.** Cyclic voltammograms for the oxidation of 3.5 nmol THPD deposited on a 4.9-mm diameter basal plane pyrolytic graphite electrode and immersed in a 1 M NaClO<sub>4</sub> electrolyte solution; **a** pH = 8, **b** pH = 5.9, **c** pH = 3.7; scan rate = 10 mV s<sup>-1</sup> [B 254]



As expected, the protonation has a tremendous effect on the voltammetry of the redox liquid [B 97]. The voltammetric redox system I<sub>ox</sub>/I<sub>red</sub> (see Fig. 6.9), recorded at neutral pH, and based upon reaction (III), Chapter 6.1.1, disappears with increasing proton concentration for a new voltammetric system, II<sub>ox</sub>/II<sub>red</sub>. The oxidation of the immobilized redox liquid, which under neutral and basic pH proceeds under anion uptake, at low pH takes place under expulsion of protons from the redox liquid into the aqueous phase:



The second oxidation step (signals III<sub>ox</sub>/III<sub>red</sub>, Fig. 6.9) remains unaffected, showing that only one amine group is involved in the protonation. As depicted in Fig. 6.10, the new voltammetric signal shows different voltammetric behavior.

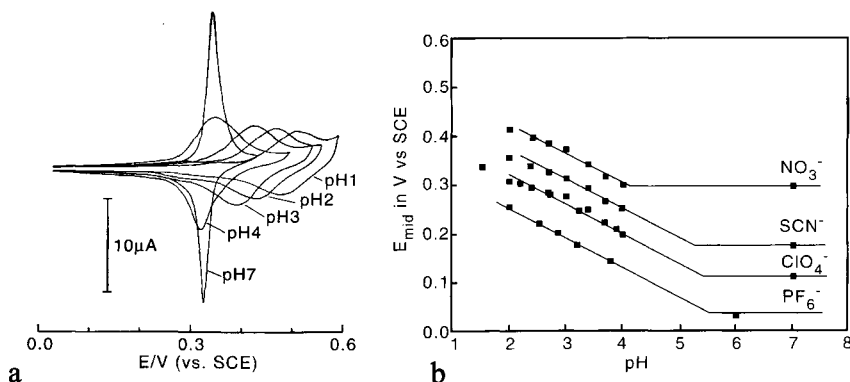


**Fig. 6.10.** **a** Cyclic voltammograms for the oxidation and re-reduction of 0.5 μg THPD deposited onto a 4.9-mm diameter basal plane pyrolytic graphite electrode and immersed in aqueous 0.1 M KNO<sub>3</sub> solution. The pH was adjusted by addition of 0.1 M HNO<sub>3</sub>. Scan rate 10 mV s<sup>-1</sup>. **b** Plot of the mid-peak potential,  $E_{\text{mid}} = 1/2(E_{\text{p,ox}} + E_{\text{p,red}})$ , for the oxidation and re-reduction of 0.5 μg THPD, immersed in aqueous 0.1 M KNO<sub>3</sub> (pH adjusted with HNO<sub>3</sub>), 0.1 M KSCN (pH adjusted with HNO<sub>3</sub>), 0.1 M NaClO<sub>4</sub> (pH adjusted with HClO<sub>4</sub>), 0.1 M KPF<sub>6</sub> (pH adjusted with HNO<sub>3</sub>) [B 94]

A first attempt to determine the acidity constant  $\text{p}K_{\text{A}2}$  for THPD from voltammetric data has been made by Schröder and coworkers [B 171]. The authors have derived  $\text{p}K_{\text{A}2}$  from the extent of ionic (protonated) liquid formation, as a function of the pH of the electrolyte solution, and determined from the analysis of the voltammetric responses process  $I_{\text{ox}}/I_{\text{red}}$  and  $\Pi_{\text{ox}}/\Pi_{\text{red}}$  (Fig. 6.9). This approach, however, is oversimplified since it does not include the Gibbs free energy of the transfer of the accompanying anions. This quantity needs to be taken into account in order to appropriately regard the influence of the electrolyte anion co-inserted into the redox liquid in the process of protonation.

As an important side effect the chemically facilitated ion transfer into the redox liquid considerably changes the phase properties of the redox liquid. Originally being ionically non-conducting the liquid now turns into an ionic liquid with the consequence that electrochemical reactions are not anymore initially confined to the three-phase junction but can start at the entire droplet | electrode interface (Fig. 6.11)

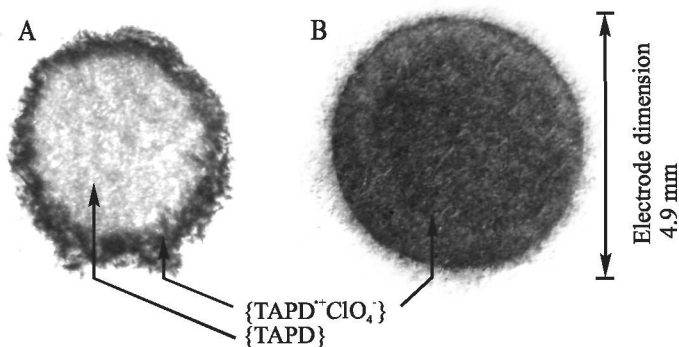


**Fig. 6.11a.** Photographic image of a stamp imprint of the interface layer of TriHPD at a graphite electrode. The electrode was modified with a continuous layer of the redox liquid and electrolyzed at a potential of +500 mV for 60 s in order to form the colored radical cation. **A** the neutral redox liquid and **B** the protonated, ionic liquid [B 171]

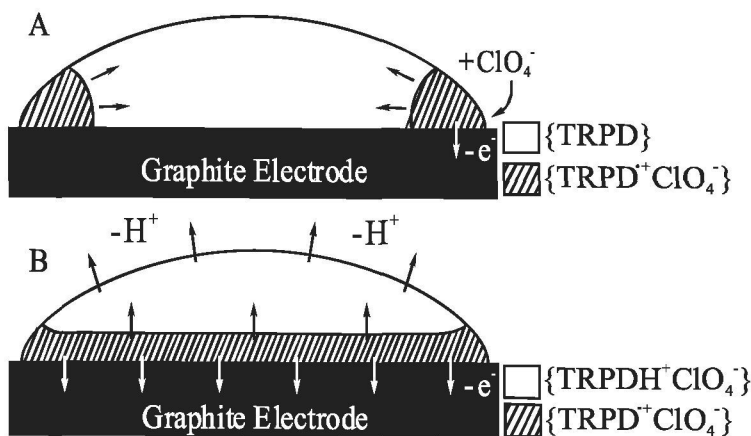


**Fig. 6.12b.** Schematic drawing of the mechanism of the oxidation of deposits of TRPDs of the unprotonated form **A**, and of the protonated form **B** [B 171]

### 6.1.3 Photochemical and Chemical Reactions at Immobilized Microdroplets of Redox Liquids

The known ability of  $\text{TMPD}^{2+}$ , Würster's blue, to mediate the homogeneous solution oxidation of biological redox compound, like ascorbic acid, NADH, or ferrocyclochromes inspired researchers in the lab of Richard Compton, to study the heterogeneous catalysis of immobilized microdrop-



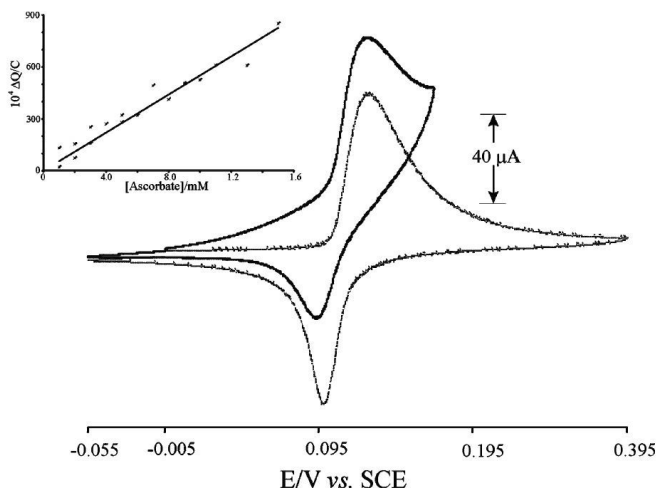


**Fig. 6.13.** Cyclic voltammograms (scan rate  $10 \text{ mV s}^{-1}$ ) illustrating the electrocatalytic oxidation of ascorbate; 5.4 nmol of THPD deposited on the surface of a 4.9-mm diameter bppg electrode immersed into aqueous 0.1 M sodium perchlorate solution, in the presence (solid line) and absence (dotted line) of 50 mM ascorbic acid at pH 7. The insert illustrates the charge difference inferred from cyclic voltammogram (scan rate  $5 \text{ mV s}^{-1}$ ) variation with ascorbic acid concentration for the oxidation of 5.4 nmol of THPD; 0.1 M potassium hexafluorophosphate containing 0.1 M phosphate buffer solution at pH 7 [B 284]

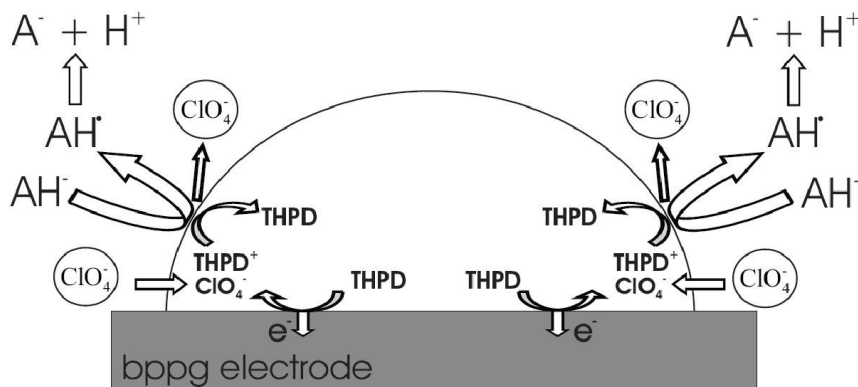
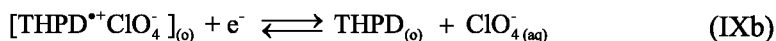


**Fig. 6.14.** Schematic diagram illustrating the electrocatalysis of L-ascorbate by  $\text{THPD}^+\text{ClO}_4^-$ . For simplicity, only one microdroplet is considered. Reproduced from [B 284]

lets of long-chain TRPDs. Thus, Wadhawan et al. [B 284] reported on the electrocatalytic oxidation of L-ascorbate at the electrode-oil-electrolyte tri-

ple phase junction of THPD microdroplets. They demonstrate that the presence of ascorbate ions in 0.1 M perchlorate or hexafluorophosphate electrolyte solutions has a dramatic effect on the voltammetry (Fig. 6.13). During the oxidation scan, more charge is passed compared to the case when ascorbic acid is not present. Second, on reverse scan, the magnitude of the back peak is considerably diminished in the presence of ascorbate ions. The authors suggest that the oxidation of ascorbate takes place at the liquid | liquid interface (see Fig. 6.14). A transfer of ascorbate into the oil droplet seems unlikely since the ascorbate ion is more hydrophilic than perchlorate and hexafluorophosphate. The voltammetry that is established in the presence of ascorbate ions is characterized by the competition of the catalytic oxidation of ascorbate ( $\text{AH}^-$ , reaction IXa), and the electrochemical reduction of  $\text{THPD}^+$ .



From their observations the authors have derived a kinetic model describing the electrocatalytic oxidation of ascorbate at immobilized droplets of TRPD. The model is based on the assumptions that: (i)  $\text{TRPD}^+$  is electrochemically generated at the three-phase junction electrode | redox liquid | electrolyte, however, for simplicity reasons, the electrochemical oxidation is considered as in a “thin film” regime; (ii) the catalytic oxidation of ascorbate proceeds at the droplet | electrolyte interface, and no transfer of ascorbate into the droplet takes place; (iii) the microdroplet-modified electrode consists of a monodispersed set of  $N$  femtoliter, each of radius  $R_0$ . The increase in the charge passed in the presence of ascorbate (bulk concentration in the aqueous phase  $[\text{AH}^-]_{\text{bulk}}$ ),  $\Delta Q_{\text{obs}}$ , is then expressed by Eq. 6.5.

$$\Delta Q_{\text{obs}} = \frac{6d}{R_0} k_{\text{cat}} F \tau N_0 [\text{AH}^-]_{\text{bulk}} \quad (6.5)$$

$d$  represents the spherical thickness of a  $\text{TRPD}^+$  ion;  $\tau$  is the time, in which the electron transfer rate across the oil | water interface can take place. It is defined by the scan rate of the voltammetric experiment,  $\nu$ , and the difference between the starting and finishing potentials of the sweep,  $\Delta E$ , with  $\tau = \Delta E/\nu$ ;  $N_0$  is the number of moles TRPD immobilized at the electrode surface.

**Table 6.4.** Reaction-on-a-drop analysis (Eq. 6.5) of the reaction between DEDRPD and TRPD radical cations and L-ascorbate<sup>a</sup> (reproduced from [B 284])

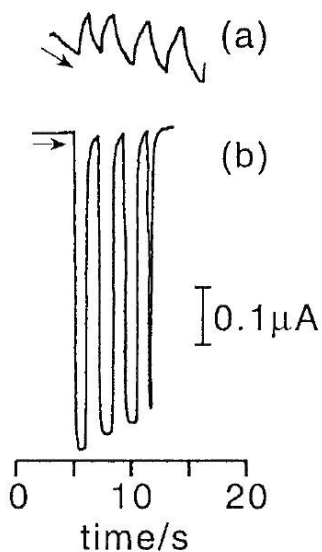
	Gradient of plot / C M <sup>-1</sup>	$6dk_{\text{cat}}/R_0$ / M <sup>-1</sup> s <sup>-1</sup>	$k_{\text{cat}}^b$ / M <sup>-1</sup> s <sup>-1</sup>
DEDBPD <sup>c</sup>	0.2373 ± 0.012	10.9 ± 0.5	7237 ± 366
DEDHPD <sup>d</sup>	0.1298 ± 0.012	5.8 ± 0.5	3876 ± 358
TBPD <sup>e</sup>	0.0798 ± 0.012	2.3 ± 0.3	1257 ± 230
THPD <sup>f</sup>	0.0553 ± 0.012	3.2 ± 0.7	2139 ± 464
DEDHePD <sup>g</sup>	0.0289 ± 0.012	1.3 ± 0.5	866 ± 360
THEPD <sup>h</sup>	0.0245 ± 0.012	1.8 ± 0.9	1184 ± 580
TNPD <sup>i</sup>	0.0232 ± 0.012	3.0 ± 1.6	2005 ± 1039

<sup>a</sup> Data obtained from cyclic voltammograms recorded at a scan rate of 5 mV s<sup>-1</sup>, in 0.1 M phosphate buffer solution containing 0.1 M potassium hexafluorophosphate, using a modified 4.9-mm diameter bppg electrode. <sup>b</sup> Assuming  $d = 5 \text{ \AA}$  and  $R_0 = 2 \text{ \mu m}$ . <sup>c</sup> Electrode modified with 5.7 nmol of DEDBPD,  $\tau = 40 \text{ s}$ . <sup>d</sup> Electrode modified with 5.8 nmol of DEDHPD,  $\tau = 40 \text{ s}$ . <sup>e</sup> Electrode modified with 6.0 nmol of TBPD,  $\tau = 60 \text{ s}$ . <sup>f</sup> Electrode modified with 6.0 nmol of THPD,  $\tau = 30 \text{ s}$ . <sup>g</sup> Electrode modified with 5.8 nmol of DEDHePD,  $\tau = 40 \text{ s}$ . <sup>h</sup> Electrode modified with 6.0 nmol of THEPD,  $\tau = 24 \text{ s}$ . <sup>i</sup> Electrode modified with 5.7 nmol of TNPD,  $\tau = 14 \text{ s}$ .

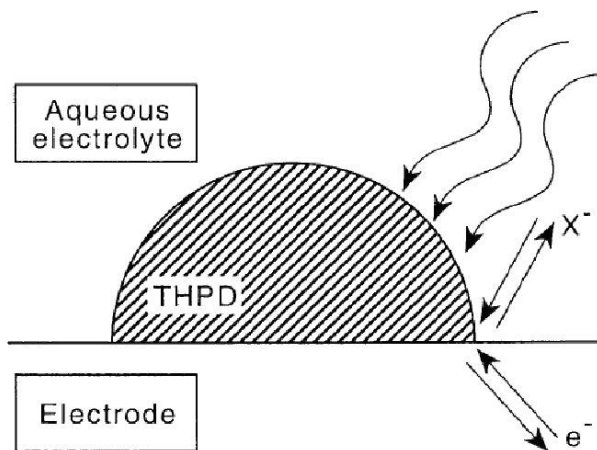
Based on these assumptions, the rate constants of the electrocatalytic oxidation of ascorbate by different TRPDs are given in Table 6.4. The table shows that the reactivity generally increases with decreasing length of the substituent, viz in the order DEDBPD > DEDHPD > TBPD = THPD > DEDHePD = THEPD > TNPD. The authors attribute this order to the greater number of cations per unit surface area for lower homologous.

For electrodes modified with tetrahexylphenylenediamines, Wadhawan et al. have reported photoelectrochemically induced catalytic processes [B 284]. The authors made use of the property of THPD to undergo facile photoexcitation coupled to redox conversion when exposed to light of ca. 300 nm wavelength. This behavior, which was already known for the tetramethyl-substituted phenylenediamine, TMPD <sup>6</sup>, has been investigated by Wadhawan with respect to (i) its occurrence at THPD microdroplet-

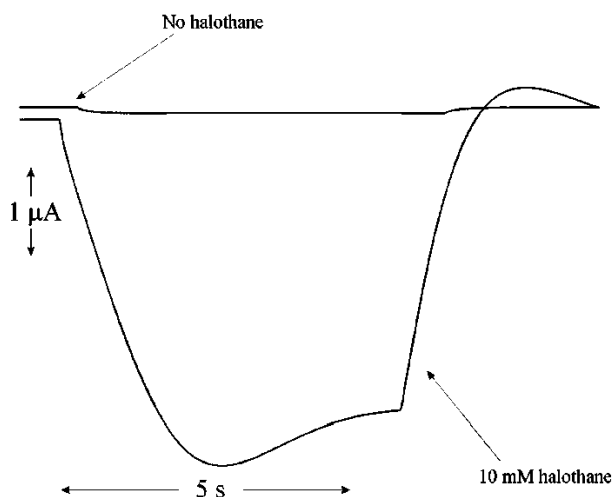
<sup>6</sup> Richtol HH, Fitzgerald EA Jr, Wuelfing P Jr (1971) J Phys Chem. 75: 2737-2741; Avdievich NI, Jeevarajan AS, Forbes MDE (1996) J Phys Chem 100: 5334-5342



**Fig. 6.15.** Photocurrents observed for the oxidation at 0.4 V vs. SCE (a) and for the photoreduction at 0.0V vs. SCE (b) of 80 nmol THPD (35  $\mu\text{g}$ ) deposited onto a 3x3 mm basal plane pyrolytic graphite electrode immersed in 0.1 M  $\text{NaClO}_4$  (10  $\text{mW cm}^{-2}$ , 280 nm, solution flow rate 0.02  $\text{cm}^3 \text{s}^{-1}$ ). The arrows indicate the initial part of the trace with the light switched off [B 182]



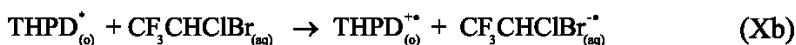
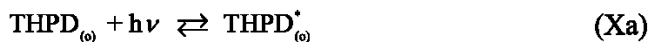
**Fig. 6.16.** Schematic drawing of the THPD|electrode|electrolyte triple interface reaction zone [B 182]

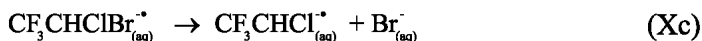


**Fig. 6.17.** Phototransients ( $2 \text{ mW cm}^{-2}$  illumination at  $320 \text{ nm}$ ) observed for  $5.4 \text{ nmol}$  of THPD deposited on the  $3 \times 3 \text{ mm}^2$  basal plane pyrolytic carbon electrode potentiostated at  $0.0 \text{ V}$  vs SCE, immersed  $0.1 \text{ M NaClO}_4$  containing  $10 \text{ mM}$  halothane (solution flow rate  $0.003 \text{ cm}^3 \text{ s}^{-1}$ ) [B 284]

modified electrodes, (ii) the role of the three-phase junction, and the effects introduced by anion insertion processes associated with the redox processes [B 182]. As Fig. 6.15 demonstrates, both, a significant photoreduction, and photooxidation current are observed. From the dependence of the magnitude of the photocurrent on the coverage of the electrode surface the authors have concluded that, as depicted in Fig. 6.16, the photoelectrochemical processes are confined to the triple-phase interface THPD|electrode|electrolyte.

In a later communication [B 284] the authors have demonstrated that this photoactivity can be utilized for the photochemically induced catalytic reduction of the lipophilic anaesthetic halothane (2-bromo-2chloro-1,1,1-trifluoroethane), Fig. 6.17. The mechanism of this process is proposed as follows:





Noteworthy, under similar conditions photoinduced electron transfer from excited chlorophyll a to vitamin K<sub>1</sub> has been observed [B 287], which bears possible potential in the development of solar cells based on photosynthesis.

Recently, the same group interrogated the electrochemistry of vitamin K<sub>1</sub>, deposited as an array of microdroplets onto the surface of a pyrolytic carbon electrode. The results of this study [B 273] are highly interesting

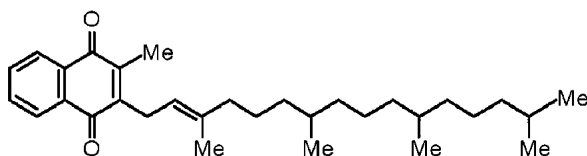


**Fig. 6.18.** Structure of vitamin K<sub>1</sub>, phylloquinone [B 273]

from several viewpoints. The electrochemical reduction of vitamin K<sub>1</sub> at low pH (Reaction XI) is accompanied by a proton uptake and the protonation of the reduced phylloquinone.



That means that very much in contrast to most other examples of electrochemical reactions of immobilized microdroplets or particles, both, the precursor liquid and the product are ionically non-conducting. Hence, it must be assumed that there cannot be a spatial proceeding of the reaction zone into the droplets. The electron and ion transfer remains confined to the three-phase junction. Most likely based on diffusion and convection processes, however, a conversion of the femtoliter droplets is achieved. When in the presence of acidic solutions alkali metal cations are added to the electrolyte the authors find a profound change in the voltammetric response. The voltammogram (see Fig. 6.19) now shows an additional peak in the reductive scan. The appearance of two well-defined reductive signals was also connected with extra charge in the reductive scan, which can be explained only on the basis of an additional Faradaic process. After a thorough analysis of the occurring phenomena, Wain and coworkers conclude the following mechanism: initially, vitamin K<sub>1</sub> is reduced in a two-electron two-proton wave to yield quinole as in process III. The second Faradaic process is likely due to further reduction within the redox liquid. The authors suggest that, due to the strong naphthaquinole-potassium ion

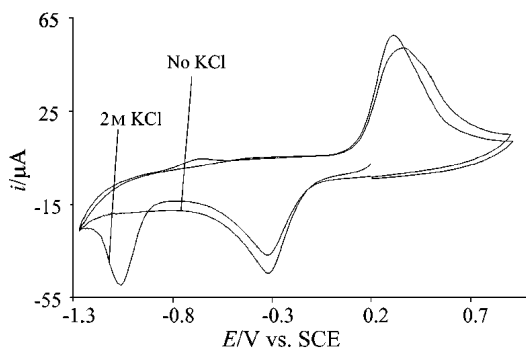
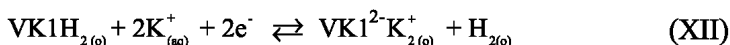
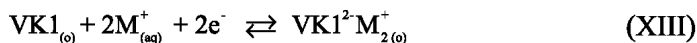


**Fig. 6.19.** Cyclic voltammograms (scan rate  $20 \text{ mV s}^{-1}$ ) for the reduction of  $5.6 \text{ nmol}$  vitamin  $\text{K}_1$  immobilized on a  $4.9\text{-mm}$ -diameter basal plane pyrolytic carbon electrode immersed into both  $0.1 \text{ M}$  aqueous  $\text{HCl}$  and  $0.1 \text{ M}$   $\text{HCl}$  containing  $2.0 \text{ M}$   $\text{KCl}$  [B 273]

pair bonding and the formation of the strong H-H bond process XII occurs, leading to hydrogen evolution:



In the presence of strongly alkaline solutions, the electrochemical reduction again takes place in a two-electron two-cation reaction that is sensitive to the nature of the transferred cation (Reaction XIII).



Apart from a study of the redox switching of 4-nitrophenyl nonyl ether by Wain et al. [B 286] this is the first time that alkali-metal uptake has been demonstrated in such environments.

A different kind of 'reactive electrochemistry' has been presented by Gergely and Inzelt [B 197]. In their communication the authors report on the electropolymerization that takes place when droplets of 3-methylthiophene are oxidized in the presence of aqueous solutions of  $\text{LiClO}_4$ . As Fig. 6.20 shows, during the first redox cycles, only the oxidation of the starting material can be seen. During repetitive voltammetric cycling additional redox systems in the potential range between  $0.3$  and  $0.8 \text{ V}$  appear and start growing. This growing process goes on with further cycling (Fig. 6.21). It shows the formation of poly(3-methylthiophene) at the electrode surface. The evaluation of the growth of the polymer film by integration of

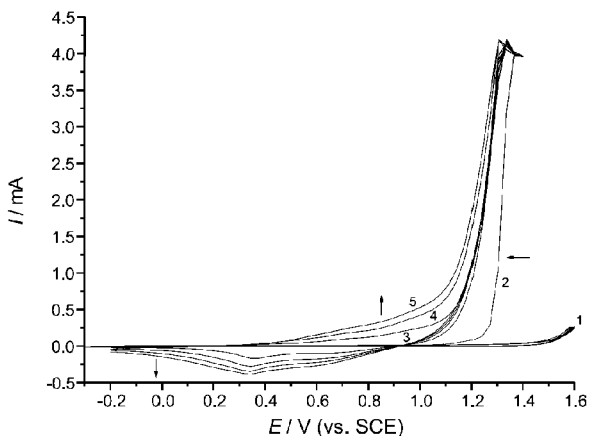


**Fig. 6.20.** Consecutive cyclic voltammetric curves obtained for 3-methylthiophene droplets attached to a paraffin-impregnated graphite electrode, PIGE, in the presence of an aqueous solution containing  $0.5 \text{ mol L}^{-1} \text{ LiClO}_4$ . Cycles 1-5 (curves 2-5, curve 1 shows the background current), scan rate  $100 \text{ mV s}^{-1}$  [B 197]

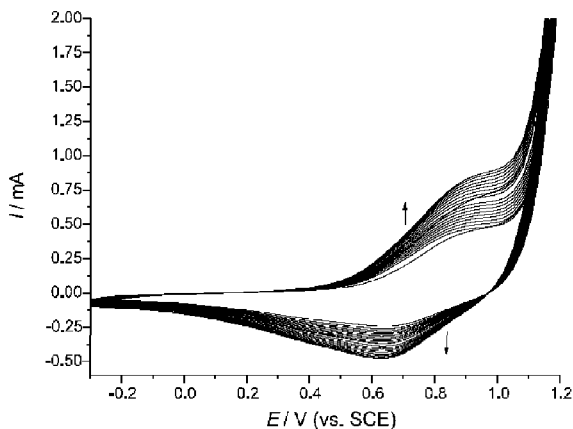


**Fig. 6.21.** Consecutive cyclic voltammetric curves obtained for 3-methylthiophene droplets attached to a paraffin-impregnated graphite electrode, PIGE, in the presence of an aqueous solution containing  $0.5 \text{ mol L}^{-1} \text{ LiClO}_4$ . Cycles 15-34, scan rate  $100 \text{ mV s}^{-1}$  [B 197]

the electric charge of the redox process caused by polymethylthiophene, however, showed that only about 1% of the monomer was electropolymerized up to the 35<sup>th</sup> cycle.

Reactive chemistry in deposited redox liquid microdroplets can be interesting also from the analytical point of view. Thus, a reaction mechanism



has been proposed that can be utilized for the accumulation and detection of sulfide. The approach makes use of the reaction of the oxidized  $N^l$ -[4-(dihexylamino)phenyl]- $N^l, N^d, N^d$ -trihexyl-1,4-phenylenediamine (DTPPD) with  $\text{HS}^-$  leading to the formation of a methylene blue derivative [B 289].

## 6.2 The Electrochemistry of Compounds Dissolved in Droplets

The electrochemistry of electroactive compounds dissolved in water immiscible solvents and attached to the surface of solid electrodes in the form of droplets is an interesting topic. This chapter, will be focused on one feature of such electrodes, namely the *ion transfer* between the adjacent liquid phases, which always accompanies the electron transfer between the solid electrode and the electroactive compound. Figure 6.22 schematically depicts the situation at the electrode when a droplet of a solution of an electroactive compound is attached to an electrode surface. Very similar to the situation of immobilized solid particles that are undergoing insertion electrochemical reactions (see, for example, the electrochemistry of metal hexacyanoferrates in previous chapters), and even more similar to the situation of immobilized electroactive droplets (Chapter 6.1) one can observe a reaction scenario that could be called “insertion electrochemistry with droplets”. This approach offers a unique access to the standard Gibbs energy of ion transfer across a liquid | liquid interface [B 132].

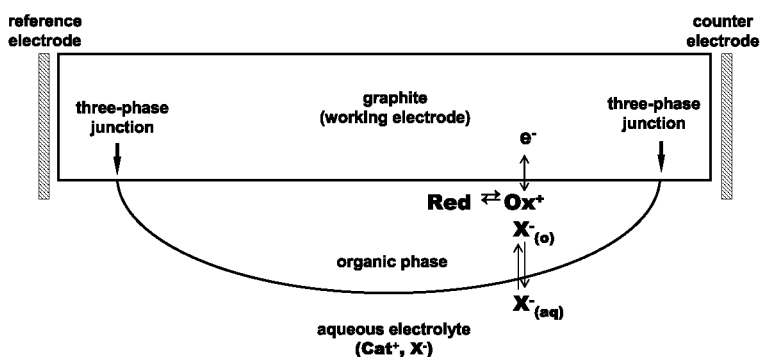


**Fig. 6.22.** Three-phase electrode consisting of a droplet of an organic solvent containing an electrochemically oxidizable compound Red. The droplet adheres to a solid electrode (graphite) and it is immersed in an aqueous electrolyte solution. The oxidation of Red at the graphite-organic liquid interface is accompanied by a transfer of  $X^-$  from aqueous to the organic phase [B 280]

The standard Gibbs energy of ion transfer between two solvents is an important thermodynamic quantity since its value portrays the difference between the free energies of solvation of an ion  $i$  in two solvents  $\alpha$  and  $\beta$ . The standard Gibbs energy of ion transfer from phase  $\alpha$  to phase  $\beta$  ( $\Delta G_{\alpha, i}^{\beta, \circ}$ ) is related to the standard potential of ion transfer ( $\Delta\phi_{\alpha, i}^{\beta, \circ}$ ), and to the standard partition coefficient ( $P_i$ ) through the following equations:

$$\Delta\phi_{\alpha, i}^{\beta, \circ} = \frac{-\Delta G_{\alpha, i}^{\beta, \circ}}{z_i F} \quad (6.6)$$

$$P_i = \exp\left(\frac{-\Delta G_{\alpha, i}^{\beta, \circ}}{RT}\right) \quad (6.7)$$

The logarithm of the partition coefficient ( $\log P$ ) is a measure of the lipophilicity of compounds. It helps understanding a variety of biological phenomena, such as passive transfer through membranes, enzyme-receptor interactions, drug activities, etc., and it is a major parameter in quantitative structure activities relationships (QSAR) and quantitative structure properties relationships (QSPR) <sup>7</sup>. While  $\log P$  of neutral compounds is relatively easily accessible by different partition techniques, such as shake-flask methods, partition chromatography, high-performance liquid chromatography, extraction <sup>1</sup>, etc.,  $\log P$  of single ions was accessible until recently only by four-electrode voltammetry at the interface of two immiscible electrolyte solutions (ITIES) <sup>8</sup>. The inevitable presence of electrolytes in the two immiscible solvents, as well as the non-polarizability of some important water | organic solvent interfaces <sup>9</sup> severely restricts the use of that technique.

In this chapter the applicability of the three-phase electrode approach for determining standard Gibbs energies of transfer of ions will be discussed. To achieve an ion transfer across the organic droplet|aqueous solution interface, a small amount of a neutral electroactive compound is dissolved in an organic and water-immiscible solvent that is devoid of any electrolyte. A droplet (e.g., 1  $\mu\text{L}$ ) of that solution is attached to the surface of a suit-

<sup>7</sup> Testa B, van de Waterbeemd H, Folkers G, Gay R (2001) Pharmacokinetic Optimization in Drug Research. Wiley-VCH, Weinheim

<sup>8</sup> Girault HHJ, Schiffrin DJ (1989) Electrochemistry of liquid-liquid interfaces. In: Bard, AJ (ed) Electroanalytical Chemistry, A Series of Advances. vol 15. Dekker, New York, pp 1-141

<sup>9</sup> Marcus Y (1997) Ion Properties. Dekker, New York

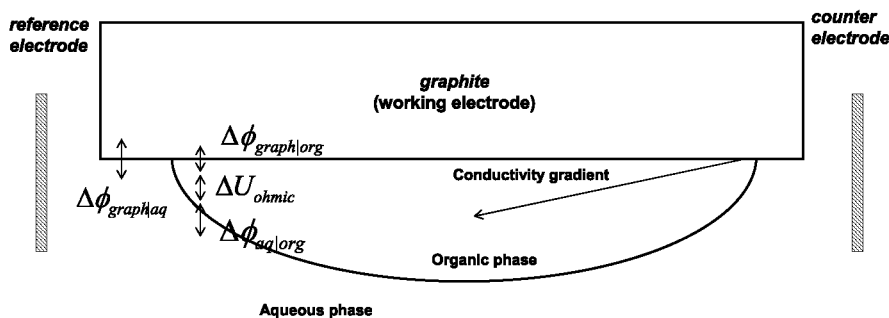


Fig. 6.23. Potential drops at three-phase electrode (details see text) [B 280]

able electrode. Graphite electrodes (e.g., PIGE) are superior compared to metal electrodes because the stability of the attachment of a nonaqueous droplet is very good. The electrode with the attached droplet is immersed in an aqueous electrolyte solution of the salt  $\text{Cat}^+\text{A}^-$ . In this solution the reference and counter electrodes are placed as in a conventional voltammetric cell. A prerequisite for the proper operation of the experiment is the existence of the *three-phase junction line* where the three phases working electrode, organic solution, and aqueous solution boarder to each other. Since no electrolyte is added to the organic solvent, the initial conductivity in the region near the edge of the droplet results only from free partition of the salt present in the aqueous solution. The applied potential between the working and the reference electrode can initially act in a restricted area only, i.e., at the three-phase junction where all three phases meet. Figure 6.23 depicts the potential drops at such a three-phase electrode.

The potential drop at the graphite | organic phase interface is given by the following expression:

$$\Delta\phi_{\text{graph|org}} = \Delta\phi_{\text{graph|aq}} - \Delta U_{\text{ohmic}} - \Delta\phi_{\text{aq|org}} \quad (6.8)$$

The potential drop  $\Delta\phi_{\text{graph|aq}}$  at the interface graphite electrode | aqueous solution in Eq. 6.8 is controlled potentiostatically. However, the potential drop  $\Delta\phi_{\text{graph|org}}$  at the interface graphite | organic solution is in fact the applied potential difference ( $\Delta\phi_{\text{graph|aq}}$ ) diminished (i) by the value of the ohmic drop  $\Delta U_{\text{ohmic}}$  inside the organic phase, and (ii) by the value of the potential drop  $\Delta\phi_{\text{aq|org}}$  (i.e., the potential drop due to the partition of ionic species) at the interface aqueous solution | organic solution. Indeed, the value of  $\Delta\phi_{\text{aq|org}}$  will be different for different ions that are initially present

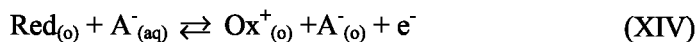
in the aqueous phase. Consequently, the potential  $\Delta\phi_{\text{graph|org}}$  will be altered in the same way as the nature of the ions in the aqueous phase is changed. When the organic droplet does not contain any deliberately added electrolyte  $\Delta U_{\text{ohmic}}$  will be very large all over the graphite | droplet interface with the only exception of the very edge, i.e., the three-phase junction region. A thin layer that is situated at the droplet-water interface will acquire a higher ionic conductivity due to salt partition from the aqueous phase. Therefore, an electrochemical oxidation of Red (see Fig. 6.22) can start without ohmic impediment only in that three-phase junction region. The ohmic drop will decrease within the droplet with progressing of the electrode reaction because  $\text{Ox}^+$  and  $\text{X}^-$  are ions that provide ionic conductivity (the concentration of Red is usually rather high, e.g., higher than  $10^{-2}$  M).

The *electron transfer* process occurring at the electrode | organic phase interface is *necessarily coupled* to a *transfer of ions* across the aqueous phase | organic phase interface in order to maintain the electroneutrality of the organic phase. In voltammetric experiments, both the electron and ion transfer processes are recorded together. The nature of the ion transfer takes place, i.e., the transfer of anions from water to the organic phase or the transfer of electrochemically created cations from the organic phase to water, depends primarily on the ratio of the standard Gibbs energies of ion transfer of both candidates. Generally, if the solvation of the electrochemically created cations  $\text{Ox}^+$  in the organic phase is stronger than the hydration of the anions in the aqueous phase  $\text{X}^-$ , then a transfer of anions from the aqueous phase to the organic phase will take place, as depicted in the Fig. 6.22.

A *transfer of cations* from aqueous phase to the organic phase can be achieved if the solvation of electrochemically generated anions in the organic phase, created by reduction of a neutral electro-reducible compound present in the organic phase, is stronger than the hydration of the cations in the aqueous phase.

In both cases the standard Gibbs energies of ion transfer can be deduced from the formal potentials of cyclic or square-wave voltammograms (or of any other voltammetric technique), following the algorithm described next.

According to Fig. 6.22, the overall reaction proceeding at a microdroplet-modified electrode can be written as follows:



If no kinetic constraints exist with respect to the electron and ion transfer, the thermodynamic treatment applied to Reaction XIV leads to the following form of the Nernst equation:

$$E = E_{\text{Ox}^+/\text{Red}}^{\ominus} + \Delta\phi_{\text{aq}, \text{A}^-}^{\ominus} + \frac{RT}{F} \ln \frac{a_{\text{Ox}^+} a_{\text{A}^-}}{a_{\text{Red}} a_{\text{A}^-}} \quad (6.9)$$

In Eq. 6.9  $E$  is the applied potential between the working and the reference electrode,  $E_{\text{Ox}^+/\text{Red}}^{\ominus}$  is the standard potential of the redox couple  $\text{Ox}^+/\text{Red}$  in the organic solvent,  $\Delta\phi_{\text{aq}, \text{A}^-}^{\ominus}$  is the standard potential of transfer of anions from the aqueous phase to the organic phase,  $a_{\text{Ox}^+}$  and  $a_{\text{Red}}$  are the activities of the oxidized and reduced forms of the electroactive compound in the organic phase, while  $a_{\text{A}^-}$  and  $a_{\text{A}^-}$  are the activities of anions in the organic phase and aqueous solutions, respectively. In a first approximation, the activities in the Nernst equation have been replaced by concentrations. Since the concentration of the anions in the aqueous phase does not change significantly during the experiment, Eq. 6.9 can be rewritten as:

$$E = E_{\text{Ox}^+/\text{Red}}^{\ominus} + \Delta\phi_{\text{aq}, \text{A}^-}^{\ominus} - \frac{RT}{F} \ln c_{\text{A}^-} + \frac{RT}{F} \ln \frac{c_{\text{Ox}^+} c_{\text{A}^-}}{c_{\text{Red}}} \quad (6.10)$$

Electroneutrality requires that

$$c_{\text{Ox}^+} = c_{\text{A}^-} \quad (6.11)$$

The mass conservation law in respect to the organic phase leads to

$$c_{\text{Red}} + c_{\text{Ox}^+} = c^*_{\text{Red}} \quad (6.12)$$

where  $c^*_{\text{Red}}$  is the initial concentration of the oxidizable compound in the organic phase. When the applied potential equals the formal potential of the redox pair it follows that

$$c_{\text{Red}} = c_{\text{Ox}^+} \quad (6.13)$$

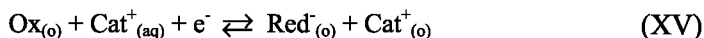
By substitution of Eqs. 6.11-6.13 in Eq. 6.10 allows calculating the formal potential ( $E_c^{\ominus}$ ) of the system:

$$E_c^{\ominus'} = E_{\text{Ox}^+_{(o)}/\text{Red}_{(o)}}^{\ominus} + \Delta\phi_{\text{aq}, \text{A}^-}^{\ominus} - \frac{RT}{F} \ln c_{\text{A}^-_{(\text{aq})}} + \frac{RT}{F} \ln \frac{c^*_{\text{Red}_{(o)}}}{2} \quad (6.14)$$

Since the voltammetric systems obtained by these experiments, at least with the used redox probes, possess all features of electrochemical reversibility and the transfer coefficients are obviously near to 0.5, it is reasonable to take the mid-peak potentials of cyclic voltammograms as the formal potential of the system.

The last equation shows that the formal potential of the voltammograms depends on the *nature of the anions in aqueous phase* (via the values of  $\Delta\phi_{\text{aq}, \text{A}^-}^{\ominus}$ ). Generally, the more lipophilic the anions are, the more negative is the value of  $\Delta\phi_{\text{aq}, \text{A}^-}^{\ominus}$ . Consequently, the oxidation of the compound Red in the organic phase will occur at more negative potentials (i.e., it will be easier oxidized) as the lipophilicity of the transferable anions increases. Further, the formal potential should shift by about 59 mV in negative direction for a ten-fold increase of the concentration of the transferable anions in aqueous phase. This criterion, taken together with the stability of the voltammograms recorded during consecutive cycling serves as an important indicator for the reversibility of the processes occurring at the droplet-modified electrodes.

When an *electroreducible* compound is dissolved in the organic phase, then its reduction at a three-phase electrode can provoke the transfer of cations from water to the organic phase. This can be described by the following reaction:



Analogously to the previous case, the thermodynamic treatment of Reaction XV leads to the following Nernst equation, which is valid when cations are transferred from the aqueous to the organic phase:

$$E_c^{\ominus'} = E_{\text{Ox}_{(o)}/\text{Red}^-_{(o)}}^{\ominus} + \Delta\phi_{\text{aq}, \text{Cat}^+}^{\ominus} + \frac{RT}{F} \ln c_{\text{Cat}^+_{(\text{aq})}} + \frac{RT}{F} \ln \frac{2}{c^*_{\text{Ox}_{(o)}}} \quad (6.15)$$

The more lipophilic the cations present in the aqueous phase are, the more positive will be  $\Delta\phi_{\text{aq}, \text{Cat}^+}^{\ominus}$ . Subsequently, the reduction of the organic compound Ox in the oil phase will occur at more positive potentials as the lipophilicity of the cations in the aqueous phase increases. The formal potential of the coupled electron/ion reaction at the three-phase electrode will

shift by 59 mV in positive direction for a ten-fold increase of the concentration of the transferable cations in the aqueous solution.

### 6.2.1 The Determination of Standard Gibbs Energies of Transfer of Anions

The oxidation of a neutral lipophilic organic compound dissolved in an organic solvent is a precondition for transferring anions across the aqueous | organic interface. The compound decamethylferrocene (dmfc) (bis(pentamethylcyclopentadienyl)iron(II)) possesses that ability (see Fig. 6.24). It is a lipophilic compound, soluble in various organic solvents, but almost insoluble in water<sup>10</sup>. It exhibits an electrochemically reversible one electron redox reaction in organic solvents and it is commonly used as a reference standard for potential in measurements in nonaqueous media<sup>4</sup>. The oxidation of dmfc in a droplet of nitrobenzene (NB) attached to an electrode and immersed in aqueous solutions of different sodium salts gives rise to well-defined square-wave voltammograms, the formal potentials of which are sensitive to the nature and concentrations of the anions present in the aqueous solutions (see Fig. 6.25). Of course, in principle, any voltammetric measuring technique can be applied, however, square-wave voltammograms offer a simple way to measure the formal potential as it is the peak potential of the signals. The overall electrode process pro-

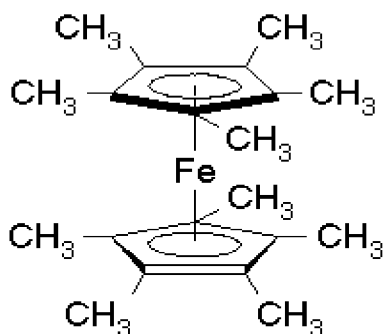
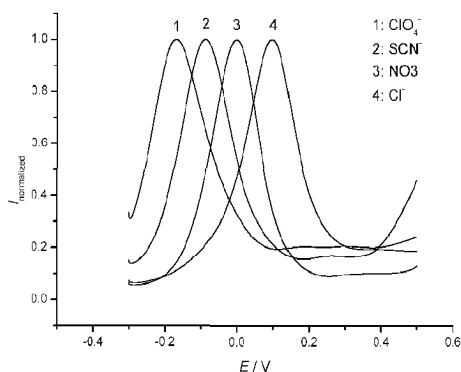
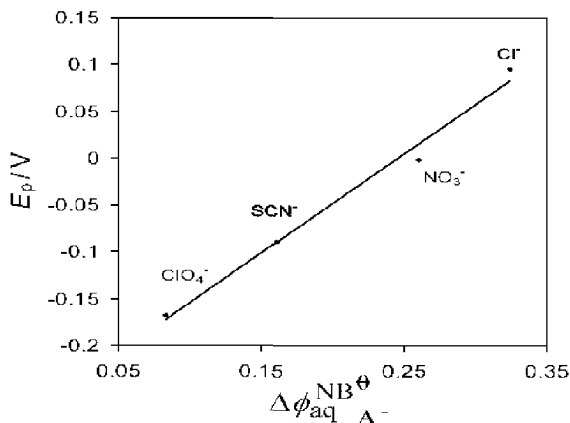


Fig. 6.24. Structure of decamethylferrocene (dmfc)

<sup>10</sup> Noviantri I, Brown KN, Fleming DS, Gulyas PT, Lay PA, Masters AF, Philips L (1999) *J Phys Chem B*, 103:6713-6722

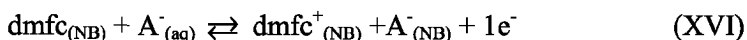


**Fig. 6.25.** Normalized square-wave voltammograms recorded at electrodes of a dmfc solution in nitrobenzene (0.1 M) and immersed in 1 M aqueous solutions of different sodium salts. The instrumental parameters were: frequency ( $f$ ) of 100 Hz, amplitude ( $E_{sw}$ ) of 50 mV, and scan increment ( $dE$ ) of 0.15 mV



**Fig. 6.26.** Dependence of the formal potentials of the square-wave voltammograms depicted in Fig. 6.25 on the standard potentials of transfer of anions across the water nitrobenzene interface [B 240]

ceeding at the three-phase electrode can be written as follows:



The dependence of the formal potentials of the square-wave voltammograms (Fig. 6.25) on the standard potentials of transfer of the anions from water to nitrobenzene is linear and characterized by a slope of 0.95 and an intercept of  $-0.259$  mV (cf. Fig. 6.26). The slope of this dependence is near to 1, just as predicted by Eq. 6.14. From the intercept of this dependence one can evaluate the standard potential of the couple  $\text{dmfc}^+/\text{dmfc}$  in nitrobenzene which reads  $-0.184$  V (vs. Ag/AgCl, saturated KCl). This value



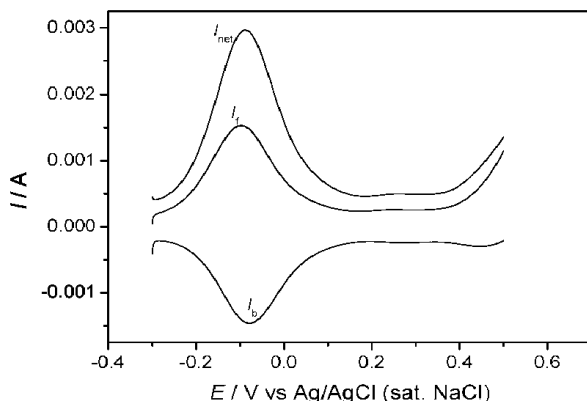


**Fig. 6.27.** Forward ( $I_f$ ), backward ( $I_b$ ) and net ( $I_{net}$ ) components of a square-wave voltammetric response of a nitrobenzene droplet containing 0.1 M dmfc attached to the surface of the working electrode and immersed in 1 M aqueous solution containing  $\text{SCN}^-$  anions. The experimental conditions were: frequency  $f = 100$  Hz, amplitude  $E_{sw} = 50$  mV, and scan increment  $dE = 0.15$  mV [B 240]

can be also determined by common measurements in the non-aqueous phase in the presence of a reference standard.

Knowing the value of the standard potential of  $\text{dmfc}^+/\text{dmfc}$  in nitrobenzene, and studying the oxidation of nitrobenzene solution of dmfc at a droplet-modified electrode which is immersed in aqueous solutions containing different anions, one can estimate the standard potentials of transfer (and thus the standard Gibbs energies of transfer) of the anions from water to nitrobenzene using Eq. 6.14. To identify the electrode system to follow Reaction XVI, one can use the dependence of the formal potentials on the logarithm of concentration of anions in the aqueous phase, and the stability of the voltammetric responses during consecutive cycling.

The electrochemical reversibility of the electrode process should be checked by studying the dependence of the formal potentials on the frequency (in square-wave voltammetry) or on the scan rate (in cyclic voltammetry). Representative square-wave voltammogram of all current components of the electrode process of dmfc obtained at a three-phase electrode with coupled transfer of thiocyanate anions is given in Fig. 6.27.

This approach has been utilized for the determination of the standard Gibbs energies of transfer of a large number of inorganic anions [B 132, 206, 240, 259] as well as of various organic anions, such as the anions of aliphatic and aromatic carboxylic acids [B 240, 259], substituted phenols [B 240, 269], drugs [B 269], and amino acids and peptides [B 262, 266]. As organic phases the common solvents nitrobenzene and dichloroethane

[B 132, 240, 259, 262, 266] have been used. Remarkably, also *n*-octanol [B 206, 269], nitrophenyl octyl ether [B 282], and D- and L-menthol [B 221] have been exploited as organic solvents. Some of the data of lipophilicities of anions are given in Table 6.5.

It was an important achievement in the field of ion transfer studies that the determination of lipophilicities of ions across the water|*n*-octanol interface became feasible with the help of the three-phase electrode approach [B 206, 269]. This is so important because the traditional measure of lipophilicity as a predictor of solute membrane partitioning is the partition coefficient in the *n*-octanol-water system ( $\log P_{\text{aq}}^{n\text{-oct}}$ ). The lipophilic chain of *n*-octanol together with the hydrophilic hydroxyl group make *n*-octanol a good mimic for the major constituents of biological membranes (i.e., phospholipids). However, due to the non-polarizability of the water | *n*-octanol interface in the 4-electrode ITIES technique, no lipophilicity data of ions measured in that system were accessible until now. The non-polarizability of that interface is a result of not having yet found an appropriate lipophilic electrolyte for *n*-octanol to perform the necessary 4-electrode ITES measurements. Using the three-phase electrode approach the determination of standard Gibbs energies of ion transfer across the water | *n*-octanol interface is quite easy [B 206, 269].

The knowledge of the lipophilicities of amino acids and peptides [B 262, 266] is of essential importance to understand their biological activity, peptide interactions and peptide folding. Studying the transfer of mono anionic forms of various oligo peptides was performed to determine the individual contributions of the amino acid residues to the overall lipophilicity of the oligo peptides [B 266]. The effect of the *position* of an amino acid residue in the chain of a peptide is in some cases very pronounced, especially when an aromatic amino acid residue is placed next to the terminal amino acid at which the negative charge is located in the anionic form. Therefore, it is unreasonable to approximate the entire lipophilicity of peptide anions as additive functions of the contributions of their amino acid residues, as it has been proposed in all theoretical models for neutral peptides. A first study of the lipophilicities of various peptide anions and amino acid anions has been published [B 262, 266]. A part of the data is given here in Table 6.6.

**Table 6.5.** Formal potentials  $E_c^{\circ}$ , slope of the formal potentials vs. concentration of anions in aqueous phase, standard deviation of formal potentials, and standard Gibbs energies of ion transfer of some anions across the water|NB interface [B 259]

Anion	$E_c^{\circ}$ /mV	slope $E_c^{\circ}$ vs. log (c) / mV	$s(E_c^{\circ})$ /mV	$\Delta G^{\circ}$ /kJ mol <sup>-1</sup>
ClO <sub>3</sub> <sup>-</sup>	2	-55.3	6.43	25.40
BrO <sub>3</sub> <sup>-</sup>	60	-58.7	7.17	30.90
IO <sub>3</sub> <sup>-</sup>	74	-54.3	8.08	32.40
IO <sub>4</sub> <sup>-</sup>	-132	-56.4	2.00	12.50
OCN <sup>-</sup>	45	-50.5	2.45	29.50
SeCN <sup>-</sup>	-136	-43.0	5.30	11.80
CN <sup>-</sup>	41	-58.1	4.43	29.60
N <sub>3</sub> <sup>-</sup>	14	-52.1	3.44	26.80
Monofluoroacetate	44	-54.4	5.48	29.90
Difluoroacetate	34	-48.5	3.90	28.90
Trifluoroacetate	-2	-60.1	1.79	25.30
Monochloroacetate	36	-51.5	4.73	29.10
Dichloroacetate	9	-58.0	1.15	26.40
Trichloroacetate	-66	-60.1	1.97	18.80
Monobromoacetate	12	-39.3	3.44	26.70
Dibromoacetate	-7	-59.0	2.00	24.80
Tribromoacetate	-94	-59.8	1.03	16.00
Monoiodoacetate	0	-54.6	1.20	25.10
Formiate	58	-56.4	2.40	30.60
Acetate	52	-58.0	1.50	30.10
Propionate	29	-54.6	0.80	27.98
Butyrate	11	-53.1	2.20	26.25
Valeriate	-31	-63.5	2.80	22.30
Capronate	-75	-60.3	1.40	18.10
Oenanthatate	-115	-55.2	1.80	14.20
Caprylate	-125	-57.4	4.20	12.64
Pelargonate	-120	-52.9	3.20	13.40
Caprinate	-118	-58.4	2.50	13.60
Cyclopropane carboxylate	-20	-60.0	1.10	23.25
Cyclobutane carboxylate	-61	-57.8	1.40	19.30
Cyclopentan carboxylate	-100	-63.2	1.60	15.54
Cyclohexane carboxylate	-131	-56.8	2.80	12.54
Cycloheptane carboxylate	-155	-55.4	2.00	10.22

**Table 6.6.** The standard Gibbs energies of transfer, the standard potential of transfer, and the logarithm of the partition coefficients of monoanionic forms of amino acids and peptides as determined by three-phase electrode approach [B 266]

Peptide anions	$\Delta\phi_{\text{aq}, \text{A}^-}^{\text{NB}, \circ} / \text{V}$	$\Delta G_{\text{aq}, \text{A}^-}^{\text{NB}, \circ} / \text{kJ mol}^{-1}$	$\log P_{\text{aq}, \text{A}^-}^{\text{NB}, \circ}$	slope $E_c^{e^-}$ vs. $\log[c] / \text{mV}$
Trp <sup>-</sup>	0.115	10.80	-1.90	-64
Trp-Ala <sup>-</sup>	0.165	15.75	-2.75	-80
Trp-Gly <sup>-</sup>	0.162	15.60	-2.73	-73
Trp-Val <sup>-</sup>	0.120	11.60	-2.05	-75
Trp-Leu <sup>-</sup>	0.100	9.50	-1.66	-73
Trp-Tyr <sup>-</sup>	0.075	7.40	-1.30	-65
Trp-Phe <sup>-</sup>	0.055	5.30	-0.93	-77
Trp-Trp <sup>-</sup>	0.050	4.80	-0.85	-70
Trp-Gly-Gly <sup>-</sup>	0.165	15.80	-2.75	-75
Trp-Gly-Tyr <sup>-</sup>	0.165	15.00	-2.65	-74
Trp-Gly-GlyTyr <sup>-</sup>	0.160	15.50	-2.70	-74
Leu-Leu <sup>-</sup>	0.245	23.70	-4.15	-71
Leu-Leu-Ala <sup>-</sup>	0.293	28.20	-4.95	-57
Leu-Leu-Gly <sup>-</sup>	0.290	28.00	-4.91	-80
Leu-Leu-Leu <sup>-</sup>	0.240	23.20	-4.05	-80
Leu-Leu-Tyr <sup>-</sup>	0.205	19.70	-3.45	-56
Leu-Leu-Phe <sup>-</sup>	0.180	17.50	-3.05	-64
Gly-Gly-Val <sup>-</sup>	0.275	26.40	-4.60	-57
Gly-Gly-Leu <sup>-</sup>	0.280	26.80	-4.70	-56
Gly-Gly-Phe <sup>-</sup>	0.270	26.00	-4.55	-58
Gly-Trp-Gly <sup>-</sup>	0.165	15.80	-2.75	-48
Gly-Gly-Trp <sup>-</sup>	0.195	19.00	-3.35	-56
Lys-Tyr-Thr <sup>-</sup>	0.310	30.00	-5.25	-58
Tyr-Ala-Gly <sup>-</sup>	0.260	24.90	-4.40	-48

### The Transfer of Chiral Ions Across the Water | Chiral Organic Liquid Interface

It has been shown that the transfer of ions from water to a *chiral* organic solvent can be studied with three-phase electrodes. Thus, it was possible to measure the differences in Gibbs energies of transfer for *chiral* ions from water to *chiral* liquids. By attaching a single droplet of a *chiral* liquid containing decamethylferrocene on a paraffin-impregnated graphite electrode and immersing that electrode in an aqueous solution containing *chiral* anions, the Gibbs energies of all four ion-solvent combinations can be determined (see Fig. 6.28).

For symmetry reasons it is expected that the Gibbs energies of transfer of a D-ion from water to the D-liquid is the same as that of the L-ion to the L-liquid. The same holds true for the combinations D-ion / L-liquid and L-ion / D-liquid. Square-wave voltammetric experiments conducted in aqueous solutions containing D- or L-anionic forms of some amino acids (phenylalanine, tyrosine, and lysine) performed with dmfc solutions in D- and L-2-octanol droplets allowed to determine these Gibbs energies of transfers relative to each other, i.e., the differences between  $\Delta G_{D-ion}^{\theta, w \rightarrow D-liq}$  and  $\Delta G_{D-ion}^{\theta, w \rightarrow L-liq}$ , i.e.  $\Delta \Delta G_{D-ion}^{\theta, w \rightarrow L-liq; D-liq}$ , and between  $\Delta G_{L-ion}^{\theta, w \rightarrow L-liq}$  and

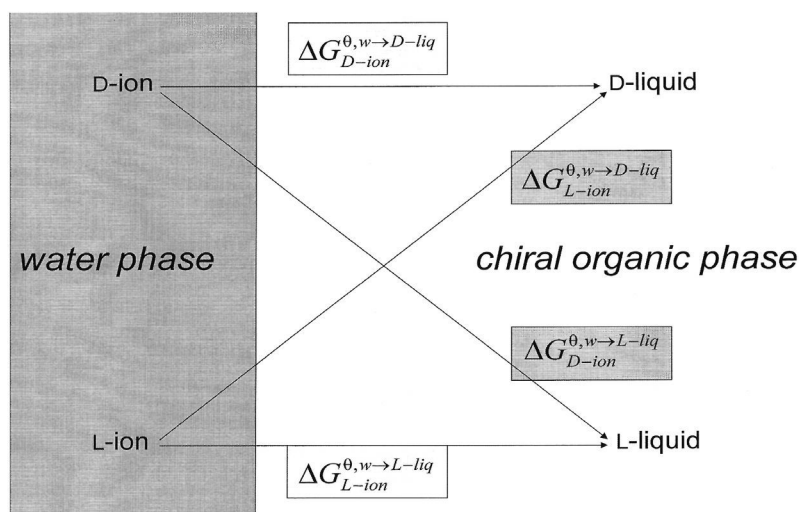


**Fig. 6.28.** Accessible Gibbs energies of transfer of D- and L-ions between water and a D- and L-liquid

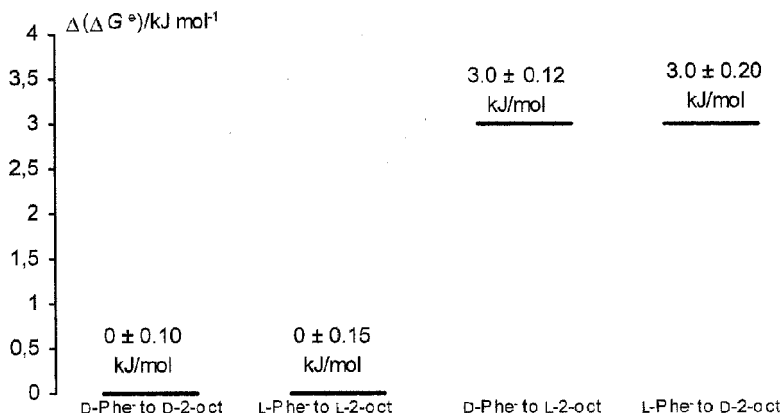


**Fig. 6.29.** Relations between the Gibbs energies of transfer of the anions of D- and L-phenylalanine from water to D- and L-2-octanol. The values for D-Phe- and L-Phe- have been set arbitrarily to zero. The values following the signs “±” denote to standard deviations

$\Delta G_{L-ion}^{\theta, w \rightarrow D-liq}$ , i.e.,  $\Delta \Delta G_{L-ion}^{\theta, w \rightarrow L-liq; D-liq}$ . In all studied combinations symmetrical solvation behavior has been observed, which is in complete agreement with theory. Thus, the energy of interactions between D-anions and D-2-octanol were identical with those between L-anions and L-2-octanol. The same holds true for the combinations D-anions and L-2-octanol and L-anions and D-2-octanol (see the example in Fig. 6.29). This figure illustrates that the three-phase electrodes with immobilized droplets allow a reproducible measurement of the rather small energetic differences caused by the chirality of solvents and dissolved ions, which have not yet been determined by other techniques.

When the transfer of D- and L-monoanionic forms of the amino acid tryptophan was followed across the water|D-menthol and water|L-menthol interface, asymmetrical solvation behavior was observed [B 221]. The reasons for this asymmetry may be adsorption or precipitation at the liquid|liquid interface, or even different kinetics.

### 6.2.2 The Determination of Standard Gibbs Energies of Transfer of Cations

Following the principles outlined for anion transfer with three-phase electrodes, the *reduction* of an electro-reducible compound dissolved in an organic liquid is required to transfer cations from water to an organic liquid. Figure 6.30 visualizes the electrode system. The reduction of Fe(III) tetra-

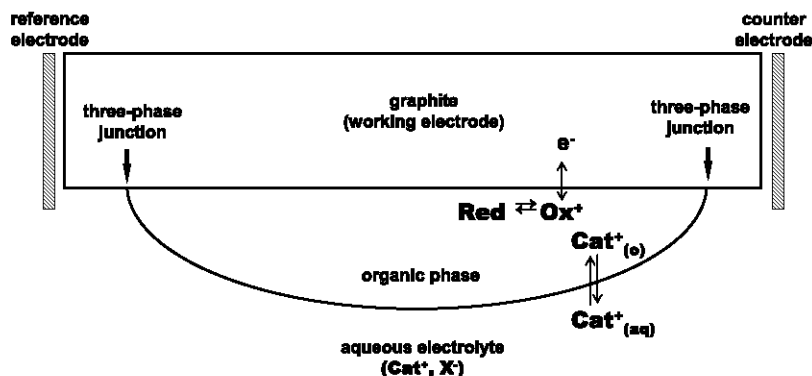


Fig. 6.30. Processes occurring at a three-phase electrode when an electroreducible compound is dissolved in the organic phase and cations are transferred across the interface water | organic liquid [B 271]

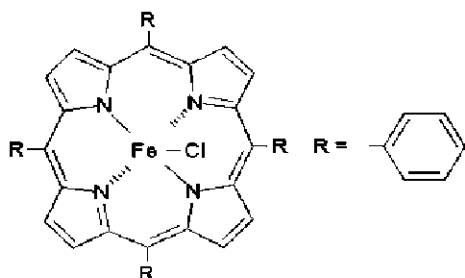
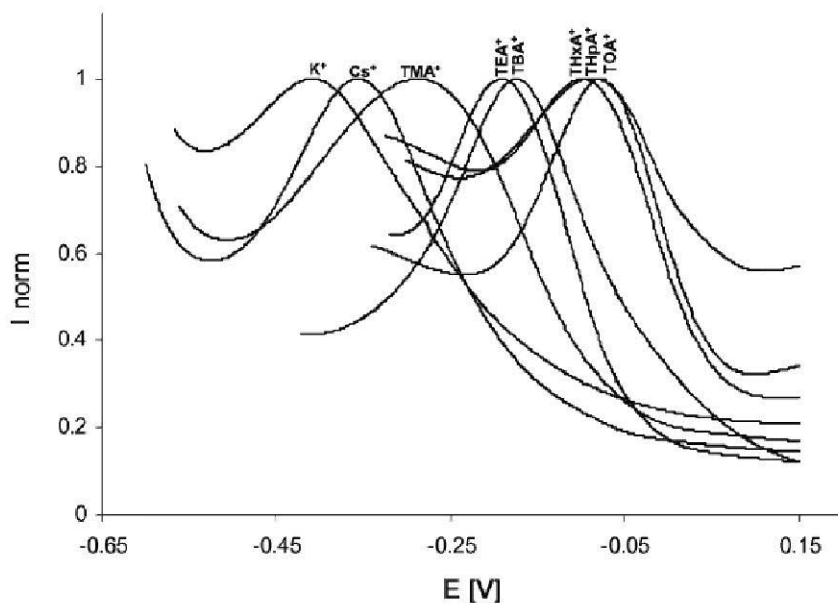


Fig. 6.31. Fe(III) tetraphenyl porphyrin chloride

phenyl porphyrin chloride [Fe(III)TPP-Cl] (Fig. 6.31) in a nitrobenzene microdroplet in a three-phase arrangement gives rise to well-developed square-wave voltammetric signals with a peak potential depending on the nature of the cations present in the aqueous phase [B 271]. The more lipophilic the cations in the aqueous phase are, i.e., the more *positive* the standard potentials of cation transfer from water to the organic liquid are, the easier is the reduction of [Fe(III)TPP-Cl]. As predicted by Eq. 6.15, this shifts the reduction to more positive potentials. Representative voltammograms showing the transfer of cations across the water|NB interface are shown in Fig. 6.32.

The standard Gibbs energies of transfer of several common inorganic cations as well as of some tetraalkyl ammonium cations across the water | NB interface have been determined using this approach. The data are given in Table 6.7.



**Fig. 6.32.** Normalized square-wave voltammograms of the redox reaction of Fe(III)TPP-Cl in NB droplets accompanied by the transfer of cations from aqueous solution to NB [B 271]

**Table 6.7.** Standard Gibbs energies of transfer of cations across the water | NB interface determined from the formal potentials of the voltammograms of Fe(III)TPP-Cl at three-phase electrode [B 271]

Cations	$\Delta G_{\text{aq, Cat}^+}^{\text{NB}^0} / k$ $\text{J mol}^{-1}$
$\text{K}^+$	22.65
$\text{Rb}^+$	19.80
$\text{Tl}^+$	19.30
$\text{Cs}^+$	17.80
$\text{TMA}^+$	9.60
$\text{TEA}^+$	-0.50
$\text{TBA}^+$	-8.20
$\text{THxA}^+$	-8.21
$\text{THpA}^+$	-8.78
$\text{TOA}^+$	-10.10



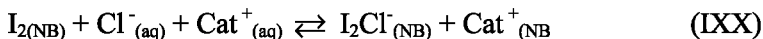
### **Standard Gibbs Energies of Transfer of Cations Determined by Utilizing the Reduction of Iodine**

The reduction of iodine dissolved in the organic droplet of a three-phase electrode is a reversible process, characterized by well-defined square-wave voltammograms. With aqueous solutions that do not contain any halide anions but different cations, the electrode reaction of iodine is accompanied by the expulsion of created iodide anions from the NB to the aqueous phase [B 215]:



An interesting effect is observed when the electrode with the attached NB droplet containing dissolved iodine is immersed in aqueous solutions of *chlorides* of different cations [B 234]. Additionally to the previous peak (Reaction XVII and XVIII; peak I in Fig. 6.33) a new reversible process is observed at more positive potentials (peak II in Fig. 6.33). The last peak shifts about 60 mV in negative direction per decade increase of chloride concentration in the aqueous phase [B 215, B 234], and it is attributed to the reduction of iodine in the NB droplet followed by expulsion of chloride ions from NB into the aqueous phase.

The electrochemical behavior of the system can be explained by assuming a preceding chemical reaction, i.e., the partition of the chloride salt between the aqueous and the NB phases, mainly driven by the formation of  $I_2Cl^-$  ions in NB [B 234]. The ratio of peak currents of peak II and I, i.e.,  $I_p(\text{II})/I_p(\text{I})$ , increases linearly with increasing chloride concentration in the water phase. This is mainly due to the absolute increase of  $I_p(\text{II})$ . In chloride solutions with different cations, the peak current ratio depends linearly on the standard Gibbs energies of transfer of the cations across the water | NB interface (Fig. 6.34). The overall reaction associated with peak II is of CE type (electrochemical reaction coupled to a preceding chemical reaction) [B 234] and can be formulated as follows:



The equation corresponding to the calibration line given in Fig. 6.34 can be used to determine the standard Gibbs energies of transfer of cations

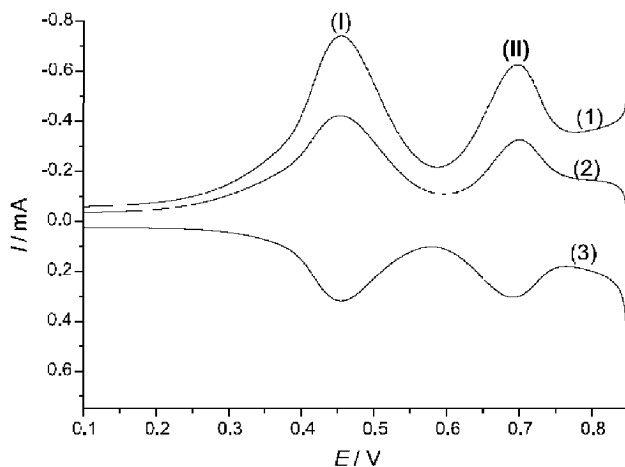


**Fig. 6.33.** The net (1), forward (2), and backward (3) components of the square-wave voltammetric response of a NB droplet containing  $0.1 \text{ mol L}^{-1}$  iodine attached to the paraffin-impregnated graphite electrode and immersed in  $0.25 \text{ M}$  aqueous solution of NaCl: frequency  $f = 50 \text{ Hz}$ , SW amplitude  $E_{sw} = 50 \text{ mV}$ , scan increment  $dE = 0.15 \text{ mV}$ , and starting potential  $E_s = +0.90 \text{ V}$  [B 234]

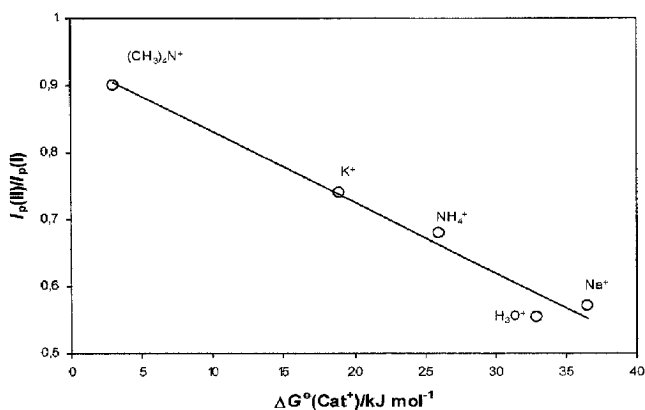


**Fig. 6.34.** Correlation of the peak currents ratio with the standard Gibbs energies of transfer of cations across the water|NB interface. The other conditions are the same as in Fig. 6.33 [B 234]

present in aqueous chloride solutions. This approach has been used to determine these data of several amino acid cations for the transfer across the water | NB interface [B 234, B 262]. The application of the iodine method

is limited by the high reactivity of iodine towards organic compounds, as well as by the complexity of the entire mechanism.

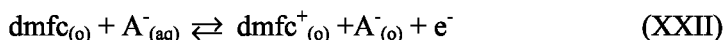
### 6.3 Theoretical Models for the Voltammetry of Immobilized Droplets

The modeling of the processes occurring at the droplet-modified electrodes is not a simple task since several effects have to be taken into account. The mass transfer is for sure achieved by diffusion and migration. Convection may play a role, perhaps as Marangoni convection. Due to the absence of supporting electrolyte in the organic phase at the start of the experiments, the Ohmic drop can play a role. These effects have been studied theoretically by different groups and some progress has been achieved.

#### 6.3.1 Droplets of Organic Solvents with Dissolved Electroactive Compound

##### *Semi-Infinite Planar Diffusion Model*

Considering the reaction



and following the analogy with the theoretical model for electron transfer across the liquid | liquid interface developed by Stewart et al.<sup>11</sup>, a theoretical model has been developed taking into account the diffusion of all species [B 174, B 188]. The model considers a mass transfer through semi-infinite planar diffusion, and was solved under the following initial and boundary conditions:

$$\begin{aligned} t = 0, x \geq 0; c_{\text{dmfc}_{(o)}} &= c^*_{\text{dmfc}_{(o)}}; \\ c_{\text{A}_{(aq)}^-} &= c^*_{\text{A}_{(aq)}^-} \\ c_{\text{A}_{(o)}^-} &= c_{\text{dmfc}_{(o)}^+} = 0 \end{aligned} \quad (6.16)$$

<sup>11</sup> Stewart AA, Campbell JA, Girault HH, Eddowes M (1990) Ber Bunsen Ges Phys Chem 94:83-87

$$\begin{aligned}
 t > 0, x \rightarrow \infty; c_{\text{dmfc}(o)} &\rightarrow c^*_{\text{dmfc}(o)}; \\
 c_{A^-(\text{aq})} &\rightarrow c^*_{A^-(\text{aq})} \\
 c_{A^-(o)} = c_{\text{dmfc}^+(o)} &\rightarrow 0
 \end{aligned} \tag{6.17}$$

$t > 0;$

$$\begin{aligned}
 \frac{\partial c_{\text{dmfc}(o)}}{\partial t} = D_{\text{dmfc}(o)} \frac{\partial^2 c_{\text{dmfc}(o)}}{\partial x^2}; \quad \frac{\partial c_{\text{dmfc}^+(o)}}{\partial t} = D_{\text{dmfc}^+(o)} \frac{\partial^2 c_{\text{dmfc}^+(o)}}{\partial x^2}; \\
 \frac{\partial c_{A^-(\text{aq})}}{\partial t} = D_{A^-(\text{aq})} \frac{\partial^2 c_{A^-(\text{aq})}}{\partial x^2}; \quad \frac{\partial c_{A^-(o)}}{\partial t} = D_{A^-(o)} \frac{\partial^2 c_{A^-(o)}}{\partial x^2};
 \end{aligned} \tag{6.18}$$

For  $x = 0$ , the fluxes are given by:

$$\begin{aligned}
 \frac{\partial c_{\text{dmfc}(o)}}{\partial x} = - \frac{\partial c_{\text{dmfc}^+(o)}}{\partial x} = \frac{I}{nFSD}; \\
 \frac{\partial c_{A^-(\text{aq})}}{\partial x} = \frac{I}{nFSD A^-(\text{aq})}; \\
 \frac{\partial c_{A^-(o)}}{\partial x} = \frac{I}{nFSD};
 \end{aligned} \tag{6.19}$$

(it is assumed that the diffusion coefficients of  $A^-$  and  $\text{dmfc}^+$  in the organic phase are the same, i.e.,  $D$ ). In this model the distance  $x$  represents a distance to the three-phase junction, i.e., the position where the reaction can start.

The integral solutions for all species involved in Reaction XXII, which were obtained by means of Laplace transformation, read:

$$\begin{aligned}
 c_{\text{dmfc}(o)}(x=0) &= c^*_{\text{dmfc}(o)} - \frac{1}{\sqrt{\pi}} \int_0^t \frac{I(\tau)}{nFS\sqrt{D}} (t-\tau)^{-0.5} d\tau \\
 c_{\text{dmfc}^+(o)}(x=0) &= \frac{1}{\sqrt{\pi}} \int_0^t \frac{I(\tau)}{nFS\sqrt{D}} (t-\tau)^{-0.5} d\tau \\
 c_{A^-(aq)}(x=0) &= c^*_{A^-(aq)} - \frac{1}{\sqrt{\pi}} \int_0^t \frac{I(\tau)}{nFS\sqrt{D}} \frac{D}{A^-(aq)} (t-\tau)^{-0.5} d\tau \quad (6.20) \\
 c_{A^-(o)}(x=0) &= \frac{1}{\sqrt{\pi}} \int_0^t \frac{I(\tau)}{nFS\sqrt{D}} (t-\tau)^{-0.5} d\tau
 \end{aligned}$$

The solutions given in Eq. 6.20 were substituted in the below Nernst equation:

$$\begin{aligned}
 \frac{c_{A^-(o)}(x=0) c_{\text{dmfc}^+(o)}(x=0)}{c_{A^-(aq)}(x=0) c_{\text{dmfc}(o)}(x=0)} &= \exp(\phi), \text{ where} \\
 \phi &= \left( E - E^\ominus_{\text{dmfc}^+(o)/\text{dmfc}(o)} - \Delta\phi_{\text{aq}, A^-}^0 \right) \left( \frac{F}{RT} \right) \quad (6.21)
 \end{aligned}$$

Equation 6.21 was solved under conditions of cyclic [B 188] and square-wave voltammetry [B 174]. The concentration gradients of all species involved in the redox process are given in Fig. 6.35.

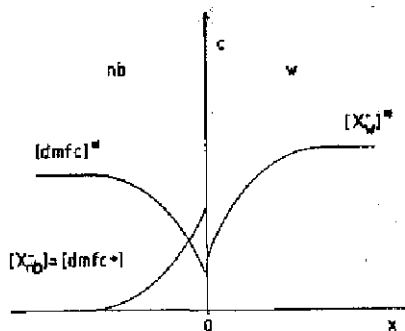
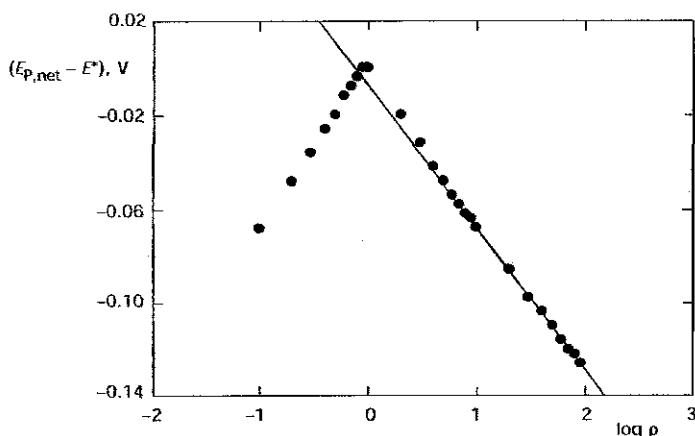


Fig. 6.35. A scheme of concentrations of active species in the organic (here NB) and water (w) phases in the vicinity of the three-phase junction [B 174]



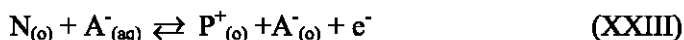
**Fig. 6.36.** Relationship between the theoretical square-wave voltammetric peak potentials and the logarithm of the dimensionless parameter  $\rho$  [B 174]

The formal potentials (i.e., the mid-peak potentials of the cyclic voltammograms, or the peak potentials of the net square-wave voltammograms) of the simulated voltammograms depend on one dimensionless parameter  $\rho$ , defined as a ratio between the initial concentrations of anions in the aqueous phase and dmfc in the organic phase, i.e.,  $\rho = c^*_{A^-_{(aq)}} / c^*_{dmfc(o)}$ . If  $c^*_{A^-_{(aq)}} \sqrt{D_{A^-_{(aq)}}} \geq c^*_{dmfc(o)} \sqrt{D}$ , then the dependence of the formal potential on the logarithm of the dimensionless parameter  $\rho$  is linear, with a slope of  $dE_c^{0'}/d\log(\rho) = -60\text{mV}$  (at 25 °C), which is identical with the slope in Equation 6.14, i.e., in an equation derived on a purely thermodynamic basis. This behavior has also been experimentally observed [B 132, 174, 206, 240, 259, 262, 266].

However, when  $c^*_{A^-_{(aq)}} \sqrt{D_{A^-_{(aq)}}} < c^*_{dmfc(o)} \sqrt{D}$ , then the slope of the dependence  $dE_c^{0'}/d\log(\rho)$  is +60 mV (see Fig. 6.36). This behavior has not been observed in the experiments, which suggests that the experiments are more complicate and affected by additional effects.

### **A Convulsive Model for Cyclic Voltammetry in a Thin Organic Layer**

Considering the reaction



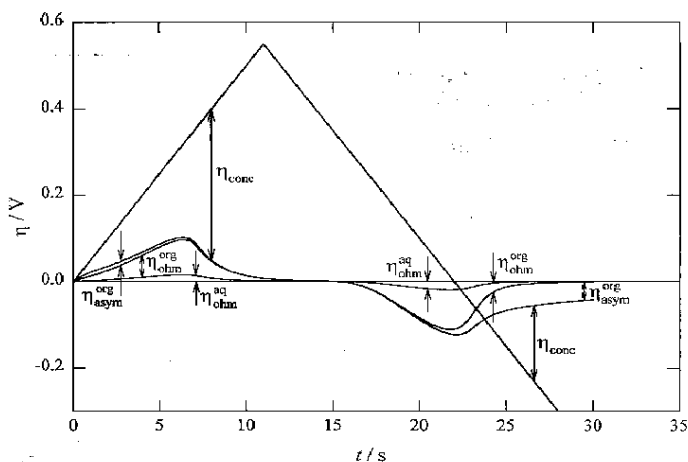


**Fig. 6.37.** Schematic drawing of the time dependence of all overpotentials affecting the voltammetric response in the Oldham model [B 237]

occurring in an insulating organic layer with surface area  $A$  and thickness  $Z$ , that is sandwiched between the working electrode and an aqueous electrolyte solution, Oldham et al. [B 237] have developed a rather robust model, comprising several effects which affect the voltammetric features of Reaction XXIII. By assuming that the ion and electron transfer in Reaction XXIII occur without kinetic constraints, i.e., there is no activation polarization, the flow of current in such a set-up may induce at least three different kinds of polarization: the concentration polarization, the ohmic polarization (in both organic and aqueous phase) and an asymmetry polarization due to the different diffusivities in the organic and aqueous phases. Each polarization can generate an overvoltage which will be reflected throughout the features of the obtained theoretical responses. A schematic drawing of all the overpotentials considered in the model [B 237] is given in Fig. 6.37.

It is a complicate task to predict the behavior of such complex systems under potentiodynamic conditions. The transport of four species, i.e.,  $N_{(o)}$ ,  $A_{(aq)}^-$ ,  $P_{(o)}^+$  and  $A_{(o)}^-$ , must be modeled, three of them migrating, and all of them diffusing. Another major problem is the existence of a significant time-dependent resistance in the organic layer, and the likely existence of a diffusion potential difference (asymmetry overvoltage) across the organic layer. By developing a rather complicated algorithm the authors succeeded to elucidate all these effects theoretically.

On the contrary to common cyclic voltammetry experiments, where the choice of the rest (starting) potential that is imposed on the working elec-

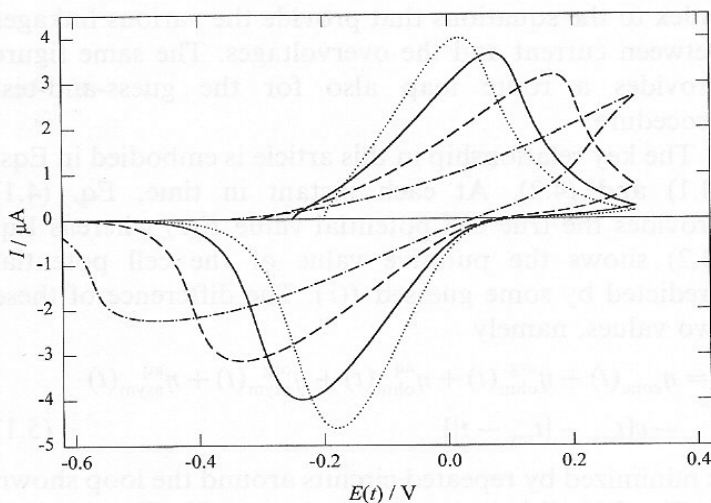


**Fig. 6.38.** Cyclic voltammograms simulated for the thin-film voltammetry obtained by varying the starting potentials of  $E_{in} = -200$  mV (dotted line),  $-250$  mV (solid line),  $-300$  mV (dashed line), and  $-350$  mV (chained line). The other simulation conditions are:  $E^{\ominus} = 0$  V,  $E_{reverse} = 300$  mV,  $v = 50$  mV s $^{-1}$ ,  $A = 10^{-5}$  m $^2$ ,  $Z = 20$   $\mu$ m,  $c(\text{salt})_{(aq)} = 0.01$  mol L $^{-1}$ ,  $c(\text{N})_{(o)} = 0.001$  mol L $^{-1}$ ,  $D(\text{N}) = D(\text{P}^+) = 10^{-10}$  m $^2$  s $^{-1}$ ,  $D(\text{A}^-)_{(o)} = 8 \times 10^{-10}$  m $^2$  s $^{-1}$ ,  $D(\text{A}^-)_{(aq)} = 10^{-9}$  m $^2$  s $^{-1}$  [B 237]

trode is innocuous, in this theoretical model the choice of the rest potential is the most important parameter. It determines the initial ionic content in the organic layer and hence strongly affects the ohmic polarization. For example, the concentration of  $\text{P}^+\text{A}^-$  in the organic phase created by choosing a rest potential of  $-250$  mV more negative than  $E_{\text{N/P}^+}^{\ominus}$ , will be about 5 mM (if  $c(\text{N})_{(o)} = 0.05$  M and  $c(\text{salt})_{(aq)} = 0.5$  M), which is far from being negligible. Indeed, the question whether the center of the thin film will be active or not depends on the time of electrolysis as well as of the film thickness. Several theoretical voltammograms simulated for different values of the starting potential are depicted in Fig. 6.38. Obviously, the obtained theoretical voltammograms differ from the conventional ones. The separation of the peak potentials is much greater than the 59 mV typical for reversible systems in cyclic voltammetry under semi-infinite planar diffusion. This is attributed mainly to the ohmic resistance in the organic layer. Figure 6.38 shows that the more positive the starting potential is, the lower will be the resistance in the organic phase due to the higher ionic content there, and consequently the simulated voltammograms are getting closer to the conventional forms. The curve in Fig. 6.38 corresponding to



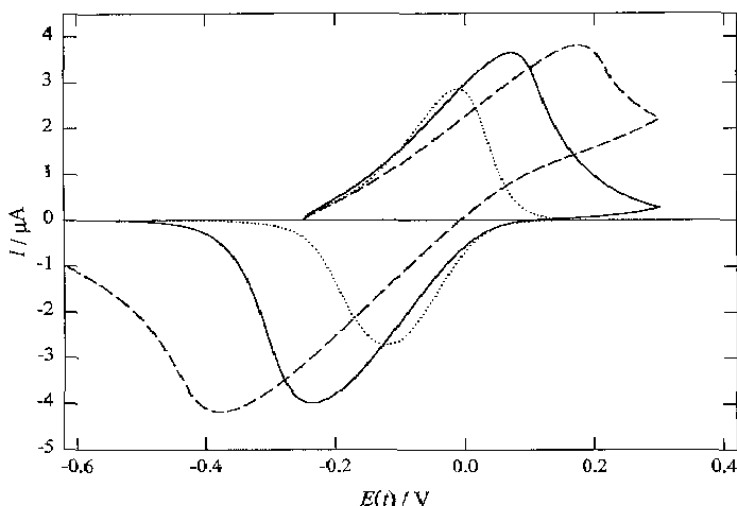


**Fig. 6.39.** Theoretical cyclic voltammograms obtained in thin-film voltammetry by varying the thickness of the organic film:  $Z = 10 \mu\text{m}$  (dotted line),  $20 \mu\text{m}$  (solid line), and  $40 \mu\text{m}$  (dashed line). The rest potential was  $E_{\text{in}} = -250 \text{ mV}$ . All other conditions were the same as in Fig. 6.38 [B 237]

an electrolysis potential of  $350 \text{ mV}$  more negative than  $E^\circ$  shows such high resistance that the voltammogram is dominated by ohmic polarization.

Voltammograms simulated for conditions that differ only in the width of the organic layer are shown in Fig. 6.39. As expected, the distortion due to the resistance becomes more pronounced as the layer becomes thicker. The features of the simulated voltammograms are additionally affected by the scan rate, concentration of the electroactive compound  $N$  in the organic phase, as well as by the concentration of the salt in the aqueous solutions. A detailed overview of all contributing overvoltages is given in reference [B 237]. The interplay of the various factors makes the result of this type of experiment complicate. In such an experimental set up, without an existing three-phase junction line, caution is needed in drawing conclusions from CV data.

### **Modeling Cyclic Voltammograms at a Conic Drop Three-Phase Electrode**

A model that more closely approaches the processes occurring at a three-phase electrode has been developed using the geometry of a conic “drop” (cf. Fig. 6.40) [B 257]. Considering Reaction XVI, i.e.,

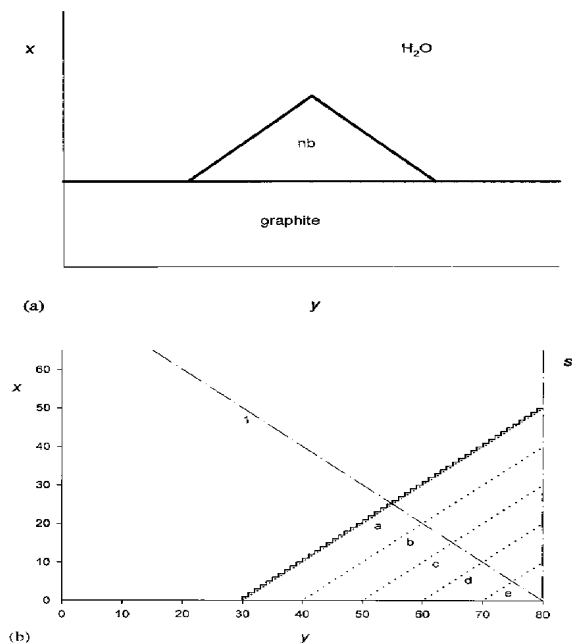
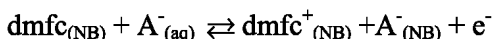


**Fig. 6.40.** Scheme of a conic drop of an organic solvent (NB) attached to a graphite electrode surface and immersed in an aqueous electrolyte **a**, and a radial section of the conic drop electrode in the Cartesian plane **b**. The axis of radial symmetry passing through the top of the cone is denoted by *s* [B 257]



occurring at a three-phase electrode (where dmfc is dissolved in nitrobenzene that is devoid of any electrolyte), the major obstacle is the origin of the initial conductivity in the organic phase, which is needed for initiating the reaction. Contrary to the model of Oldham et al. [B 237], where the authors have assumed that the initial conductivity of the organic film is established as a result of the electrode Reaction XVI proceeding at potentials below the formal potential, the authors of [B 257] have recognized in their model the *natural partition of the salt* between the aqueous solution and the organic drop as the reason for supplying the initial conductivity in the organic phase.

Before the onset of the CV experiments, when the NB modified electrode is immersed in the aqueous solution, the partition of the salt can occur under open circuit conditions. Certainly, the delay time before applying the potential will be a major factor determining how far the partitioned ions can penetrate the NB phase. Assuming that concentrations of the salts in the aqueous solution are 1 M, from the partition constant across the

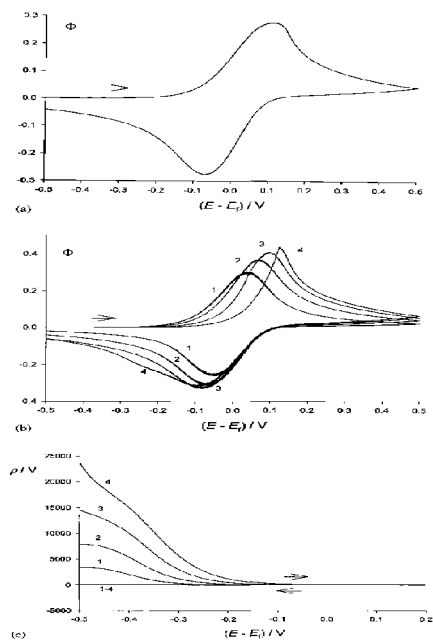


**Fig. 6.41.** **a** Cyclic voltammogram of reaction XVI in a conic drop of nitrobenzene, **b** the components of the average current and, **c** the equivalents of the resistance that correspond to the parts of the conic drop with a thickness of 10 (1), 20 (2), 30 (3) and 40 (4) space increments in the direction of  $x$  axis. The duration of the initial contact was 1000 time increments, and the partition constant of the salt  $MX$  was  $K_{MX}^{w \rightarrow NB} = 2 \times 10^{-4}$  [B 257]

water|NB interface one can estimate that in some cases the concentration of partitioned salts in NB phase can exceed some  $\text{mmol L}^{-1}$ . This gives the model creditability.

The second parameter that affects the voltammetric features of Reaction XVI in this model is certainly the resistance in the organic phase. In this model, the ohmic overvoltage has been calculated as a product of the dimensionless current and the equivalent of the resistance  $\rho$ , defined as:

$$\rho = RT / 2dF \sum_{i=1}^n (1/c_{A_{\text{org}}}), \text{ where } d = D \frac{\Delta t}{\Delta x^2}, n = \frac{L}{\Delta x}.$$

$\Delta t$  and  $\Delta x$  are the time and space increments, respectively,  $L$  is the thickness of the film, and  $D$  is the diffusion coefficient (assumed to be equal for all species in the organic film).

The effect of the thickness of the conic film on the shape of the simulated CV curves and on the equivalents of the resistance is shown in Figs. 6.41a-c. The components of Fig. 6.41b correspond to an increase of the thickness of the conic film from 10 to 40 space increments in the direction parallel to the axis of symmetry  $s$ . Obviously, for higher space increments (which correspond to higher values of the equivalent resistance) the ohmic effect is dominating the shape of the simulated voltammograms (see curve 4 in Fig. 6.41b). Moreover, this also influences the mid-peak potentials of the square-wave voltammograms. The equivalence of the resistance  $\rho$  corresponding to the same parts of the organic film as the currents in

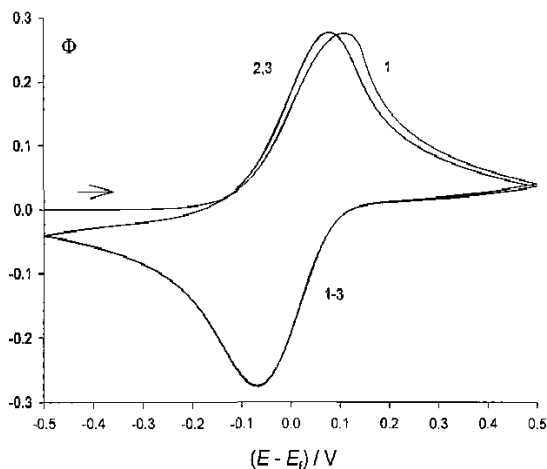


**Fig. 6.42.** Three consecutive cyclic voltammograms of the redox reaction XVI considering a conic drop of nitrobenzene simulated with 10 space increments. All other conditions are the same as in Fig. 6.41 [B 257]

Fig. 6.41b as a function of the applied potential are given in Fig. 6.41c. The dependence of  $\rho$  on the electrode potential shows that the ingress of anions from water starts at the edge of the cone. During the anodic polarization (forward scan) the equivalence of the resistance  $\rho$  decreases with increasing applied potential. In the reverse scan of the cyclic voltammograms, the equivalence of the resistance does not reach the initial value (see Fig. 6.41c). This is probably caused by the lateral diffusion of the created decamethylferrocenium cations from the center of the cone toward its edge. After the first cycle of the potential, the conductivity of the cone is significantly enhanced. Consequently, the second and further cyclic voltammograms should be less affected by the ohmic drop than the first scan. Three successive cyclic voltammograms of the conic drop simulated under conditions of Fig. 6.41 are depicted in Fig. 6.42. The second and third cycles in Fig. 6.42 are identical, which confirms the former statement. The anodic peak potential of the first scan is more positive than that of the 2<sup>nd</sup> and 3<sup>rd</sup> scans due to the influence of the ohmic drop in the first cycle. This is a very important observation since it shows that the ohmic overvoltage does not have an influence on the mid-peak potential of the second and all other subsequent cycles in multiple cyclic voltammograms of reaction XVI. This influence was significantly pronounced in the model of Oldham et al. [B 237].

### **Uncompensated Resistance and Charge Transfer Kinetics**

The theoretical model of a conic drop three-phase electrode as described above implies that the electrode process is not confined to the three-phase junction line, where it starts, but that it advances into the droplet. Depending on the contact time of the two adjacent liquid phases under open circuit condition, as well as depending on the scan rate, the thickness of the reaction zone in the organic droplet will vary. An immobilized droplet can be regarded as a film with a thickness varying from zero to rather large values. The fact that the droplet has zero thickness at the three-phase junction line enables the electron transfer reaction to be started even with lowest conductivities of the organic phase, which is a big advantage over the conventional thin-film techniques<sup>12, 13</sup>. The droplet can be treated theoretically as a thin-film electrode with a low conductivity of the film. When a fast technique like square-wave voltammetry (SWV) is used, the reaction will be restricted to a "thin-film" adjacent to the three-phase junction line. With this in mind the effect of the uncompensated resistance on the voltammetric properties of a simple electrode reaction occurring in a limited diffusion space under conditions of SWV has been studied theoretically as well as experimentally [B 281].

Considering the reaction



proceeding in a limited diffusion space ( $0 \leq x \leq L$ ), the voltammetric properties of a reversible redox reaction in the absence of ohmic polarization are a function of one dimensionless thickness parameter  $A$ , defined as  $A = L\sqrt{(f/D)}$ , where  $L$  is the thickness of the film,  $f$  is the SW frequency, and  $D$  is the common diffusion coefficient. The dimensionless peak current is a sigmoid function of  $A$ , while the peak potential does not depend on  $A$ .

In the presence of a resistance in the thin-film, the ohmic overvoltage of the system, owing to the low conductivity of the film, is represented by a complex dimensionless resistance parameter  $\rho$ , defined as  $\rho = R_{\Omega}(n^2 F^2 / RT) S c_{\text{Ox}}^* \sqrt{Df}$ , where  $R_{\Omega}$  the resistance in the film,  $S$  is the electrode surface area, and the meaning of other symbols is as usual. The influence of the resistance parameter  $\rho$  upon the voltammetric features of the reaction depends on the thickness of the film. The thicker the film, the smaller is the effect of the resistance parameter.

<sup>12</sup> Shi C, Anson FC (1999) J Phys Chem B 103:6283-6289

<sup>13</sup> Shi C, Anson FC (1998) Anal Chem 70:3114-3118

**Table 6.8.** Minimal values of the resistance parameter  $\rho_{\min}$  that affect the SW voltammetric response of a reversible electrode reaction for different thicknesses of the film. The conditions of the simulations were: diffusion coefficient  $D = 10^{-5} \text{ cm}^2 \text{ s}^{-1}$ , SW frequency  $f = 100 \text{ Hz}$ , SW amplitude  $E_{\text{sw}} = 50 \text{ mV}$ , and scan increment  $dE = 10 \text{ mV}$  [B 281]

$L/\mu\text{m}$	$\rho_{\min}$
1	0.1
2	0.03
5	0.04
10	2
50	3
500	4

The minimal values of the resistance parameter that exhibit an influence on the voltammetric response of Reaction XXIV in the thin-film are given in Table 6.8. For films with lower thicknesses, the increase of the resistance parameter  $\rho$  influences all the components of the SW voltammetric response (see Fig. 6.43).

By increasing the resistance parameter  $\rho$  the symmetry of forward and backward components is lost, and the forward (cathodic) branch of the SW voltammograms shifts toward more positive potentials, whereas the backward (anodic) branch shifts toward more negative potentials. In this range of the values of  $\rho$  the overall net current increases. This is due to the specific chronoamperometric properties of a thin-film electrode reaction. During each potential pulse of the SW voltammetric excitation signal the current diminishes severely with time, as the equilibrium of Reaction XXIV is rapidly established between the species of the reversible couple that diffuse in a limiting space. Consequently, a low current remains for measuring at the end of each potential pulse. However, when a significant resistance is present in the thin-film, the equilibrium cannot be established so rapidly, causing the redox reaction to proceed to a large extent even at the end of the pulse, and thus increasing the current compared with the situation without resistance (compare the net currents of Fig. 6.43c and b with that of a). In other words, the observed feature in the presence of uncompensated resistance is a consequence of the coupled properties of the studied reaction, of the chronoamperometric properties of the used technique (SWV), and of the delay of the mass transfer (caused by increased resistance of the thin-film). The shifting of the cathodic branch toward positive

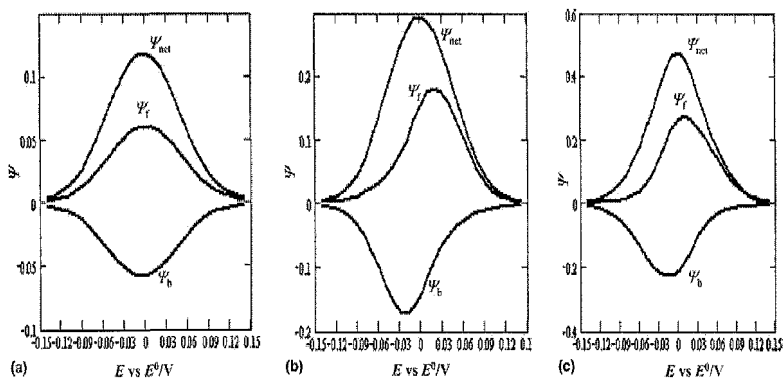


**Fig. 6.43.** The effect of the uncompensated resistance on the dimensionless SW response of a reversible electrode reaction. The resistance parameter was:  $\rho = 0$  **a**, 1 **b**, and 3 **c**. The other conditions of the simulations were:  $\Lambda = 0.362$ ,  $E_{sw} = 50$  mV,  $D = 10^{-5}$  cm<sup>2</sup> s<sup>-1</sup>,  $dE = 10$  mV.  $\Psi_f$ ,  $\Psi_b$ , and  $\Psi_{net}$  are symbols for forward, backward and net components of the SW voltammetric responses, respectively [B 281]

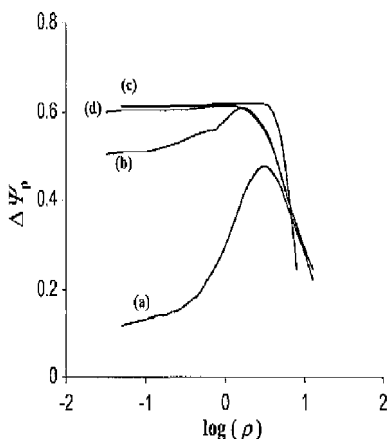


**Fig. 6.44.** Influence of the resistance parameter  $\rho$  on the dimensionless net-peak current  $\Delta\Psi_p$  of a reversible electrode reaction for different thickness parameters. The thickness parameter was:  $\Lambda = 0.632$  **a**, 0.948 **b**, 1.581 **c**, and 15.811 **d**. The other conditions of the simulations were the same as in Fig. 6.43 [B 281]

potentials and of the anodic branch toward negative potentials with increasing  $\rho$  is opposite to the influence of the resistance parameter on the voltammetric features of the same reaction occurring under semi-infinite planar diffusion<sup>14</sup>. The effect of  $\rho$  on the dimensionless net peak currents studied for films with different thicknesses is given in Fig. 6.44. For thicker films, a parabolic dependence exists between the dimensionless net

<sup>14</sup> Mirčeski V, Lovrić M (2001) J Electroanal Chem 497:114-124

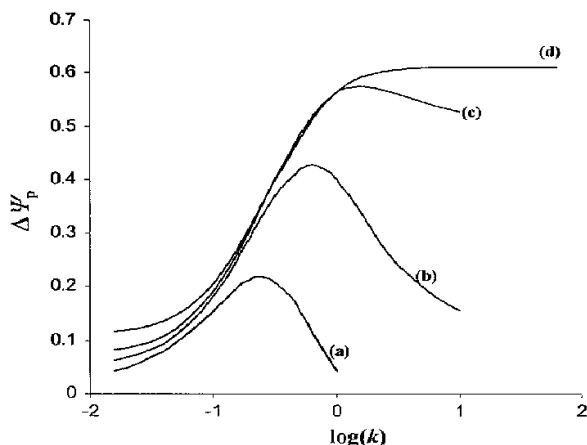


**Fig. 6.45.** Influence of the kinetic parameter  $k$  on the dimensionless net-peak current  $\Delta\Psi_p$  of a quasireversible electrode reaction for different thickness parameters. The thickness parameter was:  $\Lambda = 0.316$  **a**,  $0.632$  **b**,  $0.948$  **c**, and  $1.581$  **d**. The other conditions of the simulations were the same as in Fig. 6.43 [B 281]

peak currents  $\Delta\Psi_p$  and the logarithm of  $\rho$ . In the same direction, increasing  $\rho$  causes a growing of the half-peak width of the net SW voltammograms, however, the peak potentials remain unaltered. This effect of  $\rho$  in a reversible reaction occurring in thin-film voltammetry resembles completely the effect of charge transfer kinetics in a thin-film without resistance (see Fig. 6.45). The kinetic parameter  $k$  in Fig. 6.45 is defined as  $k = k_s / \sqrt{Df}$ , where  $k_s$  ( $\text{cm s}^{-1}$ ) is the standard rate constant of electron transfer. Considering a quasireversible reaction in a thin-film under conditions of SWV the so-called “quasireversible maximum” (see curves a, b, and c in Fig. 6.45) appears in films with a thickness parameter  $\Lambda \leq 0.949$ . Within the same range of  $\Lambda$  values ( $\Lambda \leq 0.949$ ) a parabolic dependence of  $\Delta\Psi_p$  on  $\log\rho$  appears (see Fig. 6.44). Since, in thin-film voltammetric experiments, the frequency of the SW voltammetric signal simultaneously influences both  $\rho$  and  $k$ , criteria must be found to distinguish between the effect of ohmic overvoltage and that of the kinetics of charge transfer. *The shape of the net voltammograms and the half-peak width can serve as simple and safe criteria for this purpose.* The uncompensated resistance effect is associated with an increase of the half-peak width [B 281], and under extreme conditions, by a strong distortion of the SW voltammograms. On the contrary, the effect of charge transfer kinetics does not influence the half-peak width and this parameter remains unaltered. Both effects have



been experimentally observed for two different types of reactions proceeding at three-phase electrodes [B 281].

### **The Effect of Migration**

Studying Reaction XVI, i.e.,  $\text{dmfc}_{(\text{NB})} + \text{A}^-_{(\text{aq})} \rightleftharpoons \text{dmfc}^+_{(\text{NB})} + \text{A}^-_{(\text{NB})} + \text{e}^-$ , in a thin-film arrangement, one fundamental question concerns the type of involved mass transfer. In the models described before the diffusion was considered to be the major mass transport process (except in the model of Oldham et al. [B 237] where migration was also taken into account). However, since in *thin-film experiments* the flux of  $\text{dmfc}^+$  cations at the electrode surface and the flux of the anions at the liquid | liquid interface are separated by the thickness of the film, it must be migration of ionic species through the film that ensures the electroneutrality in the film. Recently, the effect of migration and distribution of all active species in the thin-film have been theoretically analyzed<sup>15</sup>. Two models of thin-film voltammetry have been considered, one for the presence of a supporting electrolyte and one for the absence of supporting electrolyte in the organic film. Here, the second one is described since it is closer to the reality of the experiments considered in this book. In the model the initial ionic conductivity of the film is achieved by free partition of the aqueous electrolyte MX between water and the film. The concentration of the partitioned salt in the film is rather small, since the partition constant is taken to be  $K_{\text{MX}}^{\text{w} \rightarrow \text{NB}} = 4 \times 10^{-4}$ . Figure 6.46a shows the profile of the dimensionless concentration of the electrolyte MX in the thin film after a short contact with the aqueous electrolyte. Figure 6.46b is a theoretical cyclic voltammogram of dmfc obtained in this set-up. Dimensionless concentrations of dmfc,  $\text{dmfc}^+$ ,  $\text{X}^-$ , and  $\text{M}^+$  in the thin film, estimated at four different potentials corresponding to the Fig. 6.46b are shown in Fig. 6.47a-d. Contrary to the situation shown in Fig. 6.46a, where  $c(\text{X}^-) = c(\text{M}^+)$  in the organic film under the conditions of open circuit, when a potential is applied, the oxidation of dmfc to  $\text{dmfc}^+$  at a potential of  $E$  vs  $E_c^{\text{O}'} = -0.30$  V (see Fig. 6.47a) causes a change of distributions of  $\text{M}^+$  and  $\text{X}^-$  ions in order to compensate the charge of  $\text{dmfc}^+$  cations. However, at higher potentials the current is carried almost completely by  $\text{dmfc}^+$  and  $\text{X}^-$  ions due to the low concentrations of  $\text{M}^+$  ions. Thus, the concentrations of  $\text{dmfc}^+$  and  $\text{X}^-$  are almost equal (see Fig. 6.47b). The curves in Fig. 6.47c correspond to the cathodic (backward) branch of the cyclic voltammogram in Fig. 6.46b estimated at a potential of 0.1 V. At this potential the film is rapidly exhausted of dmfc. As the current ap-

<sup>15</sup> Lovrić M, Komorsky-Lovrić Š (2003) *Electrochem Commun* 5:637-643

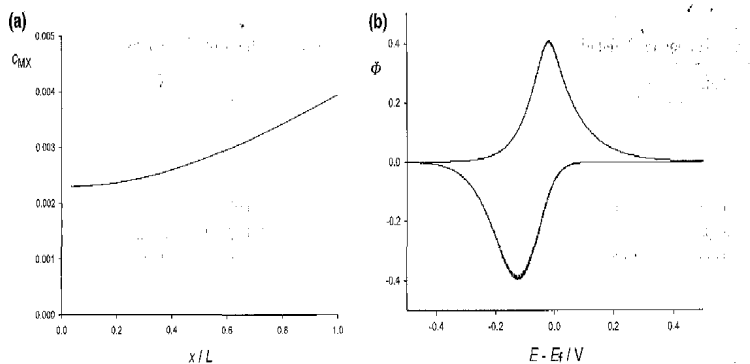


**Fig. 6.46.** **a** The dimensionless concentration of the electrolyte MX in the film at the end of the initial contact with aqueous solution and **b** a simulated cyclic voltammogram of decamethylferrocene in the film electrode.  $[MX]_{(NB)}^*/[dmfc]^* = 10^9$

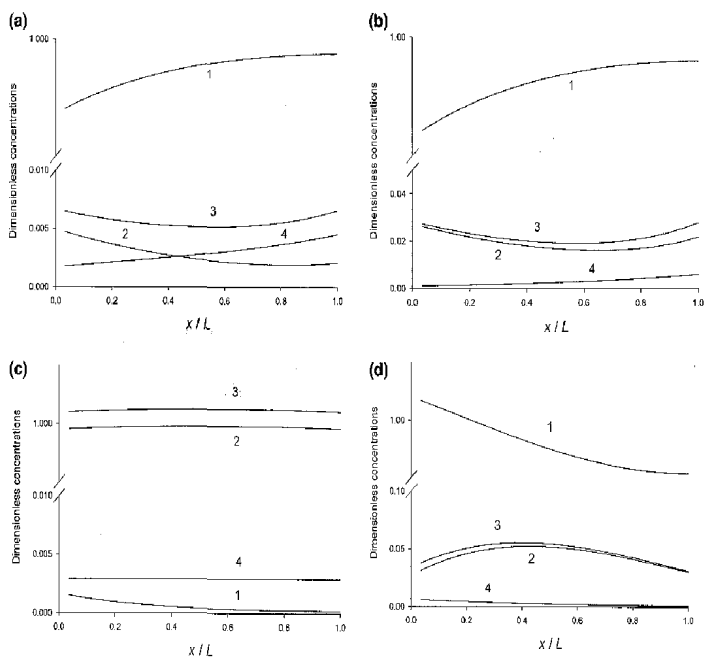


**Fig. 6.47.** Dimensionless concentrations of decamethylferrocene (1),  $dmfc^+$  (2),  $X^-$  anion (3) and  $M^+$  cation (4) in the film at the potentials  $E/V = -0.3$  **a** and  $-0.2$  **b** on the anodic branch, and  $0.1$  **c** and  $-0.3$  **d** on the cathodic branch of cyclic voltammogram shown in Fig. 6.46b<sup>9</sup>

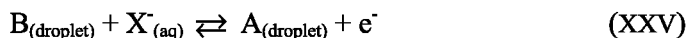
proaches zero in this potential range (see Fig. 6.46b) the gradients of concentrations of ionic species in the thin film are very small. However, the reduction of  $\text{dmfc}^+$  at potential of  $-0.3$  V in the cathodic branch of the cyclic voltammogram causes migration of  $\text{M}^+$  ions toward the electrode surface and the flux of  $\text{X}^-$  anions from the film toward the water, as can be seen in Fig. 6.47d.

The present model shows that in simple thin-film voltammetry the current of the redox Reaction XVI mainly depends on the diffusion and migration of decamethylferrocenium cations and anions of the aqueous electrolyte, although the separation of charges appearing in the very beginning of the oxidation of  $\text{dmfc}$  can be compensated only by the migration of cations of the electrolyte in the film. The single contributions of the migration and diffusion currents of all species can be found in reference<sup>9</sup>.

### 6.3.2 Droplets of Electroactive Liquids

#### *Numerical Modeling of Three Possible Mechanisms*

The mathematical modeling of the processes occurring in microdroplet experiments conducted with electroactive liquids is similar to the theoretical considerations described previously in this chapter. Considering the reaction of the type



Compton et al. [B 149] have developed theoretical models for three different types of three-phase electrode voltammetry with droplets, considering different geometries, and corresponding to different electroactive regions (see Fig. 6.48):

- A) The electrochemical reactions starts from the oil-electrode surface interface;
- B) A rapid charge conduction over the droplet surface is assumed so that ion insertion occurs from the droplet-aqueous electrolyte interface;
- C) The electrochemical reaction occurs only at the three-phase junction electrode-electroactive droplet-aqueous electrolyte.

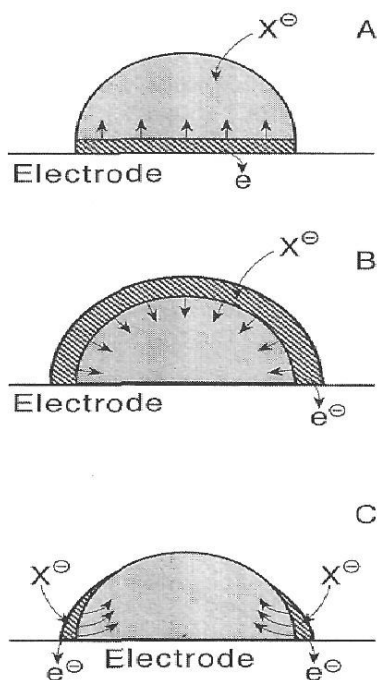


**Fig. 6.48.** Scheme of three mechanistic models for processes occurring at a three-phase electrode with immobilized droplets [B 149]

In all cases the diffusion is taken as the only way of mass transport and the solutions of Fick's equations corresponding to each separate case were solved numerically using the dual reciprocity finite element method. In model A the planar diffusion is considered, while in the models B and C concave and convex diffusions have been taken into account, respectively. The influence of the scan rate on the shape of the linear sweep voltammograms, on the potential separations, as well as on the normalized peak currents for all three geometries has been examined theoretically.

At low scan rates identical linear sweep voltammograms are obtained in all cases. This behavior is due to the complete conversion to the product during the time scale of the potential sweep so that no effect of mass transport or geometry is evident. Unlike in the case of low scan rates, three different types of voltammograms are obtained by faster scan rates (see Fig. 6.49). While the voltammograms corresponding to the models A and B have conventional diffusion forms, the result for model C exhibit an entirely different feature. A steady state voltammogram was obtained similar to that known for microelectrodes.

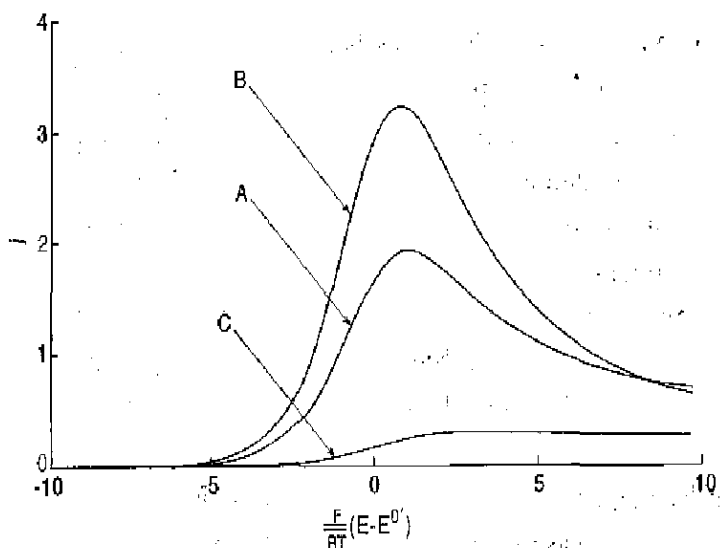


**Fig. 6.49.** Superimposed linear sweep voltammograms for the three models shown in Fig. 6.48 obtained with intermediate scan rates [B 149]

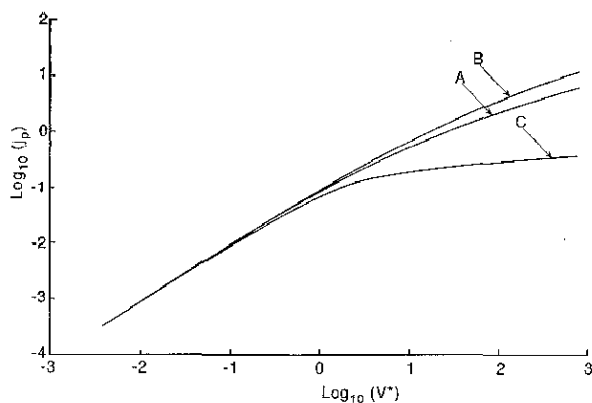


**Fig. 6.50.** Dependence of the dimensionless normalized peak currents on the dimensionless scan rate for the three models shown in Fig. 6.48 [B 149]

The dimensionless peak currents for all considered models depend linearly on the scan rates (with slope of 1) in the regions of low scan rates (see Fig. 6.50). Such behavior is typical for thin-film voltammetry. For the faster scan rates the peak currents for models A and B increase in proportion to

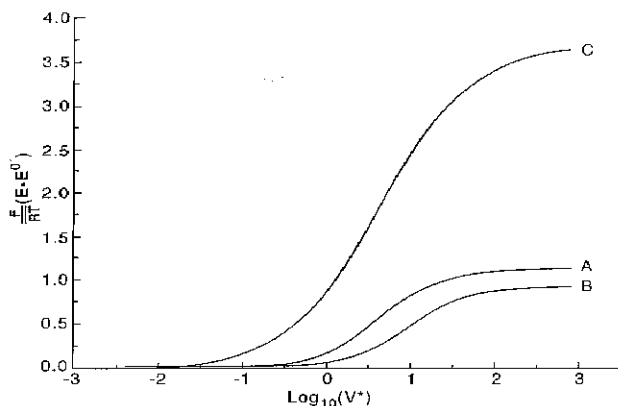


**Fig. 6.51.** Dependence of the separation between the peak potential and the formal potential on dimensionless scan rate [B 149]

the square-root of the scan rate, with a slope of 0.5. However, the normalized peak currents corresponding to the model C are almost independent on the scan rate for faster scan rates, like for microband electrodes.

The potential separation between the peak potentials and the formal potential of Reaction XXV for all three models is characterized by sigmoid dependences (see Fig. 6.51). By increasing the scan rates the magnitude of the peak-to-peak separation of the model A converges to the value of 56 mV as typical for planar diffusion. The hemispherical model B gives a smaller potential separation converging to 49 mV. The most pronounced peak-to-peak separation was observed in model C, where that value converges toward 140 mV (at 298 K).

Conducting the experiments with electroactive liquid *para*-tetrahexylendiamine (THPD) microdroplets deposited on a pyrolytic graphite electrode and immersed in  $\text{SCN}^-$  solution, Compton et al. [B 150] have shown that the obtained experimental results fit best the theoretical results obtained with model C, i.e., for convex diffusion. However, the authors have determined experimentally the values for the diffusion coefficient of  $\text{SCN}^-$  that are three orders of magnitude lower than that estimated theoretically. It means that the mass transport process under fast scan rate conditions is orders of magnitude faster than possible by diffusion! This feature was ascribed to additional convection processes like that of Marangoni type. Probably the neglecting of migration in the modeling is a major reason for the poor fit of experimental results.

### Cyclic Voltammetry Response of Partially Blocked Electrodes

In the last few decades significant attempts have been undertaken to quantify the electrochemistry of partially blocked electrodes, primarily to produce a reliable method for interrogating the characteristics of surface blocking. Compton et al. [B 288] have recently developed a theoretical model in order to characterize the voltammetric responses of a partially blocked electrode (PBE) for which the blocks are distributed at random intervals.

The first mathematical model considers a circular inert disk of radius  $R_b$  situated at the bottom of a cylinder of radius  $R_o$  (see Fig. 6.52) and the following electrode reaction:  $A \rightleftharpoons B + e^-$ .

The authors developed a protocol that allowed calculating the dimensionless peak current,  $\Psi_{\max}$ , from the dimensionless scan rate,  $v_{dl}$ , microscopic coverage  $\theta$ , and dimensionless rate constant,  $k_{dl}^0$ , using the relation  $\Psi_{\max} = f(v_{dl}, \theta, k_{dl}^0)$ . The three variables on which the dimensionless peak current depends are given by:

$$\begin{aligned} v_{dl} &= \frac{nFR_o^2}{DRT} v; \\ \theta &= \left(\frac{R_b}{R_o}\right)^2; \\ k_{dl}^0 &= \frac{k^0 R_o}{D} \end{aligned} \quad (6.22)$$

where  $v$  is the scan rate,  $k^0$  is the heterogeneous rate constant for the redox reaction, while the other symbols have their usual meaning. In the theo-

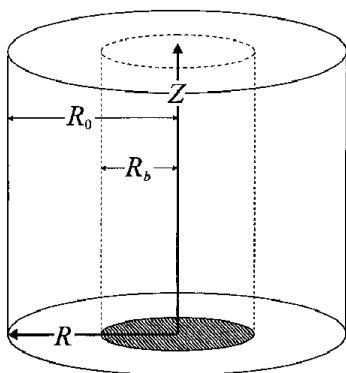


**Fig. 6.52.** The cylindrical polar coordinate system used to model the blocked electrode surface [B 288]

retical model random distribution of inert disks and inert microdroplets has been considered. Here we shall consider the model of randomly distributed inert microdroplets.

For modeling a random distribution of inert microdroplets it has been assumed that each droplet is hemispherical and that it is attached to the electrode surface with a circular base of surface radius  $R_b$ . The diffusion around each droplet is symmetric and the volume of the blocking material,  $V_{\text{block}}$ , is given by:

$$V_{\text{block}} = \frac{2}{3} N_{\text{block}} \pi R_b^3 \quad (6.23)$$

where  $N_{\text{block}}$  is the number of the droplet locks. The global coverage,  $\Theta$ , is given by:

$$\Theta = \frac{N_{\text{block}} \pi R_b^2}{A_{\text{elec}}} \quad (6.33)$$

In the model of a *monodisperse distribution of diffusion domains* (model A) it is assumed that all droplets are regularly dispersed on the electrode surface, i.e., every diffusion domain is identical. Consequently,  $R_0$  is constant for a certain value  $R_b$ , and the dimensionless peak current for one diffusion domain will be equal to that for the whole electrode ( $\Theta = \theta$ ). In this model no overlap of the droplets occurs. In such a case, one needs to calculate a value of  $R_0$  for particular value of  $R_b$ . This can be done by using the relation  $R_0 = R_b / \sqrt{\Theta}$ , where the global coverage  $\Theta$  is given by Eq. 6.33. However, in the case of microdroplets, one has no prior knowledge of  $\Theta$  or  $N_{\text{block}}$ , so there is an equation with two unknowns. Thus, rearranging Eq. 6.32 to obtain an expression for  $N_{\text{block}}$ , one can use Eq. 6.33 to obtain an expression for  $\Theta$ . The resulting equations contain just one unknown ( $V_{\text{block}}$  can be measured experimentally, and it is assumed a certain value of  $R_b$ ):

$$N_{\text{block}} = \frac{3V_{\text{block}}}{2\pi R_b^3} \quad (6.34)$$

$$\Theta = \frac{3V_{\text{block}}}{2R_b A_{\text{elec}}} \quad (6.35)$$

For a certain volume of blocking material, using Eq. 6.35 with the relationship  $R_0 = R_b / \sqrt{\Theta}$  one can calculate values of  $v_{\text{dl}}$ ,  $\theta$  and  $k_{\text{dl}}^0$  for a given  $R_b$ .



Hence,  $\Psi_{\max}$  can be determined for a range of  $R_b$  values assuming that  $V_{\text{block}}$  is known.

In the model of a *polydisperse distribution of diffusion domains* (model B<sub>1</sub>) it is assumed that when the droplets overlap, their geometry at the surface does not change, whereas their shape above the surface is undefined. Thus, one can use the following equation for calculating the  $\Psi_{\max}$  for a range of  $R_b$  values:

$$\Psi_{\max} = \frac{\pi N_{\text{block}}}{A_{\text{elec}}} \int_0^{3R_0} R_0^2 \Psi_{\max}(R_0) P(R_0) dR_0 \quad (6.36)$$

where  $P(R_0)$  is the probability of domains with radii greater than  $3R_0$ .

In the additional model B<sub>2</sub>, the authors [B 288] have approximated overlapping droplets of model B<sub>1</sub> as *larger droplets that do not overlap*. These larger droplets have a surface radius of  $R_b'$ .  $R_b'$  is related to the real coverage  $\Theta_R$ , in exactly the same way as  $R_b$  is related to  $\Theta$ , i.e.,

$$\Theta_R = \frac{3V_{\text{block}}}{2R_b' A_{\text{elec}}} \quad (6.37)$$

The relation between the real coverage,  $\Theta_R$ , and the total coverage  $\Theta$  is given by  $\Theta_R = 1 - e^{-\Theta}$ . For each value of  $R_b$ , one can calculate an average radius that accounts for overlapping,  $R_b'$ , by using Eq. 6.37. Because the value of  $\Theta_R$  is always less than  $\Theta$ ,  $R_b'$  is always larger than  $R_b$ .

Figures 6.53a-f illustrate the dependence of the dimensionless peak current on the droplet size,  $R_b$ , for the models A, B<sub>1</sub> and B<sub>2</sub> over a range of six block volumes at a scan rate of 50 mV/s. The effect of taking an overlapping into account is apparent in the differences between the models A and B. As  $R_b$  increases, there is a decrease in both  $\Theta$  and  $N_{\text{block}}$ . Thus, the spread of probable  $R_0$  values in models B<sub>1</sub> and B<sub>2</sub> increases, and one observes a gentle increase to the limiting value of  $\Psi_{\max}$ . At large values of  $R_b$ , models A and B converge to one limiting peak dimensionless current. These theoretical models have been applied to experimental systems with electrodes modified by THPD in order to deduce the most "realistic case" [B 288].

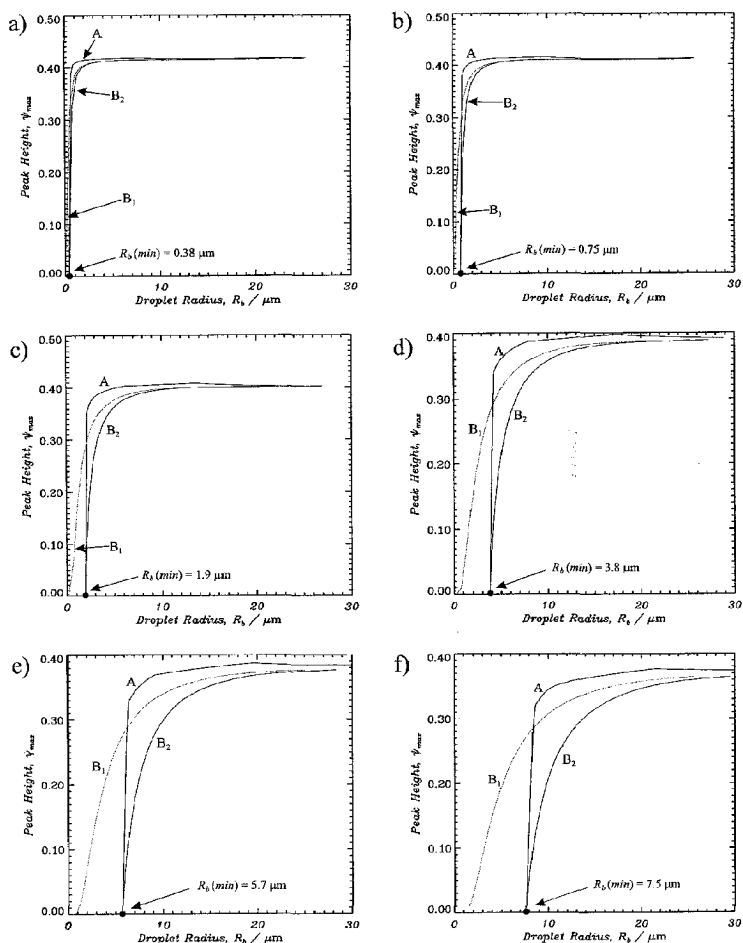


**Fig. 6.53.** Simulation of the dimensionless peak current response over a range of  $R_b$  values to models A, B<sub>1</sub> and B<sub>2</sub> for a microdroplet partially blocked electrode. In all cases  $\nu = 50 \text{ mV/s}$ ,  $D = 6.7 \times 10^{-6} \text{ cm}^2 \text{ s}^{-1}$ ,  $k^0 = 7 \times 10^{-3} \text{ cm s}^{-1}$ ,  $A_{\text{elec}} = 0.19 \text{ cm}^2$ , and  $T = 298 \text{ K}$ . The volume of blocking material on electrode is: **a**  $4.77 \times 10^{-6}$ , **b**  $9.55 \times 10^{-6}$ , **c**  $2.39 \times 10^{-5}$ , **d**  $4.77 \times 10^{-5}$ , **e**  $7.16 \times 10^{-5}$  and **f**  $9.55 \times 10^{-5} \text{ cm}^3$  [B 288]

## Conclusions

The theoretical modeling of the processes occurring at three-phase electrodes is an extraordinarily difficult task since the mathematical models have to take into account various effects. A major issue is the influence of the time-dependent ohmic resistance in the organic phase on the voltam-

metric properties of the studied systems. The origin of the initial conductivity in the organic phase that enables the start of the electrochemical reaction is another important point. Further, the modeling of the mass transfer through the organic phase is difficult because of its geometry.

The influence of the ohmic overvoltage on the voltammetric characteristics has been considered theoretically by several groups. It could be shown that the ohmic overvoltage influences mainly the current and shape of the voltammograms, but not the formal potentials, which is of importance for using these data to determine thermodynamic quantities. The ohmic drop effect in square-wave voltammetry resembles the effect of electron transfer kinetics, and criteria for distinguishing both effects in SWV have been proposed [B 281]. All the features owing to the ohmic overvoltage have been experimentally confirmed [B 281]. It has been also confirmed that the initial conductivity in the organic phase which is necessary for initiating the electrochemical reaction can be provided by the natural partition of the electrolyte from the adjoined aqueous phase. The mass transfer in the organic phase has been shown to be achieved by diffusion and migration. The effect of the migration on the overall current should not be underestimated, as shown in a recent publication<sup>9</sup>.

The question of the *three-phase junction line* is probably the most exciting one. In order to follow the development of the reaction zone inside the organic droplets, experiments have been performed to probe the dmfc or ferrocene (fc) concentration in the immobilized NB droplets with a Pt microdisk electrode [B 207]. The authors have shown that in the three-phase electrode arrangement the oxidation of dmfc and fc starts at the electrode-NB droplet-aqueous electrolyte three-phase junction line, where the anions from the aqueous phase can balance the excess charge of the electrochemically created cations in the organic phase. From that three-phase junction line the ferrocenium and decamethylferrocenium cations diffuse into the bulk of the NB droplet and they can be detected at the Pt microelectrode. The delay in detecting these cations was longer as the distance between the microdisk surface and the three-phase junction line increases [B 207]. The detection time of these cations at a Pt microelectrode depends additionally on the droplet volume, as well as on the electrolyte concentration in the aqueous phase. Placing the microelectrode in the center of the NB droplet at a distance of some 25  $\mu\text{m}$  from the carbon surface, the authors observed delay times for ferrocenium and decamethylferrocenium cations ranging from 10 to 30 seconds, depending on the experimental conditions (see Fig. 6.54). However, one can easily estimate that the time necessary to pass a distance of 25  $\mu\text{m}$  by taking into account the diffusion only is more than 100 s. Similar results regarding the progress of the reaction zone have been

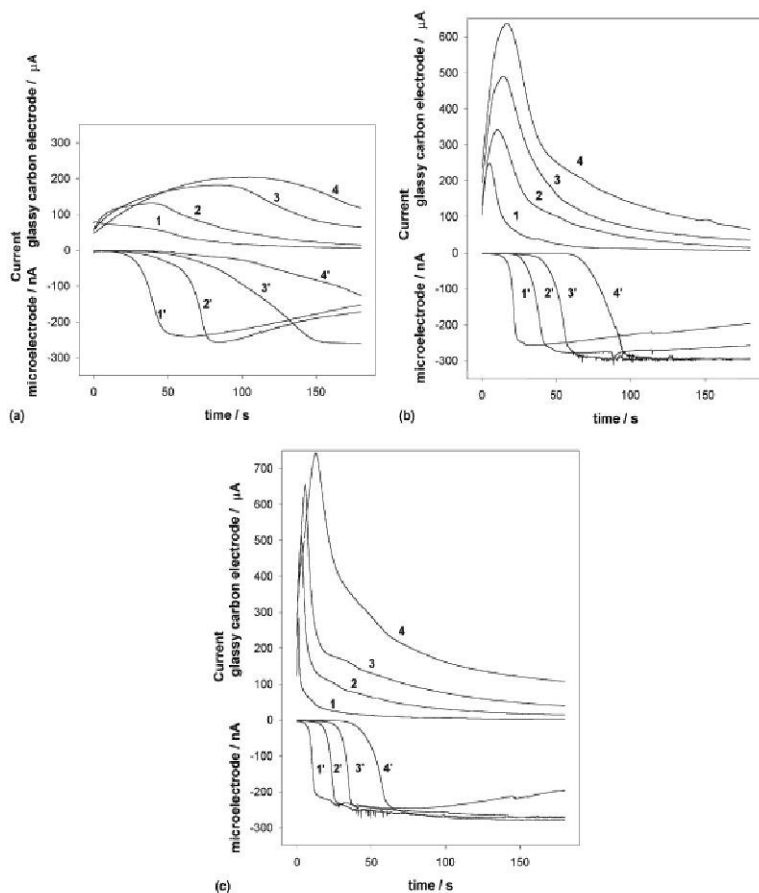


**Fig. 6.54.** Chronoamperometric oxidation of ferrocene at GC electrode-top, and reduction of  $\text{Fc}^+$  at Pt microelectrode in NB drop-bottom. NB droplets contain 0.1 M ferrocene. Volume of NB drops: 1  $\mu\text{L}$  (1, 1'), 2  $\mu\text{L}$  (2, 2'), 4  $\mu\text{L}$  (3, 3') and 8  $\mu\text{L}$  (4, 4'). Water phase contains  $\text{LiClO}_4$  at 0.01 mol  $\text{L}^{-1}$  a, 0.1 mol  $\text{L}^{-1}$  b, and 1 M c [B 207]

obtained also by conducting experiments in a specially designed spectroelectrochemical cell [B 280]. By an in-situ spectroelectrochemical study of the simultaneous transfer of electrons and ions at a three-phase electrode, the authors [B 280] observed a rather fast propagation of the reaction of dmfc oxidation that can not be explained by a simple diffusion only. These results imply that the diffusion is not the only way of mass transport through the NB droplet. Indeed, migration and/or the Marangoni effect [B 150] may play a role in the mass transport, too. These studies clearly showed that the reactions occurring at three-phase droplet-modified

electrodes are not exclusively confined to the three-phase junction line, but they advance toward the center of the droplet.

The questions addressing to the structure of the liquid | liquid interface are also attractive owing to the importance of such interfaces in organic synthesis, chemical separations and ion transfer processes. An issue of particular interest is whether the interfacial region is molecularly sharp or whether the interface is comprised of a diffuse mixed interfacial region. By using the vibrational sum-frequency spectroscopy as a probe of the structure, orientation and bonding of the interfacial water Richmond et al.<sup>16-18</sup> have recently shown that the interfaces between water and nonpolar organic liquids, like alkanes (C<sub>6</sub>-C<sub>8</sub>) or CCl<sub>4</sub>, are very sharp on a molecular level. Beside these interfaces, the interface of water and polar 1,2-dichlorethane was proven to be molecularly disordered with properties similar to a mixed-phase interfacial region<sup>19</sup>.

---

<sup>16</sup> Scatena LF, Richmond GL (2001) *J Phys Chem B* 105:11240-11250

<sup>17</sup> Brown MG, Walker DS, Raymond EA, Richmond GL (2003) *J Phys Chem B* 107:237-244

<sup>18</sup> Scatena LF, Brown MG, Richmond GL (2001) *Science* 292:908-912

<sup>19</sup> Walker DS, Brown MG, McFearin CL, Richmond GL (2004) *J Phys Chem B* 108:2111-2114

## 7 Bibliography

All "B" references are cited below.

1. Scholz F, Nitschke L, Henrion G (1989) A New Procedure for Fast Electrochemical Analysis of Solid Materials. *Naturwiss* 76:71-72
2. Nitschke L, Henrion G, Damaschun F (1989) A New Technique to Study the Electrochemistry of Minerals. Scholz F, *Naturwiss* 76:167-168
3. Scholz F, Nitschke L, Henrion G (1989) Identification of Solid Materials with a New Electrochemical Technique - the Abrasive Stripping Voltammetry. *Fresenius Z Anal Chem* 334:56-58
4. Scholz F, Nitschke L, Henrion G, Damaschun F (1989) Abrasive Stripping Voltammetry - the Electrochemical Spectroscopy for Solid State: Application for Mineral Analysis. *Fresenius Z Anal Chem* 335:189-194
5. Scholz F, Nitschke L, Kemnitz E, Olesch T, Henrion G, Hass D, Bagchi RN, Herrmann R, Pruss N, Wilde W (1989) A Simple and Convenient Solid State Microanalytical Technique for Identification and Characterization of the High Temperature Superconductor  $YBa_2Cu_3O_{7-x}$ . *Fresenius Z Anal Chem* 335:571-572
6. Nitschke L (1989) Neue Methoden in der voltammetrischen Analytik. Ph D thesis, Humboldt-Universität, Berlin
7. Scholz F, Nitschke L, Henrion G (1990) Abrasive Stripping Voltammetric Analysis of Tin-Bismuth. *Electroanal* 2:85-87
8. Scholz F, Müller WD, Nitschke L, Rabi F, Livanova L, Fleischfresser C, Thierfelder Ch (1990) Fast and Nondestructive Identification of Dental Alloys by Abrasive Stripping Voltammetry. *Fresenius J Anal Chem* 338:37-40
9. Scholz F, Lange B (1990) High-Performance Abrasive Stripping Voltammetry. *Fresenius J Anal Chem* 338:293-294
10. Björnbom P, Bursell M (1990) A Method for Studying Microelectrodes by Means of Micromanipulators as Applied to Carbon Agglomerates from Oxygen Reduction Electrode Catalyst. *J Electrochem Soc* 137:363-365

11. Scholz F, Lange B, Jaworski A, Pelzer J (1991) Analysis of Powder Mixtures with the Help of Abrasive Stripping Voltammetry and Coulometry. *Fresenius J Anal Chem* 340:140-144
12. Bond AM, Bobrowski A, Scholz F (1991) Electrochemically Generated Copper(II), Tin(II), Bismuth(III) and Zinc(II) Complexes in Dichloromethane Containing Tetrabutylammonium Perchlorate, Tetrafluoroborate or Hexafluorophosphate as the Electrolyte. *J Chem Soc, Dalton Trans* 411-416
13. Bond AM, Scholz F (1991) Calculation of Thermodynamic Data from Voltammetry of Solid Lead and Mercury Dithiocarbamate Complexes Mechanically Attached to a Graphite Electrode. *J. Phys. Chem.* 95:7460-7465
14. Bond AM, Scholz F (1991) Electrochemical, Thermodynamic and Mechanistic Data Derived from Voltammetric Studies on Insoluble Metallocenes, Mercury Halide and Sulfide Compounds, Mixed Silver Halide Crystals and Other Metal Complexes Following their Mechanical Transfer to a Graphite Electrode. *Langmuir* 7:3197-3204
15. Lovric M, Komorsky-Lovric S, Bond AM (1991) Theory of Square-Wave Stripping Voltammetry and Chronoamperometry of Immobilized Reactants. *J Electroanal Chem* 319:1-18
16. Büchi FN, Bond AM (1991) Interpretation of the Electrochemistry of Cytochrome *c* at Macro and Micro Sized Carbon Electrodes Using a Microscopic Model Based on Partially Blocked Surfaces. *J Electroanal Chem* 314:191-206
17. Bond AM, Scholz F (1992) Field-Based Identification of Minerals Using a Battery-Operated Electrochemical Measuring System and Mechanical Transfer of the Solid to a Graphite Electrode. *J Geochem Exploration* 42:227-235
18. Scholz F, Rabi F, Müller WD (1992) The Anodic Dissolution of Dental Amalgams Studied with Abrasive Stripping Voltammetry. *Electroanal* 4:339-346
19. Scheurell S, Scholz F, Olesch T, Kemnitz E (1992) Electrochemical Evidence for  $\text{Cu}^{3+}$ - $\text{Cu}^{2+}$ - $\text{Cu}^{+}$  Transitions in the Orthorhombic  $\text{YBa}_2\text{Cu}_3\text{O}_{7-x}$  Phase. *Supercond Sc Technol* 5:303-305
20. Scholz F (1992) Abrasive Stripping Voltammetry - A New Method for the Study of the Electrochemistry of Solid Materials, *GIT Fachz Lab* 36:917-918
21. Scholz F, Lange B (1992) Abrasive Stripping Voltammetry - An Electrochemical Solid State Spectroscopy of Wide Applicability. *Trends Anal. Chem.* 11:359- 367
22. Komorsky-Lovric S, Lovric M, Bond AM (1992) Comparison of the Square-Wave Stripping Voltammetry of Lead and Mercury Following their Electrochemical or Abrasive Deposition onto a

- Paraffin Impregnated Graphite Electrode. *Anal Chim Acta* 258:299-305
23. Dueber RE, Bond AM, Dickens PG (1992) Investigation of the Mechanism of Formation of Insertion Compounds of Uranium Oxides by Voltammetric Reduction of the Solid Phase after Mechanical Transfer to a Carbon Electrode. *J Electrochem Soc* 139:2363-2371
  24. Lange B, Scholz F, Bautsch HJ, Damaschun F, Wappler G (1993) Thermodynamics of the Xanthoconite-Proustite and Pyrostilpnite-Pyrargyrite Transitions as Determined by Abrasive Stripping Voltammetry. *Phys Chem Minerals* 19:486-491
  25. Lange B, Scholz F, Weiß A, Schwedt G, Behnert J, Raezke KP (1993) Abrasive Stripping Voltammetry - the Electrochemical Alternative for Pigment Analysis. *Internat Lab* 23:23-26
  26. Jaworski A, Stojek Z, Scholz F (1993) A Comparison of Simulated and Experimental Abrasive Stripping Voltammetric Curves of Ionic Crystals. Reversible Case. *J Electroanal Chem* 354:1-9
  27. Scholz F, Düssel H, Meyer B (1993) A New pH Sensor Based on Quinhydrone. *Fresenius' J Anal Chem* 347:458-459
  28. Bond AM, Colton R, Daniels F, Fernando DR, Marken F, Nagaoa Y, Van Steveninck RFM, Walter JN (1993) Voltammetry, Electron Microscopy, and X-Ray Electron Probe Microanalysis at the Electrode-Aqueous Electrolyte Interface of Solid Microcrystalline *cis*- and *trans*- $\text{Cr}(\text{CO})_2(\text{dpe})_2$  and *trans*- $[\text{Cr}(\text{CO})_2(\text{dpe})_2]^+$  Complexes (dpe =  $\text{Ph}_2\text{PCH}_2\text{CH}_2\text{PDH}_2$ ) Mechanically Attached to Carbon Electrodes. *J Am Chem Soc* 115:9556-9562
  29. Bond AM, Marken F (1994) Mechanistic Aspects of the Electron and Ion Transport Processes Across the Electrode | Solid Solvent (Electrolyte) Interface of Microcrystalline Decamethylferrocene Attached Mechanically to a Graphite Electrode. *J Electroanal Chem* 372:125-135.
  30. Scholz F, Meyer B (1994) Electrochemical Solid State Analysis - State of the Art. *Chem Soc Rev* 23:341-347
  31. Bond AM, Colton R, Marken F, Walter JN (1994) Mechanistic Study of the Voltammetry of Nonconducting Microcrystalline *cis*- and *trans*- $\text{Cr}(\text{CO})_2(\text{dpe})_2$  Complexes (dpe =  $\text{Ph}_2\text{PCH}_2\text{CH}_2\text{PDH}_2$ ) Mechanically Attached to a Graphite Electrode and Immersed in Different Aqueous Electrolyte Media: Identification by Infrared Spectroscopy of *cis*- $[\text{Cr}(\text{CO})_2(\text{dpe})_2]^+$  Stabilized at the Electrode-Solid-Solution Interface. *Organometallics* 13:5122-5131



32. Zhang S, Meyer B, Moh G, Scholz F (1995) Development of Analytical Procedures Based on Abrasive Stripping Coulometry and Voltammetry for Solid State Phase Microanalysis of Natural and Synthetic Tin-, Arsenic-, and Antimonybearing Sulfosalts and Sulfides of Thallium, Tin, Lead, and Silver. *Electroanal Chem* 7:319-328
33. Dostal A, Schröder U, Scholz F (1995) Electrochemistry of Chromium(II) Hexacyanochromate(III) and Electrochemically Induced Isomerization of Solid Iron(II) Hexacyanochromate(III) Mechanically Immobilized on the Surface of a Graphite Electrode. *Inorg Chem* 34:1711-1717
34. Scholz F, Schröder U, Meyer S, Brainina Kh Z, Zakharchuk NF, Sobolev NV, Kozmenko OA (1995) The Electrochemical Response of Radiation Defects of Non-Conducting Materials. An Electrochemical Access to Age Determinations. *J Electroanal Chem* 385:139-142
35. Dostal A, Meyer B, Scholz F, Schröder U, Bond AM, Marken F, Shaw Sh J (1995) Electrochemical Study of Microcrystalline Solid Prussian Blue Particles Mechanically Attached to Graphite and Gold Electrodes: Electrochemically Induced Lattice Reconstruction. *J Phys Chem* 99:2096-2103
36. Meyer B, Ziemer B, Scholz F (1995) *In situ* X-Ray Diffraction Study of the Electrochemical Reduction of Tetragonal Lead Oxide and Orthorhombic Pb(OH)Cl Mechanically Immobilized on a Graphite Electrode. *J Electroanal Chem* 392:79-83
37. Grygar T, Šubrt J, Bohacek J (1995) Electrochemical Dissolution of Goethite by Abrasive Stripping Voltammetry. *Collect Czech Chem Commun* 60:950-959
38. Bond AM (1994) Mechanistic Aspects of Electron Transfer and Mass Transport Processes Associated with the Voltammetry of Microcrystalline Solids Mechanically Attached to Electrode Surfaces. 45th Annual Meeting of the International Society of Electrochemistry, Porto, Portugal, Book of Abstracts, P IV
39. Bond AM, Cooper JB, Marken F, Way DM (1995) Redox and Electroinsertion Processes Associated with the Voltammetry of Microcrystalline Forms of Dawson Molybdate Anion Salts Mechanically Attached to Graphite Electrodes and Immersed in Aqueous Electrolyte Media. *J Electroanal Chem* 396:407-418
40. Grygar T (1995) Kinetics of Electrochemical Reductive Dissolution of Iron(III) Hydroxy-Oxides. *Coll Czech Chem Commun* 60:1261-1273

41. Scholz F, Dostal A (1995) The Formal Potentials of the Solid Metal Hexacyanometalates. *Angew Chem* 107:2876-2878 (*Angew Chem Int Ed Engl* 34 (1995) 2685-2687)
42. Zakharchuk NF, Meyer B, Hennig H, Scholz F, Jaworski A, Stojek Z (1995) A Comparative Study with Prussian Blue Modified Graphite Paste Electrodes and Solid Graphite Electrodes with Mechanically Immobilized Prussian Blue. *J Electroanal Chem* 398:23-35
43. Komorsky-Lovric S (1995) Voltammetry of Microcrystals of Cobalt and Manganese Phthalocyanines. *J Electroanal Chem* 397:211-215
44. Madigan NA, Murphy TJ, Fortune JM, Hagan CRS, Coury LA (1995) Sonochemical Stripping Voltammetry. *Jr Anal Chem* 67:2781-2786
45. Downard AJ, Bond AM, Hanton LR, Heath GA (1995) A Comparison of Solution, Microcrystalline Solid, and Thin Film Phase Voltammetry of  $[\text{Co}(\text{mtas})_2](\text{X})_n$  (mtas = bis(2-(dimethylarsino)phenyl)methylarsine;  $\text{X} = \text{BF}_4^-$ ,  $n = 3$ ;  $\text{X} = \text{ClO}_4^-$ ,  $n = 2, 3$ ;  $\text{X} = \text{BPh}_4^-$ ,  $n = 2$ ). *Inorg Chem* 34:6387-6395
46. Meyer B (1995) Entwicklung von festkörperelektrochemischen Methoden für die Mikroanalyse von Mineralen und synthetischen Festkörpern. Ph D thesis, Humboldt-Universität, Berlin
47. Ura H, Nishina T, Uchida I (1995) Electrochemical Measurements of Single Particles of Pd and  $\text{LaNi}_5$  with a Microelectrode Technique. *J Electroanal Chem* 396:169-173
48. Blum D, Leyffer W, Holze R (1996) Pencil-Leads as New Electrodes for Abrasive Stripping Voltammetry. *Electroanal* 8:296-297
49. Reddy SJ, Dostal A, Scholz F (1996) Solid State Electrochemical Studies of Mixed Nickel-Iron Hexacyanoferrates with the Help of Abrasive Stripping Voltammetry. *J Electroanal Chem* 403:209-212
50. Grygar T (1996) Electrochemical Dissolution of Iron(III) Hydroxy-oxides: More Information About the Particles. *Coll Czech Chem Commun* 61:93-106
51. Dostal A, Kauschka G, Reddy SJ, Scholz F (1996) Lattice Contractions and Expansions which Accompany the Electrochemical Conversion of Prussian Blue and the Reversible and Irreversible Insertion of Rubidium and Thallium Ions. *J Electroanal Chem* 406:155-163
52. Grygar T (1996) The Electrochemical Dissolution of Iron(III) and Chromium(III) Oxides and Ferrites under Conditions of

- Abrasive Stripping Voltammetry. *J Electroanal Chem* 405:117-125
53. Shaw SJ, Marken F, Bond AM (1996) Simultaneous Electrochemical and Quartz Crystal Microbalance Studies of Nonconductin Microcrystalline Particles of *trans*-Cr(CO)<sub>2</sub>(dpe)<sub>2</sub> and *trans*-[Cr(CO)<sub>2</sub>(dpe)<sub>2</sub>]<sup>+</sup> (dpe = Ph<sub>2</sub>PCH<sub>2</sub>CH<sub>2</sub>PDh<sub>2</sub>) Attached to Gold Electrodes. *J Electroanal Chem* 404:227-235
  54. Shaw SJ, Marken F, Bond AM (1996) Detection of New Features Associated with the Oxidation of Microcrystalline Tetrathiafulvalene Attached to Gold Electrodes by the Simultaneous Application of Electrochemical and Quartz Crystal Microbalance Techniques. *Electroanal* 8:732-741
  55. Dostal A, Hermes M, Scholz F (1996) The Formation of Bilayered Nickel-Iron, Cadmium-Iron and Cadmium-Silver Hexacyanoferrates by an Electrochemically Driven Insertion-Substitution Mechanism. *J Electroanal Chem* 415:133-141
  56. Bond AM, Fletcher S, Marken F, Shaw SJ, Symons PG (1996) Electrochemical and x-Ray Diffraction Study of the Redox Cycling of Nanocrystals of 7,7,8,8-Tetracyanoquinodimethane. Observation of a Solid Phase Transformation Controlled by Nucleation and Growth. *J Chem Soc Faraday Trans* 92(20):3925-2933
  57. Meyer B, Zhang S, Scholz F (1996) The Quantitative Analysis of Mixed Crystals Cu<sub>x</sub>Se<sub>1-x</sub> with Abrasive Stripping Voltammetry and a Redetermination of the Solubility Product of CuSe and the Standard Potential of the Cu/CuSe Electrode. *Fresenius' J Anal Chem* 356:267-270
  58. Schröder U, Meyer B, Scholz F (1996) A Cell for Insitu Incident-Light Microscopy for the Study of Electrochromism of Solid State Electrochemical Reactions. *Fresenius' J Anal Chem* 356:295-298
  59. Reddy SJ, Hermes M, Scholz F (1996) The Application of Abrasive Stripping Voltammetry for a Simple and Rapid Screening of Pesticides. *Electroanal* 8:955-958
  60. Lange B, Lovric M, Scholz F (1996) The Catalytic Action of Adsorbed Thiocyanate Ions and Thiourea in the Electron Transfer from Glassy Carbon to Solid Copper(I) Selenide and Copper(I) Sulfide Particles. *J Electroanal Chem* 418:21-28
  61. Komorsky-Lovric S, Bartoll J, Stößer R, Scholz F (1997) Abrasive Stripping Voltammetry and ESR Spectroscopy of Manganese in Carbonates. *Croatica Chem Acta* 70:563-583
  62. Meyer B, Scholz F (1997) Redetermination of the Transformation Enthalpies of the Xanthoconite-Proustite, Pyrostilpnite-

- Pyrargyrite and Trechmannite-Smithite Phase Transitions. *Phys Chem of Minerals* 24:50-52
63. Komorsky-Lovric S, Lovric M, Scholz F (1997) Sulfide Ion Electrooxidation Catalysed by Cobalt Phthalocyanine Microcrystals. *Mikrochim Acta* 127:95-99
  64. Lovric M, Komorsky-Lovric S, Scholz F (1997) Staircase Voltammetry with Finite Diffusion Space. *Electroanal* 9:575-577
  65. Bond AM, Colton R, Mahon PJ, Tan WT (1997) Tetrabutylammonium Cation Expulsion Versus Perchlorate Electrolyte Anion Uptake in the Electrochemical Oxidation of Microcrystals of  $[(C_4H_9)_4N][Cr(CO)_5I]$  Mechanically Attached to a Gold Electrode: a Voltammetric and Quartz Crystal Microbalance Study. *J Solid State Electrochem* 1:53-61
  66. Grygar T (1997) Dissolution of Pure and Substituted Goethites Controlled by the Surface Reaction under Conditions of Abrasive Stripping Voltammetry. *J Solid State Electrochem* 1:77-82
  67. Schröder U, Scholz F (1997) Microscopic in situ Diffuse Reflectance Spectroelectrochemistry of Solid State Electrochemical Reactions of Particles Immobilized on Electrodes. *J Solid State Electrochem* 1:62-67
  68. Komorsky-Lovric Š (1997) Voltammetry of Azobenzene Microcrystal. *J Solid State Electrochem* 1:94-99
  69. Lovric M, Scholz F (1997) A Model for the Propagation of a Redox Reaction Through Microcrystals. *J Solid State Electrochem* 1:108-113
  70. Bond AM, Fiedler DA (1997) *In situ* Electrochemical and Electron Spin Resonance Studies of Microcrystals Mechanically Attached to an Electrode Surface. *J Electrochem Soc* 144:1566-1574
  71. Marken F, Leslie WM, Compton RG, Moloney MG, Sanders E, Davies SG, Bull SD (1997) Homogeneous and Heterogeneous Catalytic Redox Processes: Solution and Solid State Voltammetry of Lead Complexes at Carbon Electrodes. *J Electroanal Chemistry* 424:25-34
  72. Bond AM, Marken F, Hill E, Compton RG, Hügel H (1997) The Electrochemical Reduction of Indigo Dissolved in Organic Solvents and as a Solid Mechanically Attached to a Basal Plane Pyrolytic Graphite Electrode Immersed in Aqueous Electrolyte Solution. *J Chem Soc Perkin Trans* 2:1735-1742
  73. Fiedler DA, Besenhard JO, Fooker MH (1997) Rapid Electrochemical Characterization of Battery Electrode Materials in the Solid State. *J Power Sources* 69:157-160

74. Marken F, Webster RD, Bull St D, Davies St G (1997) Redox Processes in Microproplets Studied by Voltammetry, Microscopy, and ESR Spectroscopy: Oxidation of *N,N,N',N'*-Tetrahexylphenylene Diamine Deposited on Solid Electrode Surfaces and Immersed in Aqueous Electrolyte Solution. *J Electroanal Chem* 437:209-218
75. Bond AM, Colton R, Marken F, Walter JN (1997) Voltammetric, Specular Reflectance Infrared, and X-Ray Electron Probe Characterization of Redox and Isomerization Processes Associated with the  $[\text{Mn}(\text{CO})_2(\eta^3\text{-P}_2\text{P}')\text{Br}]^{+/0}$  ( $\text{P}_2\text{P}' = \{\text{Ph}_2\text{P}(\text{CH}_2)_2\}\text{PPh}$ ),  $[\text{Mn}(\text{CO})_2(\eta^3\text{-P}_3\text{P}')\text{Br}]^{+/0}$ , ( $\text{P}_3\text{P}' = \{\text{Ph}_2\text{PCH}_2\}_3\text{P}$ ), and  $[\{\text{Mn}(\text{CO})(\eta^2\text{-dpe})\text{Br}\}_2(\mu\text{-dpe})]^{2+/0}$  ( $\text{dpe} = \text{Ph}_2\text{P}(\text{CH}_2)_2\text{PPh}_2$ ) Solid State Systems. *Organometallics* 16:5006-5014
76. Gálova M, Markušová K, Lux L, Zezula I, Orináková R (1997) Determination of the Surface Activity of Powders by Electrochemical Methods, *Chem. Papers* 51:5-10
77. Bond AM, Colton R (1997) Electrochemical Studies of Metal Carbonyl Compounds. *Coord Chem Rev* 166:161-180
78. Uchida I, Fujiyoshi H, Waki S (1997) Microvoltammetric Studies on Single Particles of Battery Active Materials. *J Power Sources* 68:139-144
79. Scholz F, Lovric M, Stojek Z (1997) The Role of Redox Mixed Phases  $\{\text{ox}_x(\text{C}_{\text{Nred}})_{1-x}\}$  in Solid State Electrochemical Reactions and the Effect of Miscibility Gaps in Voltammetry. *J Solid State Electrochem* 1:134-142
80. Perdicakis M, Grosselin N, Bessière J (1997) Voltammetric Behaviour of Single Particles of Silver Chalcogenides in the Micrometric Range. Comparison with Measurements at Modified Carbon Electrodes. *Electrochim Acta* 42:3351-3358
81. Grygar T (1998) Phenomenological Kinetics of Irreversible Electrochemical Dissolution of Metal-Oxide Microparticles. *J Solid State Electrochem* 2:127-136
82. Bond AM, Colton R, Mahon PJ, Snook GA, Tan WT (1998) Voltammetric Oxidation of Solution and Solid Phases of Salts of  $[\text{V}(\text{CO})_6]^-$  in Aqueous (Electrolyte) Media. *J Phys Chem B* 102:1229-1234
83. Friedrich A, Hefele H, Mickler W, Mönner A, Uhlemann E, Scholz F (1998) Voltammetric and Potentiometric Studies of the Stability of Vanadium(IV) Complexes. A Comparison of Solution Phase Voltammetry with the Voltammetry of the Microcrystalline Solid Compounds. *Electroanal* 10:244-248

84. Komorsky-Lovric Š, Scholz F (1998) Stripping Chronopotentiometry of Immobilized Microparticles. *J Electroanal Chem* 445:81-87
85. Scholz F, Meyer B (1998) Voltammetry of Solid Microparticles Immobilized on Electrode Surfaces. In *Electroanalytical Chemistry, A Series of Advances*. (Bard AJ, Rubinstein I, Eds), vol 20, 1-86, Marcel Dekker, New York
86. Fiedler DA (1998) Rapid Evaluation of the Rechargeability of  $\gamma$ -MnO<sub>2</sub> in Alkaline Media by Abrasive Stripping Voltammetry. *J Solid State Electrochem* 2:315-320
87. Lovric M, Hermes M, Scholz F (1998) The Effect of Electrolyte Concentration in the Solution on the Voltammetric Response of Insertion Electrodes. *J Solid State Electrochem* 2:401-404
88. Oldham KB (1998) Voltammetry at a Three-Phase Junction. *J Solid State Electrochem* 2:367-377
89. Fiedler DA, Albering JH, Besenhard JO (1998) Characterization of Strontium and Barium Manganates by Abrasive Stripping Voltammetry. *J Solid State Electrochem* 2:413-419
90. Bond AM, Colton R, Humphrey DG, Mahon PJ, Snook GA, Tedesco V, Walter JN (1998) Systematic Studies of 17-Electron Rhenium(II) Carbonyl Phosphine Complexes. *Organometallics* 17:2977-2985
91. Komorsky-Lovric S (1998) A Simple Method for the Detection of Manganese in Marine Sediments. *Croat Chim Acta* 71:263-269
92. Grygar T, Bezdicka P (1998) Electrochemical Dissolution of CrIII and CrIV Oxides. *J Solid State Electrochem* 3:31-38
93. Mocellin E, Goscinska T (1998) Modified Carbon Electrodes for Microscale Electrochemistry. *J Chem Educ* 75:771-772
94. Doménech A, Ribera A, Cervilla A, Llopis E (1998) Electrochemistry of Hydrotalcite-Supported bis(2-Mercapto-2,2-Diphenyl-Ethanolate) Dioxomolybdate Complexes. *J Electroanal Chem* 458:31-41
95. Kahlert H, Retter U, Lohse H, Siegler K, Scholz F (1998) On the Determination of the Diffusion Coefficients of Electrons and Potassium Ions in Copper(II) Hexacyanoferrate(II) Composite Electrodes. *J Phys Chem B* 102:8757-8765
96. Kulesza PJ, Malik MA, Berrettoni M, Giorgetti M, Zamponi S, Schmidt R, Marassi R (1998) Electrochemical Charging, Counteraction Accomodation, and Spectrochemical Identity of Microcrystalline Solid Cobalt Hexacyanoferrate. *J Phys Chem B* 102:1870-1876

97. Marken F, Compton RG, Goeting Ch H, Foord JS, Bull SD, Davies Sehr geehrte Damen und Herren (1998) Anion Detection by Electro-Insertion Into *N,N,N',N'*-Tetrahexyl-Phenylene-Diamine (THPD) Microdroplets Studied by Voltammetry, EQCM, and SEM techniques. *Electroanal* 10:821-826
98. Nalini B, Sriraman Narayanan S (1998) Ruthenium(III) Diphenyldithiocarbamate as Mediator for the Electrocatalytic Oxidation of Sulfhydryl Compounds at Graphite Electrode. *Bull Electrochem* 14:241-245
99. Ravi Shankaran D, Sriraman Narayanan S (1998) Studies on Copper Hexacyanoferrate Modified Electrode and Its Application for the Determination of Cysteine. *Bull Electrochem* 14:267-270
100. Nalini B, Sriraman Narayanan S (1998) Electrocatalytic Oxidation of Ascorbic Acid at a Graphite Electrode Modified with a New Ruthenium(III) Dithiocarbamate Complex. *Bull Electrochem* 14:267-270
101. Bond AM, Fletcher S, Symons PG (1998) The Relationship Between the Electrochemistry and the Crystallography of Microcrystals - The Case of TCNQ (7,7,8,8-Tetracyanoquinodimethane). *Analyst* 123:1891-1904
102. Bond M, Deacon GB, Howitt J, MacFarlane DR, Spiccia L, Wolfbauer G (1998) Voltammetric Determination of the Reversible Redox Potential for the Oxidation of the Highly Active Polypyridyl Ruthenium Photovoltaic Sensitizer *cis*-Ru<sup>(II)</sup>(dcbpy)<sub>2</sub>(NCS)<sub>2</sub>. *J Electrochem Soc* 146:648-656
103. Dostal A (1998) Festkörperreaktionen an metallhexacyanometall-modifizierten Elektroden, Ph.D. thesis, Humboldt-Universität, Berlin
104. Grygar T (1998) Elektrochemické rozpouštění práškových oxidů kovů, Ph. D. thesis, Řež
105. Albering JH, Grygar T (1999) A Note Regarding the Rate-Determining Step of Reduction of Solid Manganate(V). *J Solid State Electrochem* 3:117-120
106. Bond M, Fiedler DA, Lamprecht A, Tedesco V (1999) Electron-, Anion-, and Proton-Transfer Processes Associated with the Redox Chemistry of Fe( $\eta^5$ -C<sub>5</sub>Ph<sub>5</sub>)( $\eta^6$ -C<sub>6</sub>H<sub>5</sub>)C<sub>5</sub>Ph<sub>4</sub>) and its Protonated form [Fe( $\eta^5$ -C<sub>5</sub>Ph<sub>5</sub>)( $\eta^6$ -C<sub>6</sub>H<sub>5</sub>)C<sub>5</sub>Ph<sub>4</sub>H)]BF<sub>4</sub> at Microcrystal-Electrode-Solvent (Electrolyte) Interfaces. *Organometallics* 18:642-649
107. Lovric M, Scholz F (1999) A Model for the Coupled Transport of Ions and Electrons in Redox Conductive Microcrystals. *J Solid State Electrochem* 3:172-175

108. Zezula I, Galova M (1999) Application of Abrasive Stripping Voltammetry in Corrosion Science. I. Determination of the Corrosion Potential of Metals. *J Solid State Electrochem* 3:231-233
109. Komorsky-Lovric S, Galic I, Penovski R (1999) Voltammetric Determination of Cocaine Microparticles. *Electroanal* 11:120-123
110. Lovric M (1999) Diffusion from a Three-Phase Junction into a Hemispherical Droplet. *Electrochemistry Commun* 1:207-212
111. Zakharchuk NF, Naumov N, Stösser R, Schröder U, Scholz F, Mehner H (1999) Solid State Electrochemistry, x-Ray Powder Diffraction, Magnetic Susceptibility, Electron Spin Resonance, Mössbauer and Diffuse Reflectance Spectroscopy of Mixed Iron(III)-Cadmium(II) Hexacyanoferrates. *J Solid State Electrochem* 3:5, 264-276
112. Lux L, Gálová M, Hezelová M, Markusová K (1999) Investigation of the Reactivity of Powder Surfaces by Abrasive Voltammetry. *J Solid State Electrochem* 3:5, 288-292
113. Narayanan SS, Scholz F (1999) A Comparative Study of the Electrocatalytic Activities of Some Metal Hexacyanoferrates for the Oxidation of Hydrazine. *Electroanal* 11:465-469
114. Zhuang Q, Scholz F, Pragst F (1999) The Voltammetric Behaviour of Solid 2,2-Diphenyl-1-Picrylhydrazyl (DPPH) Microparticles. *Electrochem Commun* 1:406-4103
115. Shankaran DR, Narayanan SS (1999) Characterization and Application of an Electrode Modified by Mechanically Immobilized Copper Hexacyanoferrate. *Fresenius' J Anal Chem* 364:686-689
116. Jantscher W, Binder L, Fiedler DA, Andreaus R, Kordesch K (1999) Synthesis, Characterization and Application of Doped Electrolytic Manganese Dioxides. *J Power Sources* 79:9-18
117. Grygar T (1999) Electrochemical Reactions of  $\text{La}(\text{Ni},\text{Cr})\text{O}_3$  and  $\text{La}(\text{Ni},\text{Fe})\text{O}_3$  in Acid Aqueous Solution. *J Solid State Electrochem* 3:412-416
118. Grygar T, Bezdicka P, Caspary EG (1999) Electrochemical Dissolution of Immobilized Alpha- $(\text{Fe}_x\text{Cr}_{1-x})_2\text{O}_3$  Microparticles. *J Electrochem Soc* 146:3234-3238
119. Suarez MF, Marken F, Compton RG, Bond AM, Miao WJ, Raston CL (1999) Evidence for Nucleation-Growth, Redistribution, and Dissolution Mechanisms During the Course of Redox Cycling Experiments on the C-60/NBu<sub>4</sub>C<sub>60</sub> Solid-State Redox System - Voltammetric, SEM, and in-situ AFM Studies. *J Phys Chem* 103:5637-5644



120. Shankaran DR, Narayanan SS (1999) Chemically-Modified Sensor for Amperometric Determination of Sulfur-Dioxide. *Sensors Actuators B - Chemical* 55:191-194
121. Scaboo KM, Grover WH, Chambers JQ (1999) Inverse Derivative Chronopotentiometry/Quartz Crystal Microgravimetry of Solid Conducting Films. *Anal Chim Acta* 380:47-54
122. Mohan Rao M, Jayalakshmi M, Schäf O, Wulff H, Scholz F (1999) Electrochemical Behaviour of Solid Lithium Nickelate (LiNiO<sub>2</sub>) in an Aqueous Electrolyte. *J Solid State Electrochem* 4:17-23
123. Tryk DA, Fujishima A (1999) Abrasive Stripping Voltammetry at Polycrystalline Diamond Electrodes. *Manivannan, Chem Lett* 851-852
124. Suárez MF, Bond AM, Compton RG (1999) Significance of Redistribution Reactions Detected by in situ Atomic Force Microscopy During Early Stages of Fast Scan Rate Redox Cycling Experiments at a Solid 7,7,8,8-Tetracyanoquinodimethane-Glassy Carbon Electrode-Aqueous (Electrolyte) Interface. *J Solid State Electrochem* 4:24-33
125. Bezdicka P, Grygar T, Klapste B, Vondrak J (1999) MnO<sub>x</sub>/C Composites as Electrode Materials. I. Synthesis, XRD and Cyclic Voltammetric Investigation. *Electrochim Acta* 45:913-920
126. Komorsky-Lovric S, Mirceski V, Scholz F (1999) Voltammetry of Organic Microparticles. *Mikrochim Acta* 132:67-77
127. Nishizawa M, Uchida I (1999) Microelectrode-Based Characterization Systems for Advanced Materials in Battery and Sensor Applications. *Electrochim Acta* 44:3629-3637
128. Eklund JC, Bond AM (1999) Photocatalytic Reactions at Microcrystalline *fac*-Mn(CO)<sub>3</sub>(η<sup>2</sup>-Ph<sub>2</sub>PCH<sub>2</sub>PPh<sub>2</sub>)Cl-Electrode-Aqueous (Electrolyte) Interfaces. *J Amer Chem Soc* 121:8306-8312
129. Bond AM, Lamprecht A, Tedesco V, Marken F (1999) Novel Features Associated with the Electrochemically Driven bis(eta(5)-Pentaphenyl-Cyclopentadienyl)Iron(II)-Iron(III) Redox Transformation at an Electrode-Microcrystal-Solvent (Electrolyte) Interface. *Inorg Chim Acta* 291:21-31
130. Shankaran DR, Narayanan SS (1999) Evaluation of Mechanically Immobilised Nickel Hexacyanoferrate Electrode as an Amperometric Sensor for Thiosulphate Determination. *Fresenius J Anal Chem* 365:663
131. Perdickakis M, Grosselin N, Bessière J (1999) Interaction of Pyrite Pulps with Ag<sup>+</sup> and Hg<sup>2+</sup> Ions. Electrochemical Characterization of Micrometric Grains. *Anal Chim Acta* 385:467-485

132. Scholz F, Komorsky-Lovrić Š, Lovrić M (2000) A New Access to Gibbs Free Energies of Transfer of Ions Across Liquid-Liquid Interfaces and a New Method to Study Electrochemical Processes at Well-Defined Three-Phase Junctions. *Electrochem Commun* 2:112-118
133. Scholz F, Schädel S, Schultz A, Schauer F (2000) Chronopotentiometric Study of Laccase Catalysed Oxidation of Quinhydrone Microcrystals Immobilised on a Gold Electrode Surface and of the Oxidation of a Phenol Derivatized Graphite Electrode Surface. *J Electroanal Chem* 480:241-248
134. Ramaraj R, Kabbe Ch, Scholz F (2000) Electrochemistry of Microparticles of Tris(2,2'-Bipyridine)Ruthenium(II) Hexafluorophosphate. *Electrochem Commun* 2:190-194
135. Zhuang QK, Scholz F (2000) Electrochemical Driven Introduction of Copper Ions Into the Ring of 5, 10, 15, 20-Tetraphenyl-21H, 23H-Porphyrin Mechanically Attached as Solid Microparticles to a Graphite Electrode. *J of Porphyrins and Phthalocyanines* 4:202-208
136. Schröder U, Scholz F (2000) The Solid State Electrochemistry of Metal Octacyanomolybdates, Octacyanotungstates, and Hexacyanoferrates Explained on the Basis of Dissolution and Re-precipitation Reactions, their Lattice Structures and Crystallinities. *Inorg Chem* 39:1006-1015
137. Schwudke D, Stößer R, Scholz F (2000) Solid-State Electrochemical, x-Ray and Spectroscopic Characterization of Substitutional Solid Solutions of Iron-Copper Hexacyanoferrates. *Electrochem Commun* 2:301-306
138. Jiang J, Kucernak A (2000) The Electrochemistry of Platinum Phthalocynine Microcrystals. I Electrochemical Behaviour in Acetonitrile Electrolytes. *Electrochim Acta* 45:2227-2239
139. Bond AM, Marken F, Williams ChT, Beattie DA, Keyes TE, Foster RJ, Vos JG (2000) Unusually fast Electron and Anion Transport Processes Observed in the Oxidation of "Electrochemically Open" Microcrystalline  $[\{M(\text{bipy})_2\}\{M'(\text{bipy})_2\}(-L)](\text{PF}_6)_2$  Complexes (M, M' = Ru, Os; bipy = 2,2'-bipyridyl; L = 1,4-dihydroxy-2,5-bis(pyrazol-1-yl)benzene. *J Phys Chem* 104:1977-1983
140. Myland JC, Oldham KB (2000) Modelling Reversible Cyclic Voltammetry at the One-Dimensional Junction Established by Three Phases: an Organic Liquid Containing a Neutral Electroactive Solute, an Aqueous Electrolyte Solution, and an Electronic Conductor. *Electrochem Commun* 2:541-546

141. Bakardjieva S, Bezdicka P, Grygar T, Vorm P (2000) Reductive Dissolution of Microparticulate Manganese Oxides. *J Solid State Electrochem* 4:306-313
142. Schröder U, Oldham KB, Myland JC, Mahon PJ, Scholz F (2000) Modelling of Solid-State Voltammetry of Immobilized Microcrystals Assuming an Initiation of the Electrochemical Reaction at a Three-Phase Junction. *J Solid State Electrochem* 4:314-324
143. Doménech-Carbó A, Domenéch-Carbó MT, Gimeno-Adelantado JV, Moya-Moreno M, Bosch-Reig F (2000) Voltammetric Identification of Lead(II) and (IV) in Mediaeval Glazes in Abrasion-Modified Carbon Paste and Polymer Film Electrodes. Application to the Study of Alterations in Archaeological Ceramics. *Electroanal* 12:120-127
144. Kalvoda R (2000) Netradiční použití polarografie/voltametrie. *Chem Listy* 94:2-9
145. Kulesza PJ, Malik MA, Schmidt R, Smolinska A, Miecznikowski K, Zamponi S, Czerwinski A, Berrettoni M, Marassi R (2000) Electrochemical Preparation and Characterization of Electrodes Modified with Mixed Hexacyanoferrates of Nickel and Palladium. *J Electroanal Chem* 487:57-65
146. Doménech-Carbó A, Doménech-Carbó MT, Moya-Moreno M, Gimeno-Adelantado JV, Bosch-Reig F (2000) Identification of Inorganic Pigments from Paintings and Polychromed Sculptures Immobilized Into Polymer Electrodes by Stripping Differential Pulse Voltammetry. *Anal Chim Acta* 407:275-289
147. Kucernak AR, Chowdhury PB, Wilde CP, Kelsall GH, Zhu YY, Williams DE (2000) Scanning Electrochemical Microscopy of a Fuel-Cell Electrocatalyst Deposit onto Highly Oriented Pyrolytic Graphite. *Electrochim Acta* 45:4483-4491
148. Zakharchuk N, Meyer S, Lange B, Scholz F (2000) A Comparative Study of Lead Oxide Modified Graphite Paste Electrodes and Solid Graphite Electrodes with Mechanically Immobilised Lead Oxides. *Croat Chem Acta* 73:667-704
149. Fulian Q, Ball JC, Marken F, Compton R, Fisher AC (2000) Voltammetry of Electroactive Oil Droplets. Part I: Numerical Modelling for Three Mechanistic Models Using the Dual Reciprocity Finite Element Method. *Electroanal* 12:1012-1016
150. Ball JC, Marken F, Fulian Q, Wadhawan JD, Blythe AN, Schröder U, Compton R, Bull SD, Davies SG (2000) Voltammetry of Electroactive Oil Droplets. Part II: Comparison of Experimental and Simulation Data for Coupled Ion and Electron In-

- sertion Processes and Evidence for Microscale Convection. *Electroanal* 12:1017-1025
151. Nartey VK, Binder L, Huber A (2000) Production and Characterisation of Titanium Doped Electrolytic Manganese Dioxide for use in Rechargeable Alkaline Zinc/Manganese Dioxide Batteries. *J Power Sources* 87:205-211
  152. Wadhawan JD, Schröder U, Neudeck A, Wilkins SJ, Compton RG, Marken F, Consorti CS, de Souza RF, Dupont J (2000) Ionic Liquid Modified Electrodes. Unusual Partitioning and Diffusion Effects of  $\text{Fe}(\text{CN})_6^{4-/3-}$  in Droplet and Thin Layer Deposits of 1-Methyl-3-(2,6-(*S*)-Dimethylocten-2-yl)-Imidazolium Tetrafluoroborate. *J Electroanal Chem* 493:75-83
  153. Terui N, Nakatani K, Kitamura N (2000) Kinetic Analysis of Electrochemically Induced Ion Transfer across a Single Microdroplet / Water Interface. *J Electroanal Chem* 494:41-46
  154. Bond AM, Miao W, Raston CL (2000) Identification of Processes that Occur after Reduction and Dissolution of  $\text{C}_{60}$  Adhered to Gold, Glassy Carbon, and Platinum Electrodes Placed in Acetonitrile (Electrolyte) Solution. *J Phys Chem B* 104:2320-2329
  155. Foster RJ, Keyes TE, Bond AM (2000) Protonation Effects on the Structure and Homogeneous Charge Transport Dynamics of Solid State Osmium bis(bipyridyl)tetrazine Chloride Films. *J Phys Chem B* 104:6389-6396
  156. Bond AM, Miao W, Raston CL, Sandoval CA (2000) Electrochemical, EPR, and Magnetic Studies on Microcrystals of the  $[\text{C}_{60}\text{C}(\text{p-benzyl-calix}[5]\text{arene})_2]_8\text{toluene}$  and its One-Electron-Reduced Encapsulation Complex. *J Phys Chem B* 104:8129-8137
  157. Hermes M, Scholz F (2000) The Electrochemical Oxidation of White Phosphorus at a Three-Phase Junction. *Electrochem Commun* 2:845-850
  158. Lovric M, Hermes M, Scholz F (2000) Solid State Electrochemical Reactions in Systems with Miscibility Gaps. *J Solid State Electrochem* 4:394-401
  159. Zhuang QK (2000) The Mechanistic Studies of the Electrochemical in situ Association of Copper Ions with 5, 10, 15, 20-Tetraphenyl-21H, 23H-Porphyrin. *Microchem J* 65:333-340
  160. Shankaran DR, Narayanan SS (2000) Amperometric Determination of Sulphur Dioxide at a Nickel Hexacyanoferrate Modified Electrode. *Res J Chem Environ* 6:13-16

161. Minovic A, Milosev I, Komorsky-Lovric S (2000) Voltammetry of Solid Microparticles Immobilized on Graphite Electrode Surface. *Materiali in Tehnologije* 34:23-25
162. Schröder U (2000) Methodische, stofflich-mechanistische und theoretische Aspekte insertions-elektrochemischer Reaktionen, Ph D thesis, Humboldt-Universität, Berlin
163. Bárcena Soto M (2000) Thermodynamische Untersuchungen zur Insertionselektrochemie von Metallhexacyanoferraten, Ph D thesis, Humboldt-Universität, Berlin
164. Girerd JJ, Verdaguer M (2000) Electrochimie à une particule individuelle de taille micrométrique. Une technique pour la caractérisation grain par grain des matériaux conducteurs divisés, *Lett Sc Chim* No. 73:22-28
165. Mohan Rao M, Jayalakshmi M, Schäfer O, Wulff H, Scholz F (2001) Electrochemical Behaviour of Solid Lithium Cobaltate ( $\text{LiCoO}_2$ ) and Lithium Manganate ( $\text{LiMn}_2\text{O}_4$ ) in an Aqueous Electrolyte System. *J Solid State Electrochem* 5:50-56
166. Marken F, Blythe AN, Wadhawan JD, Compton RG, Bull SD, Aplin RT, Davies SG (2001) Voltammetry of Electroactive Liquid Redox Systems: Anion Insertion and Chemical Reactions in Microdroplets of *para*-Tetrakis(6-Methoxyhexyl) Phenylendiamine, *para*- and *meta*-Tetrahexylphenylendiamine. *J Solid State Electrochem* 5:17-22
167. Jiang J, Kucernak A (2001) The Electrochemistry of Platinum Phthalocycnine Microcrystals. II. A Microelectrode Observation of Nucleation-Growth Controlled Solid-Solid Phase Transformation in Non-aqueous Solvent. *Electrochim Acta* 46:1223-1231
168. Marken F, Compton RG, Goeting CH, Foord JS, Bull SD, Davies SG (2001) Fast Electrochemical Triple-Interface Processes at Boron-Doped Diamond Electrodes. *J Solid State Electrochem* 5:88-93
169. Takeda N, Stawasz ME, Parkinson BA (2001) Electrochemical Oxidation and ex-situ STM Observation of bis(4-dimethylamino-2-dihydroxyphenyl)squaraine Dye Layers on HOPG Electrodes. *J Electroanal Chem* 498:19-33
170. Bond M, Miao W, Raston CL, Ness TJ, Barnes MJ, Atwood JL (2001) Electrochemical and Structural Studies on Microcrystals of the  $(\text{C}_{60})_x(\text{CTV})$  Inclusion Complexes ( $x = 1, 1.5$ ; CTV = Cyclotrimeratrylene). *J Phys Chem B* 105:1687-1695
171. Schröder U, Compton RG, Marken F, Bull AD, Davies SG, Gilmour S (2001) Electrochemically Driven Ion Insertion Processes

- across Liquid/Liquid Boundaries: Neutral versus Ionic Redox Liquids. *J Phys Chem B* 105:1344-1350
172. Bond AM, Feldberg SW, Miao W, Oldham KB, Raston CL (2001) Modelling of Solid-State, Dissolution and Solution-Phase Reactions at Adhered Solid-Electrode-Solvent (Electrolyte) Interfaces: Electrochemistry of Microcrystals of C<sub>60</sub> Adhered to an Electrode in Contact with Dichloromethane (Bu<sub>4</sub>NClO<sub>4</sub>). *J Electroanal Chem* 501:22-32
173. Hermes M, Lovrić M, Hartl M, Retter U, Scholz F (2001) On the Electrochemically Driven Formation of Bilayered Systems of Solid Prussian-Blue-Type Metal Hexacyanoferrates: A Model for Prussian Blue Cadmium Hexacyanoferrate Supported by Finite Difference Simulations. *J Electroanal Chem* 501:193-204
174. Komorsky-Lovrić Š, Lovrić M, Scholz F (2001) Square-Wave Voltammetry of Decamethylferrocene at the Three-Phase Junction Organic Liquid | Aqueous Solution | Graphite. *Collect Czech Chem Commun* 66:434-444
175. Doménech-Carbó MT, Casas-Catalán MJ, Doménech-Carbó A, Mateo-Castro R, Gimeno-Adelantado JV, Bosch-Reig F (2001) Analytical Study of Canvas Painting Collection from the *Basilica de la Virgen de los Desapareados* using SEM/EDX, FT-IR, GC and Electrochemical Techniques. *Fresenius' J Anal Chem* 369:571-575
176. Doménech-Carbó A, Doménech-Carbó MT, Gimeno-Adelantado V, Bosch-Reig F, Sauri-Peris MC, Casas-Catalán MJ (2001) Electrochemical Analysis of the Alterations in Copper Pigments using Charge Transfer Coefficient/ Peak Potential Diagrams. Application to Microsamples of Baroque wall Paintings Attached to Polymer Film Electrodes. *Fresenius' J Anal Chem* 369:576-581
177. Cepriá G, Abadias O, Pérez-Arantegui J, Castillo JR (2001) Electrochemical Behavior of Silver-Copper Alloys in Voltammetry of Microparticles: A Simple Method for Screening Purposes. *Electroanal* 13:477-483
178. Zhuang QK, Scholz F (2001) *In-situ* Electrochemical Synthesis of the Metalloporphyrins with Help of the Voltammetry of Immobilized Microparticles. *Chem J of Chin Univ (Gaodeng Xuexiao Huaxue Xuebao)* 22:171-174
179. Keyes TE, Foster RJ, Bond AM, Miao W (2001) Electron Self-Exchange in the Solid-State: Cocrystals of Hydroquinone and Bipyridyl Triazole. *J Am Chem Soc* 123:2877-2884

180. Ulmeanu S, Lee HJ, Fermin DJ, Girault HH, Shao Y (2001) Voltammetry at a Liquid-Liquid Interface Supported on a Metallic Electrode. *Electrochem Commun* 3:219-223
181. Grygar T, Bakardjieva S, Bezdicka P, Vorm P (2001) Electrochemical Dissolution of Mixed Oxides of Mn and Fe: the Relationship between Phase Composition and Reactivity. *Ceramics-Silikaty* 45:55- 61
182. Wadhawan JD, Compton RG, Marken F, Bull SD, Davies SG (2001) Photoelectrochemically Driven Processes at the *N,N,N',N'*-Tetrahexylphenylenediamine Microdroplet/Electrode/Aqueous Electrolyte Triple Interface. *J Solid State Electrochem* 5:348-354
183. Rao M, Liebenow C, Jayalakshmi M, Wulff H, Guth U, Scholz F (2001) High Temperature Combustion Synthesis and Electrochemical Characterisation of  $\text{LiNiO}_2$ ,  $\text{LiCoO}_2$  and  $\text{LiMn}_2\text{O}_4$  for Li-Ion Secondary Batteries. *J Solid State Electrochem* 5:348-354
184. Hasse U, Scholz F (2001) In situ Atomic Force Microscopy of the Reduction of Lead Oxide Nanocrystals Immobilized on an Electrode Surface. *Electrochem Commun* 3:429-434
185. Brown RJC, Kucernak AR (2001) The Electrochemistry of Platinum Phthalocyanine Microcrystals III. Electrochemical Behaviour in Aqueous Electrolytes. *Electrochim Acta* 46:2573-2582
186. Frangini S, Carewska M, Passerini S, Scaccia S (2001) Intercalation Behaviour of  $\text{LiCoO}_2$  Electrodes in Aqueous Alkaline Electrolytes by Microparticle Cyclic Voltammetry. *J New Mat Electrochem Systems* 4:83-88
187. Scholz F, Schwudke D, Stößer R, Boháček J (2001) The Interaction of Prussian Blue and Dissolved Hexacyanoferrate Ions with Goethite ( $\alpha\text{-FeOOH}$ ) Studied to Assess the Chemical Stability and Physical Mobility of Prussian Blue in Soils. *Ecotoxicology and Environmental Safety*, *Environmental Res* 49:245-254
188. Komorsky-Lovrić Š, Lovrić M, Scholz F (2001) Cyclic Voltammetry of Decamethylferrocene at the Three-Phase Junction Organic Liquid | Aqueous Solution | Graphite. *J Electroanal Chem* 508:129-137
189. Doménech-Carbó A, Doménech-Carbó MT, Osete-Cortina L (2001) Identification of Manganese(IV) Centers in Archaeological Glass using Microsample Coatings Attached to Polymer Film Electrodes. *Electroanal* 13:927-935
190. Jiang J, Kucernak AR (2001) The Electrochemistry of Platinum Phthalocyanine Microcrystals. IV. Temperature Dependence of

- the Electrochemical Behaviour in Non-Aqueous Solution. *Electrochim Acta* 46:3445-3456
191. Grygar T, Bezdička P, Piszora P, Wolska E (2001) Electrochemical Reactivity of Li-Mn-O and Li-Fe-Mn-O Spinel. *J Solid State Electrochem* 5:487-494
  192. Galova M, Orinakova R, Grygar T, Lux L, Hezelova M (2001) Relation Between the Dissolution Reactivity of Powder Substances and Efficiency of their Electroplating. *Particulate Sci Technol* 19:85-94
  193. Cepriá G, Aranda C, Pérez-Arantegui J, Lacueva F, Castillo JR (2001) Voltammetry of Immobilized Microparticles: a Powerful Analytical Technique to Study the Physical and Chemical Composition of Brass. *J Electroanal Chem* 513:52-58
  194. Grygar T, Bezdička P, Vorm P, Jordanova N, Krtil P (2001) Spinel Solid Solutions in the Li-Fe-Mn-O System. *J Solid State Chem* 161:152-160
  195. Doménech-Carbo A, Doménech-Carbo MT, Gimeno-Adelantado JV, Bosch-Reig F, Sauri-Peris MC, Sanchez-Ramos S (2001) Electrochemistry of Iron Oxide Pigments (Earths) from Pictorial Microsamples Attached to Graphite-Polyester Composite Electrodes. *Analyst* 126:1764-1772
  196. Wooster TJ, Bond AM, Honeychurch MJ (2001) Resistance Transitions Detected by Analysis of the Voltammetry of Tetra-thiafulvalene Microparticles Adhered to Electrode Surfaces under Conditions of Dynamic Resistance Compensation. *Electrochem Commun* 3:746-752
  197. Gergely A, Inzelt G (2001) Electropolymerization of 3-Methylthiophene at Liquid 3-Methylthiophene / Aqueous Solution / Graphite Three-Phase Junction. *Electrochem Commun* 3:753-757
  198. van Oorschot IHM, Grygar T, Dekkers MJ (2001) Detection of low Concentrations of Fine-Grained Iron Oxides by Voltammetry of Microparticles. *Earth and Planetary Sc Lett* 193:631-642
  199. Shankaran DR, Narayanan SS (2001) Mechanically Immobilized Copper Hexacyanoferrate Modified Electrode for Electrocatalysis and Amperometric Determination of Glutathione. *Bull Korean Chem Soc* 22:816-820
  200. Shankaran DR, Narayanan SS (2001) Electrochemical Determination of Hydrazine Based on Chemically Modified Electrode. *Res J Chem Environ* 5:21



201. Shankaran DR, Narayanan SS (2001) Amperometric Sensor for Thiols Based on Mechanically Immobilised Nickel Hexacyanoferrate Modified Electrode. *Bull Electrochem* 17:277-280
202. Shankaran DR, Narayanan SS (2001) Amperometric Sensor for Hydrazine Determination Based on Mechanically Immobilized Nickel Hexacyanoferrate Modified Electrode. *Russian J Electrochem* 37:1149-1153
203. McKenzie KJ, Marken F (2001) Direct Electrochemistry of Nanoparticulate  $\text{Fe}_2\text{O}_3$  in Aqueous Solution and Adsorbed onto Tin-Doped Indium Oxide. *Pure Appl Chem* 37:1885-1894
204. Grygar T, Marken F, Schröder U, Scholz F (2002) Electrochemical Analysis of Solids. *Coll Czech Chem Commun* 67:163-208
205. Dokko K, Horikoshi S, Itoh T, Nishizawa M, Abe T, Umeda M, Uchida I (2002) Rapid Evaluation of Charge/Discharge Properties for Lithium Manganese Oxide Particles at Elevated Temperature. *J Solid State Electrochem* 6:188-193
206. Gulaboski R, Mirčeski V, Scholz F (2002) An Electrochemical Method for the Determination of the Standard Gibbs Energy of Anion Transfer Between Water and *n*-Octanol. *Electrochem Commun* 4:277-283
207. Donten M, Stojek Z, Scholz F (2002) Electron Transfer – Ion Insertion Electrochemistry at an Immobilised Droplet: Probing the Three-Phase Electrode-Reaction Zone with a Pt Disk Microelectrode. *Electrochem Commun* 4:324-329
208. Jiang J, Kucernak A (2002) Nanostructured Platinum as an Electrocatalyst for the Electrooxidation of Formic Acid. *J Electroanal Chem* 520:64-70
209. Bárcena Soto M, Scholz F (2002) The Thermodynamics of the Insertion Electrochemistry of Solid Metal Hexacyanometallates. *J Electroanal Chem* 521:183-189
210. Wang J, Kawde AN (2002) Magnetic-Field Stimulated DNA Oxidation. *Electrochem Commun* 4:349-352
211. Inzelt G (2002) Cyclic Voltammetry of Solid Diphenylamine Crystals Immobilized on an Electrode Surface and in the Presence of an Aqueous Solution. *J Solid State Electrochem* 6:265-271
212. Shankaran DR, Narayanan SS (2002) Amperometric Sensor for Glutathione Based on Mechanically Immobilised Cobalt Hexacyanoferrate Modified Electrode. *Bull Chem Soc of Japan* 75:501-505
213. Marken F, Hayman CM, Bulman Page PC (2002) Phosphate and Arsenate Electro-Insertion Processes into a *N,N,N',N'*-

- Tetraoctylphenylenediamine Redox Liquid. *Electrochem Commun* 4:462-467
214. Marken F, Hayman CM, Bulman Page PC (2002) Chromate and Dichromate Electro-Insertion Process into a *N,N,N',N'*-Tetraoctylphenylenediamine Redox Liquid. *Electroanal* 14:1-5
  215. Mirčeski V, Scholz F (2002) Reduction of Iodine at the Organic Liquid / Aqueous Solution / Graphite Electrode Three-Phase Arrangement. *J Electroanal Chem* 522:189-198
  216. Wang J, Xu D, Polsky R (2002) Magnetically-Induced Solid State Electrochemical Detection of DNA Hybridization. *J Amer Chem Soc* 124:4208-4209
  217. Doménech-Carbo A, Doménech-Carbo MT, Osete-Cortina L, Gimeno-Adelantado JV, Bosch-Reig F, Mateo-Castro R (2002) Electrochemical Identification of Metal Ions in Archaeological Ceramic Glazes by Stripping Voltammetry at Graphite/Polyester Composite Electrodes. *Talanta* 56:161-174
  218. Fehér K, Inzelt G (2002) Electrochemical Quartz Crystal Microbalance Study of Formation and Redox Transformation of Poly(diphenylamine). *Electrochim Acta* 47:3551-3559
  219. Bárcena Soto M, Kubsch G, Scholz F (2002) Cyclic Voltammetry of Immobilized Microparticles with *in situ* Calorimetry. Part I: The thermistor electrode, *J Electroanal Chem* 528:18-26
  220. Bárcena Soto M, Scholz F (2002) Cyclic Voltammetry of Immobilized Microparticles with *in situ* Calorimetry, Part II: Application of a Thermistor Electrode for *in situ* Calorimetric Studies of the Electrochemistry of Solid Metal Hexacyanoferrates. *J Electroanal Chem* 528:27-32
  221. Scholz F, Gulaboski R, Mirčeski V, Langer P (2002) Quantification of the Chiral Recognition in Electrochemically Driven Ion Transfer Across the Interface Water | Chiral Liquid. *Electrochem Commun* 4:659-662
  222. Grygar T, Dedecek J, Hradil D (2002) Analysis of low Concentrations of Ferric Oxides in Clays by Diffuse Reflectance Spectroscopy and Voltammetry. *Geologica Carpathica* 53:1-7
  223. Long JW, Ayers KE, Rolison DR (2002) Electrochemical Characterization of High-Surface-Area Catalysts and other Nanoscale Electroactive Materials at Sticky-Carbon Electrodes. *J Electroanal Chem* 522:58-65
  224. Chatterjee A, Wiltshire R, Holt KB, Compton RG, Foord JS, Marken F (2002) Abrasive Stripping Voltammetry of Silver and tin at Boron-Doped Diamond Electrodes. *Diamond and Related Mat* 11:646-650

225. A. Doménech, Perez-Ramirez J, Ribera A, Kapteijn F, Mul G, Moulijn JA (2002) Characterization of Iron Species in Ex-Framework FeZSM-5 by Electrochemical Methods. *Catalysis Letters* 78:303-312
226. Doménech A, Perez-Ramirez J, Ribera A, Mul G, Kapteijn F, Arends IWCE (2002) Electrochemical Characterization of Iron Sites in Ex-framework FeZSM-5. *J Electroanal Chem* 519:72-84
227. Doménech A, Alarcon J (2002) Determination of Hydrogen Peroxide using Glassy Carbon and Graphite/Polyester Composite Electrodes Modified by Vanadium-Doped Zirconias. *Anal Chim Acta* 452:11-22
228. Doménech-Carbo A, Sanchez-Ramosa S, Doménech-Carbo MT, Gimeno-Adelantado JV, Bosch-Reig F, Yusa-Marco DJ, Sauri-Peris MC (2002) Electrochemical Determination of the Fe(III)/Fe(II) Ratio in Archaeological Ceramic Materials using Carbon Paste and Composite Electrodes. *Electroanal* 14:685-696
229. Grygar T, Bezdicka P, Hradil D, Doménech-Carbo A, Marken F, Pikna L, Cepria G (2002) Voltammetric Analysis of Iron Oxide Pigments. *Analyst* 127:1100-1107
230. Wadhawan JD, Evans RG, Banks CE, Wilkins SJ, France RR, Oldham NJ, Fairbanks AJ, Wood B, Walton DJ, Schröder U, Compton RG (2002) Voltammetry of Electroactive Oil Droplets: Electrochemically-Induced Ion Insertion, Expulsion and Reaction Processes at Microdroplets of *N,N,N',N'*-Tetraalkyl-Para-Phenylenediamines (TRPD, R = *n*-Butyl, *n*-Hexyl, *n*-Heptyl and *n*-Nonyl). *J Phys Chem B* 106:9619 – 9632
231. Shankaran DR, Narayanan SS (2002) Amperometric Sensor for Thiosulphate Based on Cobalt Hexacyanoferrate Modified Electrode. *Sensors and Actuators B* 86:180-184
232. Fiedler DA, Scholz F (2002) Electrochemical Studies of Solid Compounds and Materials, Chapter II.8, In: *Electroanalytical Methods – Guide to Experiments and Applications*, F. Scholz (Ed.): Springer, ISBN 3-540-42229-3, 331 pp
233. Doménech A, Alarcón J (2002) Electrochemistry of Vanadium-Doped Tetragonal and Monoclinic ZrO<sub>2</sub> Attached to Graphite/Polyester Composite Electrodes. *J Solid State Electrochem* 6:443-450
234. Mirčeski V, Gulaboski R, Scholz F (2002) Determination of the Standard Gibbs Energies of Transfer of Cations Across the Nitrobenzene/Water Interface Utilizing the Reduction of Iodine in an Immobilized Nitrobenzene Droplet. *Electrochem Commun* 4:813-818

235. McKenzie KJ, Asogan D, Marken F (2002) Adsorption and Reactivity of Hydrous Iron Nanoparticles on Boron-Doped Diamond. *Electrochem Commun* 4:819-823
236. Wang J, Liu G, Polsky R, Merkoci A (2002) Electrochemical Stripping Detection of DNA Hybridization Based on Cadmium Sulfide Nanoparticle Tags. *Electrochem Commun* 4:722-726
237. Myland JC, Oldham KB (2002) A Model of Cyclic Voltammetry for a Thin Organic Layer Sandwiched Between an Electrode and an Aqueous Solution. Convolutional Modelling in the Absence of Supporting Electrolyte. *J Electroanal Chem* 530:1-9
238. Yuan Y, Gao Z, Guo J, Shao Y (2002) Study of Facilitated Potassium Ion Transfer Across a Water Vertical Bar 1,2-Dichloroethane Interface using Different Phase Volume Ratio Systems. *J Electroanal Chem* 526:85-91
239. McKenzie KJ, Marken F (2002) Electrochemical Characterization of Hydrous Ruthenium Oxide Nanoparticle Decorated Boron-Doped Diamond Electrodes. *Electrochem Solid State Lett* 5:E47-E50
240. Komorsky-Lovrić Š, Riedl K, Gulaboski R, Mirčeski V, Scholz F (2002) Determination of Standard Gibbs Energies of Transfer of Organic Anions Across the Water | Nitrobenzene Interface. *Langmuir* 18:8000-8005 (and Komorsky-Lovrić Š, Riedl K, Gulaboski R, Mirčeski V, Scholz F (2003) *Langmuir* 19:3090)
241. Wadhawan JD, Evans RG, Compton RG (2002) Voltammetric Characteristics of Graphite Electrodes Modified with Microdroplets of n-Butylferrocene. *J Electroanal Chem* 533:71-84
242. Tasakorn P, Chen J, Aoki K (2002) Voltammetry of a Single Oil Droplet on a Large Electrode. *J Electroanal Chem* 533:119-126
243. Jinag J, Kucernak A (2002) Electrooxidation of Small Organic Molecules on Mesoporous Precious Metal Catalysts I: CO and Methanol on Platinum. *J Electroanal Chem* 533:153-165
244. Sánchez Ramos S, Bosch Reig F, Gimeno Adelantado JV, Yusá Marco DJ, Doménech Carbó A (2002) Application of XRF, XRD, Thermal Analysis, and Voltammetric Techniques to the Study of Ancient Ceramics. *Anal Bioanal Chem* 373:893-900
245. Lawrence NS, Thompson M, Davis J, Jiang L, Jones TGJ, Compton RG (2002) Carbon-Epoxy Electrodes: Unambiguous Identification of Authentic Triple-Phase (Insulator/Solution/ Electrode) Processes. *Chem Commun* 1028-1029
246. Perez-Ramirez J, Mul G, Kapteijn F, Moulijn JA, Overweg AR, Doménech A, Ribera A, Arends IWCE (2002) Physicochemical

- Characterization of Isomorphously Substituted FeZSM-5 During Activation. *J Catalysis* 207:113-126
247. Widmann A, Kahlert H, Petrovic-Prelevic I, Wulff H, Yakhmi JV, Bagkar N, Scholz F (2002) Structure, Insertion Electrochemistry and Magnetic Properties of a New Type of Substitutional Solid Solutions of Copper, Nickel and Iron Hexacyano-Ferrates/Hexacyanocobaltates. *Inorg Chem* 42:5706-5715
248. Almáida CMVB, Giannetti BF (2002) A New and Practical Carbon Electrode for Insoluble and Ground Samples. *Electrochem Commun* 4:985-988
249. Yang M, Li HL (2002) Determination of Trace Nitrite by Differential Pulse Voltammetry using Magnetic Microspheres. *Coll Czech Chem Commun* 67:1173-1180
250. Domenech-Carbo A, Domenech-Carbo MT, Gimeno-Adelantado JV, Bosch-Reig F (2002) Electrochemical Solid State Analysis: Analytical Applications of Electrode Modification by Solid Microparticles. *Rec Res Developm in Pure & Appl Anal Chem* 4:107-121
251. Keane L, Hogan C, Forster RJ (2002) Dynamics of Charge Transport Through Osmium Tris Dimethoxy Bipyridyl Solid Deposits. *Langmuir* 18:4826-4833
252. Walsh DA, Keyes TE, Forster RJ (2002) Redox Switching in Solid Deposits: Triazole Bridged Osmium Dimmers. *J Electroanal Chem* 538/539:75-85
253. Shankaran DR, Narayanan SS (2002) Cobalt Hexacyanoferrate-Modified Electrode for Amperometric Assay of Hydrazine. *Russ J Electrochem* 38:987-991
254. Schröder U, Wadhawan J, Evans RG, Compton RG, Wood B, Walton DJ, France RR, Marken F, Bulman Page PC, Hayman CM (2002) Probing Thermodynamic Aspects of Electrochemically Driven Ion-transfer Processes Across Liquid/Liquid Interfaces: Pure Versus Diluted Redox Liquids. *J Phys Chem B* 106:8697-8704
255. Wooster TJ, Bond AM, Honeychurch MJ (2003) An Analogy of an Ion-Selective Electrode Sensor Based on the Voltammetry of Microcrystals of Tetracyanoquinodimethane or Tetrathiafulvalene Adhered to an Electrode Surface. *Anal Chem* 75:586-592
256. Cepriá G, Usón A, Pérez-Arantegui J, Castillo JR (2003) Identification of Iron(III) Oxides and Hydroxyl-Oxides by Voltammetry of Immobilised Microparticles. *Anal Chim Acta* 477:157-168.

257. Lovric M, Scholz F (2003) Modeling Cyclic Voltammograms of Simultaneous Electron and Ion Transfer Reactions at a Conic Film Three-Phase Electrode. *J Electroanal Chem* 540:89-96
258. Aoki K, Tasakorn P, Chen J (2003) Electrode Reaction at Sub-Micron Oil|Water|Electrode Interfaces. *J Electroanal Chem* 542:51-60
259. Gulaboski R, Riedl K, Scholz F (2003) Standard Gibbs Energies of Transfer of Halogenate and Pseudohalogenate Ions, Halogen Substituted Acetates, and Cycloalkyl Carboxylate Anions at the Water|Nitrobenzene Interface. *PCCP* 5:1284-1289
260. Marken F, Cromie S, McKee V (2003) Electrochemically Driven Reversible Solid State Metal Exchange Processes in Polynuclear Copper Complexes. *J Solid State Electrochem* 7:141-146
261. Cepriá G, Bolea E, Laborda F, Castillo JR (2003) Quick, Easy, and Inexpensive way to Detect Small Metallic Particles in Suspension using Voltammetry of Immobilized Microparticles. *Anal Letters* 36:921-929
262. Gulaboski R, Mirceski V, Scholz F (2003) Determination of the Standard Gibbs Energies of Transfer of Cations and Anions of Amino Acids and Small Peptides Across the Water | Nitrobenzene Interface. *Amino Acids* 24:149-154
263. Tan WT, Lim EB, Bond AM (2003) Voltammetric Studies on Microcrystalline C<sub>60</sub> Adhered to an Electrode Surface by Solvent Casting and Mechanical Transfer Methods. *J Solid State Electrochem* 7:134-140
264. Grygar T, Hradilova J, Hradil D, Bezdiccka P, Bakardjieva S (2003) Analysis of Earthy Pigments in Grounds of Baroque Paintings. *Anal Bioanal Chem* 375:1154-1160
265. Doménech-Carbó A, Dménéch-Carbó MT, Saurí-Peris MC, Gimendo-Adelantado JV, Bosch-Reig F, (2003) Electrochemical Identification of Anthraquinone-Based Dyes in Solid Microsamples by Square Wave Voltammetry Using Graphite/Polyester Composite Electrodes. *Anal Bioanal Chem* 375:1169-1175
266. Gulaboski R, Scholz F, (2003) The Lipophilicity of Peptide Anions – An Experimental Data Set for Lipophilicity Calculations. *J Phys Chem B* 107:5650-5657
267. Tan WT, Ng GK, Bond AM (2000) Electrochemical Oxidation of Microcrystalline Tetrathiafulvalene (TTF) at an Electrode-Solid-Aqueous (KBr) Interface. *Malaysian J Chem* 2: 34-42
268. Tan WT, Chan SY, Lee CK, (2002) Electrochemical Reduction of Microparticles of Bismuth Vanadate (Bi<sub>4</sub>V<sub>2</sub>O<sub>11</sub>) Mechanically

- Attached to a Carbon Electrode Surface. *Malaysian J Chem* 4:34-42
269. Bouchard G, Galland A, Carrupt PA, Gulaboski R, Mirčeski V, Scholz F, Girault HH (2003) Standard Partition Coefficients of Anionic Drugs in the *n*-Octanol/Water System Determined by Voltammetry at Three-Phase Electrodes. *Phys Chem Chem Phys* 5:3748-3751
270. Jayalakshmi M, Mohan Rao M, Scholz F (2003) Electrochemical Behaviour of Solid Lithium Manganate ( $\text{LiMn}_2\text{O}_4$ ) in Aqueous Neutral Electrolyte Solution. *Langmuir* 19:8403 – 8408
271. Scholz F, Gulaboski R, Caban K (2003) The Determination of Standard Gibbs Energies of Transfer of Cations Across the Nitrobenzene | Water Interface with the Help of a Three-Phase Electrode. *Electrochem Commun* 5:929-934
272. Inzelt G (2003) Formation and Redox Behaviour of Polycarbazole Prepared by Electropolymerisation of Solid Carbazole Crystals Immobilized on an Electrode Surface. *J Solid State Electrochem* 7:503-510
273. Wain AJ, Wadhawan JD, Compton RG (2003) Electrochemical Studies of Vitamin  $\text{K}_1$  Microdroplets: Electrocatalytic Hydrogen Evolution. *Chem Phys Chem* 4:974-982
274. Grygar T, Dedecek J, Kruiver PP, Dekkers MJ, Bezdicka P, Schneeweiss O (2003) Iron Oxide Mineralogy in Late Miocene Red Beds from La Gloria, Spain: Rock-Magnetic, Voltammetric and Vis Spectroscopy Analyses. *Catena* 53:115-132
275. Kovanda F, Grygar T, Dornicak V (2003) Thermal Behaviour of Ni-Mn Layered Double Hydroxide and Characterization of Formed Oxides. *Solid State Sci* 5:1019-1026
276. Hasse U, Nießen J, Scholz F (2003) Atomic force Microscopy of the Electrochemical Reductive Dissolution of Sub-Micrometer Sized Crystals of Goethite Immobilized on a Gold Electrode. *J Electroanal Chem* 556:13-22
277. Gulaboski R, Caban K, Stojek Z, Scholz F (2004) The Determination of the Standard Gibbs Energies of Ion Transfer Between Water and Heavy Water by using the Three-Phase Electrode Approach. *Electrochem Commun* 6:215-218
278. Hasse U, Wagner K, Scholz F (2004) Nucleation at Three-Phase Junction Lines: *In situ* Atomic Force Microscopy of the Electrochemical Reduction of Sub Micrometer Size Silver and Mercury(I) Halide Crystals Immobilized on Gold Electrodes. *J Solid State Electrochem* 8: 842-853

- 
279. Hasse U, Scholz F (2004) In situ AFM Evidence of the Involvement of an Oversaturated Solution in the Course of Oxidation of Silver Nanocrystals to Silver Iodide Crystals. *Electrochem Commun* 6:409-412
280. Komorsky-Lovrić Š, Mirčeski V, Kabbe Ch, Scholz F (2004) An *in situ* Microscopic Spectroelectrochemical Study of a Three-Phase Electrode where an Ion Transfer at the Water | Nitrobenzene Interface is Coupled to an Electron Transfer at the Interface ITO | Nitrobenzene. *J Electroanal Chem* 566:371-377
281. Mirčeski V, Gulaboski R, Scholz F (2004) Square-Wave Thin-Film Voltammetry in the Presence of Uncompensated Resistance. *Electroanal Chem*, 566:351-360
282. Gulaboski R, Galland A, Bouchard G, Caban K, Kretschmer A, Carrupt PA, Stojek Z, Girault HH, Scholz F (2004) A Comparison of the Solvation Properties of 2-Nitrophenyloctyl Ether, Nitrobenzene, and *n*-Octanol as Assessed by Ion Transfer Experiments. *J Phys Chem, B* 108:4565
283. Bond AM (2002) Illustration of the Principles of Voltammetry at Solid-Electrode-Solvent (Electrolyte) interfaces when Redox Active Microparticles are Adhered to an Electrode Surface. In: *Broadening Electrochemical Horizons, Principles and Illustration of Voltammetric and Related Techniques*, Oxford University Press
284. Wadhawan JD, Wain AJ, Kirkham AN, Walton DJ, Wood B, France RR, Bull SD, Compton RG (2003) Electrocatalytic Reactions Mediated by *N,N,N',N'*-Tetraalkyl-1,4-Phenylenediamine Redox Liquid Microdroplet-Modified Electrodes: Chemical and Photochemical reactions in, and at the Surface of, Femtoliter Droplets. *J Am Chem Soc* 125: 11418-11429
285. Banks CE, Davies TJ, EvansRG, Hignett G, Wain AJ, Lawrence NS, Wadhawan JD, Marken F, Compton RG (2003) Electrochemistry of Immobilised Redox Droplets: Concepts and Applications. *Phys Chem Chem Phys* 5: 4053-4069
286. Wain AJ, Lawrence NS, Greene PR, Wadhawan JD, Compton RG (2003) Reactive Chemistry Via the Redox Switching of Microdroplets of 4-Nitrophenyl Nonyl Ether in the Presence of Aqueous Electrolytes. *Phys Chem Chem Phys* 5: 1867-1875
287. Wadhawan JD, Wain AJ, Compton RG (2003) Electrochemical Probing of Photochemical Reactions Inside Femtolitre Droplets Confined to Electrodes. *Chem Phys Chem* 4: 1211-1215
288. Davies TJ, Brooks BA, Fisher AC, Yunus K, Wilkins AJ, Greene PR, Wadhawan JD, Compton RG (2003) A Computational and



- Experimental Study of the Cyclic Voltammetry Response of Partially Blocked Electrodes. Part II: Randomly Distributed and Overlapping Blocking Systems. *J Phys Chem B* 107:6431-6444
289. Marken F, Blythe A, Compton RG, Bull SD, Davies SG (1999) Sulfide Accumulation and Sensing Based on Electrochemical Processes in Microdroplets of  $N^1$ -[4-(dihexylamino)phenyl]- $N^1,N^4,N^4$ -triethyl-1,4-Phenylenediamine. *Chem. Commun.* 1823-1824
290. Snook G (2000) Investigation of Solid-State Reactions by Electrochemical and Quartz Crystal Microbalance Measurements, Ph. D. Thesis, Monash University, Melbourne, 2000
291. Neufeld A (2003) Investigations Using a Kelvin Probe Instrument and Solid State Electrochemical Techniques: The Initiation Mechanism of Corrosion of Zinc and The Solid-Solid Electrochemical Transformation of CuTCNQ, Ph. D. Thesis, Monash University, Melbourne
292. Widmann A (2003) Insertionselektrochemie von festen Metallhexacyano-metallaten, Ph. D. Thesis, Universität Greifswald, 2003
293. Gulaboski R: The Determination of Standard Gibbs Energies of Ion Transfer across Liquid/Liquid Interfaces with the Help of Three-Phase Electrodes, Ph. D. Thesis, Universität Greifswald, 2004
294. Zhang J, Bond AM (2004) Voltammetric Studies with Adhered Microparticles and the Detection of a Dependence of Organometallic Cis + Trans First-Order Isomerization Rate Constants on the Identity of the Ionic Liquid, *J Phys Chem B* 108:7363-7372
295. Snook G, Bond AM, Fletcher S (2003) The catalysis of solid state intercalation processes by organic solvents. *J Electroanal Chem* 554-555: 157-165
296. Neufeld AK, Madsen I, Bond AM, Hogan CF (2003) Phase, Morphology, and Particle Size Changes Associated with the Solid-Solid Electrochemical Interconversion of TCNQ and Semiconducting CuTCNQ (TCNQ = Tetracyanoquinodimethane). *Chem Mat* 15: 3573-3585
297. Guo S, Zhang J, Elton DM, Bond AM (2004) Fourier Transform Large-Amplitude Alternating Current Cyclic Voltammetry of Surface-Bound Azurin. *Anal Chem* 76:166-177
298. Wu P, Cai C (2004) The Solid State Electrochemistry of Samarium(III) Hexacyanoferrate. *J Solid State Electrochem* 8:538-543

299. Wooster TJ, Bond AM (2003) Ion Selectivity Obtained under Voltammetric Conditions when a TCNQ Chemically Modified Electrode is Presented with Aqueous Solutions Containing Tetraalkylammonium Cations. *Analyst* 128:1386-1390
300. Thompson M, Lawrence NS, Davis J, Jiang L, Jones TGJ, Compton RG (2002) A Reagentless Renewable *N,N'*-Diphenyl-*p*-phenylenediamine loaded Sensor for Hydrogen Sulfide. *Sens Actuat B-Chem* 87:33-40
301. Domenech A, Alvaro M, Ferrer B, Garcia H (2003) Electrochemistry of Mesoporous Organosilica of MCM-41 Type Containing 4,4'-Bipyridinium Units: Voltammetric Response and Electrocatalytic Effect on 1,4-Dihydrobenzoquinone Oxidation. *J Phys Chem B* 107:12781-12788
302. Grygar T, Kuckova S, Hradil D, Hradilova J (2003) Electrochemical Analysis of Natural Solid Organic Dyes and Pigments. *J Solid State Electrochem* 7:706-713
303. Fay N, Dempsey E, Kennedy A, McCormac T (2003) Synthesis and Electrochemical Characterisation of  $[\text{Ru}(\text{bpy})_3]_3[\text{P}_2\text{W}_{18}\text{O}_{62}]$ . *J Electroanal Chem* 556:63-74
304. Domenech-Carbo A, Domenech-Carbo MT, Osete-Cortina L, Gimeno-Adelantado JV, Sanchez-Ramos S, Bosch-Reig F (2003) Quantitation of Metal Ions in Archaeological Glass by Abrasive Stripping Square-Wave Voltammetry using Graphite/Polyester Composite Electrodes. *Electroanal* 15:1465-1475
305. Wildgoose GG, Pandurangappa M, Lawrence NS, Jiang L, Jones TGJ, Compton RG (2003) Anthraquinone-Derivatised Carbon Powder: Reagentless Voltammetric pH Electrodes: *Talanta* 60:887-893
306. Zhang J, Bond AM, Belcher J, Wallace KJ, Steed JW (2003) Electrochemical Studies on the Modular Podand 1,3,5-tris(3-((ferrocenylmethyl)amino)pyridiniumyl)-2,4,6-triethylbenzene Hexafluorophosphate in Conventional Solvents and Ionic Liquids. *J Phys Chem B* 107:5777-57
307. Galova M, Grygar T, Pikna L, Lux L (2003) Electrochemical Study on the Reactivity of Fe Powders. *Chem Analit* 48:293-303
308. Zhang J, Bond AM (2003) Conditions Required to Achieve the Apparent Equivalence of Adhered Solid- and Solution-Phase Voltammetry for Ferrocene and other Redox-active Solids in Ionic Liquids. *Anal Chem* 75:2694-2702
309. Pandurangappa M, Lawrence NS, Compton RG (2002) Homogeneous Chemical Derivatisation of Carbon Particles: A Novel Method for Functionalising Carbon Surfaces. *Analyst* 127:1568-1571

310. Pandurangappa M, Lawrence NS, Jiang L, Jones TGJ, Compton RG (2003) Physical Adsorption of *N,N'*-Diphenyl-*p*-phenylenediamine onto Carbon Particles: Application to the Detection of Sulfide. *Analyst* 128:473-479
311. Grygar T, Bezdicka P, Hradil D, Pikna L (2003) Electrochemical Analysis of Metal Oxides. *Solid State Chem Solid State Phenomena* 90-91:45-49
312. Cepria G, Uson A, Perez-Arantequi J, Castillo JR (2003) Identification of Iron(III) Oxides and Hydroxy-oxides by Voltammetry of Immobilised Microparticle. *Anal Chim Acta* 477:157-168
313. Uzun D, Ozser ME, Yoney K, Icil H, Demuth M (2003) Synthesis and Photophysical Properties of *N,N'*-bis(4-Cyanophenyl)-3,4,9,10-perylene-bis(dicarboximide) and *N,N'*-bis(4-Cyanophenyl)-1,4,5,8-naphthalenediimide. *J Photochem Photobiol A Chem* 156:45-54
314. Alonso Sedano AB, Tascón García L, Vázquez Barbado D, Sánchez Batanero P (2004) Electrochemical Study of Copper and Iron Compounds in the Solid State by Using Voltammetry of Immobilized Microparticles: Application to Copper Ferrite Characterization. *J Electroanal Chem* 566: 433-441
315. Wildgoose GG, Leventis HC, Streeter I, Lawrence NS, Wilkins SJ, Jiang L, Jones TGJ, Compton RG (2004) Abrasively Immobilised Multiwalled Carbon Nanotube Agglomerates: A Novel Electrode Material Approach for the Analytical Sensing of pH. *ChemPhysChem* 5:669-677
316. Rees NV, Wadhawan JD, Klymenko OV, Coles BA, Compton RG (2004) An Electrochemical Study of the Oxidation of 1,3,5-Tris[4-[(3-methylphenyl)phenylamino]phenyl]benzene. *J Electroanal Chem* 563:191-202
317. Domenech-Carbo A, Torres FJ, Alarcon J (2004) Electrochemical characterization of cobalt cordierites attached to paraffin-impregnated graphite electrodes. *J Solid State Electrochem* 8:127-137
318. Domenech-Carbo A, Sanchez-Ramos S, Yusa-Marco DJ, Moya-Moreno M, Gimeno-Adelantado J, Bosch-Reig F (2004) Electrochemical determination of boron in minerals and ceramic materials. *Anal Chim Acta* 501:103-111

# Subject Index

## A

Abrasive stripping voltammetry 78, 255  
Acetylene black 154  
Acridine 123  
Ag<sub>2</sub>S 148  
Ag<sub>2</sub>Se 148  
Ag<sub>2</sub>Te 148  
Ag<sub>3</sub>AsS<sub>3</sub> 96  
Ag<sub>3</sub>SbS<sub>3</sub> 96  
AgCl-AgBr 102  
Alloys 77  
  - dental 255  
  - Pb-Sn 78  
  - silver-copper 80, 271  
  - tin-mercury 80  
Amino acids 218  
Ascorbic acid 155, 200  
Azobenzene 123, 261  
Azurin 123, 282  
Azurite 89

## B

Ba-hexaferrite 144  
Batteries 261, 262, 266, 269,  
Berlin green 131, 178  
Berlin white 131, 178  
Bi<sub>4</sub>V<sub>2</sub>O<sub>11</sub> 279  
Bilayered systems 178  
Bipyridyl triazole 271

Bis( $\eta^5$ -pentaphenyl-  
cyclopentadienyl)iron(II)-iron(III)  
122  
Born-Haber cycles 136  
Boulangerite 82  
Butylferrocene 188, 277

## C

C<sub>60</sub> 265, 270, 279  
Cadmium hexacyanoferrate 130  
Cadmium sulfide 277  
Calibration 91  
Calomel 94  
Carbazole 123, 280  
Carbon black 154  
Ceramic glazes 275  
Chalcogenides 262  
Charcoal 5  
Charge transfer kinetics 237  
Chiral ions 221  
Chiral liquids 221  
Chlorophyll 206  
Chromium(II) hexacyano-  
chromate(III) 258  
Chromium(III) hexacyano-  
ferrate(II) 124  
Chronoamperometry 158, 169, 256  
Chronocoulometry 83  
Cobalt cordierites 91

Cobalt hexacyanoferrate 263  
Cobaltocene 123  
Cocaine 117, 123, 265  
Colloids 4  
[Co(mtas)<sub>2</sub>] 123, 259  
Contact angle 183  
Convolutive model 230  
Copper hexacyanoferrate 71, 155,  
263, 264, 273  
Copper-nickel hexacyanoferrate-  
hexacyano-cobaltate 103  
Cordierites 284  
Corrosion 81, 265  
Cr(CO)<sub>2</sub>(dppe)<sub>2</sub> 122  
Cr(CO)<sub>2</sub>(dpe)<sub>2</sub> 45, 56, 108, 257,  
260  
[(C<sub>4</sub>H<sub>9</sub>)<sub>4</sub>N][Cr(CO)<sub>5</sub>I] 122, 261  
Cr oxides 146  
Cu(C<sub>2</sub>H<sub>3</sub>O<sub>2</sub>)<sub>2</sub>·2Cu(OH)<sub>2</sub> 89  
Cu<sub>2</sub>(OH)<sub>3</sub>Cl 90  
CuCO<sub>3</sub>·Cu(OH)<sub>2</sub> 90  
CuS-CuSe 100  
CuS<sub>x</sub>Se<sub>1-x</sub> 260  
CuTCNQ 282  
Cysteine 155, 264  
Cytochrome *c* 256

**D**

Dawson molybdate anion salts 258  
Decamethylferrocene 43, 49, 112,  
123, 215, 242, 257, 271, 272  
Decaphenylferrocene 123  
DEDRPD 187, 192  
Dental amalgams 256  
Dichloro ethane 217  
Diffuse reflectance spectroscopy  
275  
Dihydrobenzoquinone 283  
Diphenylamine 123, 274  
2,2-Diphenyl-1-picrylhydrazyl  
(DPPH) 123, 265  
Dissolution reactions 141  
Dithiocarbamates 123, 138, 256  
DNA 274, 275, 277  
Droplets 25

- attachment of 25  
Dyes 123, 279, 283

**E**

Eicosane 154  
Electrocatalysis 153, 201, 265, 273  
Electrochemical dissolution 263  
Electrochemical quartz crystal  
microbalance 56  
Electrode 2, 19  
- paraffin impregnated graphite  
19  
- basal plane pyrolytic graphite  
20  
- boron doped diamond 21, 270  
- carbon-wax composite 154  
- compact 2  
- composite 7, 20  
- glassy carbon 21  
- highly oriented pyrolytic carbon  
(HOPG) 20  
- immobilized droplets 11  
- immobilized particles 11  
- ITO 29, 32  
- modified paste 87  
- partially blocked 247  
- paste 7, 268  
- pencil lead 20  
- sandwich 8  
- thermistor 62  
- three-phase 11

Electrography 3  
Electrolytes 19, 22  
Electron transfer 212  
Electropolymerisation 207, 280  
Entropy 73  
Enzymatic conversion 149  
Extrathermodynamic assumption 13

**F**

Facilitated ion transfer 197  
Fe( $\eta^5$ -C<sub>5</sub>Ph<sub>5</sub>)( $\eta^6$ -C<sub>6</sub>H<sub>5</sub>)C<sub>5</sub>Ph<sub>4</sub>) 122,  
264  
Fe(III) tetraphenyl porphyrine  
chloride 223

$(\text{Fe}_x\text{Cr}_{1-x})_2\text{O}_3$  265  
 $\text{Fe}_2\text{O}_3$  143, 274  
 $\text{Fe}_3\text{O}_4$  143  
 $\text{FeOOH}$  143  
 $\text{FeOOH}/\text{MnO}_2$  91  
 Ferrihydrite 143  
 Ferrocene 112, 123, 251, 283  
 Ferrocyclochrom 200  
 Finite diffusion space 155  
 Formal potentials 135, 195, 216, 219  
 Fullerene 57, 121, 123, 269

## G

Gibbs energy of ion transfer 209, 219, 224  
 Gibbs free energy 194  
 Glutathione 155  
 Goethite 50, 144, 152, 258, 261, 272, 280

## H

Halothane 205  
 Hematite 144  
 Hexacyanoferrates 128, 267, 268, 271  
 Hexacyanometalates 134  
 $\text{Hg}(\text{Et}_2\text{dte})_2$  139  
 $\text{HgS}/\text{HgO}$  91  
 High-temperature superconductor 94, 255  
 High-performance abrasive stripping voltammetry 255  
 Hydrazine 154, 155  
 Hydroquinone 151, 271  
 Hydrotalcite 263  
 Hyphenated techniques 31

## I

Immiscibility polarization 172  
 Immiscible liquids 9  
*In situ* calorimetry 62, 275  
*In situ* X-ray diffraction 58, 258  
 Indigo 34, 123, 261  
 Inner standard 91

Interface of two immiscible electrolyte solutions (ITIES) 210  
 Interfacial tension 183  
 Iodine 225  
 Iodopentacarbonyl chromium(0) 57  
 Ion potential 137  
 Ion transfer 209  
 Iron oxides 90, 273  
 Iron(II) hexacyanochromate(III) 124, 258  
 Iron(II) hexacyanomanganate(III) 125  
 Iron(III) hexacyanoferrate 73  
 Iron(III) hydroxy-oxides 258, 259  
 Iron(III) hydroxide 6  
 Iron(III) oxides 141, 278  
 Iron(III)-cadmium(II) hexacyanoferrates 265  
 Isomerization 124

## K

Kubelka-Munk function 38

## L

$\text{La}(\text{Ni},\text{Cr})\text{O}_3$  265  
 $\text{La}(\text{Ni},\text{Fe})\text{O}_3$  265  
 Laccase 151  
 $\text{LaNi}_5$  147, 259  
 Lead oxide 268, 272  
 $\text{LiCoO}_2$  148, 270, 272  
 Li-Fe-Mn-O spinels 107  
 $\text{LiMn}_2\text{O}_4$  148, 270, 272, 280  
 Li-Mn-O spinels 144  
 $\text{LiNiO}_2$  266, 272  
 Liphophilicity 210  
 Liquid | liquid interface 209

## M

Maghemite 144  
 Magnetic microspheres 278  
 Magnetite 144  
 Malachite 89  
 Manganates 147, 263  
 Manganese oxides 268

Manganese(II) hexacyanoferrate 125  
Marangoni streaming 185, 227, 252  
Mars black 90  
Mass transfer parameter 162  
Mediaeval glazes 89, 268  
Menthol 218  
Mercury halides 256  
Mercury(I) iodide 5  
Metal hexacyanometalates 102, 259, 274  
Metallocenes 256  
Metalloporphyrins 271  
Metals 77  
Methylthiophene 188, 207, 273  
Microdroplets 140  
Microelectrode 251  
Micromanipulator 255  
Microscopy 35  
- atomic force 49, 280  
- *in situ* incident light 35  
- *in situ* transmission light 41  
- scanning tunnelling 49  
Migration 241  
Minerals 81, 256  
Miscibility gap 171, 262, 269  
Mixing entropy 99  
[ $\{\text{Mn}(\text{CO})(\eta^2\text{-dpe})\text{Br}\}_2(\mu\text{-dpe})$ ] 262  
 $\text{Mn}(\text{CO})_2(\eta^3\text{-P}_2\text{P}')\text{Br}$  127, 262  
 $\text{Mn}(\text{CO})_3(\eta^2\text{-Ph}_2\text{PCH}_2\text{PPh}_2)\text{Cl}$  110, 122, 266  
[ $\text{Mn}(\text{CN})(\text{CO})_2\{\text{P}(\text{OPh})_3\}(\text{dppm})$ ] 122  
 $\text{Mn}_2\text{O}_3\text{-}\alpha\text{-Fe}_2\text{O}_3$  106  
 $\text{MnO}_2$  93, 147, 263  
Multiwalled carbon nanotube 284

**N**

NADH 200  
Nickel hexacyanoferrate 130, 155, 266  
Nickel-iron hexacyanoferrates 259  
Nitrobenzene 215, 217, 281  
4-Nitrophenyl nonyl ether 188, 281  
Nitrophenyl octyl ether 218, 281

Nucleation growth 14, 118, 260, 270

**O**

Octacyanomolybdates 267  
Octacyanotungstates 267  
*n*-octanol 218, 281  
Ohmic drop 211  
Organic compounds 107  
Organometallics 107  
Organosilica 283  
Osmium bis(bipyridyl)tetrazine chloride 122, 269  
Osmium tris dimethoxy bipyridyl 115, 122, 278  
Oxides 106, 259, 280

**P**

Paraloid B72 87  
Particles 23  
- immobilization of 23  
 $\text{Pb}(i\text{-Pr}_2\text{dte})_2$  139  
 $\text{Pb}(\text{OH})\text{Cl}$  59, 258  
 $\text{Pb}_3\text{O}_4$  87  
 $\text{PbO}$  14, 49, 59, 87  
 $\text{PbO}/\text{HgO}$  91  
 $\text{PbO}_2$  87  
Pd 259  
Peltier heat 69  
Pencil-leads 259  
Peptides 218  
Perovskites 146  
Pesticides 260  
Phase  
- identification 82  
- segregation 174  
- transition 96, 261  
Phenylendiamine 270  
Phosphorus 15, 269  
Photoactivity 110  
Photosynthesis 206  
Phthalocyanine 123, 259, 261, 267, 270, 272  
Phylloquinone 206

Pigments 81, 257, 268, 273, 276,  
279, 283  
Platinum particles 154  
Platinum phthalocyanine 114  
Point of zero charge 5  
Poly(3-methylthiophene) 207  
Polynuclear copper complexes 116  
Porphyrin 133, 267, 269  
Powder mixtures 256  
Pressed cells 2  
Proustite 257, 260  
Prussian blue 47, 102, 128, 130,  
152, 178, 258, 259, 272  
Pyrrargyrite 257, 261  
Pyrostitpnite 257, 260

## Q

Quartz crystal microbalance 260  
Quinhydrone 151, 123, 257

## R

Re(Br)(CO)X 122  
Redox liquids 187  
Redox mixed phases 172, 262  
Redox solid solutions 172  
Rhenium(II) carbonyl phosphine  
complexes 122, 263  
Robinson type 116  
[Ru(bpy)<sub>3</sub>]<sub>3</sub>[P<sub>2</sub>W<sub>18</sub>O<sub>62</sub>] 283  
Ru<sup>(II)</sup>(dcbpy)<sub>2</sub>(NCS)<sub>2</sub> 264  
RuO<sub>2</sub>-PVC film 163  
Ruthenium oxide 277  
Ruthenium(III) 155  
Ruthenium(III)  
diphenyldithiocarbamate 122,  
264

## S

Samarium(III) hexacyanoferrate  
282  
Silver halides 51  
Silver hexacyanoferrate 130  
Silver iodide 281  
Silver octacyanomolybdate(IV) 37  
Single particles 147, 262

Smithite 261  
Solid solutions 98  
Spectroelectrochemistry 32, 252, 281  
Spectroscopy  
- *in situ* electron spin resonance  
(ESR) 45  
- scanning electron 47  
Spinels 273  
Squaraine 178  
Stability constants 138  
Staircase voltammetry 155, 174,  
261  
Standard partition coefficient 210  
Standard potential of ion transfer  
210  
Stripping chronopotentiogram 150  
Stripping potential 149  
Substitution  
- electrochemically initiated 128  
Sulfhydryl compounds 155  
Sulfosalts 258  
Sulfur dioxide 155  
Surface current 159  
Suspensions 4

## T

Tafel plots 90  
TCNQ (Tetracyanoquinodimethane)  
36, 45, 49, 57, 118, 123, 176, 260,  
264, 266, 278, 282, 283  
Tetraalkyl-1,4-phenylenediamine  
28, 41, 187, 262, 264, 272, 275,  
281, 284  
Tetrahexylphenylenediamine 45  
Tetraphenylarsomium 14  
Tetraphenylborate 14  
Tetraphenylviologen 123  
Tetrathiafulvalene 57, 120, 260,  
273, 278, 279  
Thallium sulfides 93  
Thallium-tin sulfides 87  
Thermodynamic data 96  
Thin-film voltammetry 232, 281  
Thiocyanate 260  
Thiols 155  
Thiosulfate 155



Thiourea 260  
THPD 188, 246  
Three-phase electrode 183  
Three-phase junction 15, 52, 158,  
160, 164, 211, 251, 263, 268, 269  
TMHPD 196  
TMPD 189  
TOPD 196  
Trechmannite 261  
Tris(2,2'-bipyridine) ruthenium(II)  
hexafluorophosphate 122, 267  
TRPD 187, 192, 276  
TTF 123

### U

Uhlich approximation 96  
Umber 90  
Uncompensated resistance 237  
Uranium oxides 257

### V

Van Dyke brown 90

Vanadium-doped zirconias 276  
Vitamin K<sub>1</sub> 188, 206, 280  
Voltammetry of immobilized  
microparticles 78

### W

[W(CO)<sub>2</sub>(dppe)] 122  
Wagner factor 160  
Würster's blue 200

### X

Xanthoconite 257, 260  
X-ray electron probe microanalysis  
47

YBa<sub>2</sub>Cu<sub>3</sub>O<sub>7-x</sub> 255, 256  
Young equation 184

### Z

ZrO<sub>2</sub> 276